Heidi Nordmark

Microstructure studies of silicon for solar cells

Defects, impurities and surface morphology

Thesis for the degree of Philosophiae Doctor

Trondheim, January 2009

Norwegian University of Science and Technology
Faculty of Natural Sciences and Technology
Department of Physics

NTNU
Norwegian University of
Science and Technology

NTNU
Norwegian University of Science and Technology

Thesis for the degree of Philosophiae Doctor

Faculty of Natural Sciences and Technology
Department of Physics

ISBN 978-82-471-1400-1 (printed ver.)
ISBN 978-82-471-1401-8 (electronic ver.)
ISSN 1503-8181

Doctoral theses at NTNU, 2009:16

Printed by NTNU-trykk

Abstract

This thesis consists of three different topics with applications within silicon solar cell technology, (i) Study of impurities and defects in multicrystalline silicon grown from metallurgical feedstock, (ii) Hydrogen induced defects in hydrogenated Cz and multi-crystalline silicon, and (iii) Texturing and silicon whiskers growth using tungsten hot filament and hydrogen as source gas. The common aim is to produce cheaper, more efficient solar cells.

In the first three papers, a multicrystalline silicon ingot grown from metallurgical feedstock is characterized by glow discharge mass spectroscopy, Fourier transform infrared spectroscopy, transmission electron microscopy techniques, electron beam induced current, electron back-scattered diffraction, and photo luminescence. A very high impurity level, resulted in a lifetime of only ~ 1 μs, diffusion length of about 12 μm and conversion efficiency of only 60 % of that of commercial multicrystalline silicon. Silicon oxide precipitates contaminated almost all dislocations, stacking faults and grain boundaries. Nickel-rich multi-metallic silicides were frequently observed in grain boundaries, while a few multi-metallic clusters, consisting of a nickel-rich core precipitate with copper nodules and small spherical Cu_3Si precipitates surrounded by dislocation cascades, were observed close to grain boundary triplet points. Iron was found to be partly precipitated in the core of most multi-metallic precipitates and partly interstitially dissolved via Fe_iB_s pairs, or atomically segregated to the core of structural defects. Small angle grain boundaries contaminated with metallic impurities showed strong recombination activity. Grain boundaries heavily contaminated with oxides were also found to be recombination active, while clean twins showed no recombination activity. The high concentration of oxide precipitates was found to be the main factor responsible for the low-quality of wafers after gettering. The oxide precipitates have a strong recombination activity, and an ability to act as internal gettering sinks during the solidification step and device processes. The possibility of using this material depends mainly on controlling the precipitation process during crystallization and the ability to reduce the density of oxygen or oxygen-containing defect centres during post-solidification.

In part 2, paper 4-7, Hydrogen defect formation after hydrogenation of differently doped Si substrates has been studied by Raman spectroscopy, atomic force microscopy, scanning and transmission electron microscopy, secondary ion mass spectroscopy and lifetime measurements. Substrate texturing of polished and as cut Cz and multi-crystalline Si surfaces was observed after hydrogen plasma treatment due to etching and redeposition of $Si\text{-}H_x$ species on the surface. The surface roughness was found to depend on doping, defect formation in the bulk and grain orientation, being almost flat for {211} oriented grains, and consisting of symmetrical cones ~ 100 nm, in {100} oriented samples. In the bulk, high hydrogen concentrations, well above the solubility level of hydrogen in silicon, lead to hydrogen induced defect formation, mainly plates in {111} and {100} planes consisting of $Si\text{-}H_x$ bonds filled with H_2 gas bubbles. The platelets were found to nucleate with high density, in areas with high concentration of damage from implantation or at extended defects, like dislocations, surfaces or cracks from sawing and with low density, homogenous in the bulk. The platelets were found to be more stable in p type silicon than in similarly doped n type silicon. After annealing at 1000 °C in air, evidence for oxygen and in some cases copper segregation to the remnants

of the hydrogen induced platelets was observed. A dose of 10^{15} H^+ implantation resulted in only a few platelets forming, mainly in {111} planes, while the same dose of Si^+ implantation + one hour H^+-plasma treatment, lead to similar microstructure, hydrogen profile and hydrogen concentration as archived by solely a dose of 3 x 10^{16} cm^{-2} H^+ implantation.

In paper 8 and 9, scanning and transmission electron microscopy were used to study silicon substrate texturing and whiskers growth on Si substrates using pure hydrogen source gas in a tungsten hot filament reactor. Substrate texturing in the nm-μm range of mono- and as-cut multicrystalline silicon was observed after deposition of WSi_2 particles that acted as a mask for subsequent hydrogen radical etching. For a specific experimental condition, simultaneous surface texturing and Si whisker growth were observed. The whiskers formed via vapour-solid-solid growth well below the eutectic temperature. Si whiskers were found to be partly crystalline and partly amorphous, consisting of pure Si with WSi_2 particles on their tips as well as incorporated into their structure.

Preface

This thesis is submitted in partial fulfillment on the requirements for the PhD degree at the Norwegian University of Science and Technology (NTNU). The work has been carried out at the Department of Physics from January 2004 to November 2008.

The main part of this thesis, including all TEM results, has been performed at NTNU at Department of Physics in the TEM Gemini Centre. Several other important contributions can be mentioned. SEM, (EBSD), PV-scan and GDMS have been performed at Department of Materials technology, NTNU; SIMS, Raman and AFM at University of Oslo; Lifetime and iron map at IFE and EBIC and FT-IR at the University in Milano, Bicocca.

The thesis consists of three parts. Part I contains the general introduction including theoretical background, limited literature review and a short description of the techniques used. Due to the huge amount of papers that deals with silicon and silicon solar cell related subjects, the literature review is far from complete, and to a large degree based on review articles. Part II contains the papers and is divided into three subparts with different subject; i) Investigation of multicrystalline silicon grown from metallurgical feedstock, ii) Hydrogen defect formation in silicon and iii) Surface texturing and silicon whisker growth. Part III contains unpublished results.

My contributions to the papers are all the TEM results, most of the SEM results and most of the Raman and PV-scan results. I also participated in the EBIC measurements. The experimental part will be dominated by the techniques I have used the most, scanning and transmission electron microscopy. Only a short description will be given of the other techniques.

Below is a list of all journal papers and conference proceedings that have resulted from my work. In all papers where I am the first author, I have done most of the experimental work. In the rest of the papers, I have contributed with TEM and SEM results, while the other coauthors have done the rest of the experimental work and written the paper. The papers included in this thesis are all the journal papers and one conference proceeding paper. In addition, three appendixes with additional results, closely related to the papers, have been included.

In addition to the scientific papers, I have contributed with posters and oral presentations at four different conferences, 20th European Photovoltaic Solar Energy Conference, Barcelona, Spain 2005 (poster), EMRS meeting spring 2006, Nice, France (oral presentation), 22nd European Photovoltaic Solar Energy Conference, Milano, Italy 2007 (two posters) and Gettering and defect engineering in semiconductor technology (GADEST) 2007 (one oral presentation and one poster).

Journal papers:

Published:

Evolution of hydrogen induced defects during annealing of plasma treated Czochralski silicon
H. Nordmark, A. Ulyashin, J. C. Walmsley, B. Tøtdal and R. Holmestad
*Nuclear Instruments and Methods in Physics Research B **253**, p 176-181 (2006)*

A Comparative Analysis of Structural Defect Formation in Si^+ Implanted and then Plasma Hydrogenated and in H^+ Implanted Crystalline Silicon
H. Nordmark, A. Ulyashin, J. C. Walmsley and R. Holmestad
*Solid State Phenomena **131-133**, p. 309-314 (2008)*

The Temperature Evolution of the Hydrogen Plasma Induced Structural Defects in Crystalline Silicon
H. Nordmark, A. Ulyashin, J. C. Walmsley, A. Holt and R. Holmestad
*Solid State Phenomena **131-133**, p. 315-320 (2008)*

Silicon Whisker Growth using Hot Filament Reactor with Hydrogen as Source Gas
H. Nagayoshi, H. Nordmark, N. Matsumoto, S. Nishimura, K. Terashima, J. C. Walmsley, R. Holmestad and A. Ulyashin
*Japanese Journal of Applied Physics **47**, p. 4807-4809 (2008)*

Accepted:

Study of defects and impurities in multicrystalline silicon grown from metallurgical silicon feedstock
S. Binetti , J. Libal, M. Acciarri, M. Di Sabatino, H. Nordmark, E. J. Øvrelid, J. C. Walmsley, R. Holmestad
Accepted for publication in Materials Science and Engineering B (2008)

TEM study of hydrogen defect formation at extended defects in hydrogen plasma treated polished and as cut multicrystalline silicon
H. Nordmark, A. Ulyashin, J. C. Walmsley and R. Holmestad
Accepted for publication in Journal of Applied Physics (2008)

Si substrate texturing and vapour-solid-solid Si nano-whiskers growth using pure hydrogen as source gas
H. Nordmark, H. Nagayoshi, A. Ulyashin, N. Matsumoto, S. Nishimura, K. Terashima, J. C. Walmsley and R. Holmestad
Accepted for publication in Journal of Applied Physics (2009)

To be submitted:

TEM study of oxide and metal silicide precipitation on structural defects in multicrystalline silicon
H. Nordmark, M. Di Sabatino, E. J. Øvrelid, J. C. Walmsley, P. Manshanden, L. J. Geerligs and R. Holmestad
(To be submitted)

Conference proceedings:

Studies of selected silicon feedstock impurities on properties of multicrystalline silicon ingots
E. Olsen, H. Nordmark and E. Øvrelid
Proceedings of the 20th European Photovoltaic Solar Energy Conference, Barcelona, Spain, p. 1082-1085 *(2005)*

Influence of an intensive hydrogenation on structural and point defect formation in silicon
A. Ulyashin, H. Nordmark, John C. Walmsley B. Tøtal and Randi Holmestad
Proceedings of the 21st European Photovoltaic Solar Energy Conference, Dresden, Germany, p. 1448-1451 *(2006)*

Comparative analysis of surface texturing of silicon by hydrogen plasma treatments or hydrogen radicals generated by a tungsten hot filament
H. Nordmark, A. Ulyashin, J. C. Walmsley and R. Holmestad
Proceedings of the 22nd European Photovoltaic Solar Energy Conference, Milano, Italy, p. 1686-1689 *(2007)*

TEM characterization of a multicrystalline Si material for PV applications
H. Nordmark, M. Di Sabatino, E. J. Øvrelid, J. C. Walmsley and R. Holmestad
Proceedings of the 22nd European Photovoltaic Solar Energy Conference, Milano, Italy, p. 1710-1714 *(2007)*

EBIC, EBSD and TEM study of grain boundaries in multicrystalline silicon cast from metallurgical feedstock
H. Nordmark, M. Di Sabatino, M. Acciarri, S. Binetti , J. Libal, E. J. Øvrelid, J. C. Walmsley and R. Holmestad
Proceedings of the 33rd IEEE Photovoltaic Specialists Conference, San Diego, USA (2008)

Unpublished work:

Appendix A: *TEM study of mc ingot with 100 ppm Ca contamination and unintentionally Cu contamination*

Appendix B: *Attachment to paper 5: Raman and SIMS analysis of H plasma treated n and p type silicon*

Appendix C: *Attachment to paper 7: Comparative SIMS analysis of H implanted and low dose Si^+ implanted + H^+ plasma treated Cz silicon*

Acknowledgement

First, I would like to thank my supervisors. Associate professor Bård Tøtdal was my main supervisor the first two years. He has been very supporting, always had time for questions and used a lot of his time helping me on the microscope. Professor Randi Holmestad has been my main supervisor for the rest of the period. She helped me finding new tasks when my first samples did not give any results and have guided me through the writing process. She is always positive, always has time for meetings and to correct papers. I would also like to thank Professor II John Walmsley who has been my co-supervisor, for good advices, help on the microscope and assistance with manuscripts.

A special thanks goes to Dr. rer. nat. habil. Alexander G. Ulyashin who introduced me into the field of hydrogen related phenomena in silicon. He has provided me with all of the hydrogen treated samples characterized in part 2 and 3 and supported me with his own measurements. Dr. Marisa Di Sabatino, Dr. Eivind Johannes Øvrelid and Dr. Espen Olsen who have provided me with the "dirty" mc Si materials that constitute the first part of this thesis, are gratefully acknowledged. Marisa also have supported me with measurement and introduced me for the Milano group.

In addition, coauthors Dr. Hiroshi Nagayoshi from Tokyo national college of technology; Dr. Nobuo Matsumoto, Dr. Suzuka Nishimura and Dr. Kazutaka Terashima from Shonan institute of technology, Japan; Dr. Bart Geerligs and Dr. Petra Manshanden from ECN, the Netherlands; Dr. Arve Holt from IFE; associate professor Maurizio Acciarri, associate professor Simona Binetti and Dr. Joris Libal, University of Milano, Italy, are greatly acknowledged for their contributions.

Heimir Magnusson, associate professor Ton van Helvoort and Bjørn Soleim are greatly acknowledged for keeping the microscopes running. The TEM group and Si lunch meetings and Si related meetings and workshops at materials technology have been very useful.

Financial support from NTNU, the Norwegian Research Council through the SUP programme "Micro- and nanostructural materials development", and the European Project FoXy (SES 6-019811) are greatly acknowledged.

Trondheim, December 2008 Heidi Nordmark

Abbreviations

AFM	Atomic force Microscopy
BF	Bright Field
CLS	Coincidence site lattice
Cz	Czochralski
DF	Dark Field
EBIC	Electron Beam Induced Current
EBSD	Electron Back Scattered Diffraction
EDS	X-ray Energy Dispersive Spectroscopy
EQE	External quantum efficiency
FT-IR	Fourier Transform- InfraRed spectroscopy
GDMS	Glow Discharge Mass Spectroscopy
HRTEM	High Resolution Transmission Electron Microscopy
IQE	Internal Quantum Efficiency
mc	multicrystalline
OSF	Oxygen stacking fault
MG-Si	Metallurgical grade silicon
PECVD	Plasma enhanced chemical vapour deposition
ppbw	parts per billion by weight
ppma	atomic parts per million
PV scan	Photo Voltaic scan (Dislocation density measurement)
QSSPC	Quasi-Steady-State Photo-Conductance
RMS	Root mean square
SAD	Selected Area Diffraction
sccm	Standard cubic centimeters per minute
SEM	Scanning Electron Microscopy
Si	Silicon
SIMS	Secondary Electron Mass Spectroscopy
SiNW	Silicon NanoWires
SoG-Si	Solar grade silicon
SOI	Silicon on insulator
STEM	Scanning Transmission Electron Microscopy
TEM	Transmission Electron Microscopy
UMG-Si	Upgraded metallurgical silicon

Table of contents

I. General introduction

1. Motivation

Due to climate changes and shortage of fossil fuel, together with growing energy consumption in the world, renewable energy resources, like solar energy, become more and more important. The last years, the solar cell market has experienced more than 40 % yearly growth, rapidly approaching 3 GWp installations a year [1]. About 90 % of the solar cells are made of crystalline silicon. Multicrystalline (mc) silicon solar cells have the highest market share and constitute about 50 % of the total production of solar cells [2]. The energy payback time for mc silicon solar cells a few years ago was 2-3 years, for regions with high irradiation (2200 kWh/m^2 yearly) and 5-6 years for regions with low irradiation (1100 kWh/m^2 yearly) [3]. Compared to the expected lifetime of solar cells of 25-30 years, this is acceptable [3].

The solar constant normal to the earth above the atmosphere is 1353 W/m^2. However, the radiation is attenuated at least 30 % by the atmosphere depending on at which angle it hits the surface [4]. In Norway only 700-1100 kWh/m^2 solar energy is received every year due to the nights, latitude, and bad weather [5]. By covering less than 0.5 % of the land area south in Norway with 15 % effective mc Si solar cells, our total yearly energy consumption, 225 TWh [6] (thereof ca. 120 TWh electrical energy), can be produced. The price of electricity from solar cells cannot yet compete with cheap hydropower in Norway. However, in some countries electricity from solar cells is subsided and can compete with commercial electricity.

Traditionally, the source material for production of solar cells has been scrap silicon from the semiconductor industry. However, during the last years the raw material demand for solar cells has increased far beyond the scrap silicon available, and new routes for producing sufficiently clean solar grade silicon have been developed [7,8]. The easiest and cheapest route is to produce silicon directly from a metallurgical feedstock. In this way, both the material cost and the energy payback time can be significantly reduced [7]. The disadvantage is the much higher amount of incorporated impurities, especially transition metals, which can lower the efficiency of the material by introducing recombination centres for electrons and holes in the bulk. In the first three papers, a mc silicon ingot produced in this way has been characterized.

Hydrogen treatment is widely used within silicon solar cell industry to improve the minority carrier lifetime by passivating defects and impurities at the surface and in the bulk [9]. However, hydrogen can also induce recombination active defects when present at high concentration in silicon. These defects are mainly platelets aligned in {111} or {100} planes, consisting of an array of Si-H_x bonds filled with molecular hydrogen gas [10]. Heat treatment of the platelets formed after high dose H^+ implantation can lead to exfoliation of a thin silicon layer (~ 1 μm) used for the Silicon-On-Insulator (SOI) industry [11]. Hydrogen induced defects can also be used to getter impurities during high temperature treatments [12]. Direct hydrogenation of silicon substrates is regarded as a potential method for texturing of surfaces [13]. The subject of paper 4-7 is characterization of bulk defects and substrate surface modification after hydrogenation.

The interest of silicon nanostructures has exploded during the last years. Silicon nanowires (SiNW) technology is particularly important, because silicon-based nanoelectronics is compatible with silicon-based microelectronics [14]. Because of the SiNWs narrow size, their electrical and optical properties differ from the silicon bulk properties. A potential application of Si whiskers with p-n junctions may be to provide a solution for fabrication of higher efficiency solar cells, compared to those based on conventional planar p-n junction solar-cell geometry [15]. The two last papers deal with a new way to grow silicon nano-whiskers with potential applications within photonics and electronics.

References

[1] D. Ginley, M. A. Green and R. Collins, MRS Bullentin **33**, 355 (2008)
[2] H. Matsuo, R.B. Ganesh, S. Nakano, L. Liu, K. Arafune, Y. Ohshita, M. Yamaguchi, and K. Kakimoto, J. Cryst. Growth **310**, 2204 (2008)
[3] E. Alsema, *Practical Handbook of Photovoltaics*: *Fundamentals and Applications, Elsevier* (2003), p. 869-886
[4] M. A. Green, *Solar cells: Operating principles, technology and system applications*, Centre for photovoltaic devices and systems, Sydney (1995)
[5] Norges vassdrag og energidirektorat sine nettsider (Norwegian) www.nve.no/modules/module_109/publisher_view_product.asp?iEntityId=9381
[6] Næringslivets klimapanel, *Energiproduksjon og energibruk i Norge*, 07 Gruppen AS, (2008) ISBN 978-82-7511-119-5 (Norwegian)
[7] Dominique Sarti and Roland Einhaus, Sol. Energy Mater. Sol. Cells **72**, 27 (2002)
[8] J. Degoulange, I. Perichaud, C. Trassy and S. Martinuzzi, Sol. Energy. Mater. Sol. Cells **92**, 1269 (2008)
[9] *Hydrogen in crystalline semiconductors*, J. Pearton, W. Corbett and M. Stavola, Springer-Verlag, 1992 and references therein
[10] N. M. Johnson, F. A. Ponce, R. A. Street and R. J. Nemanich, Phys. Rev. B. **35**, 4166 (1987)
[11] M. Bruel, B. Aspar, A.-J. Auberton-Herve´, Jpn. J. Appl. Phys. **36**, 1636 (1997)
[12] J. Wong-Leung, C. E. Ascheron, M. Petravic, R. G. Elliman, and J. S. Williams, Appl. Phys. Lett. **66**, 1231 (1995)
[13] M. Ishii, K. Nakashima, I. Tajima and M. Yamamoto, Jpn. J. Appl. Phys. **31**, pp 4422-4427 (1992)
[14] B. K. Teo and X. H. Sun, Chem. Rev. **107**, 1454 (2007) and references therein
[15] J. Goldberger, R.R. He, Y.F. Zhang, S.W. Lee, H.Q. Yan, H.J. Choi, and P.D. Yang, Nature **422**, 599 (2003).

2. Silicon Solar cells

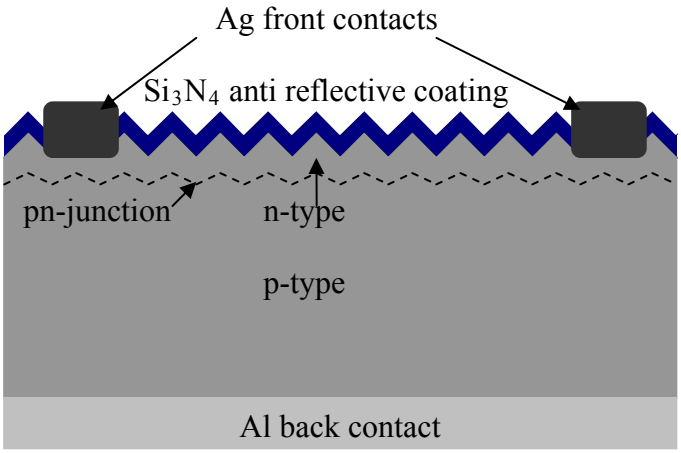

Figure 2.1. Conventional textured silicon solar cell (the proportions are oversized) with Ag front contacts, Si_3N_4 antireflective coating, n- and p-type silicon and Al back contact.

Silicon is an indirect semiconductor with a band gap of 1.124 eV. Atoms from group III and V in the periodic table, usually boron and phosphorous, act as dopants in silicon. A phosphorous atom has an extra electron and is called a donor, while a boron atom with an excess hole is called an acceptor. Undoped silicon, intrinsic silicon, has a resistivity of $\rho = 2.3 \times 10^5$ Ωcm [1]. Doping increases the electrical conductivity of silicon. Doping concentrations are usually in the range of 10^{15}-10^{16} cm^{-3}, which corresponds to a resistivity between 1 and 10 Ωcm [2].

A solar cell consists of an n-type and a p-type region. A pn junction is formed between the two semiconductor regions of opposite doping types. When light illuminates the solar cell, photons of energy higher than the band gap will excite electrons that flow from the n-type silicon to the p-type silicon through an external circuit [3].

A conventional silicon solar cell is shown in Figure 2.1. Producing a solar cell out of a p-type silicon wafer involves several steps [2]. In the first step, the wafer is etched and cleaned to remove damage from sawing. Simultaneously, texture etching of the surface is performed to reduce the reflectivity of the surface. The second step involves phosphorus in-diffusion to form a p-n junction. In this step, also phosphorous gettering is performed at ~ 800 °C that allows metallic impurities to diffuse to the phosphorous layer where their solubility is increased. Then an antireflective coating, usually Si_3N_4, is deposited on the front side to absorb radiation more effectively. The antireflective coatings usually also contain hydrogen that diffuses into the bulk and passivates defects and impurities in the cell during the firing step. The last step is front side and back side metallization. For a p-type solar cell, usually an Al paste is used for the back side contact and an Ag paste for the front side. A short firing treatment allows the metal contacts on the front side to penetrate the antireflective coating.

2.1 Solar cell efficiency, quantum efficiency and radiation losses

The finished solar cells are characterized by their short circuit current I_{sc}, open circuit voltage V_{oc}, fill-factor FF, and conversion efficiency η. The conversion efficiency is given by [2]

$$\eta = \frac{P_{out}}{P_{in}} = \frac{FF \cdot V_{OC} \cdot I_{SC}}{P_{in}}, \tag{2.1}$$

where P_{in} is the power due to the incidence radiation of the solar cell and P_{out} is the power due to the output of the solar cell. The efficiency of silicon solar cells is low, but cost effective. All energy from photons with lower energy than the band gap is lost. All incoming photons with energy greater than the band gap will excite an electron from the valence band to the conduction band. The excess photon energy is lost as thermal energy. This limits the maximum achievable energy for single junction silicon solar cells to about 45 %. Radiative recombination reduces the limit down to 31.7 % and Auger recombination lowers the limit further to about 29.8 %, defining the theoretical limit [4]. Loss from reflection (optical), recombination at crystal defects and impurities and resistive losses reduce the efficiency of average industrial cells further to about 18 % for Cz silicon and 15 % for mc silicon [4].

The quantum efficiency of a solar cell is defined as the ratio of the number of electrons in the external circuit produced by an incident photon of a given wavelength [5,6]. Both external (EQE) and internal quantum efficiencies (IQE) can be defined. All photons that hit the cell are taken into account in EQE, while only photons not reflected are accounted for in IQE [7]. The IQE is given by [7]

$$\mathrm{IQE} = \frac{1}{1 - \mathrm{R}(\lambda)} \frac{\mathrm{hc}}{\mathrm{e}\lambda} \frac{\mathrm{I_{SC}}(\lambda)}{\mathrm{I_{light}}(\lambda)}, \tag{2.2}$$

where I_{SC} (λ) is the short circuit current of the cell and I_{light} (λ) is the light intensity. R(λ) is the reflectance for the given wavelength.

2.2 Lifetime, recombination and diffusion length

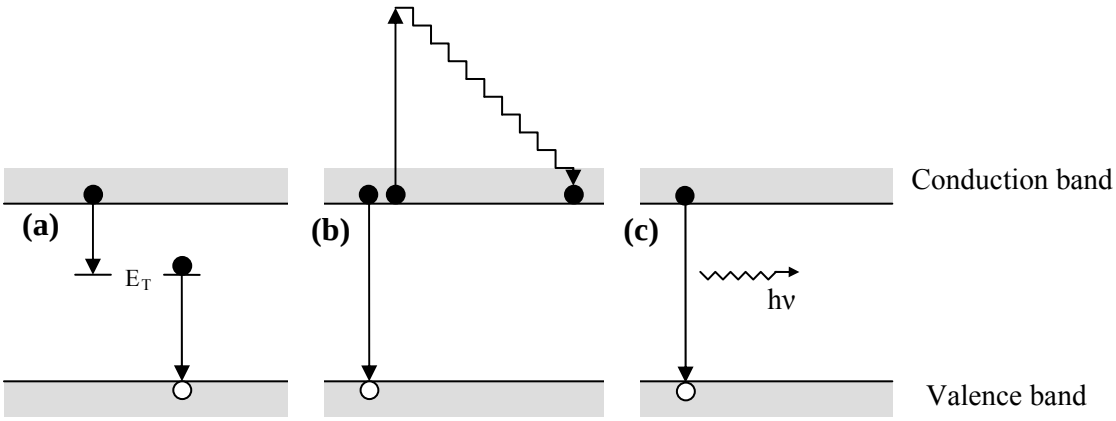

Figure 2.2 (a) SRH recombination of an electron and a hole, via a deep level in the forbidden band gap, (b) Auger recombination, the energy is given to a second electron in the conduction band, (c) Radiation recombination, the energy is given to a photon.

There are two categories of lifetime, generation lifetimes τ_g and recombination lifetimes τ_r. Recombination lifetime is given by [8]

$$\tau_n = \frac{\Delta n}{U} \text{ and } \tau_p = \frac{\Delta p}{U}, \tag{2.3}$$

where Δn and Δp are excess electrons and holes, respectively, and U is the recombination rate. Generation lifetime is the time it takes on average to generate an electron-hole pair. Recombination lifetime is the time it takes before an electron-hole pair ceases to exist (recombine). Recombination lifetime τ_r is very effective in characterizing the purity of a material or a device and is sensitive to impurity concentrations as low as 10^{10} cm^{-3}. Effective lifetime consists of both bulk and surface components.

At the surface, the recombination and generation velocities are s_r and s_g, respectively. Bare Si surfaces have very high surface recombination velocity, s_r = 10^3-10^4 cm/s or higher, while good quality thermal oxidized Si surfaces can have surface velocity, s_r, as low as 1-20 cm/s. Surface passivation is therefore very important.

Three types of recombination exist in the solar cells, Shockley-Read-Hall (SRH) or multiphonon recombination, U_{SRH}, radiative recombination, U_{rad}, and Auger recombination, U_{Auger} as illustrated in Figure 2.2. The total bulk recombination lifetime is given by [9]

$$\tau_r = \frac{1}{\tau_{SRH}^{-1} + \tau_{rad}^{-1} + \tau_{Auger}^{-1}}. \tag{2.4}$$

In SRH-recombination, electron-hole pairs recombine through deep-level impurities (in the forbidden band gap), as illustrated in Figure 2.2 (a). It is a two-step process, characterized by the impurity density N_T, the energy level E_T in the band gap and

capture cross-sections σ_n and σ_p for electrons and holes, respectively. The energy liberated during recombination is dissipated by lattice vibrations or phonons. The SRH-recombination lifetime is given by [9]

$$\tau_{SRH} = \frac{\tau_p(n_0 + n_1 + \Delta n) + \tau_n(p_0 + p_1 + \Delta p)}{p_0 + n_0 + \Delta n}, \tag{2.5}$$

for p type Si, where p_o and n_o are equilibrium hole and electron densities, Δn and Δp are the excess carriers densities taken to be equal in the absence of trapping, and n_1, p_1, τ_p and τ_n are defined as $n_1 = n_i e^{(Et-Ei)/kT}$, $p_1 = p_i e^{(Et-Ei)/kT}$, $\tau_p = (\sigma_p v_{th} N_T)^{-1}$ and $\tau_n = (\sigma_n v_{th} N_T)^{-1}$, respectively.

SRH recombination takes place whenever there are impurities or defects in the semiconductor, and is particularly important for indirect band gap semiconductors such as silicon. For mc Si solar cells, this is the most important recombination process because of the high density of impurities and defects [6]. SRH recombination depends inversely on the density of recombination centres and capture cross sections, but does not depend directly on the energy level of the impurity. It does depend indirectly because the capture cross section tends to be highest for impurities with E_T close to the centre of the band gap and lowest for E_T close to the valence or conduction band. Recombination centres with E_T close to the mid band gap are the most effective recombination centres, as also holds for surface recombination [3].

In the Auger recombination process, the electron recombining with the hole gives the excess energy to a second electron in the conduction or valence band, instead of emitting light, as illustrated in Figure 2.2 (b). Auger recombination is typically observed, when either the doping density or the excess carrier density is very high, independent on impurity level. The Auger recombination lifetime is given by [9]

$$\tau_{\text{Auger}} = \frac{1}{C_p(p_0^2 + 2p_0 + \Delta n + \Delta n^2)}, \tag{2.6}$$

where C_p = Auger recombination coefficient = $1.1\text{x}10^{-30}$ cm^6/s or 10^{-31} cm^6/s.

In radiative recombination, the excess energy is emitted as a photon as illustrated in Figure 2.2 (c). For silicon, such recombination is negligible. At high carrier densities (high doping), the lifetime in Si is controlled by Auger recombination and at low densities by Shockley-Read-Hall recombination [9].

The minority carrier diffusion length is given by

$$L = \sqrt{D\tau}, \tag{2.7}$$

where τ = lifetime and D = diffusion coefficient for the minority carriers [5].

2.3 Metallurgical grade, solar grade and electronic grade silicon

Silicon is the second most abundant element in the earth's crust and exists in nature mostly in the form of silicon dioxide or silicates. Reduction of quartzite by carbon in large arc furnaces produces silicon according to the reaction [3]

$SiO_2 + 2C \rightarrow Si + 2CO$.

The result is metallurgical grade silicon, which is 98-99 % pure silicon. Typical impurity levels are given in Table 2.1.

Table 2.1. Target impurity concentrations in UMG-Si and SoG-Si [11].

Impurity	**MG-Si** (ppmw)	**UMG-Si** (ppmw)	**SoG-Si** (ppmw)
B	40	< 30	< 1
P	20	< 15	< 5
O	3000	< 2000	< 10
C	600	< 250	< 10
Fe	2000	< 150	< 10
Al	100-200	< 50	< 2
Ca	500-600	< 500	< 2
Ti	200	< 5	< 1
Cr	50	< 15	< 1

Electronic grade silicon, 99.99999999 % pure, is produced from metallurgical silicon by the Siemens process [10]. The Siemens process requires a lot of energy, and has a low yield (~ 37%) so that the price is high [3]. Solar grade silicon (SoG-Si) is 99.99999 % pure silicon. Traditionally solar cells were made of scrap silicon from the electronics industry. Today, due to shortage of electronically grade silicon scrap, many routes for producing upgraded metallurgical silicon (UMG-Si) for solar cell manufacture have been developed [11,12,13]. The impurity requirements for UMG-Si and SoG-Si are given in Table 2.1. Using dirtier materials significantly lowers the energy consumption and feedstock costs.

References

[1] S. M. Sze, *Physics of Semiconductor Devices*, 2nd ed. ~Wiley, New York, Appendix H, p. 850 (1981)
[2] J. Twidell and T. Weir, Renewable energy resources, Spon Press, 1986
[3] M. A. Green, *Solar cells: Operating principles, technology and system applications*, Centre for photovoltaic devices and systems, Sydney (1995)
[4] D. H. MacDonald, PhD thesis, Australian National University, 2001
[5] T. Markvart and L. Castaner, *Solar Cells: Materials, Manufacture and Operation*, Elsevier Ltd (2005)
[6] E. Antonccík, Czechosl. Journ. Phys. **7**, 674 (1957)
[7] W. J. Yang, Z. Q. Ma, X. Tang, C. B. Feng, W. G. Zhao and P. P. Shi, Sol. Energy **82**, 106 (2008)
[8] G. Stokkan*, Characterisation of multicrystalline silicon solar cells; Development of characterization method for the combined effect of dislocations and grain boundaries on the minority carrier lifetime*, PhD thesis, NTNU (2004)
[9] D, C, Gupta, F. R. Bacher, W. H. Hughes, *Recombination lifetime measurements in silicon*, West Conshohocken, Pa. ASTM, STP **1340** (1998)
[10] C. L. Yaws, P. N. Shan, P. M. Patel, G. Hsu, R. Lutwack, Sol. state Techn. 63 (1979)
[11] D. Sarti and R. Einhaus, Sol. Energy Mater. Sol. Cells **72**, 27 (2002)
[12] J. Degoulange, I. Perichaud, C. Trassy and S. Martinuzzi, Sol. Energy. Mater. Sol. Cells **92**, 1269 (2008)
[13] J. L. Geerligs, G. P. Wyers, R, Jensen, O. Raaness, A. N. Waernes, S. Santén, A. Reinink and B. Wiersma, Proceedings 12th Workshop on Crystalline Silicon Solar Cell Materials and Processes, Breckenridge CO, USA, (2002)

3. Crystalline silicon

3.1 Crystal lattice

Silicon is a semiconductor with atomic number 14 in the periodical system. Its density is 2.33 g/cm^3 with 5x10^{22} at/cm^3 and a band gap of 1.12 eV at 300 K. The melting point of silicon is 1412 ± 2 °C or 1687 K [1]. The crystal lattice has the cubic diamond structure which is made up of two face centered cubic (fcc) unit cells, the second shifted ¼ of the fcc unit cell diagonal as shown in Figure 3.1 (a) [2]. The space group is Fd3m (Space group number: 227) and the lattice vector is a = 5.43 Å at room temperature. Each silicon atom is covalently bonded to four other silicon atoms making up a tetrahedral. Figure 3.1 (a) shows the silicon unit cell and its substitutional and interstitial sites. Interstitial positions in the lattice are indicated in the figure. The stacking sequence of a diamond cell is AaBbCcAaBbCcAaBbCc, where the ABC denotes one of the fcc cells and abc the other one. In {111} orientation, the two letters of the same kind are sitting on top of each other. Glide can happen between planes of the same letters, called shuffle plane or planes with letters of different type, called glide plane as shown in Figure 3.1 (b).

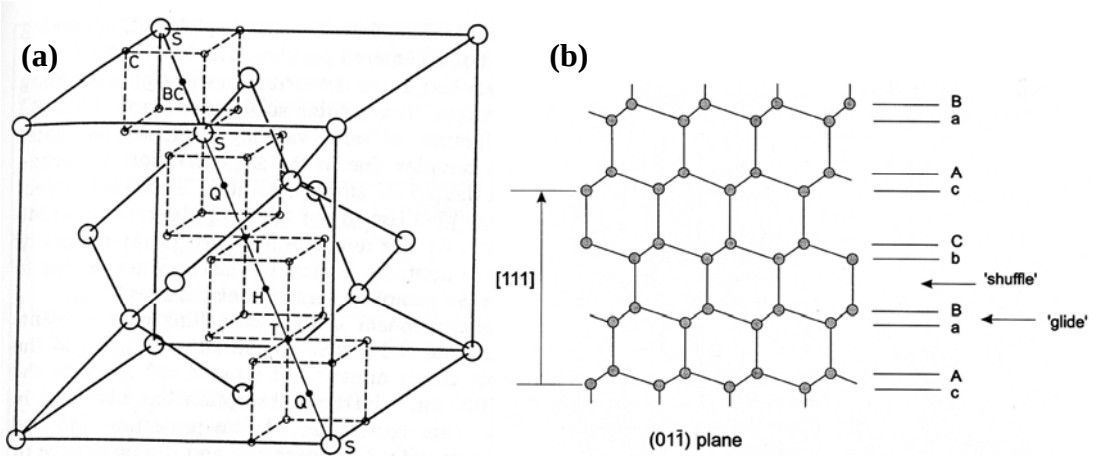

Figure 3.1. (a) A unit cell in the silicon lattice showing substitutional (S), bond-centered (BC), antibonding (Q), tetrahedral interstitial (T), hexagonal interstitial (H) and C sites [3], (b) (01-1) plane in silicon showing the stacking sequence and glide planes [2].

3.2 Crystal Defects

Structural lattice defects can disturb the periodical array of a crystal lattice. These can be divided into several types; i) point defects which involve vacancies, self interstitials and impurity atoms, ii) one-dimensional defects or line defects include dislocations, iii) 2-dimensional defects or planar defects, which include grain boundaries, stacking faults and surfaces and iv) 3-dimensional defects or volume defects like voids and precipitates. The different defects may interact. At thermal equilibrium, only point

defects have sufficient low formation energy to form. More complex structural defects can occur during growth or processing of the material [4].

Point defects

An isolated vacancy in the lattice is termed a Schottky defect when the missing atom has migrated to the surface or is trapped by an extended defect. A vacancy associated with a self-interstitial atom is called a Frenkel defect. Impurity atoms can occupy either interstitial or substitutional sites in the silicon lattice, as indicated in figure 3.1 (a). Most interstitial impurities occupy tetrahedral interstitial sites. Dopants are substitutionally dissolved in the silicon lattice, while most transition metal impurities are interstitially dissolved, and can form deep levels in silicon [4].

Dislocations

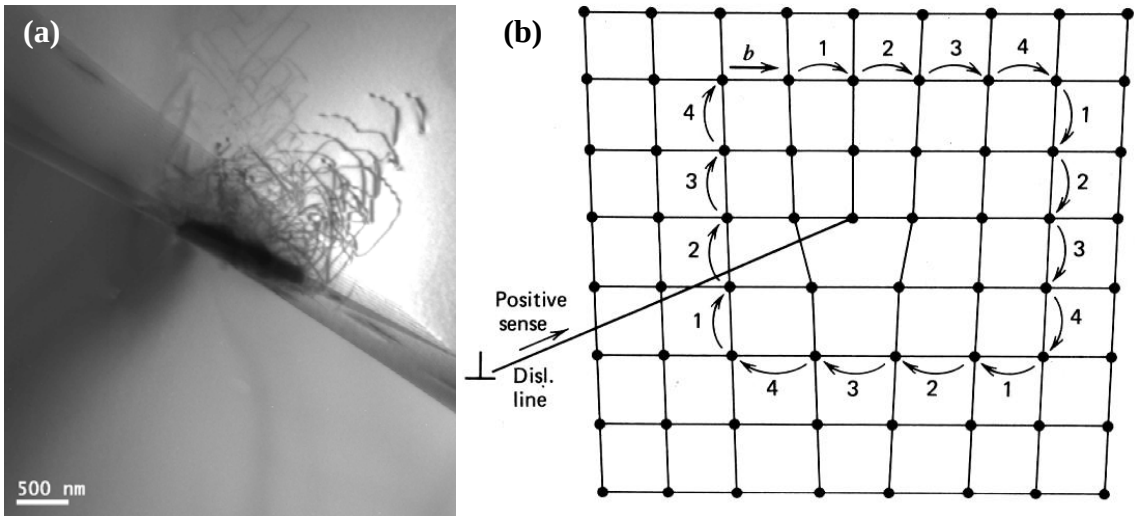

Figure 3.2. (a) Dislocation cluster in a contaminated grain boundary, (b) The Burgers circuit for an edge dislocation [5].

In Figure 3.2 (a), cascades of dislocations are shown, formed due to lattice misfit or different thermal expansion coefficient between the precipitate and the Si matrix or a dislocation source in the grain boundary. Dislocations are important because they can change the optical and electrical behaviour of a crystal. In addition, they also interact strongly with other defects and impurities and can lower the formation energy for precipitates [4]. The two main types of dislocations are edge dislocations and screw dislocations. Edge dislocations can be described as the edge of an extra half plane inserted into the crystal, while screw dislocations introduce a helical distortion into the crystal [4]. The defects are described by Burgers vector, **b,** that can be found by constructing a Burgers circuit around the dislocation, as shown in figure 3.2 (b). Equal number of lattice translation vectors is counted in each direction around the dislocation line. The Burgers vector is the closure vector that for an edge dislocation is normal to the dislocation line, while for a screw dislocation is parallel to the dislocation line. Most

dislocations are combinations of the two. Dangling bonds are formed along the core of the dislocation.

Dislocations can slip in planes containing both the dislocation and the Burgers vector. For a screw dislocation, the dislocation and the Burgers vector are parallel, so the dislocation may slip in any plane containing the dislocation. For an edge dislocation, the dislocation and the Burgers vector are perpendicular, so there is only one plane in which the dislocation can slip. Dislocation climb allows an edge dislocation to move perpendicular to its slip plane. Climb occurs at high temperatures and involves point defect absorption or emission. Climbing dislocations are associated with repeated nucleation and growth of small precipitates [6-10]. The dislocations move by the rejection of self interstitials from the precipitates due to volume extraction. When individual or small clusters of vacancies diffuse to a dislocation, a short section of the dislocation line will climb resulting in the formation of two small steps called jogs [2]. Steps which displace short sections of the dislocation on the same slip plane are called kinks. Screw dislocations that move in {111} planes can cross-slip by switching from one set of {111} planes to another if it contains the direction of **b.** Glissile dislocations can move by glide, while sessile ones only move conservative under the action of applied stress.

Perfect dislocations in silicon lie in the {111} planes, have Burgers vectors in a/2 <110> directions and often align in <110> directions at 0° or 60° because of low core energy in those directions [11]. Screw dislocations and the 60° dislocations that have a Burgers vector that makes an angle of 60° to the direction of the dislocation, are such dislocations [11]. 60° dislocations belong to either glide set or shuffle set as shown in Figure 3.1(b). Shuffle happens between letters of same type and glide between letter of different type [2,12]. The two 60° dislocations are shown in Figure 3.3. Both types are glissile and can dissociate, but the mechanism of dissociation is different for the two cases. In a perfect dislocation, two half planes are removed (one in plane and one below). The dislocation can split into two single Shockley partial dislocations with Burgers vector of a/6 [112] and a stacking fault in between. The energy of a dislocation is proportional to b^2. Splitting into two partial dislocations is energetically favorable, $a^2/2$ versus $a^2/3$, for partial dislocations.

In the glide set, the dislocation dissociates into two a/6 <112> Shockley partial dislocations with an intrinsic stacking fault in between. Dissociation of the shuffle dislocation occurs by the nucleation and glide of a Shockley partial of the glide type between adjacent pair of {111} layers. This results in a fault of the glide set bounded on one side by a Shockley partial and on the other side by a Shockley partial, and in addition, depending on whether the glide plane is above or below the shuffle plane, a row of interstitials or vacancies [2]. Climb transforms shuffle set dislocations into glide set dislocations and vise versa. Imperfect dislocations lie along the boundaries of stacking faults in the lattice [13].

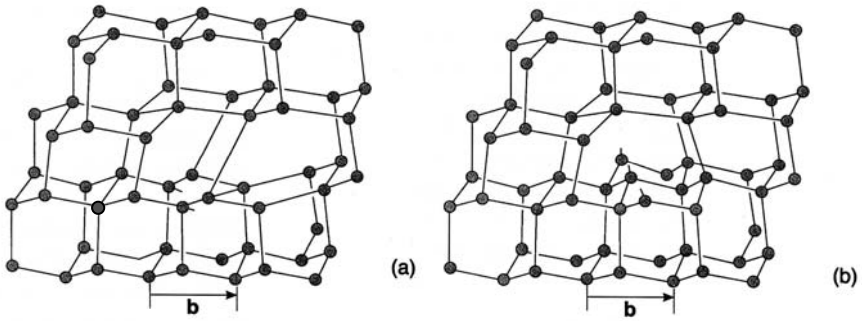

Figure 3.3. Perfect 60° dislocations of (a) the glide set and (b) the shuffle set [2].

Prismatic loops are dislocation loops with Burgers vector not in the plane of the loop. They can only expand or shrink by climb. They can be formed from supersaturated vacancies during quenching from high temperature or by irradiation, forming vacancy platelets that collapse into loops.

A Frank partial dislocation is formed from the boundary line of a fault by inserting or removing one close packed {111} layer of atoms, giving a Burgers vector normal to the {111} plane of **b** = 1/3 [111]. Removal of a layer gives an intrinsic stacking fault, while insertion of a layer gives an extrinsic stacking fault. A stacking fault can end in a Frank partial dislocation in the middle of the grain. Frank partial dislocations are sessile, but can move by climb. A closed Frank partial dislocation loop can be produced by the collapse of a platelet of vacancies or by the displacement caused by a cascade of interstitials. Diffraction fringes due to stacking faults can be observed. A Shockley partial dislocation can react with a Frank partial dislocation, producing a perfect dislocation a/2 [110] = a/6 [11-2] + a/3 [111]. The Shockley partial forms inside the Frank partial loop and spread across the loop removing the fault [2].

Frank-Read sources are dislocation lines that are held at each end by other parts of the dislocation network being sessile [14]. The line expands in its slip plane according to its Burger vector, and starts to spiral around its edges. Eventually, the dislocation becomes unstable and the two parts of the expanding line intersect, annihilate (different opposite b-vector) and form a dislocation loop. A regenerated dislocation line repeats the process. A (screw) dislocation cross-slip its loop in one of the slip planes and can act as a Frank-Read source, since both ends will be in other slip planes. Thereby, one dislocation line can multiple cross-glide and form many Frank-Read sources connected by jogs [2].

Dislocations form at high temperatures (1000-1300 °C) during cooling of the solidified material. Local internal stresses during growth and subsequent cooling can cause dislocation formation. Neighboring parts of the crystal, like precipitate-bulk interfaces can expand or contract differently due to; a) thermal gradients, b) change in composition or c) change in lattice structure. When the stresses reach a critical value, dislocations will form. Homogenous dislocation formation in a dislocation free crystal requires very large stress. Prismatic dislocation loops can be punched out from inclusions in the matrix because of different contraction during cooling. Grain boundaries can act as

sources for dislocations. In low angle grain boundaries consisting of dislocation arrays, the segment of dislocation networks forming the boundary can act as Frank-Read sources. The dislocations formed in grain boundaries can multiply within grains by a multiple cross slip process. Dislocations generated by sources within a grain produce large stress concentrations when piled up at the grain boundary and can trigger boundary sources at relatively low applied stress. Migrating grain boundaries generate dislocations in the lattice when they pass through. Dislocations can also be generated by accidental mispacking of atoms at the boundary, when one grain grows at the expense of another grain [2].

Stacking faults

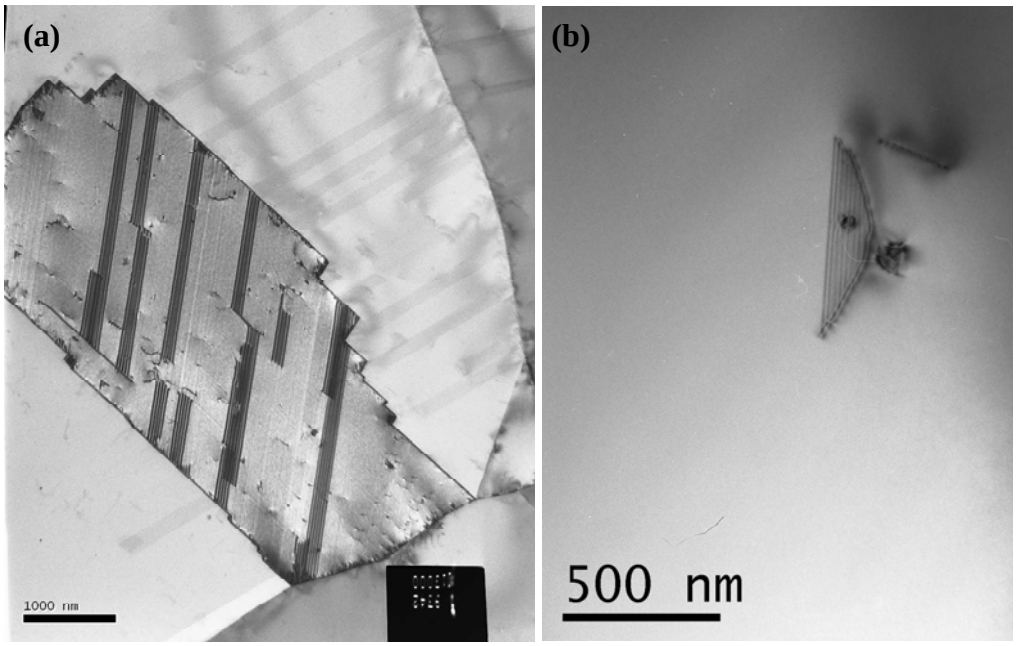

Figure 3.4. (a) Stacking faults in a grain in fcc stainless steal, (b) Stacking fault in silicon bound by a partial dislocation.

A stacking fault arises when there is a fault (short range) in the stacking sequence of a crystal. The fault can be either extrinsic, insertion of an extra plane, AaBbCc**Bb**AaBbCc, or intrinsic, missing a plane, AaBbCcAa**BbAa**BbCc. Faults formed between adjacent layers of the same letter, do not restore tetrahedral bonding and have high energy [15]. The stacking fault can initiate or terminate in a grain boundary or a partial dislocation, as shown in Figure 3.4 (a). Stacking faults can be formed between two partial dislocations or inside a dislocation loop, as described in the dislocation chapter. Figure 3.4(b) shows a stacking fault with typical fringes that is bounded by a partial dislocation. O induced stacking faults (OSF) have hexagonal ABAB-structure [11]. Stacking faults associated with oxide precipitates, were found to be recombination active only at temperatures below 100 K, while the bounding Frank partial dislocations were found to be active up to 200 K [16].

Grain boundaries

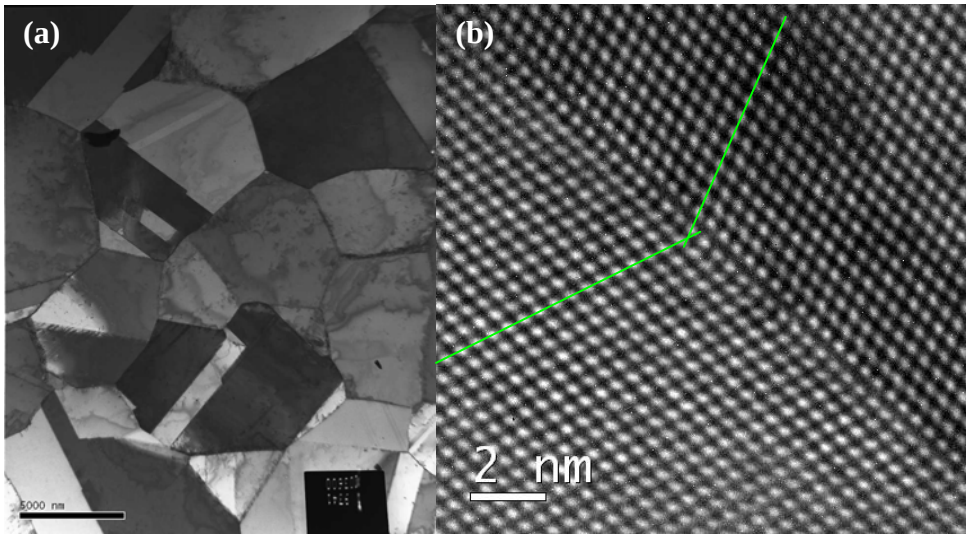

Figure 3.5 (a) Grain boundaries in a fcc stainless steal sample. Notice the diffraction contrast arising from differently oriented grains (Bragg contrast). (b) Twin boundary (Σ = 3) in Si

Grain boundaries are the boundaries between grains of different orientations, as shown in Figure 3.5. Grain boundaries can be divided into three groups; Random angle grain boundaries, co-incidence site lattice (CSL) grain boundaries and low angle or sub-grain boundaries. When the misorientation between neighboring grains is below 10-15°, it is called a low angle grain boundary, which consists of an array of dislocations. For larger misorientations, the boundary is continuous [4]. Low angle grain boundaries are called tilt boundaries if they consist of edge dislocations, and twist boundaries if they consist of screw dislocations [4]. Grain boundaries with very low misorientation angle of a few degrees are frequently called small angle grain boundaries.

Two neighboring grains of different orientations can still occupy common lattice sites. These common lattice sites constitute a second lattice, the CSL [11]. The ratio between the number of atoms per volume in the original lattice and the number of atoms in the CSL defines a number Σ given by [11].

$$\Sigma = \frac{n_{original}}{n_{CLS}}, \tag{3.1}$$

where $n_{original}$ is the atom density in the original lattice and n_{CSL} is the atom density in the CSL lattice. In cubic crystals, only odd numbers of Σ are allowed. The CSL boundaries with the highest symmetry are the Σ3 boundaries, known as twins. They are formed by rotating the lattice 60° around a <111> axis [11]. A twin boundary is shown in Figure 3.5 (b). For twin boundaries, the atomic arrangements on each side of the boundary are mirror images and they form parallel to {111} planes [4]. Higher order twins also exist. A second order twin is formed if a grain is twinned with respect to another grain and the second grain also has a twin. The boundary between the first grain

and the third grain is a second order twin or a Σ9 boundary [11]. Third order twins are denoted Σ27 boundaries. A low angle grain boundary is a Σ = 1 grain boundary. A list of the different Σ boundaries and their properties is given in ref [11].

It is well known that recombination activity depends on grain boundary character and contamination [17-19]. While grain boundaries in clean samples show very low recombination activity, almost independent of misorientation and temperature, the recombination activity increases with contamination level. Random and high-Σ grain boundaries show stronger recombination activity than low-Σ grain boundaries [17]. Small angle grain boundaries, with a tilt angle between 0 and 10° show weak recombination activity at room temperature and strong recombination activity at low temperature [18,19]. The recombination activity has been found to decrease with increasing temperature, showing a minimum at 250 K, and then increase with further increase in temperature [20]. This temperature dependence has been attributed to two types of recombination processes; i) a shallow level associated with an inherent grain boundary structure and ii) a deep level associated with impurities segregated at grain boundaries [20]. In addition, irregularities like boundary steps, give contrast variation in the EBIC signal along grain boundaries [20]. The recombination activity of the grain boundaries is also found to vary within an ingot. Grain boundaries in the top and bottom of an ingot show strongest recombination activity due to their higher Fe contamination level than the middle of the cast [21,22]. In Fe contaminated samples, small angle grain boundaries show stronger recombination activity than low-Σ grain boundaries and random grain boundaries, indicating that their boundary dislocation structures act as effective internal gettering sites for Fe [18,19].

3.3 Impurities

Although solar cell silicon contains very low levels of impurities [23,24], they still have a high impact on the material. Especially transition metals can strongly degrade the material by introducing deep levels in the forbidden band gap that act as recombination centres for electrons and holes [25]. Table 3.1 shows the experimental determined threshold concentrations of impurities above which the efficiency of p- and n-type solar cells decreases, together with maximum solubility and the diffusion coefficient at 1100 °C [25]. In paper 1-3 impurity precipitates in an ingot grown from metallurgical feedstock has been studied. O, Fe, Cu and Ni were the main impurities observed. In addition, tungsten silicide deposition of the Si surface has been studied in paper 8 and 9. Only these impurities will be studied in detail.

Table 3.1 Experimental determined threshold concentrations of impurities above which the efficiency of p- and n-type solar cells decreases, together with maximum solubility and the diffusion coefficient at 1100 °C [25].

Impurity	P-base solar cell N_{th} [cm^{-3}]	N-base solar cell N_{th} [cm^{-3}]	Max solubility N_{eq}^{max} [cm^{-3}]	Diff. coefficient D_{1100} [cm^2/s]
Copper	4.1×10^{17}	8.0×10^{16}	2×10^{18}	1×10^{-4}
Nickel	5.0×10^{15}	—	7×10^{17}	4×10^{-5}
Cobalt	1.1×10^{15}	—	3×10^{16}	1×10^{-5}
Iron	2.5×10^{14}	1.8×10^{14}	2×10^{16}	4×10^{-6}
Manganese	1.8×10^{14}	9.5×10^{14}	2×10^{16}	3×10^{-6}
Chromium	1.3×10^{14}	1.2×10^{14}	1×10^{16}	2×10^{-6}
Vanadium	2.5×10^{12}	4.1×10^{13}	2×10^{16}	1×10^{-7}
Titanium	2.6×10^{12}	3.7×10^{13}	1×10^{15}	4×10^{-9}
Silver	4.0×10^{15}	—	5×10^{17}	3×10^{-9}
Palladium	2.0×10^{15}	—	3×10^{16}	—
Molybdenum	6.0×10^{11}	1.3×10^{12}	2×10^{14}	—
Niobium	1.6×10^{12}	—	5×10^{14}	—
Zirconium	3.6×10^{11}	—	5×10^{14}	—
Gold	1.0×10^{13}	—	1×10^{17}	1×10^{-6}
Tungsten	1.2×10^{12}	—	9×10^{13}	—
Tantalum	2.3×10^{11}	—	1×10^{14}	4×10^{-14}
Carbon	1×10^{18}	—	3.5×10^{17}	8×10^{-12}
Oxygen	1×10^{19}	—	2.0×10^{18}	9×10^{-11}
Aluminium	4.4×10^{15}	8.5×10^{16}	1.5×10^{21}	2×10^{-12}
Phosphorus	1.7×10^{18}	—	1.8×10^{22}	3×10^{-13}

Impurities are incorporated during growth of an ingot and contamination sources are mainly the feedstock itself, together with the crucible, the coating and the gas ambient [99].The segregation or distribution coefficient of impurities in silicon is given by [25]

$$k_0 = \frac{C_s}{C_m}, \tag{3.2}$$

where C_s is the concentration of the impurity in the solid and C_m is the impurity concentration in the melt. Most impurities have segregation coefficients < 10^{-4} and are strongly segregated towards the top of an ingot [26]. Exceptions are the doping elements and C that are much less segregated and O with a segregation coefficient > 1. When all the melt has solidified, during cooling, impurities from the highly contaminated top will start diffusing back into the ingot.

The key of understanding the behaviour of impurities is to find their lowest energy location. Solubility and diffusivity annealing time and temperature, together with defect density and nature, determine their location and chemical state. Defects in the materials represent misfit locations where the nucleation energy barrier usually is lowered compared to the bulk and can enhance precipitation and segregation. The maximum solubility (close to the melting point of silicon) of different impurities is given in table 3.1. At room temperature most impurities have very low solubility and tend to segregate to extended defects or precipitates. However some slow diffusing elements like the dopants and light elements remain in supersaturated solution.

Particles can precipitate in two ways, heterogeneously or homogenously. Homogenous precipitation gives a uniform distribution of the particles in the matrix. Heterogeneous precipitation gives precipitation along discontinuities in the crystal lattice, like grain

boundaries, dislocations or other particles [5]. For precipitation to happen spontaneously, the free energy change must be a negative number. Particle precipitation depends on several conditions like the strain energy, the surface free energy and the bulk free energy change per atom in the nucleus created and is given by [5]

$$\Delta G = n \cdot \Delta G_B + \eta \cdot n^{2/3} \gamma + n \cdot E_s \tag{3.3}$$

where n= number of atoms in nucleus

$\Delta G_B = \frac{(G_{nucleus} - G_{matrix})}{n}$ = bulk free energy change per atom in nucleus

η = shape factor such that $\eta n^{2/3}$ = surface area

γ = surface tension ≈ surface energy

E_s = strain energy per atom in nucleus

Precipitation is inhibited by the positive energy required to generate the interface between the particle and the matrix. This energy will be lowered when the particle precipitates on an already existing interface in the matrix [5].

3.3.1 *Light elements*

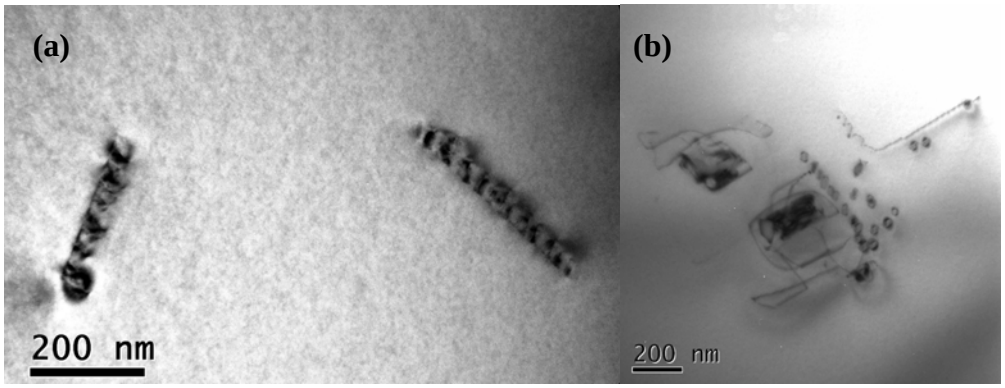

Figure 3.6. Light element defects in mc Si, (a) Multi-platelet defects, (b) SiO_2 precipitation on dislocations and dislocation loop generation.

O, C and N are the most common impurities in mc Si [27]. Figure 3.6 shows multi-platelet defects (a), and O contaminated dislocations (b). O comes from the feedstock and crucible quarts, N from the crucible coating and C from various furnace parts [27]. N is found to form large ~ µm facetted inclusions, hexagonal shaped rods or fibers of the β-Si_3N_4-structure, while C forms large, ~ µm, cubic β-SiC inclusions on the Si_3N_4-precipitates, inclusions in grain boundaries or branched filaments growing several mm in the solidification direction [28]. Both form precipitates in the ~ µm range and are studied with SEM and TEM [28-33]. Such large inclusions are not very recombination active, but can cause shunting of the cell [30]. N-doped highly conductive SiC filaments were found to cause ohmic shunts [32]. Both SiC and Si_3N_4 mainly form in the top 1/3 part of the ingot and N has been found to enhance SiC formation [28,33]. Nanoclusters of $FeSi_2$ and Cu_3Si have been observed on SiC inclusions [33]. The SiC filaments are

often observed in grain boundaries and align in the growing direction and are assumed to form during crystallization of the ingot, or by solid state diffusion into pre-existing Si grains. The large inclusions observed in grain boundaries were assumed to grow in C-contaminated melt [32]. C atoms at interstitial sites have been found to be electrically active [25]. Both N and C have been found to increase precipitation in Si after heat treatment [25,34]. Since C is a smaller atom than Si and occupies substitutional lattice sites, it leads to contraction of the volume contrary to O at interstitial sites that leads to volume expansion. O and C are therefore assumed to form complexes to reduce lattice strain [25].

Oxygen impurities

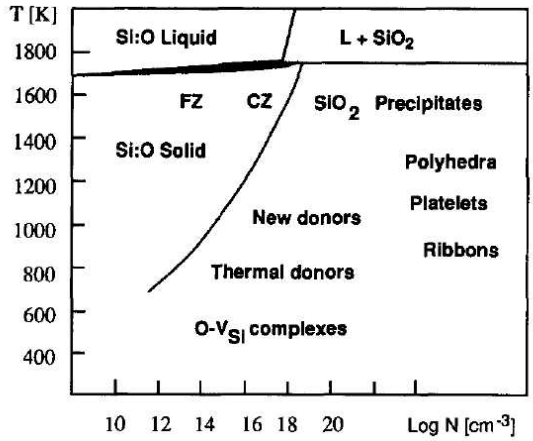

Figure 3.7. Si-O phase diagram and typical temperature ranges for the occurrence of O related defects after annealing. Shaded area indicates the narrow liquid-solid two phase regime [25].

For the materials studied in this thesis, O was found to be the dominating impurity. O is incorporated into Si during growth of the ingot. Both mono- and multicrystalline Si contain 10^{17}-10^{18} cm^{-3} O [25,37]. The concentration of O in Si is highest in the bottom of the ingot unlike most impurities that are segregated towards the top. The segregation coefficient of O has been found to vary between 0.25 and 1.48, but is in general believed to be ~ 1.25 [25,35]. The solubility of O in Si is given by [36]

$$S_O(T) = 9\times10^{22}\exp\left(-\frac{1.52eV}{k_BT}\right)(cm^{-3}), \tag{3.4}$$

and the diffusivity of O in Si is given by [35]

$$D_O = 0.13\exp\left(-\frac{2.53eV}{k_BT}\right)\left(cm^2/s\right) \tag{3.5}$$

At the melting point of Si, the O solubility has been found to be 2.75±0.15 x 10^{18} cm^{-3} [35]. Because of the low diffusivity of O in Si, most of the O is frozen in interstitially dissolved, during cooling of the ingot. This leads to high supersaturation of O that can

precipitate at later high temperature processing steps. Precipitation of O is associated with volume expansion that leads to plastic deformation of the Si matrix or self-interstitials are emitted. One Si atom is emitted for every two O atoms in a precipitate, leading to the formation of dislocation loops and interstitial type stacking faults. Intentional O precipitation in the bulk of devices can enhance their performance via internal gettering. O precipitates and their related defects are well known to act as preferential gettering sites for metallic impurities during heat treatments. In this way detrimental impurities can be removed from critical parts of the devices [25,35].

In Figure 3.7 typical temperature ranges for the occurrence of O related defects after annealing are indicated as a function of temperature. O diffuse interstitial in Si and can form a broad specter of complexes and defects, some of which introduce levels in the band gap. O forms electrically active defects in Si in the temperature range 350-600 °C and 600-900 °C for old thermal donors (OTD) and new thermal donors (NTD), respectively. Old thermal donors are complexes of only a few atoms and can exist in densities up to 10^{16} cm^{-3}. They are double donors and annihilate at temperatures > 650 °C. New thermal donors are associated with SiO_x precipitates and disappear above 1050 °C. Precipitates formed at higher temperatures are less electrical active. Nucleation of Si oxide precipitates is favoured in the temperature range between 600-900 °C, and precipitate growth is predominant from about 1000-1200 °C. At low temperatures, < 1000 °C, rods/ribbons, dislocation dipoles, prismatic dislocation loops and platelike defects may form. The platelets form in {100} planes and the rods align along <110> directions. At higher temperatures, after two-step annealing, octahedral and platelike precipitates, stacking faults and different kind of dislocation loops form. Octahedral precipitates are amorphous SiO_2, have facets along {111} and {100} planes and form for T > 1000 °C. Frank extrinsic stacking faults formed by an extra plane of interstitials, are hexagonal shaped for $T \leq 1000$ °C, and circular shaped for $T \geq 1000$ °C [25,35].

Oxidation induced stacking faults (OSF) are formed in the near surface region under oxidizing annealing conditions and are half elliptical shaped. Precipitates that form around T = 1150 °C during cooling, probably serve as nuclei for OSF during oxidation. Prismatic punching has been observed after high temperature two step annealing and the loops are formed in {110} planes. Dislocation loops can also form by cross-glide of a shear loop in {111} planes [25].

In mc Si, O has been found to preferentially precipitate at dislocations and in grain boundaries if there is sufficient time for the O atoms to diffuse to the defects. In addition, both spherical, platelike and multi-platelet precipitates have been observed in the Si bulk for O concentrations > 2×10^{17} cm^{-3}. The precipitate density can be as high as 10^{11} cm^{-3} after growth and increase to 10^{12}-10^{13} cm^{-3} after annealing [37]. Spherical precipitation is enhanced for T = 900 °C and disappear for annealing temperatures above 1050 °C, due to dissolution and diffusion to dislocations [38]. Stacking faults were seen to form at 1050 °C. Spherical SiO_2 precipitates were seen to be amorphous. The thin platelets are only one or two layers thick and differ from the platelike defects formed in Cz Si [37].

The strong recombination activity associated with SiO_2 precipitate formation might be related to the Si/SiO_x interface [39]. Alternatively it can be due to gettered impurities. O contaminated dislocations are more recombination active than clean dislocations, but it might be due to metal contamination [25,37].

3.3.2 *Transition metals*

Transition metals are of special concern for devices and Si solar cells because they introduce deep energy levels with high capture cross-sections in the band gap, thereby increasing the carrier recombination rate [25]. Fe, Cu, Ni and Co are the most common impurities in Si device fabrication [40]. Cu, Ni and Co have the highest diffusivity and solubility in Si among the transition metals and can be easily introduced into the Si bulk during any heat treatment [40].

Most transition metals form $MeSi_2$ phases in equilibrium with Si at room temperature, where Me is the metallic impurity [25]. Cu forms Cu_3Si. Interstitially dissolved, fast diffusing, elements like Ni and Cu, can be almost totally removed from solid solution by the formation of precipitates at structural defects or by a gettering process, while slowly diffusing elements, like Ti and V, remain in solid solution.

Iron impurities

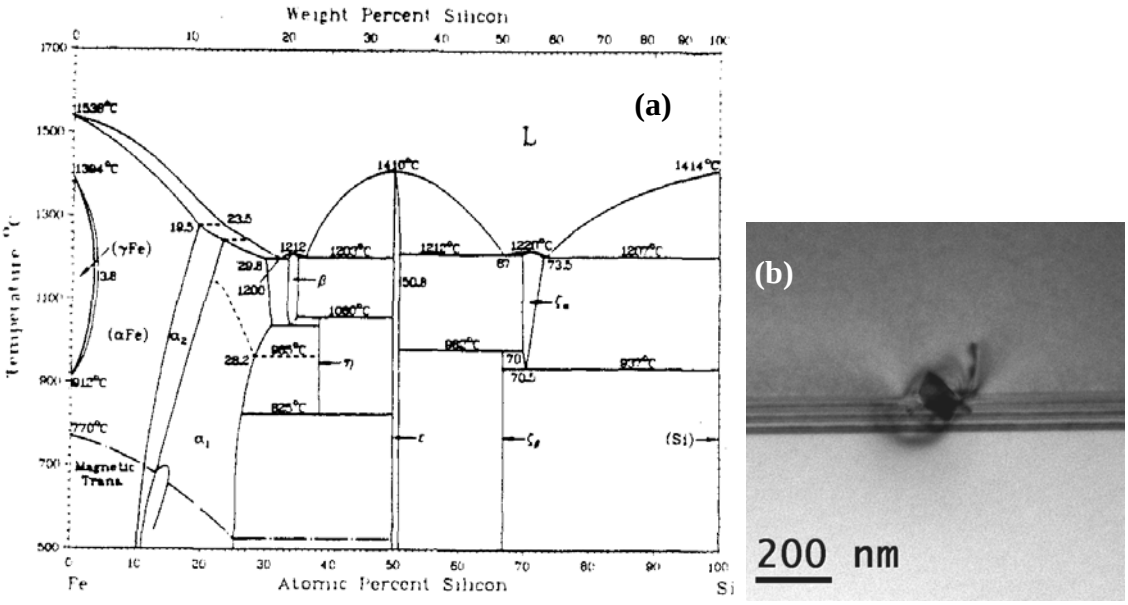

Figure 3.8 (a) The Fe-Si phase diagram [41], (b) Fe rich precipitate in a grain boundary.

Fe is one of the most common and harmful impurities in Si. The diffusivity and solubility of interstitial Fe in intrinsic Si are given by [42]

$$D_{Fe_i} = (1.0^{+0.8}_{-0.4}) \times 10^{-3} \exp\left(-\frac{0.67eV}{k_B T}\right)(cm^2/s) \quad (3.6)$$

and

$$S_{Fe_i} = (8.4^{+5.4}_{-3.4}) \times 10^{25} \exp\left(-\frac{2.86 \pm 0.05eV}{k_B T}\right)\left(cm^{-3}\right), \quad (3.7)$$

respectively. From the solubility equation above, the solubility of Fe in Si at room temperature is ~ 10^{-24} cm^{-3}, but the solubility strongly increases with the doping level [42]. However, Fe has a very high precipitation barrier in Si, which is not diffusion limited, and high concentrations of Fe remain in solid solution even at room temperature [24,43-45]. Fe concentrations up to 10^{14}-10^{15} cm^{-3} have been observed in mc Si [23,24] and concentrations up to 10^{12}-10^{14} cm^{-3} of dissolved Fe have been detected in mc Si [24,43]. At room temperature interstitial Fe forms complexes with substitutional B, Fe_iB_s-pairs, with a binding energy of ~ 0.58-0.65 eV and dissociation energy of ~ 1.2 eV [42]. More than 98 % pairing in a 1 Ωcm B doped mc Si has been observed [24]. Upon heating at 200 °C for some minutes or by illuminating the device, the pairs dissociate into interstitial Fe_i and substitutional B_s [24]. Fe can form more than 30 different complexes with impurities and defects [42].

Fe forms deep levels in Si, both as interstitially dissolved with energy level $E_T \approx E_v$ + 0.38 eV and as Fe_iB_s-pairs with one shallow donor state $E_T = E_v + 0.1$ eV and one acceptor state $E_c - 0.29$ eV. The capture cross-sections for interstitial Fe are $\sigma_n = 5x10^{-14}$ cm^{-2} and $\sigma_p = 7x10^{-17}$ cm^2, while for the a Fe_iB_s pairs they are $\sigma_n = 3x10^{-14}$ cm^2 and $\sigma_p = 2x10^{-15}$ cm^2 for electrons and holes respectively [45]. The recombination activity is about 10 times higher for interstitial dissolved Fe compared to Fe-B pairs, mainly due to their much higher electron to hole capture cross-section ratio, 714 compared to 15 [45].

Figure 3.8 (a) shows the complicated phase diagram for Fe-Si with eutectic temperature at 1220 °C. In Figure 3.9 (b), a Fe-rich precipitate has formed in a grain boundary. Fe is a moderate to fast diffuser in Si with a diffusivity of ~ $4x10^{-6}$ cm^2/s at 1100 °C and precipitates heterogeneous in Si at structural defects. Five different Fe silicide phases have been observed; ε-FeSi cubic phase [46], tetragonal α-$FeSi_2$ [47], orthorhombic β-$FeSi_2$ [48], cubic γ-$FeSi_2$ [49,50] and rarely observed cubic s-$FeSi_2$ [51]. The thermal stability of $FeSi_2$ precipitates has been studied in ref [52]. Interstitial Fe was found to rapidly precipitate at temperatures between 500 °C and 600 °C and to dissolve at temperatures above 760 °C, leading to the conclusion that precipitated $FeSi_2$ is unstable above 760 °C. Buonassisi et al. [1] have reported that a certain annealing, 500 °C for 90 minutes, can promote Fe precipitation [1]. Furthermore, Fe is found to form ε-FeSi or α-$FeSi_2$ precipitates after Fe contamination followed by slow cooling from 1200 °C in a Si bicrystal [53]. After rapid cooling, evidence for segregation of Fe in the grain boundaries was observed by EBIC [53]. Segregation of Fe to dislocations and grain boundaries, in particular small angle grain boundaries due to their dislocation structure, in mc Si has been observed with EBIC [54,55]. In Fe contaminated Cz Si, indications for segregation of Fe to O related defects has been observed [56]. Recently, Fe has also

been detected in multi-metallic precipitates, usually coprecipitated with Cu and Ni [57-59].

Copper impurities

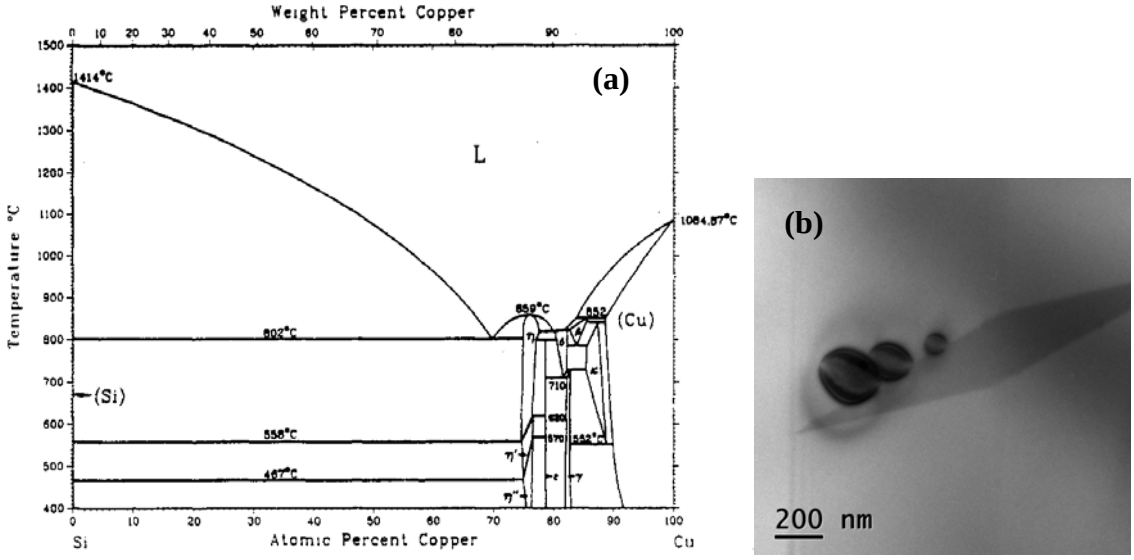

Figure 3.9 (a) The Cu Si phase diagram [41], (b) Cu_3Si precipitates in a grain boundary

Cu is a 3d transition metal and one of the most common impurities in Si. Cu is among the fastest interstitial diffusers in Si and can diffuse through a wafer in hours at room temperature [60]. In B doped Si, positively charged interstitial Cu_i^+ forms pairs with negatively charged substitutional B_s^- that influence the diffusivity [61]. Taking into account the partly trapping of Cu by B, the effective diffusion for Cu in p-type Si is [61]

$$D_{eff} = \frac{3\times10^{-4}\exp(-2090/T)}{1+2.584\times10^{20}\exp(4990/T)\times(N_a/T)}(cm^2/s), \tag{3.8}$$

where $N_a \leq 10^{-17}\ cm^{-3}$ equals the B concentration. For intrinsic Si, the diffusivity was found to be [61]

$$D_{\text{int}} = (3.0\pm0.3)\times10^{-4}\exp\left(-\frac{0.18\pm0.01eV}{k_BT}\right)\left(cm^2/s\right) \tag{3.9}$$

A similar dependence is also assumed for n-type Si. The solubility of Cu in Si is given by [60]

$$S_{Cu_i} = 5.51\times10^{23}\exp\left(-\frac{1.49eV}{k_BT}\right)(cm^{-3}) \tag{3.10}$$

This gives a solubility of only 0.5 cm^{-3} Cu_i at room temperature, resulting in that almost all Cu after slow cooling will be involved in defect reactions. The five main defect reactions observed in Cu are (i) Formation of point defects and their complexes, (ii) Formation of Cu silicide precipitates in the bulk, (iii) Decoration of extended structural defects like dislocations and grain boundaries, (iv) Out-diffusion to the surface and (v) Segregation in p^+ areas [60]. Although Cu_iB_s pairs can form at room temperature, they are unstable because of the low dissociation energy of only 0.61 eV, and dissociate within milliseconds [60]. Cu_3Si formation in Si is associated with a large volume expansion of 150 % [62]. Strain relaxation phenomena, like intrinsic staking fault formation, intrinsic point defect emission and elastic deformation of matrix and precipitates are associated with such precipitates [62].

Four Cu related energy levels in the band gap have been observed, one acceptor state E_c – (0.15-0.2), and three donor states E_v + (0.41-0.46) eV, E_v + (0.20-0.23) eV and E_v + (0.09-0.1) eV [40]. However, Cu does not form electrically active point defects in densities higher than 0.1% of its concentration [40]. Cu silicide precipitates give rise to a broad band of deep level states [63,64]. After annealing at 900 °C and rapid cooling two types of precipitates were observed in grain boundaries, colonies and small precipitates, recognized as the η-Cu_3Si phase. The precipitates were found to give rise to a continuum of acceptor states ranging from E_c-0.30 - E_c-0.56 [64]. Different annealing conditions were found to give rise to different shape of the deep level bands [63,64].

Figure 3.9 (a) shows the complicated phase diagram for Si-Cu with eutectic temperature of 802 °C. In Figure 3.9 (b), Cu precipitates have formed at the interface between two stacking faults in Si. Nes and Washburn [6-8] and later Solberg [9] studied Cu silicide precipitates in Cz Si. Star shaped colonies of spherical precipitates were found to form by repeated nucleation and growth on climbing edge dislocations after air cooling from high temperatures (900 °C). The precipitates were identified as orthorhombic (C) η''-Cu_3Si with lattice parameters, a = 76.76 Å, b = 7.00 Å and c = 21.94 Å [9]. The phase was found to be polymorph and the superperiods in the phase were found to vary with composition. Two precursor phases were also suggested, a high temperature η-phase and an intermediate η'-phase. Both phases were found to be trigonal space groups with symmetry operations $R\bar{3}m$ and $R\bar{3}$, respectively, and lattice parameters $a_n = 2.47\text{Å}$, $\alpha_n = 109.74°$ and $a_{n'} = 4.72\text{Å}$, $\alpha_{n'} = 95.72°$ [9]. Recently, the η and η' phases were studied with in situ TEM and were found to differ from the previous suggested structures [65]. Their space groups were found to be $P\bar{3}m1$ and $R\bar{3}$, respectively. The lattice parameters of η were found to be a = 4.06 Å and c = 7.33 Å and the unit cell to be hexagonal. The η' phase was found to result from faulted stacking of the η phase and its lattice parameters were found to be a = 35.16 Å and c = 21.99 Å [65].

After rapid quenching from high temperatures, large supersaturation due to fast cooling forces the Cu to precipitate as metastabile Cu silicide platelets parallel to {111} planes in Cz Si [66]. An extrinsic stacking fault surrounding the platelet was found to allow strain relaxation by self-interstitial emission. For slow cooling, when Cu has time to diffuse, colony formation has been observed, consistent with the observations of Nes

and Solberg [6-9]. However in this case, the dislocations were seen to form as a result of homogenous Cu precipitation. Moreover, the phase of the particles was found to be hexagonal with lattice vectors a = 7.08 Å and c = 0.738, close to the η' phase [67]. The difference was suggested to be due to double diffraction from the bulk in the case of Solberg [9]. During slow cooling, Cu colonies frequently precipitate at or close to the surface in mono-crystalline Si [40]. In mc Si, Cu preferentially precipitates in grain boundaries [68,69]. However, disk shaped poly-crystalline platelets have been observed either in {111} planes or in {001} planes, surrounded by large strain fields in a rapid cooled bicrystal [70]. Two types of Cu silicide precipitates were observed in disc shaped colonies in grain boundaries after rapid cooling from high temperature [68,69]. The colonies were found to contain between 10 and 200 precipitates with sizes from 10 to 2000 nm, the largest precipitates located in the centre [69]. Type A particles were found to have bcc lattice, containing at least 72 % Cu [69]. Also solid disc shaped precipitates have been observed in grain boundaries, but their composition were not determined [71]. Cu silicide precipitates decorate extended defects and have been observed on dislocations, stacking faults, O related defects, grain boundaries and on He-implantation induced vacancies [40].

Cu precipitates show strong recombination activity in Si [40]. Ihlal et. al [71] studied, in 1994, Cu contamination in a Si bicrystal by EBIC and TEM and found that the strong EBIC contrast was mainly attributable to Cu_3Si precipitates, although O also had to be taken into account. The increase of the EBIC contrast with temperature and its nature, discontinuous or uniform, were found to be controlled by the precipitate density at the grain boundary [71].

Nickel impurities

Ni is a common impurity in Si. The solubility of Ni in intrinsic Si below eutectic temperature is given by [72]

$$S_{Ni} = 1.227 \times 10^{24} \exp\left(-\frac{1.68eV}{k_B T} \right) \left(cm^{-3} \right) \tag{3.11}$$

Unlike Fe and Cu, the solubility of Ni is independent of P doping and increases slowly with increasing B doping [73]. This means that Ni cannot be effectively gettered by heavily doped layers, and that Ni is mostly in its neutral state in Si [73]. Ni is a fast interstitial diffuser in Si and its diffusivity is given by [72]

$$D_{Ni_i} = 2 \times 10^{-3} \exp\left(-\frac{0.47eV}{k_B T} \right) (cm^2 / s) \tag{3.12}$$

Even at room temperature interstitially dissolved Ni is unstable and rapidly precipitates during or after a quench [40]. Four energy level in the band gap have been frequently observed after Ni diffusion, two acceptor levels E_c - (0.15-0.21) eV and E_c - (0.36-0.47) eV and two donor levels E_v + (0.15-0.21) eV and E_v + (0.31-0.35) eV. The

concentration of the defects has been found to depend on the cooling rate after diffusion [74].

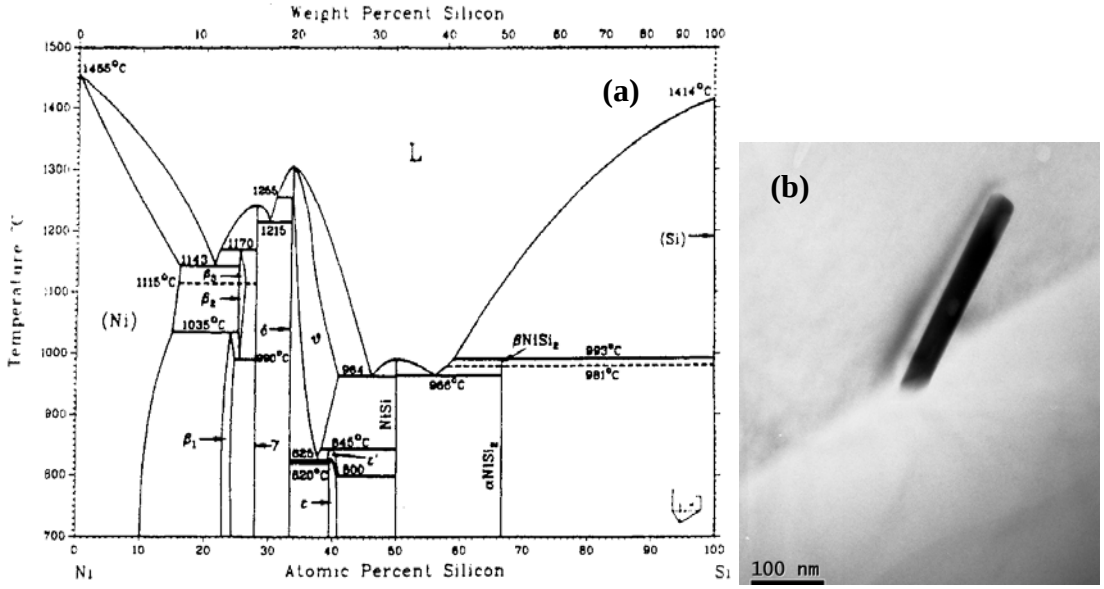

Figure 3.10 (a) The Ni-Si phase diagram [41], (b) Ni rich precipitate in a grain boundary.

The precipitation phase of Ni in Si is $NiSi_2$, which has the fcc cubic unit cell of fluoride CaF_2 and space group Fm3m. The Ni atom is placed at origin and the two Si atoms at ± a/4<111> [40]. The lattice vector of $NiSi_2$ is only 0.46 % less than that of pure Si, 5.405 Å and 5.428 Å respectively, such that the volume expansion is very low [40]. Most of the Ni precipitates at the surface after slow cooling in defect free, monocrystalline Si wafers [40]. After quenching from high temperatures, Ni forms thin $NiSi_2$ platelets, with diameters from 20-900 nm, consisting of two atomic (111) layers. The platelets were found to have seven-fold symmetry. The platelets are associated with a stacking fault in the matrix and bound by a dislocation loop with Burgers vector, **b** = a/4<111> [62,75]. The dislocation establishes a fast precipitate growth by incorporation of interstitial Ni via its core [62]. Deep band-like states have been attributed to the platelets [62]. A continuum of states between E_c - 0.63 and E_c - 0.52 were observed after annealing at 600 °C [76]. For higher temperatures the band was found to shift to shallower levels due to different precipitates forming [76]. For slow cooling, or after an internal ripening process of the thin platelets, thicker, more solid precipitates formed in monocrystalline Si [77].

If present, Ni decorates extended defects like dislocations, O defects, grain boundaries and He-implanted induced cavities in Si and significantly increases their recombination activity [40]. Figure 3.10 (a) shows the complicated Ni-Si phase diagram with eutectic temperature 966 °C. In Figure 3.9 (b) a Ni-rich rod shaped precipitate has formed in a grain boundary. Individual $NiSi_2$ was found to give strong recombination activity that increased slightly with the temperature [78]. In mc Si, Ni was found to precipitate in certain grain boundaries that showed strong recombination activity [79]. Two different orientation relationships of $NiSi_2$ precipitates after rapid cooling have been observed, a

cube/cube type A with coincidence Σ=1 and a twin type B with Σ=3 [75]. The interface configurations between the type A $NiSi_2$ and the Si matrix have been widely studied as discussed in ref [80]. In a Σ = 25 bicrystal, both types of precipitates were observed in the grain boundary. Almost coherent octahedral or decahedral shaped type A precipitates were found to present (111) and (100) facets with one of the grains, while the type B precipitates were platelet shaped and were found to grow along (111) planes [80]. The precipitate type, their size and density have been found to depend on the annealing temperature [81]. For annealing temperatures below 600 °C, no precipitates were observed. Small type B precipitates were found to dominate for low annealing temperatures, while large type A precipitates dominated for high annealing temperatures [81]. Large B´ type platelets, ~ 1.5 μm, were observed after anneal at 1200 °C [81]. The large size of the precipitates was proposed to be due to liquid droplets forming, as observed for $NiSi_2$ at the Si surface due to its low eutectic temperature (Fig 3.9 (a)) [81,82]. Moreover, dislocations with Burgers vector **b** = a/2 [110] were observed around the largest precipitates due to volume misfit [81]. Dislocations with Burgers vectors a/4[111], a/2[110] and a/6[211] and a/2[110] observed at silicide/Si interfaces, can relieve the misfit strain for type A and B precipitates, respectively [83,84].

Tungsten impurities

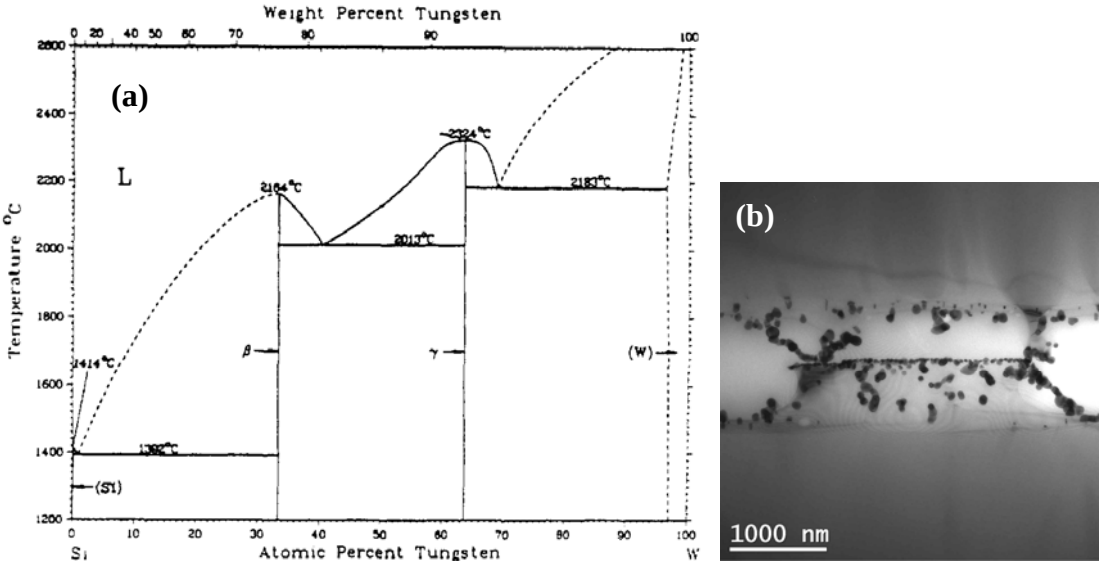

Figure 3.11 (a) The Si-tungsten phase diagram showing the eutectic temperature of 1392 °C, (b) SiW_2 precipitates on the Si surface.

W is introduced into Si wafers either by direct processing (used for metallization) or as a contaminant. W concentrations down to $5x10^9$ cm^{-3} can be harmful for devices [85]. W has very low diffusivity in Si, of the order of magnitude of B or P [85], and therefore the contamination introduced remains localized in the surface region [85]. However a very small amount of the W atoms rapidly diffuse interstitially deeper into the Si bulk, seriously degrading device characteristics [86]. After long diffusion and slow cooling to room temperature, W forms electrically active defects. Several papers have reported formation of deep levels in Si after W diffusion [86-90], both acceptor and donor levels.

However they are very inconsistent, E_c - 0.22 eV and E_v + 0.41 eV for substitutional positions [86], E_c- 0.28 eV and E_c- 0.25 eV [87], E_v+ 0.31 eV, E_v+ 0.34 eV, E_c - 0.37 eV, E_c - 0.30 eV, and E_c - 0.22 eV [88], E_v + 0.41 eV [89] and E_v + 0.22 eV, E_v + 0.33 eV, and E_c - 0.59 eV [90]. It was proposed that some of the observed states in [86-88] might be due to impurities in the W [89].

The Si-W phase diagram is shown in figure 3.10 (a) and WSi_2 precipitates deposited on the Si surfaces are shown in figure 3.10 (b). Thin WSi_2 films on Si surfaces can be formed by deposition of a W thin film on a Si wafer by chemical vapour deposition (CVD) [91,92], sputtering [93] or evaporation [94], followed by furnace annealing or rapid thermal annealing at temperatures below 800 °C. WSi_2 has low electrical resistivity, high thermal and chemical stability and has been used in the semiconductor industry as gate electrodes or interconnections [95,96].

Multi-metallic precipitates

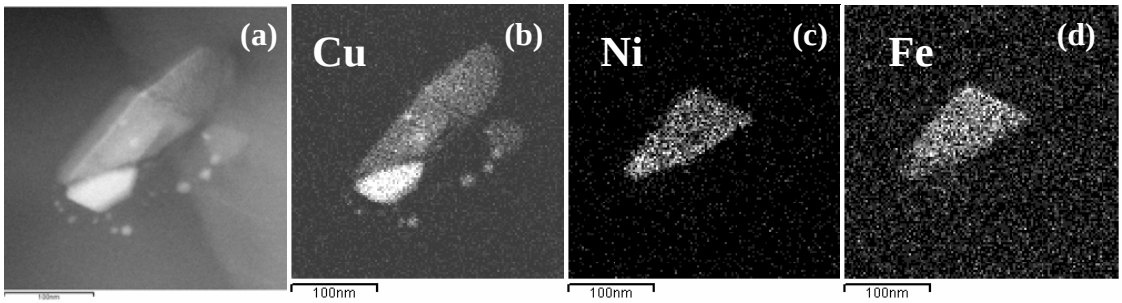

Figure 3.12 EDS elemental mapping of multi-metallic precipitates in a grain boundary, (a) Bright field TEM image of the precipitates consisting of (b) Cu, (c) Ni and (d) Fe in addition to Si.

Multi-metallic silicide precipitates containing Ni and Cu were first observed by Ryoo et al. in 1988 [97]. Two types of precipitates, colonies and plates, were found to decorate O induced dog-bone stacking faults in monocrystalline Si. Both precipitate types were found to have $NiSi_2$ structure, the colony type consisting of (75 % Cu and 25 % Ni)Si_2 and the platelet type was found to be almost pure $NiSi_2$ [97]. Recently, multi-metal silicide precipitates have been studied using X-ray synchrotron techniques and TEM [57-59]. Large precipitates containing Ni, Cu and Fe were observed in Si doped with transistion metals consisting of clusters separated into a Cu_3Si phase and a Ni-Cu-Fe phase with $NiSi_2$ structure. In the Ni rich $NiSi_2$ structure, Fe has been proposed to replace Ni and Cu to replace Si [57,58]. After slow cooling from low temperature (~ 600 °C) annealing, single metallic silicides were observed, while multi-metal silicides were observed after high temperature (~1200 °C) annealing [59]. In a Si ingot grown from metallurgical feedstock, similar multi-metallic precipitates have been observed [98]. In addition, several types of smaller Ni-rich multi-metallic precipitates were observed in such samples, often with a Fe rich core [98].

A multi-metallic cluster consisting of Cu_3Si precipitate and a Ni-Fe-rich precipitate is shown in figure 3.12. The multi-metallic precipitates are probably more stable and have

less lattice misfit with Si than the mono-metal silicides, and are therefore favored [59]. Also from thermodynamic entropy considerations, multi-metallic precipitates are favorable. The formation of multi metallic precipitates containing a central Ni rich structure with Cu_3Si nodules can occur via solid state diffusion, where a multi metallic precursor decomposes into one Ni-rich phase and one Cu-rich phase upon cooling, to minimize lattice mismatch [58]. The solubility of metal impurities in metal silicides is probably higher than in the Si bulk. During cooling of the ingot, the different phases might separate according to the complex phase diagram of the coprecipitated impurities. Another possible formation mechanism of the two phase precipitates is the liquid droplet theory proposed by Buonassisi et al. [59]. In this theory supersaturated metals in the Si melt, which have a lower melting point than the rest of the melt, can form liquid droplets that act as internal gettering centers for metals, during cooling from high temperatures. Cu, which has the lowest solidifying temperature, 802 °C, probably expels the other metallic species during cooling, while being the last part of the droplet to solidify, as Cu nodules on the Ni rich precipitate [59]. Liquid droplets of $NiSi_2$ (eutectic temperature 966 °C) have been observed on the Si surface during diffusion of Ni into Si at 1200 °C [82], and have been suggested to cause formation of large $NiSi_2$ inclusions in the Si grain boundaries after annealing at 1200 °C [81]. Also a liquid Cu - containing phase has been observed on the Si surface at 840 °C [65].

Multi-metallic precipitates have been observed in low angle grain boundaries [99]. Grain boundaries contaminated with multi-metallic precipitates showed strong recombination activity [99].

3.4 Gettering and defect engineering

Gettering is a process in which harmful impurities are removed from critical parts of the wafer, by introducing impurity sinks in noncritical parts of the wafer [100]. In microelectronics the active area is limited to a thin region below the wafer surface such that internal gettering of the impurities to bulk defects to clean the near surface region is necessary [101]. This is called internal or intrinsic gettering and usually refers to removal of harmful impurities by Si oxide and its induced defects [102]. For solar cells the bulk is the critical region and the impurities are gettered to external layers usually by P diffusion gettering or aluminium gettering [103].

During P diffusion gettering, impurities segregate in the P layer due to higher solubility in highly n doped Si. Impurity migration towards gettering sites takes place as a consequence of a large emission of Si interstitials due to the formation of SiP particles by heavy P-diffusion. Enhanced solubility of metallic impurities in such heavily P-diffused regions together with impurity segregation at Si_3P_4 precipitates, lead to efficient gettering. Aluminium gettering is efficient because of the higher solubility of metals impurities in the Al:Si eutectic compared to the bulk [103].

Defect engineering is use of heat treatments to improve the performance of the solar cell [105]. By engineering the distributions of the metallic impurities in the solar cell, the minority carrier diffusion length can be increased up to a factor of four [104].

Precipitated metal impurities have been found to be less detrimental for the solar cells than dissolved impurities. Reducing impurities like the slow diffusing Ti is therefore crucial to enhance lifetime and diffusion length. The use of time temperature transformation (TTT) diagrams to enhance Fe precipitation [105], can probably be extended to other elements.

The dislocation density has been found to be lower after fast cooling of the solidified ingot compared to slow cooling [106]. High temperature treatments (~ 1300 °C), have recently been found to significantly reduce the dislocation density in the bulk Si [107]. Controlled dendritic growth associated with twin formation, might provide less nucleation sites for the precipitates and can also lower the dislocation density [108,109].

References

[1] M. D. Pickett and T. Buonassisi, Appl. Phys. Lett. **92**, 122103 (2008)
[2] D. Hull and D. J. Bacon; *Introduction to dislocations*, Butterworth-Heinemann, fourth edition (2001) and references therein.
[3] *Hydrogen in crystalline semiconductors*, J. Pearton, W. Corbett and M. Stavola, Springer-Verlag (1992) and references therein
[4] B. G.Yacobi, *Semiconductor materials: An introduction to basic principles*, Secaucus, NJ, USA; Kluwer academic publishers (2002) and references therein.
[5] John D. Verhoeven, *Fundamentals of Physical Metallurgy*, John Wiley & Sons (1975)
[6] E. Nes and J. Washburn, J. Appl. Phys. **42**, 3562 (1971)
[7] E. Nes and J. Washburn, J. Appl. Phys. **43**, 1835 (1972)
[8] E. Nes and J. Washburn, J. Appl. Phys. **44**, 3682 (1973)
[9] J. K. Solberg and E. Nes, Acta Crystallogr. A **34**, 684 (1978)
[10] J. M. Silcock and W. J. Tunstall, Phil. Mag. **10**, 361 (1964)
[11] G. Stokkan, *Characterisation of multicrystalline silicon solar cells; Development of characterization method for the combined effect of dislocations and grain boundaries on the minority carrier lifetime*, PhD thesis, NTNU (2004) and references therein
[12] J. P. Hirth and J. Lothe, *Theory of dislocations*, New York: McGraw-Hill (1968)
[13] A. H. Cottrell, *Progress in metal physics*, Pergamon Press, London and New York (1956)
[14] F. C. Frank and W. T. Read, Phys. Rev. **72**, 722 (1950)
[15] D. B. Holt and B. G. Yacobi, *Extended defects in semiconductors : electronic properties, device effects and structures*, Cambridge University Press (2007)
[16] T. Sekiguchi, B. Chen, T. Watanabe and K. Sumino, Mat. Sci. Eng. B **42**, 235 (1996)
[17] J. Chen, T. Sekiguchi, D. Yang, F. Yin, K. Kido and S. Tsurekawa, J. Appl. Phys. **96**, 5490 (2004)
[18] J. Chen, T. Sekiguchi, R. Xie, P. Ahmet, T. Chikyo, D. Yang, S. Ito and F. Yin, Scripta materialia **52,** 1211 (2005)
[19] J. Chen and T. Sekiguchi, Jpn. J. Appl. Phys. **46**, 6489 (2007)
[20] Z.-J. Wang, S. Tsurekawa, K. Ikeda, T. Sekiguchi and T. Watanabe, Interface Sci. **7**, 197 (1999)
[21] J. Chen, T. Sekiguchi, S. Nara and D. Yang, J. Phys.: Condens. Matter **16,** S211 (2004)
[22] M. Acciarri , S. Binetti , A. Le Donne, S. Marchionna, M. Vimercati, J. Libal, R. Kopecek, K. Wambach Prog. Photovolt. Res. Appl. **15,** 375 (2007)
[23] A. A. Istratov, T. Buonassisi, R. J. McDonald, A. R. Smith, R. Schindler, J. A. Rand, J. P. Kalejs and E. R. Weber, J. Appl. Phys. **94**, 6552 (2003)
[24] D. Macdonald, A. Cuevas, A. Kinomura, Y. Nakano and L. J. Geerligs, J. Appl. Phys. **97**, 033523 (2005)
[25] H. J. Möller, Progress in Materials Science **35**, 205 (1991) and references therein
[26] J. R. Davis, A. Rohatgi, R. H. Hopkins, P. D. Blais, P. Rai-Choudhury, J. R. McCormick and H. C. Mollenkopf, IEEE Trans. Electron Devices, ED-**27**, 677 (1980)
[27] Øyvind Mjøs, *Directional solidification of silicon for solar cells*, Doctoral thesis, NTNU, **109** (2006) and references therein
[28] Anne Karin Søyland, *Silicon for solar cells*, Doctoral thesis, NTNU, **140** (2004) and references therein
[29] Wakshum Mekonnen Tucho, *The effects of SiC and Si_3N_4 inclusions in multicrystalline silicon solar cell performance*, Master thesis, NTNU (2004)
[30] O. Breitenstein J. P. Rakotoniaina, M. H. Al Rifai and M. Werner, Prog. Photovoltaic: Res. Appl. **12**, 529 (2004)
[31] A. Lotnyk, J. Bauer, O. Breitenstein and H. Blumtritt, Sol. Energy Mater. Sol. Cells, **92**, 1236 (2008)
[32] J. Bauer, J.O. Breitenstein, M. Becker , J. Lenzner, Proceedings of the Seventh NREL Workshop on Crystalline Silicon Solar Cells and Modules: Materials and Processes, Vail, USA, p. 233 (2007)
[33] J.P. Rakotoniaina, O. Breitenstein, M. Werner, M.H. Al Rifai, T. Buonassisi, M.D. Pickett, M. Ghosh, A. Mu¨ ller, N.L. Quang, Proceedings of the 20th European photovoltaic Solar Energy Conference and Exhibition, Barcelona, Spain, p. 773 (2005)
[34] K. Nakai, Y. Inoue, H. Yokota, A. Ikari, J. Takahashi, A. Tachikawa, K. Kitahara, Y. Ohta, and W. Ohashi, J. Appl. Phys. **89**, 4301 (2001)

[35] A. Borghesi, B. Pivac, A. Sastella and A. Stella, J. Appl. Phys. **77**, 4169 (1995) and references therein
[36] J. C. Mikkelsen, *Mater. Res. Soc. Symp. Proc.* **59**, 26 (1986).
[37] H. J. Möller, L. Long, M. Werner and D. Yang, Phys. Stat. Sol. A **171**, 175 (1999)
[38] H. J. Möller, L. Long, S. Riedel, M. Rinio, D. Yang and M. Werner, *Proceedings of the 7th Workshop on the Role of Impurities and Defects in Silicon Device Processing, National Renewable Energy Laboratory, Golden, USA*, pp 41 (1997)
[39] J. M. Hwang and D. K. Schroder, J. Appl. Phys. **59**, 2476 (1986)
[40] A. A. Istratov and E. R. Weber, Appl. Phys. A **66**, 123 (1998) and references therein.
[41] Thermodynamics of solid transmission–metal silicides, Mark E. Schlesinger, Chem. Rev. **90**, 607 (1990) and references therein.
[42] A. A. Istratov, H. Hieslmair and E. R. Weber, Appl. Phys. A **69**, 13 (1999) and references therein
[43] T. Buonassisi, A.M. Lorenz, and G.J. Tarnowski, *Proc. 21st European Photovoltaic Solar Energy Conference and Exhibition*, *Dresden, Germany* p. 1505 (2006)
[44] D. Macdonald, T. Roth, L. J. Geerligs and A. Cuevas, Solid state phenomena **108-109**, 519 (2005)
[45] J. Schmidt, Prog. Photovolt. **13,** 325 (2005)
[46] J. Derrien, J. Chevrier, V. Le Thanh, I. Berbezier, C. Giannini, S. Lagomardino and M. G. Grimaldi, Appl. Surf. Sci. **70**, 90 (1993)
[47] I. Berbezier, J. Chevrier and J. Derrien, Surf. Sci. **315**, 27 (1994)
[48] I. Berbezier, J. L. Regolini and C. D'Anterroches, Microscopy Microanalysis Micro-structures **4**, 5 (1993)
[49] E. Müller, D. P. Grindatto, H. U. Nissen, N. Onda and H. von Känel Appl. Phys. Lett. **64**, 1938 (1994)
[50] M. Werner, E. R. Weber, S. McHugo, H. Hieslmair and K. L. Chapman, Sol. Stat. Phen. **47-48**, 449 (1996)
[51] N. Onda, J. Henz, E. Müller, K. Mader and H. von Känel, Appl. Surf. Sci. **56**/**58**, 421 (1992)
[52] D. A. Ramappa and W. B. Henley, J. Electrochem. Soc. **144**, 4353 (1997)
[53] X. Portier, A. Ihlal and R. Rizk, Phys. Stat. Sol. A **161**, 75 (1997)
[54] J. Chen, T. Sekiguchi, R. Xie, P. Ahmet, T. Chikyo, D. Yang, S. Ito and F. Yin, Scripta materialia **52**, 1211 (2005)
[55] J. Chen and T. Sekiguchi, Jpn. J. Appl. Phys. **46**, 6489 (2007)
[56] B. Chen, J. Jablonski, T. Sekiguchi and K. Sumino, Jpn. J. Appl. Phys. **35**, 4187 (1996)
[57] M. Heuer, T. Buonassisi, M. A. Marcus, A. A. Istratov, M. D. Pickett, T. Shibata and E.R. Weber, Phys. Rev. B **73**, 235204 (2006)
[58] M. Heuer, T. Buonassisi, A. A. Istratov and M. D. Pickett, J. Appl. Phys **101**, 123510 (2007)
[59] T. Buonassisi, M. Heuer, A. A. Istratov, M. D. Pickett, M. A. Marcus, B. Lai, Z Cai, S. M. Heald, E. R. Weber, Acta Materialia, **55**, 6119 (2007)
[60] A. A. Istratov and E. R. Weber, J. Electrochem. Soc. **149**, G21 (2002) and references therein
[61] A. A. Istratov, C. Flink, H. Hieslmair, E. R. Weber and T. Heiser, Phys. Rev. Lett. **81**, 1243 (1998)
[62] M. Seibt, H. Hedemann, A. A. Istratov, F. Riedel, A. Sattler and W. Shröter, Phys. Stat. Sol. A **171**, 301 (1999)
[63] A. A. Istratov, H. Hedemann, M. Seibt, O. F. Vyvenko, W. Schröter, T. Heiser, C. Flink, H. Hieslmair and E. R. Weber, J. Electrochem. Soc. **145**, 3889 (1998)
[64] J. F. Hamet, R. Abdelaoui and G. Nouet, J. Appl. Phys. **68**, 638 (1990)
[65] C-Y. Wen and F. Spaepen, Phil. Mag. **87**, 5581 (2007)
[66] M. Seibt, M. Griess, A. A. Istratov, H. Hedemann, A. Sattler and W. Schröter, Phys. Stat. Sol. A **166**, 171 (1998)
[67] M. Seibt, Solid State Phenomena **19**/**20**, 45 (1991)
[68] J.-L. Maurice and C. Colliex, Appl. Phys. Lett. **55**, 241 (1989)
[69] M. Elkajbaji, J. Dessus and J. Thibault, Phil. Mag. A **66**, 873 (1992)
[70] M. E. Kajbaji and J. Thibault, Phil. Mag. Lett. **71**, 335 (1995)
[71] A. Ihlal and G. Nouet, Phys. Stat. Sol. A **141**, 81 (1994)
[72] E. R. Weber, Appl. Phys. A **30**, 1 (1983) and references therein.
[73] A. A. Istratov, P. Zhang, R. J. McDonald, A. R. Smith, M. Seacrist, J. Moreland, J. Shen, R. Wahlich and E. R. Weber, J. Appl. Phys. **97**, 023505 (2005)
[74] H. Indusekhaar and V. Kumar, J. Appl. Phys. **61**, 1449 (1987)
[75] M. Seibt, and W. Schröter, Phil. Mag. A **59**, 337 (1999)

[76] R. Rizk, A. Ihlal and X. Portier, J. Appl. Phys. **77**, 1875 (1995)
[77] F. Riedel, H. Hedemann and W. Schröter, Nucl. Instrum. Meth. Phys. Res. A **476**, 596 (2002)
[78] M. Kittler, W. Seifert and Z. J. Radzimski, Appl. Phys. Lett. **62**, 2513 (1993)
[79] Z. Xi, D. Yang, J. Chen and T. Sekiguchi, Mater. Sci. Semicond. Proc. **9**, 304 (2006)
[80] X. Portier, R. Rizk, G. Nouet and G. Allais, Phil. Mag. A **71**, 1109 (1995)
[81] X. Portier and R. Rizk, Phys. Stat. Sol. A **155**, 125 (1996)
[82] J. Li, W. S. Yang, T. Y. Tan, S. Chevacharoenkul and R. Chapman, J. Appl. Phys. **71**, 196 (1992)
[83] H. Foll, P. S. Ho and K. N. Tu, J. Appl. Phys. **52**, 461 (1981)
[84] H. von Känel, Mater sci. Rep. **8**, 193 (1992)
[85] D. Cali, C. M. Camalleri and V. Raineri, Mater. Sci. Semicond. Proc. **4**, 19 (2001)
[86] Y. Fujisaki, T. Ando, H. Kozuka and Y. Takano, J. Appl. Phys. **63**, 2304 (1988)
[87] H. H. Busta and H. A. Waggener, J. Electrochem. Soc. **124**, 1424 (1977)
[88] Y. A. Zibuts, L. G. Paritskii and S. M. Ryvkin, Sov. Phys. Solid State **5**, 2416 (1964)
[89] T. Ando, S. Isomae, C. Munakata and T. Abe, J. Appl. Phys. **70**, 5401 (1991)
[90] S. Boughaba and D. Mathiot, J. Appl. Phys. **69**, 278 (1991)
[91] S.-L. Zhang, R. Buchta, M. Ostling, Mater. Res. Soc. Symp. Proc. **168**, 173 (1990)
[92] S. C. Tjong and I. C. Hsieh, Mat. Res. Bull. **22**, 841 (1987)
[93] E. Ma, B.S. Lim, M.-A. Nicolet, N.S. Alvi, A.H. Hamdi, J. Electron. Mater. **17**, 207 (1988)
[94] J. Lajzerowicz, J. Torres, G. Goltz, R. Pantel, Thin Solid Films **140**, 23 (1986)
[95] M.F. Bain, B.M. Armstrong, H.S. Gamble, Vacuum **64**, 227 (2002)
[96] J.H. Liang, D.S. Chao, Surf. Coat. Technol. **140**, 116 (2001)
[97] K. Ryoo, R. Drosd and W. Wood, J. Appl. Phys. **63**, 4440 (1988)
[98] H. Nordmark, M. Di Sabatino, E. J. Øvrelid, J. C. Walmsley and R. Holmestad, *Proceedings of the 22nd European Photovoltaic Solar Energy Conference, Milano, Italy*, p 1710 (2007)
[99] H. Nordmark, M. Di Sabatino, M. Acciarri, S. Binetti , J. Libal, E. J. Øvrelid, J. C. Walmsley and R. Holmestad, *Proceedings of the 33rd IEEE conference, San Diego, USA* (2008)
[100] S. M. Myers, M. Seibt and W. Schröter, J. Appl. Phys. **88**, 3795 (2000)
[101] K. Sumino, Microelectronic Eng. **66**, 268 (2003)
[102] D. Gilles, E. R. Weber and S. K. Hahn, Phys. Rew. Lett. **64**, 196 (1990)
[103] M. Seibt, A. Sattler, C. Rudolf, O. Voß, V. Kveder and W. Schröter, Phys. Stat. Sol. A **203**, 696 (2006)
[104] T. Buonassisi, A. A. Istratov, M. A. Marcus, B. Lai, Z. Cai, S. M. Heraldand E. R. Weber, Nature Materials **4**, 676 (2005)
[105] M. D. Pickett and T. Buonassisi, Appl. Phys. Lett. **92**, 122103 (2008)
[106] R. Kvande, *Inncorporation of impurities during directional solidification of multicrystalline silicon for solar cells*, PhD thesis, Nowegian University of Science and Technology, Trondheim, Norway (2008)
[107] K. Hartman, M. Bertoni, J. Serdy, and T. Buonassisi, Appl. Phys. Lett. **93**, 122108 (2008)
[108] G. Stokkan, E. Olsen, *Proceedings 22nd European Photovoltaic Solar Energy Conference, Milan, Italy*, p.1389 (2007)
[109] K. Fujiwara, K. Maeda, N. Usami, G. Sazaki, Y. Nose and K. Nakajima, Scripta Materialia **57,** 81 (2007)

4. Hydrogen in silicon

Hydrogen is present in virtually every step during the processing of silicon devices, either as an annealing or sintering ambient, as part of plasma used for dry etching, or as a component of the chemicals used for conventional wet etching or solvent cleaning [1]. Thereby, atomic hydrogen can easily be introduced into silicon, intentionally or unintentionally. Atomic hydrogen can alter the electrical and optical properties in silicon. In amorphous and mc Si solar cells, atomic hydrogen is used to passivate/saturate electrically active dangling bonds from crystal defects, both surface defects and bulk defects. Hydrogen also interacts with impurities and deactivates dopants [1]. Hydrogen plasma exposure can passivate more than 99 % of the boron near the exposed surface [2,3]. Deep levels in the band gap from several transmission metals, are passivated by hydrogen and the passivation can be stable up to 400 °C. Hydrogen itself and most of the complexes involving H are neutral, but there are also examples of deep levels that are either unaffected by hydrogen or are generated by hydrogenation [1].

Hydrogen is an amphoteric specie with both an acceptor and a donor state in the silicon band gap. In p-type silicon, hydrogen is in the form of H^+, while in n type silicon, atomic hydrogen can form negatively charged species, H^- or H^0 [1]. In addition, hydrogen can form two types of dimers in silicon, interstitial H_2 and H_2^*. Hydrogen diffuses interstitially in silicon, ~ 10^{-10} cm^2/s (H^+) [1] at room temperature. Temperature dependent hydrogen diffusivity is given by

$$D_{H^+} = 9.4\times10^{-3}\exp\left(\frac{-0.48eV}{kT}\right)\ (cm^2/s), \tag{4.1}$$

in undoped, defect free silicon [4], but is strongly affected by doping, impurities and structural defects [1]. Since hydrogen atoms can passivate dopants, impurities and structural defects, the diffusivity is 2-6 orders of magnitude lower in mc Si and doped mono Si [5]. The solubility of hydrogen molecules in undoped silicon is given by [4]

$$s = 4.96\times10^{21}\exp\left(\frac{-1.86eV}{kT}\right)\ (\text{at/cm}^3) \tag{4.2}$$

at 1 atm, while in ~ 10^{17} cm^{-3} boron doped silicon the solubility was found to be [6]

$$s_H = 9.1\times10^{21}\exp\left(\frac{-1.80eV}{kT}\right)\ (\text{at/cm}^3) \tag{4.3}$$

However, the atomic H solubility has been found to be greater than the solubility given by [7]

$$s_H = 5.6\times10^{18}\exp\left(\frac{-0.95eV}{kT}\right)\ (\text{at/cm}^3) \tag{4.4}$$

The solubility curves are shown in Figure 4.1 below. Hydrogen can passivate thermal donors, and hydrogen containing defects in O-rich Si can give rise to photoluminescence. Hydrogen is also found to enhance O diffusion [8]. Heavy hydrogenation can introduce recombination active extended hydrogen induced defects, mostly platelets in {111} and {100} planes [9]. Direct hydrogenation can also cause orientation dependent texturing of the surface [10].

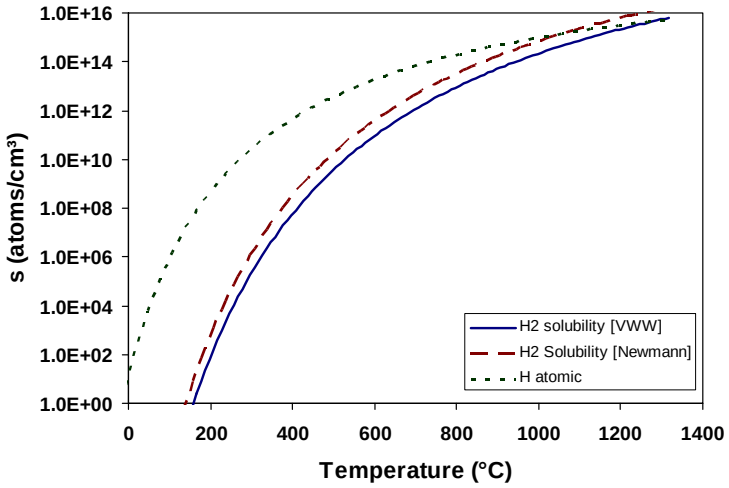

Figure 4.1. Hydrogen solubility in silicon as a function of temperature.

4.1 Introduction methods

The two most common methods to intentionally introduce high doses of hydrogen into silicon are by use of hydrogen plasma or hydrogen implantation. A combination of the two techniques is also sometimes used.

Hydrogen plasma exposure

Molecular hydrogen is pumped through a quartz tube with reduced pressure (~ 0.1-0.3 torr, flow rate < 10^3 cm^3/min). The plasma is excited by inductively coupling low frequency (~ 30 kHz) or radio frequency (~ 13.56 MHz) power via a high frequency oscillator. The substrate temperature is typically 100-400 °C and exposure times of 0.5-3 hours either downstream from (remote plasma) or directly immersed (direct plasma) in the plasma. Typical power densities are 0.1-1 W/cm^2. At high power densities the plasma is more ionized, and hence more efficient in providing atomic hydrogen, but higher ion and electron bombardment energies can cause damage to the near-surface of the sample. Hydrogen is incorporated up to several tens of µm into the sample bulk, depending on the material and doping [1]. Typical energies of the H^+ are 100-1000 eV. Surface damage can occur for energies higher than ~ 15 eV. Alternatively, plasma-assisted deposition or etching reactor in which the electrodes are inside the chamber can be used. Hydrogen is introduced at reduced pressure into the system and ionized by an

applied field. Direct plasma hydrogenation can cause surface damage of the substrate. [1].

In paper 4-7, the samples were directly exposed to hydrogen plasma in the reactor using a plasma enhanced chemical vapour deposition (PECVD) setup. In the PECVD setup a 110 MHz plasma generator was used. The radio frequency (RF) plasma density during hydrogenation was 0.04 W/cm^2. Plasma ignition was done at higher densities (above 0.1 W/cm^2) when samples were removed from the plasma area and then reintroduced after stabilisation of the discharge at the density of 0.04 W/cm^2 with a hydrogen gas flux of 200 sccm. The treatment lasted for between 0.5 and 2 hours and a frequency of 13.56 or 110 MHz, a power of 50 W and a substrate temperature of ~ 250 °C were used.

Hydrogen implantation

Hydrogen can be introduced into the Si bulk at a certain depth by implantation using low ion energy (400-1500 eV) and high beam current (0.5-1.5 mAcm^2). The hydrogen is usually obtained from a broad beam, multi-aperture ion source commonly called a Kaufman ion source. The advantages are their close control of H^+ ion energy, dose and dose rate and short exposure times. The major disadvantage is the extensive damage to the near-surface region by the high level of hydrogen bombardment [1].

The energetic H atoms penetrate into the Si bulk and interact with the Si atoms in their path. The ions are scattered in different angles and have different paths and range in the bulk, giving rise to a statistical depth distribution of the ions after implantation. The mean projected range, R_p, of the ions is a straight line from the surface normal to the ion concentration peak and is a complicated function, depending on the interaction of the ions with electrons and atom cores together with the mass of the energetic ions. Light ions penetrate deeper than heavy ions and cause less damage [11]. When the energetic ions collide with the atoms of the Si bulk, they can displace the silicon atoms, create Frenkel pairs of interstitial Si atoms and vacancies, or induce a cascade of atom collisions. The peak damage has been found to be located slightly shallower than the ion peak [11], and to increase with annealing temperature [11]. At $R_p/2$ an excess of vacancies has been observed and at Rp an excess of interstitials and dislocation loops form [12].

Hydrogen incorporation in silicon by the “smart cut” method uses ion energies 20-400 keV and doses of ~ 10^{16}-10^{17} ions/cm^2. The range of H^+ ions is roughly 1 μm pr 100 keV. Post annealing between 400 to 600 °C is necessary to evolve the hydrogen defects and achieve exfoliation [11]. Also combinations of implantation of low doses of ions ~ 10^{15} ions/cm^2, not necessarily hydrogen, followed by plasma hydrogenation and post annealing lead to exfoliation, called “soft cut “ or “ion cut”. By this method a lower dose of hydrogen is needed to cut the silicon. Implantation of heavy elements can be used to cut very thin Si layers [13].

In paper 7, implantation of hydrogen and silicon was performed at room temperature using energies 80 keV for hydrogen and 180 keV for silicon, respectively.

4.2 Hydrogen concentration

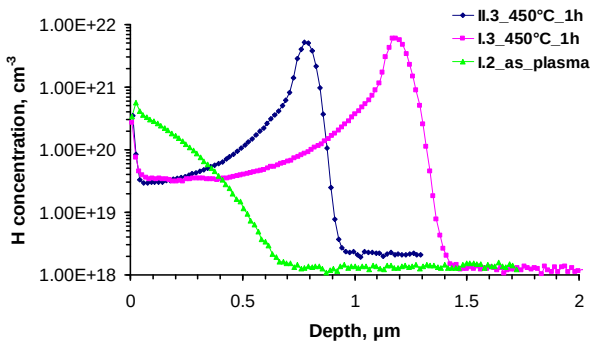

Figure 4.2. Raman spectra from hydrogenated silicon samples, Hydrogen plasma treated (green), hydrogen implanted + 450 °C anneal for 1 hour (blue) and silicon implanted + hydrogen plasma treated sample + 450 °C anneal for 1 hour (pink).

The hydrogen profile in the substrates can be measured by Secondary Ion Mass Spectroscopy (SIMS), Elastic Recoil Detection Analysis (ERDA) or Nuclear Reaction Analysis (NRA). The concentration profile depends on the energy of the atomic hydrogen used, and the substrate properties. During H plasma treatment, most of the hydrogen accumulates close to the surface of the substrate. After ion implantation, however, most of the hydrogen accumulates at its projected range, R_p, [11,9]. The depth profile after direct deuterium plasma treatment was found to depend on both doping type and concentration, as well as substrate temperature [9,14]. Both for n and p type silicon, the diffusion profile was found to depend on doping concentration. While in p-type samples, clear evidence for trapping of hydrogen for doping levels 0.1 Ωcm and 1 Ωcm was observed as plateaus followed by exponential decay, trap-dependent diffusion was not clearly observed in n-type silicon [14]. After 30 min H plasma treatment at 250 °C and 110 MHz, up to 1.6 % hydrogen was detected at the surface of a p type Si substrate [15]. The H concentration decreased rapidly to about 0.2 % 100 nm deep below the surface and then remained almost constant up to 500 nm below surface [15]. After annealing at 400 °C the H concentration was significantly lowered, about 0.3 %, at the surface. Some of the hydrogen diffused out of the sample and some diffused deeper into the sample, such that a higher amount of hydrogen was detected deeper below the surface in the annealed sample [15]. After annealing at 600 °C almost no hydrogen could be detected in the H plasma treated samples [15].

After hydrogen implantation the H-concentration peak is found to be at the projected range, R_p, of the ions, slightly deeper than the implantation damage peak, independent of implantation dose [11]. H concentrations of 10^{21}-10^{22} atoms/cm^3 can be observed close to R_p after implantation, as shown in Figure 4.2. Higher implantation doses give wider hydrogen peaks [11]. Upon annealing the H peak concentration remains stable up to about 410 °C both in n and p type samples, while the Si damage peak increases [11]. The H peak gets narrower after annealing due to out-diffusion of hydrogen in shallower regions of the sample. This occurs already at low temperatures. For high annealing temperatures, hydrogen rapidly starts to diffuse out of the bulk [11].

A combination of ion implantation and H plasma treatment leads to a hydrogen profile similar to that after H implantation. The H from the plasma diffuses to the damage layer created by the ion implantation and gets trapped there. For high implantation doses, trapping at $R_p/2$ in addition to R_p, have been observed. It is believed that the $R_p/2$ region contains an excess of vacancies, while at R_p an excess of interstitials and dislocation loops effectively trap the H atoms [16]

4.3 Hydrogen bonds

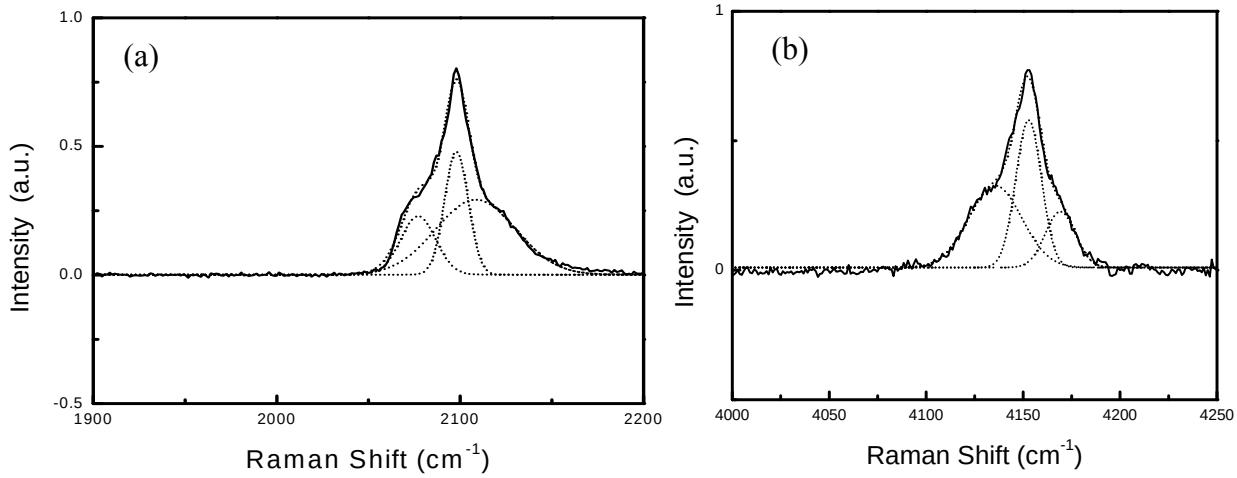

Figure 4.3. Raman spectra showing the Si-H_x stretching frequency bonds (a), and the H_2 stretching frequencies (b), in p-type (100) oriented 12 Ωcm Cz Si sample taken from ref [6].

Hydrogen bonds in silicon have been extensively studied during the last 40 years. The earliest studies [17-19] discovered several hydrogen bending and stretching modes in the frequency region 1900-2200 cm^{-1} together with their appearance and disappearance temperature, but their interpretation was unclear. Although theoretical calculations and other experiments strongly suggested that molecular hydrogen existed in silicon after hydrogenation [2,20], it was not until 1996 that the first observation of a vibrational frequency of H_2 molecules at 4158 cm^{-1} was reported [21]. The H_2 line was assumed to stem from interstitial H_2 at tetrahedral sites. Later observations ascribed this line to the H_2 gas inside platelets, very close to the vibration frequency of free hydrogen gas, 4162 cm^{-1} [22, 23]. Interstitial H_2 at tetrahedral sites was observed with a vibrational frequency of 3601 cm^{-1} by Raman spectroscopy in 1998 [22].

Table 4.1. Vibration frequencies and assignments of the most common Si-H_x bonds and H_2 bonds observed after hydrogen plasma treatment and implantation.

Frequency (cm^{-1})	**Assignment**	**Dissociation energy**	**Reference**
856	Si-H_3, stable up to 550 °C, bending-wagging		[29]
1958	IH_2, interstitial		[25(ref 24)], [24 (ref 7)]
2065 and 2075 (Raman)	Early stage of platelet formation, before H_2 molecules form inside. Stems from $[2Si-H]_n$ structures with small and medium distances between two inner surfaces respectively. Stable up to ~ 350 °C.		[26]
2075(6)/2095 (IR/Raman)	Si-H bonds at ~200 nm plasma surface damage layer, stable up to ~ 350 °C.	2.2 eV[27]	[27], [29]
2105, 2110 (Raman)	Si-H_2 bonds at the platelets inner surfaces, the most stable, the final stage, dissociation.	2.4 eV[27]	[27], [26]
2120 (Raman)	Si-H_2 species located on the inner surfaces of the H_2 containing platelets formed at an intermediate stage.		[26]
2125 (Raman)	SiH_2, fingerprint initiation of blistering.		[25]
2128	Constrained Si-H_3, high temperature peak, stable up to ~ 525 °C.		[29]
2130, 2140 (Raman)	Vertical SiH_2 on steps or SiH_3, located on the inner surfaces of the platelets formed at an early stage, which contain H_2 molecules.		[26]
2027/2068, 2125/2121/2144, 2158 and 2185, 2191, 2208/2222/2238/2242	VH_1, VH_2, Hydrogen saturated divacancy V_2H_6, VH_3 and VH_4 respectively.		[25 (ref 22)] [24 (ref 6)] [34]
3600	H_2 at tetrahedral site		[28]
3810-3870	H_2 in multivacancies		[24]
4120-4170	H_2 in blisters		[24]
4158	H_2 in platelets		[21]
4150, 4160	Ortho H_2, para H_2 respectively		[27]

More recent Raman results of hydrogen bonds detected in silicon after H plasma treatment and implantation are shown in Table 1 [24-29]. Chemical bonds formed during hydrogenation of silicon depend on the hydrogenation method and substrate conditions. During H implantation, a high level of silicon self-interstitials and vacancies are formed and result in the formation of I-H_x and V_x-H_y bonds together with H_2 trapped in multivacancies [24]. In plasma treated samples the energy of the ions is too small to form a high concentration of Frenkel pairs (vacancies and interstitials), such that I-Si and V-Si bonds are not observed [26]. Also doping type and level have impact on the bonds being formed. The intensity of H_2 bonds were almost 4 times higher and also more stabile in p type Si compared to n type Si [30]. Substrates with (111) orientation contain less Si-H bonds than (100) oriented substrates, but they have the same amount of H_2 bonds [10]. Samples plasma treated with a frequency of 13.56 MHz show the same amount of Si-H bonds, but less H_2 bonds [10]. Raman investigations on bevelled samples indicate the depth distribution of the different bonds [26,31]. The temperature evolution of the different Si-H bonds has been assigned to hydrogen induced platelets at different stages [26,32]. Si-H bonds with a vibration frequency of about 2095 cm^{-1} are assigned to the direct plasma damage layer at the top 200 nm of the substrate. Such bonds are stable up to ~ 350 °C. Si-H_x bonds assigned to platelets in the subsurface of the wafer at 2105, 2110, 2120, 2125 and 2130 cm^{-1} are stable up to higher temperatures ~ 500 °C. The H_2 bonds in platelets have been found to be stable, up to ~ 550 °C, in p-type Si [30]. Some of the peaks belonging to the same chemical compound appear at different vibration frequencies, depending on the detection method used. A comparative Raman and IR temperature evolution study detected four different bonds [33]. Peaks centred at 2065 cm^{-1} and 2125 cm^{-1} were detected by both methods, while a peak at 2075 cm^{-1} was only observed for IR, but was found to be correlated with a peak at 2095 cm^{-1} only observed for Raman. The peak at 2065 cm^{-1} decreased rapidly upon annealing, and the peak centred at 2125 cm^{-1} was found to be the most stabile. In Figure 4.3, Raman spectra from stretching Si-H_x bonds (a), and H_2 bonds (b), consisting of several subpeaks are shown.

4.4 Surface defects

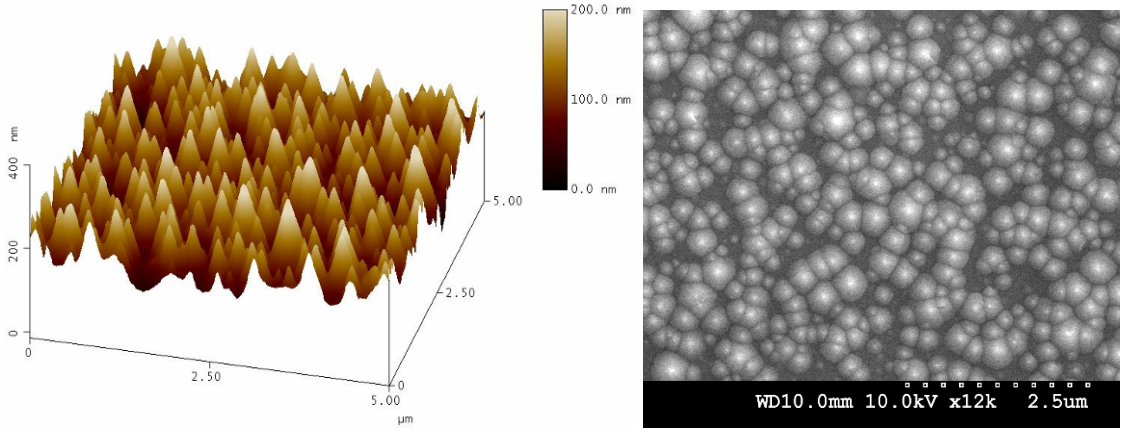

Figure 4.4. (a) AFM and (b)SEM images, showing the surface cones at the surface in n-type 1.8-2.6 Ωcm Cz Si sample

Atomic hydrogen can passivate dangling bonds on the silicon surface and thereby reduce the surface recombination velocity of the material [1]. However, atomic hydrogen can also etch silicon surfaces by breaking the Si-Si bonds and forming Si-H_x species [35]. The Si-H_x species then redeposit onto the surface forming micrograins and cones/pyramids [35]. The etching depends on the hydrogenation method. Direct plasma hydrogenation of the substrate, where the substrate is directly immersed into the plasma, causes about 10 times rougher surface than remote plasma [36]. A direct H plasma etched silicon surface was found to be textured with a root mean square (RMS) roughness, R_q= 8.90 nm, which gives the root mean square average of height deviations taken from the mean data plane within a given area. A similar remote plasma treated sample remained flat with R_q= 0.39 nm [36]. In Figure 4.4, the surface cones of a substrate after H plasma treatment has been measured with (a) AFM and (b) SEM.

The etching is found to depend on both substrate temperature and orientation, doping type and level, together with H plasma conditions like plasma frequency and duration [10,35,37-41]. The roughness of (100) Si surfaces irradiated with hydrogen electron cyclotron resonance plasma was investigated after H plasma treatment at different substrate temperatures, using SEM and reflection high energy electron diffraction (RHEED) [37]. For substrate temperatures below 100 °C the surface remained smooth, while for higher temperatures cones with angles of 16°, 25° and 35° forming directions [511], [311] and [211] with the surface respectively, were observed on the surface [37]. After hydrogen plasma treatments at 180 °C and 250 °C, cones with {311} lateral surfaces and cones with lateral surfaces of {211} were observed respectively. For treatments at 120 °C, no surface roughening was observed [42]. The roughness was found to increase with increasing temperature from about 200 °C to 350 °C, where it reached its maximum. For higher temperatures the cone density was found to decrease [37]. Detailed investigation of the cone surfaces showed that their surfaces consisted of a combination of {100} and {111} microsurfaces [37]. The same authors also found a relationship between the etching rate of silicon and the temperature. At temperatures below 100 °C the etching rate was found to be the highest, 137 nm/min. The etching rate was found to decrease rapidly with temperature, reaching 10 nm/min at about 450 °C [37]. SiO_2 was found to be much less etched [37].

The roughness also depends on the H plasma treatment duration as found in ref [38], where a p-type (100) Si substrate was H plasma treated at 270 °C for 10 min, 0.5 h, 1 h, 3 h and 12 h. These observations led to the establishment of the selective etching-redeposition (SER) model [38]. For short hydrogen plasma etching times, 0-30 min, hydrogen atoms break Si-Si bonds and form SiH_x, mainly SiH_2 species, leaving intrinsic stacking faults and dislocation loops on the surface. The SiH_x species agglomerate and redeposit on the surface forming micrograins. For H plasma etching duration between 0.5 and 3 hours, the surface is completely covered by μc-Si grains and large conical structure. For long H plasma treatment periods, 3-12 h etching, pyramidal texturing is formed due to selective etching on the conical structure by the plasma [38]. The roughness of the surface also depends on the orientation and doping level of the substrate, as found after hydrogen plasma treatment at 110 MHz and 13.56 MHz at 250 °C for 1 h [10]. For (111) oriented silicon the surface was found to have pyramid-like

texturing, while the (100) oriented samples had μc-Si surface structure [10]. In mc Si, grains with different grain orientation have different surface morphology. Grains with surface normal close to [211] were found to have almost flat surface, while grains oriented differently from (001) and (211) were found to have tilted surface cones after 1 hour annealing at 250 °C [43]. At this temperature the surface cones have {211} as their lateral surfaces [37].

Surface roughness has been found to be strongly related to the nucleation and growth of the {111} platelet defects at the Si subsurface region and preferentially etching at positions where the {111} platelets intersect the silicon surface [44,45]. A model for surface roughening proposed in [44] shows that both the critical size of nuclei and the activation energy for etching reactions are significantly lowered at {111} platelet positions, compared to random positions. Hydrogen induced defect formation and surface roughening are only observed in samples where the hydrogen concentration in the subsurface is higher than the solubility level of hydrogen in silicon at the given temperature [10]. Surface roughness was found to decrease for higher temperatures in the range 150-300 °C, because the concentration of hydrogen in the subsurface decreases with temperature. In silicon samples electron cyclotron resonance hydrogen plasma cleaned at 440 °C, the hydrogen never reaches its solubility level in silicon and the silicon surface remains atomically flat [44]. In a poly-crystalline sample, the etching rate was found to be more than 20 times faster for the amorphous phase than the crystalline material [40].

4.5 Bulk defects

Hydrogen complexes

Hydrogen forms various complexes in silicon and interacts with interstitials, vacancies and impurities present in the lattice [1]. Figure 3.1(a) shows the Si unit cell with substitutional and interstitial positions. Several lattice sites are important in describing hydrogen impurities in the silicon lattice; the bond-centred (BC) site, which is the mid-point of the bond; the tetrahedral interstitial site, T_d, which lies at ¼ a (-1-1-1); the anti-bonding (AB) site, lying between the lattice site at (000) and the T_d site and the C site, which is found at ½ a (100). H^+ and H^0 are found to lie at BC sites, while H^- lies at T_d sites. Hydrogen can form two types of dimers in silicon; molecular H_2 at tetrahedral interstitial sites and H^*_2 where one atom occupy a bond–centered and the other an anti bonding site [1]. The migration energy from a BC site to a T_d or another BC site is only 0.3-0.5eV, such that the hydrogen atom easily diffuses to a defect or other H-atoms [37]. The energy of H^0 in a BC site is 1.21 eV higher than for the H_2 molecule with dissolution energy of 1.8 eV.

Acceptors bond to hydrogen in BC sites and donors to hydrogen in T_d sites, forming B-H and P-H complexes respectively for B and P, with a dissociation energy of 1-2 eV [3]. Annealing at 250 °C dissociates H-B complexes. From theoretical calculations the dissociation energy of H_2 to two H_{BC} was found to be 1.6 eV, and the energy of two passivated B-H complexes to be 0.5 eV below the H_2 molecule, which is very stable

[37]. H can form complex with a vacancy, producing defects VH_n, n = 1,..4. H forms H-C defects in silicon with an electron trap at E_c - 0.15 eV, which are stable up to 80 °C in dark and dissociate with energy of 1.1 eV. H also forms complexes with oxygen and can enhance oxygen related thermal donor formation and oxide precipitation [46]. H reacts with, and can passivate several metallic impurities [1].

Hydrogen induced platelets

After heavy hydrogen plasma treatment of silicon substrates, a high density of hydrogen induced defects in the subsurface is formed, including hydrogen induced platelets (HIPs), dislocation loops, stacking faults and hydrogen bubbles [9,10]. In Figure 4.5, hydrogen induced defects after hydrogenation are shown in highly doped n type and 10-20 Ωcm p-type Si, in (a) and (b) respectively. The formation of platelets during hydrogen plasma treatment in silicon has been studied since the late 80s [3,9]. The earliest observations showed that planar defects in {100} and {111} planes or microcracks resulted after 30 min remote deuterium plasma at 150 °C of either n type or p type silicon [9]. The concentration of platelet defects in p-type silicon was found to be 100 times less than in n-type with similar doping concentration, and platelet formation was found to correlate with high concentrations of hydrogen, as observed with SIMS. The Si-H bonds, observed with Raman spectroscopy, were thought to stabilize the platelets [9]. The generation of platelets during hydrogenation, was found to induce electronic deep levels in the band gap unrelated to either the plasma damage or the radiation damage [9]. Hydrogen containing bubbles were observed after direct deuterium plasma treatment when the substrate temperature was greater than 200 °C [3]. Deuterium was found to almost fully passivate boron for certain plasma treatments [3].

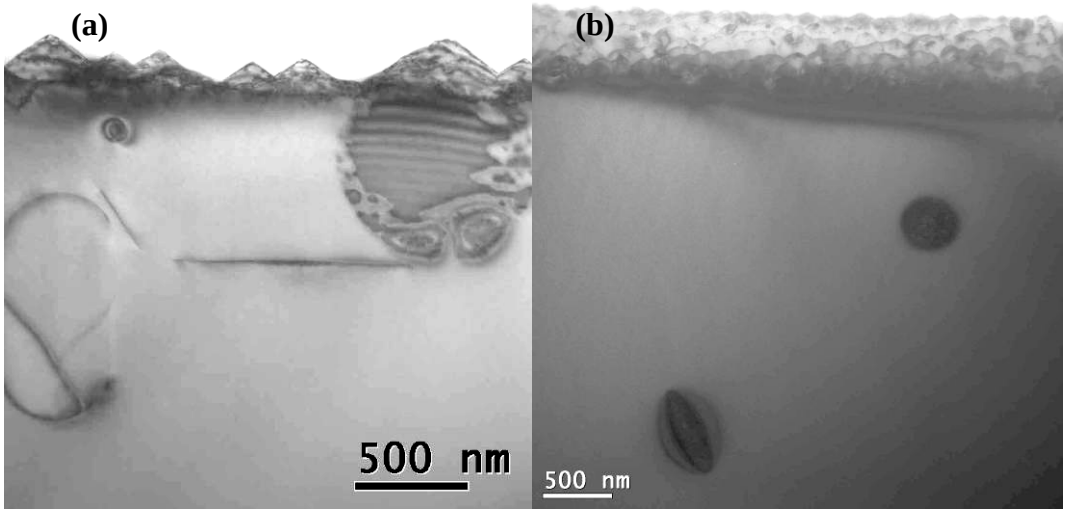

Figure 4.5. Microstructure in a silicon substrate after hydrogenation, (a) large platelets formed close to the surface, (b) large platelets formed deep into the bulk

Platelets form because of the very low solubility of hydrogen in silicon as mentioned in the first part of this chapter. The platelets observed in the subsurface are approximately ten times as large after direct H plasma treatment, compared with remote H plasma

treatments [35]. For direct hydrogen plasma treatment, platelet defects have been observed both in n and p doped samples at similar concentrations [10,30,35], while for remote plasma treated samples, the density of hydrogen induced platelets in p type silicon was found to be significantly lower or absent [9,47,48]. The absence of platelet defects in p-type silicon has been explained by the Fermi energy. Nickel et al. found that platelets were only observed in n type silicon with Fermi energy of $E_c - E_F \leq 0.3$ eV [47,48]. The platelet concentration was found to increase monotonically as E_F moved closer to the conduction band. Maximum concentration was found for $E_c - E_F \sim 0.06$ eV. The hydrogen concentration needed to nucleate platelets was found to be $\sim 10^{17}$ cm^{-3} [48]. Since hydrogen induced platelets was observed in H plasma treated B-doped silicon already in 1988 [41] and also in many resent studies [10,24,26,27,30,31,33,35,42-45,49,50,52,53,60], the Fermi energy theory is probably not correct. A possible explanation for Nickel's [47,48] observations, due to the high doping level of $\sim 10^{17}$ cm^{-3} of boron used, is passivation of dopants. No platelets were observed in a 10^{15} cm^{-3} B-doped sample after hydrogenation for 3 h at 150 °C. Instead, almost 100 % of the boron was found to be passivated by hydrogen at this temperature [3]. Since the boron concentration in the case of [9,47,48] was $\sim 10^{17}$ cm^{-3}, probably all hydrogen was used to passivate boron at the low temperature step. The boron-hydrogen complex is stable up to 200-300 °C [1,3,5], such that it is possible that also at the high temperature step, 250-275 °C, the hydrogen was trapped by boron, or that the defects formed were to small to be observed.

In [51] platelets were found to form when the total dose of deuterium atoms was more than 10^{16} ions/cm^2, and only 10 % of the implanted deuterium was found to be involved in platelets. The rest was assumed to form small defects invisible in the TEM [51]. Since all hydrogenation methods reported, direct and remote plasma, ion implanting and reactive ion etching, lead to the same hydrogen induced platelets forming, displacement damage was suggested not to play an essential role in the nucleation of hydrogen induced platelets. Instead high supersaturations of H were suggested to force the nucleation of hydrogen induced platelets, since they form in regions of high H concentration [51]. Platelet formation from supersaturated hydrogen/deuterium rather than the evolution of H_2^* defects, could also explain LVMs appearance and disappearance [51]. Platelets were found to suddenly form at a critical temperature (~ 200 °C) and grow to final size within seconds under very low electron density illumination [51].

Temperature evolution

The temperature evolution of platelets after H-plasma treatment was studied in paper 4 and 5. In Figure 4.6 the platelet evolution from H containing bubbles to voids is shown. The influence of substrate temperature on subsurface H defect formation and surface roughening after electron cyclotron resonance hydrogen plasma cleaning of silicon have has been studied earlier [44,45,52,53]. Hydrogen defect formation in the subsurface was found to be closely related to surface roughening [44,45]. Hydrogen induced platelets were found to form at temperatures between ~ 150-400 °C. At low temperatures, below 150 °C, the diffusion rate of H in Si is low and the nucleation energy barrier is hard to

overcome. At high temperatures, above 440 °C, hydrogen never reaches its solubility level in hydrogen and no defects are observed in the subsurface [45]. At substrate temperature 240 °C a high density of small platelets was observed in the subsurface, and at 335 °C coarsening of platelets was observed. At temperatures above 335 °C, only a low density of {100} platelets was observed in the subsurface, and less roughening of the surface occurred [45]. At 385 °C, the {100} platelets were found to contain oxygen and formed due to hydrogen enhanced amorphous oxygen platelet formation [52]. Oxygen is well known to form platelets in {100} planes at temperatures ~ 600 – 950 °C, while hydrogen enhanced thermal donor formation can occur in silicon at as low temperatures as 350 °C [54,55].

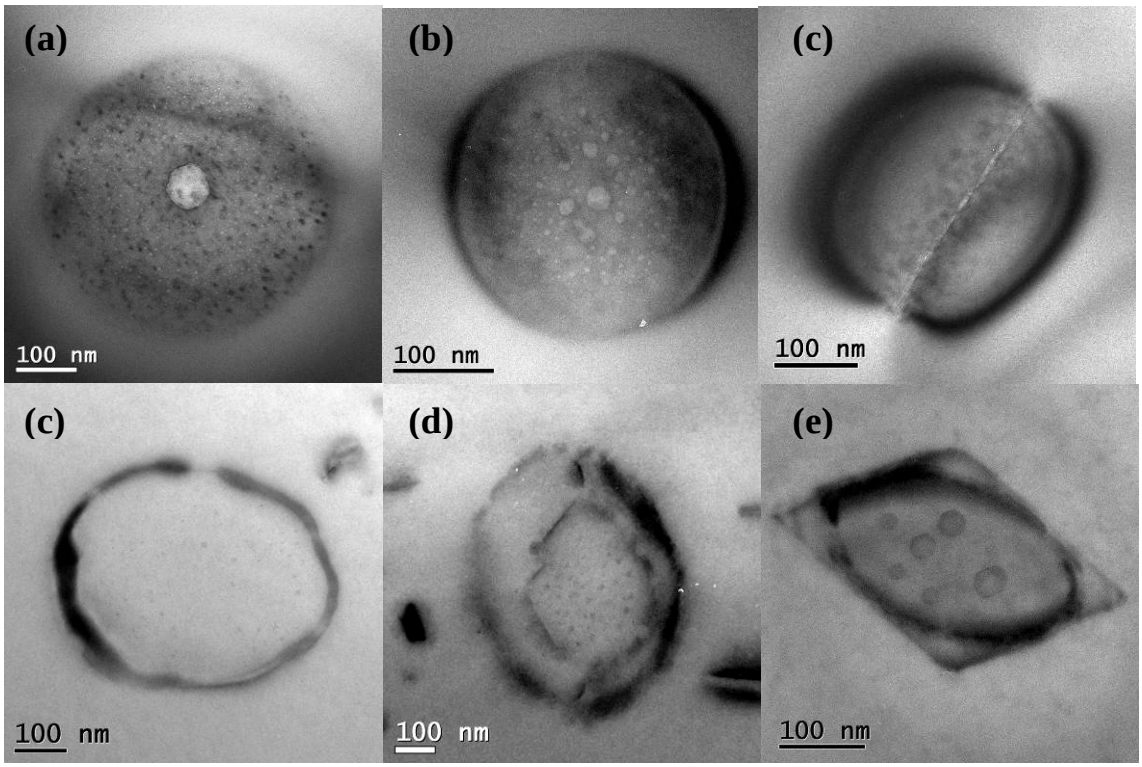

Figure 4.6. Evolution of hydrogen platelets, (a) Platelet with granular contrast and central cavity surrounded by small H containing bubbles in p type Si after annealing at 300 °C for 1 h, (b) Several large bubbles in the centre surrounded by smaller bubbles, observed in n-type Si after annealing at 400 °C for 1 h (c) Platelet defect seen edge on, same sample as in (b). Several elongated bubbles are evident, (d) Small voids formed inside a platelet in p-type Si after annealing at 700 °C for 1 hour, (e) Voids formed inside a platelet in p-type Si after annealing at 800 °C for 1 hour, (f) Empty voids and dislocation loops are evident after high temperature annealing ~ 1000 °C. Notice the paralellogram feature formed on the platelet.

Temperature evolution of H-induced platelets after H implantation at room temperature was performed at 450 °C for 1-15 minutes [56]. The platelet volume occupancy remained stable, but with increasing annealing times the platelet size was found to increase and the density decreased. This was explained by Ostwald ripening. The large platelets are most energetic favourable and hence grow on the expense of the small ones

[56]. The same authors also studied the temperature evolution of H-platelets formation after H implantation in room temperature up to 900 °C [57]. Up to 500 °C platelets were found to grow in size and reduce in density through conservative exchange of H atoms. Between 500-700 °C H was found to diffuse out of the platelets and above 700 °C empty voids were observed. The voids were found to undergo the same ripening process as the platelets, but the total volume occupied of platelets + spherical cavities remained constant ± 20 % [57]. This fits well with another study performed some years earlier [58], in which defects formed in (111) Si after implantation in the range between 1 and 2 MeV followed by annealing for 30 min at temperatures between 100 and 1100 °C were studied. Two kinds of defects were observed, named loop like, L defect and fault like, F defect, both observed in {111} planes. The L defects were found to have granular contrast resulting from a complex association of interstitials and vacancies with hydrogen bubbles at low temperatures. At higher temperatures, above 500 °C, the granular contrast was seen to vanish and several Frank dislocation loops appeared. The H-bubbles were found to transform into a macro void. Both density and size were found to be constant with annealing temperature. The F defects were found to consist of double layer of Si-H bonds. The density was found to be constant, but the size increased with temperature. From 450-700 °C they were seen to develop into microcracks [58]. Later TEM studies [51,59] argue that the F defects observed in [58] are truncated platelets of the same kind as L defects because they do not contain H_2 bubbles, the hydrogen has diffused out of the structure, and their displacement vector a/4 <111> was very close to the dilation of the lattice displacement found to be $0.812d_{111}$ in the present case [51].

Platelet structure

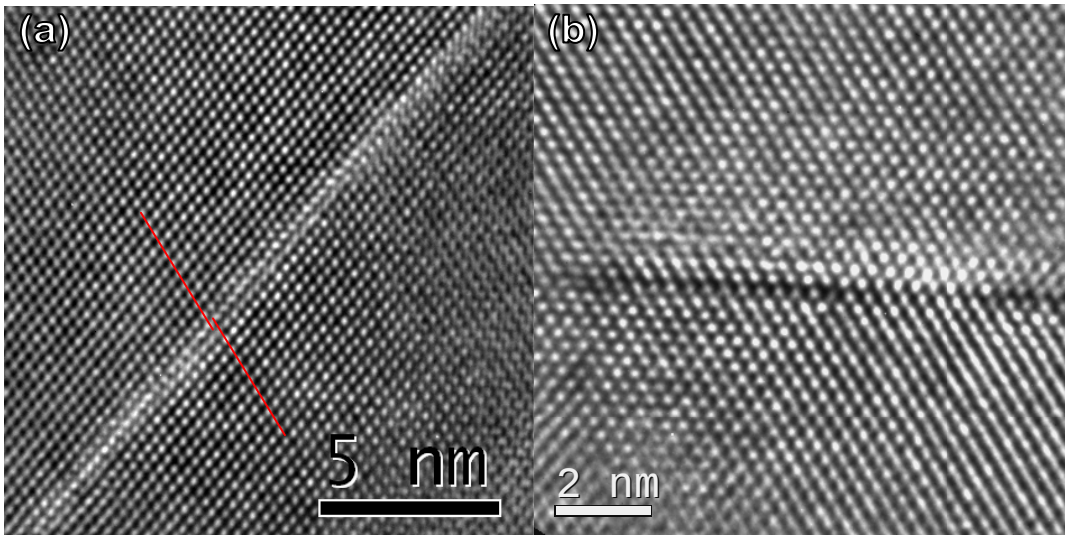

Figure 4.7. (a) {111} platelet, notice the lattice shift between left side and right side of the platelet (red lines), (b) {100} platelet

High resolution images of {111} and {100} platelets are shown in Figure 4.7 (a) and (b), respectively. Several groups have tried to solve the structure of the platelets by use of HRTEM [51,59,60,61] or by theoretical modelling techniques [62-65]. By use of

local-density-functional theory, stable configurations for H in Si were determined [64]. H_2 formation was found to be the most energetically favourable state for neutral H in Si, but also Si-H formation was found to be energetically favourable although unstable. Vacancy-formation mechanisms were probable to be involved in the defect formation [64]. Double layer H_2^* structures or half stacking faults were successfully used to determine the lowest energy for {111} platelet formation [65].

In some studies, hydrogen induced platelets were found to be bounded by Frank partial dislocation loops [58]. Frank partial dislocation loops can form due to the collapse of a vacancy disk or by accumulation of interstitials [66]. In other studies, mostly after implantation at room temperature or remote plasma treatment where only small platelets form, dislocation loops were not observed. HRTEM of {111} platelets [51,59] led to two models where {111} planes were broken and dangling bonds saturated with hydrogen [51,59]. The dilation of the lattice was found to be 0.30 nm [51]. The pressure of the H_2 gas inside hydrogen induced platelets was found to be as high as 1 GPa. Platelets were found to form when the total dose of deuterium atoms was more than 10^{16} ions/cm^2 [51]. Recent extensive high resolution TEM imaging of {111} and {100} platelet defects [60,61], showed that {111} platelets can contain jogs and migrate to adjacent {111} planes. They were found to differ from simple stacking faults because of decoration by hydrogen atoms that lead to extra strain. The most probable model was fond to involve H_2^* defects [61]. The {100} defects were found to be planar defects boarded by dislocation loops with **b** = a/2<110> Burgers vector [60]. They were formed by accumulation of self-interstitials and vacancies, resulting from the H-plasma treatment, leading to the formation of prismatic dislocation loops and nanocavities [60].

Vacancies have been found to capture hydrogen effectively [64,16]. For H plasma treatment where no excess vacancies are available, platelet formation is suggested to occur as a result of H* accumulation that transforms into $[2Si\text{-}H]_n$ structures in the {111} planes [25]. Platelet formation after implantation parallel to the surface, can be formed due to trapping of hydrogen by multi-vacancies aligned in {111} or {100} directions [25].

Blistering and exfoliation

Blistering on the silicon surface after a large dose of H implantation was first observed in 1976 [67]. When silicon is implanted with a sufficiently high hydrogen dose at low to moderate temperature and subsequently annealed at high temperature, platelets parallel to the surface nucleate and grow by a ripening process where large platelets grow on expense on small platelets. The platelets are filled with H_2-gas at a high pressure that eventually causes the platelet to collapse and turn into microcracks. High density of small cracks coalescence and turn into large microcracks that eventually lead to exfoliation of a thin silicon layer, or the formation of dome shaped gas filled blisters and/or craters of exploded blisters on the Si surface [11,68]. In some cases also H plasma treatment can give rise to blister formation. A hydrogen dose of at least 3 x 10^{16} cm^{-3} is needed to achieve exfoliation [25].

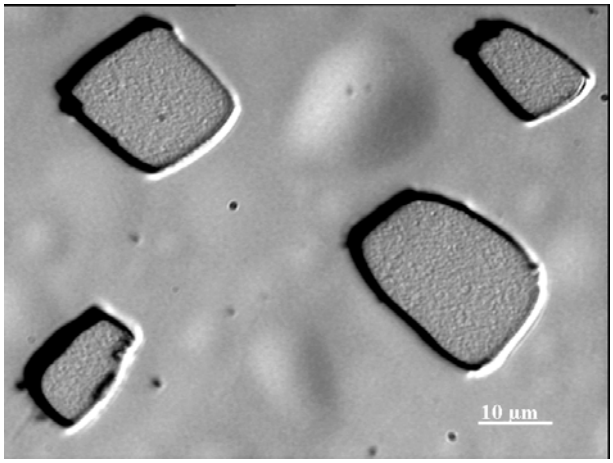

Figure 4.8. Blisters and craters are visible on the silicon surface after low dose H implantation + H plasma treatment

An alternative approach to achieve blistering and exfoliation is to combine implantation and H plasma treatment [13,35]. In this way, a much lower dose of hydrogen is needed to achieve crack formation and exfoliation [13]. The most effective substrate temperature during H plasma treatment to achieve blistering, was found to be 350 °C [35]. Also the combination of He and H implantation can reduce the total dose needed for exfoliation [69,70]. To achieve an even thinner Si layer, implantation of heavier ions can be used to create a defect layer followed by H plasma treatment. In [13], the delimitation took place at $R_p/2$, half of the projected range, where the concentration of vacancies was highest for low dose implantation. For high dose implantation the delimitation took place at the projected range, R_p of the ions. The H atoms from the plasma diffuse to the defect layer from the implantation and nucleate defects in the same way as in the case of H implantation [13]. The advantage of using heavier atoms for implantation is that the damage region gets narrower and that a lower dose is needed, since heavier atoms create more damage [13]. Implantation of boron [71], silicon and argon [72] subsequent to hydrogen plasma treatment all resulted in blistering and exfoliation.

4.6 Applications

Hydrogenation of silicon has found many applications in the silicon industry, both within the semiconductor industry and solar cells. The applications dealt with in this thesis are briefly described below.

Ion-cut

The blistering phenomena observed after implantation has been commercially utilized to cut wafers, called ion-cut or smart-cut. The smart-cut technique was developed by Michael Bruel and his group in 1995 [73] as a new technology for the production of SOI wafers. This technique replaces conventional SOI production methods like SIMOX

(separation by oxide implantation) [74] and BESOI (based on wafer bonding and etch back) [75]. Today, 95 % of the silicon on insulator (SOI) wafers is produced by the smart-cut method, and the company Soitec is the world's leading producer of such wafers [76]. The advantages of the smart-cut method are that less material is needed because the donor wafer can be recycled, and a lower dose of implantation is needed compared to the SIMOX process [73].

In the smart-cut method, atomic hydrogen is implanted into the silicon to a well-defined depth. The surface of the implanted wafer is cleaned and then bonded to another cleaned substrate that has been capped with a silicon dioxide layer by a heat treatment at 200 °C to establish strong bonds between the wafers. The wafers then undergo a second heat treatment at 400-600 °C to induce microcracks and exfoliation of a thin silicon layer. Eventually, the exfoliated surface is polished to remove the damage layer caused by the ion implantation [41,73,77,78]. An alternative to solely H implantation is to combine H implantation and H plasma treatment, as discussed in chapter 4.5.

In principle, exfoliation of a thin silicon layer could also be used to produce very thin silicon solar cells. However, without the stiffener wafer, non-uniform blistering is observed on the silicon surface [67,68]. Even if it worked, handling solar cells with a thickness of just a few μm would be a challenge. Another problem is the damage produced by the ion implantation that probably is recombination active. High temperature annealing (above 1200 °C [48]) is necessary to remove implantation damage.

In paper 7 we have studied H-implanted and Si implanted + H plasma treated Si substrates to compare hydrogen defect formation in the two cases for application within the SOI industry. Similar microstructure was observed for H implanted sample with a dose of 3 x 10^{16} cm^{-3} and Si implantation dose of 10^{15} cm^{-3} followed by 1 hour H plasma treatment at 250 °C [75].

Passivation

Hydrogen's ability to passivate defects in mc silicon was first discovered in 1979 [79]. After DC plasma treatment a significantly decrease in grain boundary barrier height and density of states were observed [79]. Later, atomic H has been found to passivate shallow donors and acceptors at low temperatures (below 300 °C) leading to an increase in the resistivity [80,81]. Most of the boron was found to be neutralized and a sixfold increase in resistivity resulted after H plasma treatment. Hydrogen can interact with many transition metals, like Co, Ag, Au, Cu, Ni, Pd, Pt, and Cr, and cause a shift of the deep levels associated with them to shallower levels [5,82]. However, some levels associated with Ti and V, were not passivated [5]. Hydrogen can in addition enhance O diffusion and thermal donor formation [5,82]. H also reacts with vacancies and extended defects like dislocations and grain boundaries and passivates dangling bonds [5,82]. Introduced into silicon in high doses, H can also create electrically active defects, as discussed in most of this chapter. Extended defects in the bulk can lower the formation barrier for hydrogen defects formation in silicon. Hydrogen has been found to form

defects at extended defects like dislocations and stacking faults deep into the bulk [82,83]. This was also observed in paper 6. The density of hydrogen induced defects was found to be higher in as cut silicon than in chemically etched silicon due to the high density of sawing defects [43].

During the last years, the trend has been to use dirtier feedstock material in solar cell production. This makes it particularly important to passivate impurities effectively. Especially for mc Si that has a high content of impurities and structural defects. The most common method to passivate mc solar cells, is by post deposition annealing of a H-rich SiN_x-layer that is deposited for use as antireflective coating [5,84]. During the high temperature firing step of front and back side contact metallization, H is released from the SiN_x-layer and diffuses into the bulk, passivating both the surface and the bulk of the wafer.

Gettering of impurities

One of the limiting parameters for the efficiency of the solar cells is the high concentration of impurities. In particular transition metals introduce deep levels in the band gap. Earlier studies have shown that these can exist in high concentrations in Si materials, in the range of 10^{10}-10^{14} cm^{-3} for transition metals in mc silicon [85,86], and 10^{17}-10^{18} cm^{-3} for C and O [87]. After H or He implantation in Si, voids/cavities/bubbles are frequently observed. These cavities can be used to getter impurities, in particular transition metals, after high temperature annealing (T > 700 °C) [88-93]. Nearly 100 % of the implanted impurities were found to be located in the cavities after implantation doses up to ~ 10^{14}-10^{15} cm^{-3}. Decoration of metals has been observed both at $R_p/2$ and R_p [94]. Oxygen can also be gettered by H induced cavities after high temperature annealing [95], as shown in paper 6. After annealing for 1 hour in air, the former H induced platelets transformed into oxygen platelets [96]. In paper 7 it is demonstrated that Cu can be gettered by remnants of the H induced platelet after annealing at 1000 °C [43]. A layer of implantation induced cavities can in this way be used to remove unwanted impurities from the Si bulk. The damaged layer can subsequently be removed from the wafer by etching.

Texturing

Texturing is commonly used in the solar cell industry to reduce optical losses. Pyramidal texturing can reduce reflection of the solar cell surface from 33 % to 11 % [97]. Monocrystalline silicon can be effectively textured by use of an anisotrop alkaline etchant, usually KOH or NaOH, that forms randomly distributed pyramids on (100) oriented wafers. These etchants are anisotropic with respect to grain orientation and are not efficient for texturing of mc Si. Various methods such as acidic etching, mechanical grooving, reactive ion etching and laser texturing have received recent attention for mc Si texturing [98-104]. Most of these methods cannot be regarded as low cost candidates for industrial applications, and the development of a low cost texturing method still is required.

Direct hydrogen plasma is regarded as a "clean", chemical-free technology to texture silicon as described in chapter 4.4. The limitation is that the texturing depends on the grain orientation [10,35,43] and that recombination active defect formation in the subsurface is crucial for archiving surface texturing [44,45]. Reflectivity measurements exhibited less than 10 % surface reflectance after H plasma treatment. Texturing by H plasma treatment has been studied in Paper 4-6.

Another potential method to texture mc silicon is hydrogen radical treatment using a hot tungsten filament [105-107]. In this method WSi_2 particles are deposited on the surface and work as a mask for subsequent hydrogen radical etching. The deposited particles can be removed by a short acid dip. Texturing by this method was studied in paper 9.

Silicon nano-whiskers growth

Silicon nano-structures, such as nanorods/nanowires and nanotubes, have attracted recent attention because of their unique properties and wide applications within photonics and nanoelectronics [108]. Silicon nanowires (SiNW) are particular important because silicon-based nanoelectronics is compatible with silicon-based microelectronics. SiNWs also have applications within nanosensors, nanospintronics, nanomedicine and nanobiology [109-113]. Because of the SiNWs narrow size, their electrical and optical properties differ from the silicon bulk properties. For very narrow SiNWs, below 10 nm, quantum effects will take place. In contrast to bulk silicon, narrow SiNW show promising properties within light emitting devices [108]. The energy gap has been found to increase from 1.1 eV to 3.5 eV when the SiNW width decreased from 7 nm to 1.3 nm [114]. As the SiNW gets narrower the emitted light shifts from red to blue [64]. A potential application of Si whiskers/nanowires with p-n junctions may be to provide a solution for fabrication of higher efficiency solar cells, compared to those based on conventional planar p-n junction solar-cell geometry [115-117].

Growth of whiskers/nanowires has been reported by methods such as chemical vapour deposition (CVD), molecular beam epitaxy (MBE), and pulsed laser vaporization (PLV) [118-122]. In the case of CVD, growth can occur either via vapour-liquid-solid (VLS) growth mechanism [123,125] or vapour-solid-solid (VSS) growth [125-128]. In the latter mechanism, small metal particles are deposited onto the Si surface well below their eutectic temperature. Si from the gas source dissolves in the silicide diffuse through it and crystallizes on the silicon surface growing as a whisker. This is similar to a metal induced layer exchange process [129,130] followed by a solid-phase crystallization (SPC) [131,132], where amorphous silicon is deposited on top of a metal film on a substrate, dissolves in the metal film, diffuses through it during annealing below the eutectic temperature, forming crystalline silicon nucleus on the substrate that grow, resulting in a thin polycrystalline Si film confined at the interface between the metal film and the substrate. In paper 8 and 9 growth of SiNW without any pre-deposition of liquid metal droplets and with only pure hydrogen gas as source gas is demonstrated using a tungsten hot filament reactor. The observed whiskers consist of

pure silicon with crystalline tungsten silicide particles at their tips and incorporated in their structure. They grow in random directions with a zigzag morphology. Their width is between 10 and 50 nm. As tungsten tolerance in silicon solar cells is very low (below 1.2 $x10^{12}$ cm^{-3}), probably these substrates are not very suitable for solar cells at this stage.

References

[1] J. Pearton, W. Corbett and M. Stavola, *Hydrogen in crystalline semiconductors*, Springer-Verlag, (1992) and references therein
[2] N. M. Johnson, C. Doland, F. Ponce, J. Walker and G. Anderson, Physica B **170**, 3 (1991)
[3] S. J. Jeng, G. S. Oehrlein and G. J. Scilla, Appl. Phys. Lett. **53**, 1735 (1988)
[4] A. Van Weringen and **N.** Warmoltz, Physica**. 22**, 849 (1956).
[5] Christopher E. Dub& and Jack I. Hanoka, IEEE, p. 883 (2005) and references therein
[6] M J Binns, S A McQuaid, R C Newman and E C Lightowlers, Semicond. Sci. Technol. **8**, 1908 (1993)
[7] S. A. Mcquaid, R. C. Newman, J. H. Tucker, E. C. Lightowlers, R. A. A. Kubiak, M. Goulding, Appl. Phys. Lett. **58**, 2933
[8] R. Jones, Phil. Trans. R. Soc. Lond. A, **350**, 189 (1995)
[9] N. M. Johnson, F. A. Ponce, R. A. Street and R. J. Nemanich, Phys. Rev. B. **35**, 4166 (1987)
[10] A. G. Ulyashin, R. Job, W. R. Fahrner, O. Richard, H. Bender, C. Clayes, E. Simoen and D. Grambole, J. Phys.: Condens. Matter. **14**, 13037 (2002)
[11] T Höchbauer, PhD thesis, *On the Mechanisms of Hydrogen Implantation Induced Silicon Surface Layer Cleavage,* Philipps-Universität Marburg, (2001)
[12] J. Zhao, A. Wang and M. A. Green, *Proceedings of 21st IEEE Photovoltaic specialists conference*, p.333 (1991)
[13] A. Y. Usenko and A. G. Ulyashin, Jpn. J. Appl. Phys. **41**, 521 (2002)
[14] J. W. Corbett, J. L. Lindstrøm, S. J. Pearton and A. J. Travendale, Solar cells, **24**, 127 (1988)
[15] A. Ulyashin, R. Job, W. R. Fahrner, D. Grambole and F. Herrmann, Solid State Phenomena **82-84**, 315 (2002)
[16] A. Peeva, R. Koegler, W. Skorupa, Nuclear Instruments and Methods in Physics Research B **206**, 71 (2003)
[17] H. J. Stein, J. Electron. Mater. **4**, 159 (1975)
[18] N. N. Gerasimenko, M. Rolle, L.J. Cheng, Y.H. Lee, J.C. Corelli and J.W. Corbett, Phys. Stat. Sol. (b) **90**, 689 (1978)
[19] B. N. Mukashev, K. H. Nussupov and M. F. Tamendarov, Phys. Lett. **72**, 381 (1979)
[20] L. Meda, G.F. Cerofolini, G. Ottaviani, R. Tonini, F. Corni, R. Balboni, M. Anderle, R. Canteri and R. Dierckx, Physica B **170**, 259 (1991)
[21] K. Murakami, N. Fukata, S. Sasaki, K. Ishioka, M. Kitajima, S. Fujimura, J. Kikuchi, and H. Haneda, Phys. Rev. Lett. **77**, 3161 (1996)
[22] A. W. R. Leitch, V. Alex and J. Weber, Phys. Rev. Lett. **81**, 421 (1998)
[23] R. Job, A.G. Ulyashin and W.R. Fahrner, Mater. Sci. Semicond. Proc. **4**, 257 (2001)
[24] W. Düngen, R. Job, Y. Ma, Y. L. Huang, T. Mueller, W. R. Fahrner, L. O. Keller, J. T. Horstmann and H. Fiedler, J. Appl. Phys. **100**, 034911 (2006)
[25] W. Düngen, R. Job, T. Mueller, Y. Ma, W. R. Fahrner, L. O. Keller, J. T. Horstmann and H. Fiedler, J. Appl. Phys. **100**, 124906 (2006)
[26] Y. Ma, Y. L. Huang, W. Düngen, R. Job and W. R. Fahrner, Phys. Rev. B **72**, 085321 (2005)
[27] Y. Ma, Y. L. Huang, R. Job and W. R. Fahrner Phys. Rev. B **72**, 085321 (2005)
[28] A. W. R. Leitch, V. Alex and J. Weber, Phys. Rew. Lett. **81**, 421 (1998)
[29] W. B. Jackson, A. Franz, Y. Chabal, M. K. Weldon, H.-C. Jin and J. R. Abelson, Mat. Res. Soc. Symp. Proc. **513**, 381 (1998)
[30] R. Job, M. F. Beaufort, J.-F. Barbot, A. G. Ulyashin and W. R. Fahrner, Mat. Res. Soc. Symp. Proc. **719**, 217 (2002)
[31] R. Job, Y. Ma, Y.-L. Huang, A. G. Ulyashin, W. R. Fahrner, M. F. Beaufort and J. F. Barbot, Solid State Phenomena **95-96**, 141 (2004)
[32] E. V. Lavrov and J. Weber, Physica B **308-310**, 151 (2001)
[33] J. N. Heyman, J. W. Ager III, E. E. Haller, N. M. Johnson, J. Walker and C. M. Doland, Phys. Rev. B **44**, 13363 (1992)
[34] B. Bech Nielsen, L. Hoffmann and M. Budde Mat. Sci. Eng. B **36**, 259 (1996)
[35] A. G. Ulyashin, *Hydrogen related phenomena in silicon: Application for the processing of device structures*, Habilitationsschrift (2005)

[36] A. G. Ulyashin, J. S. Cristensen, B. G. Svensson, R. Kögler and W. Skorupa, Nucl. Inst. Met. Phys. Res. B **253**, 126 (2006)
[37] M. Ishii, K. Nakashima, I. Tajima and M. Yamamoto, Jpn. J. Appl. Phys. **31**, 4422 (1992)
[38] Y. L. Huang, Y. Ma, R. Job, M. Sherff, W. R. Fahrner, H. G. Shi, D. S. Xue and M.-L. David, J. Electrochem. Sos. **152**, C600 (2005)
[39] H. Nagayoshi, K. Konno, S. Nishimura and K Terashima, Jpn. J. Appl. Phys. **44**, 7839 (2005)
[40] I. Solomon, B. Drévillon, H. Shirai and N. Layadi, J. Non-Cryst. Sol. **164-166**, 989 (1993)
[41] M. Bruel, B. Aspar and A.-J. Auberton-Hervé, Jpn. J. Appl. Phys **36**, 1636 (1997)
[42] H. Nordmark, A. Ulyashin, J. C. Walmsley, B. Tøtdal and R. Holmestad, (Unpublished results*)*
[43] H. Nordmark, A. Ulyashin, J. C. Walmsley and R. Holmestad, Submitted to J. Appl. Phys. (2008)
[44] K.-H. Hwang, E. Yoon, K.-W. Whang and J. Y. Lee, J. Electrochem. Sos. **144**, 335 (1997)
[45] K.-H. Hwang, E. Yoon, K.-W. Whang and J. Y. Lee, Appl. Phys. Lett. **67**, 3590 (1995)
[46] H. J. Stein and S. K. Hahn, J. Appl. Phys. **75**, 3477 (1994)
[47] N. H. Nickel, G. B. Andersen, N. M. Johnson and J. Walker, Physica B **273-274**, 212 (1999)
[48] N. H. Nickel, G. B. Andersen, N. M. Johnson and J. Walker, Phys. Rev. B **62**, 8012 (2000)
[49] Y. L. Huang, Y. Ma, R. Job and W. R. Fahrner, Appl. Phys. Lett. **86**, 131911 (2005)
[50] C. Gica, L. C. Nistor, H. Bender, O. Richard, G. Van Tendeloo and A. Ulyashin, Phil. Mag. **86**, 5137 (2006)
[51] S. Muto, S. Takeda and M. Hirata, Phil. Mag. A **72**, 1057 (1995)
[52] K.-H. Hwang, J.-W. Park, E. Yoon, K.-W. Whang and J. Y. Lee, Appl. Phys. Lett. **81**, 74 (1995)
[53] H.-S. Tae, S.-J. Park, S.-H. Hwang, K.-H. Hwang E. Yoon, K.-W. Whang and S. A. Song, J. Vac. Sci. Technol. B **13**, 908 (1995)
[54] A. Borghesi, B. Pivac, A. Sastella and A. Stella, Appl. Phys. Rev. **77**, 4169 (1995)
[55] A. Bourret, J. Thibault-Desseaux, and D. N. Seidman, J. Appl. Phys. **55**, 825 (1984).
[56] J. Grisolia, G. Ben Assayag, A. Claverie, B. Aspar , C. Lagahe and L. Laanab, Appl. Phys. Lett. **76**, 852 (2000)
[57] J. Grisola, F. Cristiano, G. Ben Assayag and A. Claverie, Nucl. Inst. Met. B **178**, 160 (2001)
[58] M. F. Beaufort, H. Garem and J. Lépinoux, Phil. Mag. A **69**, 881 (1994)
[59] S. Muto, S. Takeda, M. Hirata and T. Tanabe, J. Appl. Phys. **70**, 3505 (1991)
[60] C. Gica, L. C. Nistor, H. Bender, O. Richard, G. Van Tendeloo and A. Ulyashin, J. Phys. D: Appl. Phys. **40**, 395 (2007)
[61] C. Gica, L. C. Nistor, H. Bender, O. Richard, G. Van Tendeloo and A. Ulyashin, Phil. Mag. **86**, 5137 (2006)
[62] Y.-S. Kim and K. J. Chang, Phys. Rev. Lett. **86**, 1773 (2001)
[63] N. Martsinovich, I. Suárez and M. I. Heggie, Phys. Stat. Sol. (c) **2**, 1771 (2005)
[64] C. G. Van de Walle, Y. Bar-Yam and S. T. Pantelides, Phys. Rev. Lett. **60**, 2761 (1988)
[65] S. B. Zhang and W. B. Jackson, Phys. Rev. B **43**, 12142 (1991)
[66] D. Hull and D. J. Bacon; *Introduction to dislocations*, Butterworth-Heinemann, fourth edition (2001) and references therein
[67] E. Ligeon and A. Guivarc'h, Radiat. Eff. **27**, 129 (1976).
[68] B. Terreault, Phys. Stat. Sol. (a) **204**, 2129 (2007)
[69] X. Duo, W. Liu, M. Zhang, L. Wang, C. Lin, M. Okuyama, M. Noda, W.-Y. Cheung, S. P. Wong, P. K. Chu, P. Hu, S. X. Wang and L. M. Wang, J. Appl. Phys. **90**, 3780 (2001)
[70] M. K. Weldon, M. Collot, Y. J. Chabal, V. C. Venezia, A. Agarwal, T. E. Haynes, D. J. Eaglesham, S. B. Christman and E. E. Chaban, Appl. Phys. Lett. **73**, 3721 (1998)
[71] T. Höchbauer, K. C. Walter, R. B. Schwarz, M. Nastasi, R. W. Bower and W. Ensinger, J. Appl. Phys. **86**, 4176 (1999)
[72] Y. Ma, R. Job, W. Düngen, Y. L. Huang, and W. R. Fahrner, M. F. Beaufort and S. Rousselet and J. T. Horstmann, Appl. Phys. Lett. **86**, 252109 (2005)
[73] M. Bruel, Electron. Lett. **31**, 1201 (1995)
[74] SIMOX, J. Blake, *Encyclopedia of Physical Science and Technology*, Academic press, 3rd edition, **14**, 805 (2001)
[75] H. Nordmark, A. Ulyashin, J. C. Walmsley and R. Holmestad, Solid State Phenomena **131-133**, p. 315-320 (2008)
[76] http://www.soitec.com/
[77] M. Nastasi, T. Höchbauer, J.-K. Lee, A. Misra, J. P. Hirth, M. Ridgway and T. Lafford, Appl. Phys. Lett. **86**, 154102 (2005)

[78] T. Höchbauer, A. Misra, M. Nastasi and J. V. Mayer, J. Appl. Phys. **89**, 5980 (2005)
[79] C. H. Seager and D. S. Ginley, Appl. Phys. Lett. **34**, 337 (1979)
[80] J. I. Pankove, D. E. Carlson, J. E. Berkeyheiser, and R. O. Wance, Phys. Rev. Lett. **51**, 2224 (1983)
[81] N. M. Johnson, C. Herring, and D. J. Chadi, Phys. Rev. Lett. **56**, 769 (1986)
[82] B. Sopori, Y. Zhang and N. M. Ravindra, J. Elecron. Mater. **30**, 1616 (2001) and references therein
[83] B. L. Sopori, K. M. Jones, X. Deng, R. Matson, M. Al-Jassim and S. Tsuo, IEEE *Photovoltaic specialists conference*, p. 883 (1991)
[84] A. G. Aberle, Sol. Energy Mater. Sol. Cells, **65**, 239 (2001) and references therein
[85] A. A. Istratov, T. Buonassisi, R. J. McDonald, A. R. Smith, R. Schindler, J. A. Rand, J. P. Kalejs and E. R. Weber, J. Appl. Phys. **94**, 6552 (2003)
[86] D. Macdonald, A. Cuevas, A. Kinomura and Y. Nakano, Proceedings IEEE Photovoltaic specialists conference, p. 285 (2002)
[87] H. J. Möller, Prog. Mater. Sci. **35**, 205 (1991) and references therein
[88] S. M. Myers, G. A. Petersen, and C. H. Seager, J. Appl. Phys. **80**, 3717 (1996)
[89] S. M. Myers, D. M. Bishop, D. M. Follstaedt, H. J. Stein, and W. R. Wampler, Mater. Res. Soc. Symp. Proc. **283**, 549 (1993)
[90] J. Wong-Leung, C. E. Ascheron, M. Petravic, R. G. Elliman, and J. S. Williams, Appl. Phys. Lett. **66**, 1231 (1995)
[91] A. Kinomura, J.S. Williams, J. Wong-Leung and M. Petravic, Nuclear Instruments and Methods in Physics Research B **127/128**, 291 (1997)
[92] J. Wong-Leung,a) E. Nygren, and J. S. Williams, Appl. Phys. Lett. **67**, 416 (1995)
[93] B. Mohadjeri, J. S. Williams, and J. Wong-Leung, Appl. Phys. Lett. **66**, 1889 (1995)
[94] R. Krause-Rehberg, F. Borner, F. Redmann, J. Gebauer, R. Kögler, R. Kliemann, W. Skorupa, W. Egger, G. Kogel, W. Triftshauser, Physica B, **308-310**, 442 (2001)
[95] A. G. Ulyashin, Y. A. Bumay, W. R. Fahrner, A. I. Ivannov, R. Job, L. Palmetshofer, MRS Symposium Proceedings Series **469**, 95 (1997)
[96] H. Nordmark, A. Ulyashin, J. C. Walmsley, B. Tøtdal and R. Holmestad, Nucl. Instrum. Meth. Phys. Res. B **253**,p 176-181 (2006)
[97] M. A. Green, *Solar cells: Operating principles, technology and system applications*, Kensington : University of New South Wales (1998)
[98] J. Nijs, S. Sivoththaman, J. Szlufcik, K. De Clercq, F. Duerinckx, E. Van Kerschaever, R. Einhaus, J. Poortmans, T. Vermeulen and R. Mertens, Sol. Energy Mater. Sol. Cells **48**, 199 (1997)
[99] D. H. Macdonald, A. Cuevas, M. J. Kerr, C. Samundsett, D. Ruby, S. Winderbaum and A. Leo, Solar Energy **76**, 277 (2004)
[100] U. Gangopadhyay, S. K. Dhungel, P. K. Basu, S. K. Dutta, H. Saha and J. Yi, Sol. Energy Mater. Sol. Cells, **91**, 285 (2007)
[101] P. Fath, C. Borst, C. Zechner, E. Bucher, G. Willeke, S. Narayanan, Solar Energy Materials and Solar Cells, **48**, 229 (1997)
[102] Y. Inomata, K. Fukui and K. Shirasawa, Sol. Energy Mater. Sol. Cells, **48**, 237 (1997)
[103] G. Kumaravelu , M. M. Alkaisi , A. Bittar, D. Macdonald and J. Zhao, Curr. Appl. Phys. **4**, 108 (2004)
[104] L.A. Dobrzański, A. Drygała, K. Gołombek, P. Panek, E. Bielańska and P. Zięba, J. Mat. Proc. Tech. **201**, 291 (2008)
[105] H. Nagayoshi, S. Nishimura, K. Treashima, and K. Konno, Jpn. J. Appl. Phys. **44**, 7839 (2005)
[106] H. Nagayoshi, S. Nishimura, K. Treashima and A. G. Ulyashin, *Proc. WCPEC-4, IEEE*, p. 1411 (2006)
[107] H. Nordmark, H. Nagaoyshi, K. Terashima, S. Nishimura, J. C. Walmsley, R. Holmestad, and A. Ulyashin, *Proceedings 22nd European Photovoltaic Solar Energy Conference, Milan, Italy*, p. 1686 (2007)
[108] B. K. Teo and X. H. Sun, Chem. Rev. **107**, 1454 (2007) and references therein
[109] Y. Xia, P. Yang, Y. Sun, Y. Wu, B. Mayers, B. Gates, Y. Yin, F. Kim and H. Yan, Adv. Mater**. 15**, 353 (2003)
[110] V. Schmidt, H. Riel, S. Senz, S. Karg, W. Riess and U. Gösele, Small **2**, 85 (2006)
[111] J. Goldberger, A.I. Hochbaum, R. Fan and P. Yang, Nano Lett**. 6**, 973 (2006)
[112] J.-F. Hsu, B.-R. Huang, C.-S. Huang and H.-L. Chen, Jpn. J. Appl. Phys**. 44**, 2626 (2005)
[113] J. A. Streifer, H. Kim, B.M. Nichols and R.J. Hamers, Nanotechnology **16**, 1868 (2005)
[114] D. D. D. Ma, C. S. Lee, F. C. K. Au, S. Y. Tong, S. T. Lee, Science, **299**, 1874 (2003)

[115] J. Goldberger, R. R. He, Y. F. Zhang, S. W. Lee, H. Q. Yan, H. J. Choi, and P. D. Yang, Nature.**422**, 599 (2003)
[116] B. M. Kayes, H. A. Atwater, and N. S. Lewis, J. Appl. Phys. **97**, 114302 (2005)
[117] L. Tsakalakos, J. Balch, J. Fronheiser, B. A. Korevaar, O. Sulima and J. Rand, Appl. Phys. Lett. **91**, 233117 (2007)
[118] Y. Cui, L. J. Lauhon, M. S. Gudiksen, K. L. Wang, and C. M. Lieber, Appl. Phys. Lett **78**, 2214 (2001)
[119] J. L. Liu, S. J. Cai, G. L. Jin, S. G. Thomas, and K. L. Wang, J. Cryst. Growth **200**, 106 (1999)
[120] A. M. Morales and C. M. Lieber, Science **279**, 208 (1998)
[121] Y. F. Zhang, Y. H. Tang, N. Wang, D. P. Yu, C. S. Lee, I. Bello, and S. T. Lee, Appl. Phys. Lett. **72**, 1835 (1998)
[122] R. J. Barsotti, Jr., J. E. Fischer, C. H. Lee, J. Mahmood, C. K. W. Adu, P. C. Eklund, Appl. Phys. Lett. **81**, 2866 (2002)
[123] R. S. Wagner, W. C. Ellis, K. Jackson, and S. M. Arnold, J. Appl. Phys. **35**, 2993 (1964).
[124] E. I. Giargizov, J. Cryst. Growth **31**, 20 (1975)
[125] Y. Wang, V. Schmidt, S. Senz and U. Gösele, Nature nanotechnology, **1**, 186 (2006)
[126] T. I. Kamins, R. Stanley Williams, Y. Chen, Y.-L. Chang, and Y. A. Chang, Appl. Phys. Lett. **76**, 562 (2000)
[127] T. I. Kamins, R. Stanley Williams, D. P. Basile, T.Hesjedal and J. S. Harris, J. Appl. Phys. **89**, 1008 (2001)
[128] J. Arbiol, B. Kalache, P. R. i Cabarrocas, J. R. Moranteand A. F. i Morral, Nanotechnology **18**, 305606 (2007)
[129] O. Nast, S. Brehme, D. H. Neuhaus and S. R. Wenham, IEEE Trans. Electron dev. **46**, 2062 (1999)
[130] P. I. Widenborg and A. G. Aberle, J. Cryst. Growth. **242**, 270 (2002)
[131] T. J. Konno and R. Sinclair, Philos. Mag. B, **66**, 749 (1992)
[132] P. I. Widenborg, A. Straub, A. G. Aberle, J Cryst. Growth **276**, 19 (2005)

5. Experimental techniques

5.1 Transmission Electron microscopy

The benefit of using electrons instead of light is the much better resolution achieved, in the ~ nm-Å region, compared to μm for light microscopy. The two techniques used in this thesis are scanning and transmission electron microscopy, abbreviated SEM and TEM, respectively. Figure 5.1 shows the radiation resulting from interaction of energetic electrons with matter.

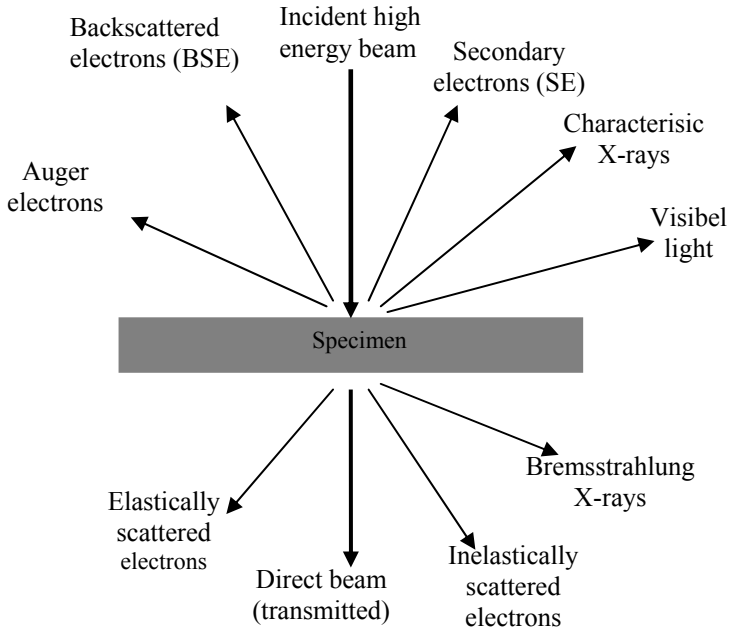

Figure 5.1. The resulting radiation after interaction of high energetic electrons with matter.

TEM is one of the most powerful techniques for characterization of materials and can be used to measure both crystal structure and chemical composition of a sample. The wavelength of the electrons depends on their energy

$$\lambda \approx \frac{1.22}{\sqrt{E}}, \tag{5.1}$$

giving a wavelength of only 4 pm for 100 keV electrons. The spatial resolution of the TEM is much worse than this, ~ 2-3 Å for conventional TEMs, because of the imperfect lenses, consisting of magnetic fields. Due to spherical aberration of the objective lens, a point on the specimen transfers into a disk in the image, such that each point in the image has contributions from many points in the specimen [1]. The spatial resolution in TEM is given by [2]

$$\Delta x = 0.6 C_s^{1/4} \lambda^{3/4} (\mathring{A}) \qquad (5.2)$$

where C_s is the spherical aberration and λ is the wavelength of the electrons.

Recently, aberration correctors for TEM have been developed, which correct spherical aberration of the objective lens and significantly increase the resolution. The distance at which two atomic contrast maxima can be separated in the image is reduced to ~ 0.8 Å for a 300 keV instrument [3]. However, the accuracy of the separation of well isolated atoms has been measured to be as low as 5-6 pm in some cases [4]. The much better resolution revolutionizes the number of structures that can be studied in the TEM. The main limitations of TEM are the small dimensions of the samples that can be studied and the comprehensive sample preparation necessary for most samples, which can damage or change the structure of the materials [5,6].

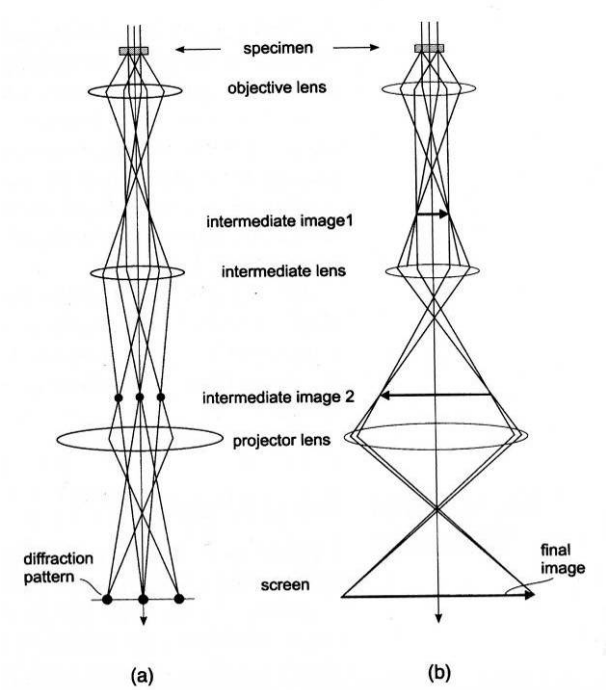

Figure 5.2. The beam path in a TEM in diffraction mode (a) and imaging mode (b)[1].

Figure 5.2 (a) and (b) show the trace of an electron beam in a typical TEM in diffraction mode and imaging mode, respectively. Most of the electrons transverse right through the specimen and just a few are being scattered. Electrons are focused by changing the current in the coils of the lenses that produce a magnetic field. The electron beam leaves the electron source and transverses through two condenser lenses, which focus the beam onto the specimen, and control the diameter of the beam. The focal length of the objective lens is adjusted to form an image of the specimen in the intermediate image plane. The two projector lenses magnify the image further and focus it onto the fluorescent screen (b). By changing the strength of one of the intermediate lenses, a diffraction pattern can be obtained on the fluorescent screen, Figure 5.2(a).

Electrons can be both elastically and inelastically scattered when going through the thin sample. The elastic scattering gives rise to Bragg diffraction, where the electrons are scattered in certain directions due to the periodical crystal lattice, while the inelastically scattered electrons give rise to diffuse background intensity. The scattered electrons interfere constructively and destructively according to Bragg's law and produce a diffraction pattern where each spot represents a set of parallel lattice planes in the crystal with different Miller indices, (hkl). The diffraction pattern is formed in the back focal plane of the objective lens [5,6].

The microscope can be operated in two conventional diffraction contrast imaging modes: Bright field imaging, where the direct beam is used to form the image, or dark field imaging, where one of the scattered beams is used to form the image. Three types of contrast can be recognized in the image. Different crystal structures, orientations and strain centres show different strength of Bragg diffraction, and this is called diffraction contrast. In Figure 3.5(a), an example of differently oriented grains in an fcc steel sample that shows diffraction contrast in bright field mode can be observed. The dark grains are close to Bragg conditions. Heavy elements scatter the electrons more efficiently than light elements because of their larger mass, and give rise to mass contrast. The metal precipitates in Figure 3.10 (b) show this type of contrast. A thicker sample spreads more electrons than a thin sample, and thickness variations in a sample give rise to thickness contrast. These two effects are called mass-thickness contrast [5,6].

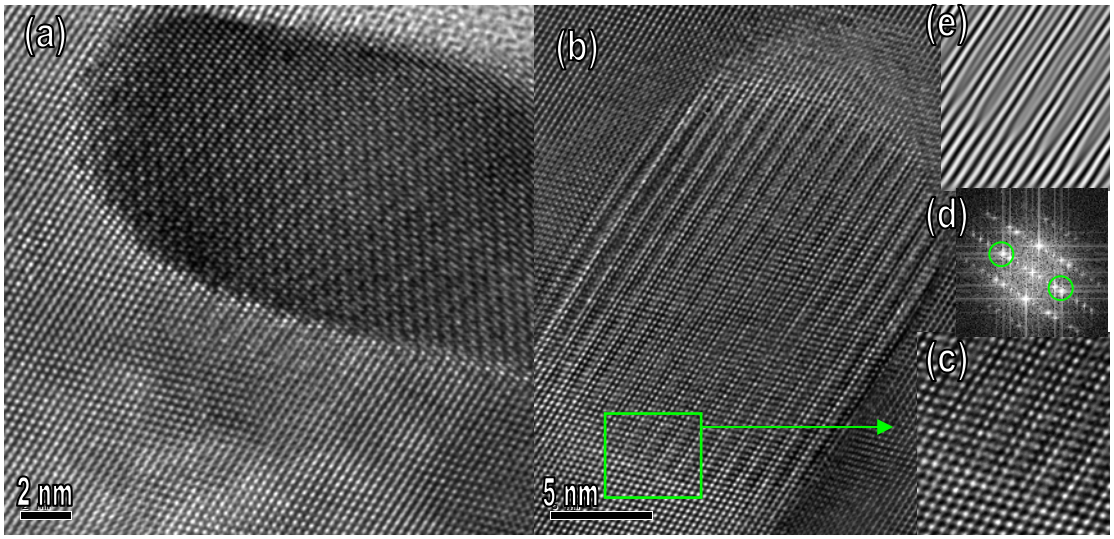

Figure 5.3. HRTEM images of palladium-silver rich precipitates in the silicon matrix tilted to a {110} zone-axis in Si. (a) The lattice of the precipitates differs from that of the silicon matrix. (b) Periodical Moiré fringes of a precipitate due to overlapping lattices of silicon matrix and precipitate are visible. While the two lattices match normal to the fringes, every third silicon row splits into two rows in the precipitate in the direction parallel to the fringes. The region inside the green rectangle is enlarged in (c). Fast Fourier transform (FFT) of the same area is shown in (d). By selecting reflections in only one direction (green circles) to contribute to the image, an inverted FFT image can be constructed (e). Dislocations are seen to form in the Si matrix - precipitate interface.

Mass contrast is similar to Z contrast in scanning TEM (STEM), where the transmitted and scattered electrons are detected by bright field (BF) and dark field (DF) detectors respectively. In this case, heavy atoms show dark contrast in BF, and bright contrast in DF as visualised in Figure 5.4 (a) and (b), for Cu_3Si precipitates in a grain boundary.

The third contrast mechanism is the phase contrast, giving rise to high resolution images. High resolution TEM (HRTEM) is a technique based on phase contrast. The transmitted and diffracted beams that pass through the objective aperture are recombined to form an image. The phase interference between the two beams result in periodic intensity fringes due to Bragg diffracting planes. The contrast in the image due to the periodic fringes gives rise to lattice imaging [2]. Figure 5.3 shows an example of atomic resolution of Pd-Ag rich precipitates in a Si matrix. The lattice of the precipitate clearly differs from that of the Si matrix, Figure 5.3(a). While fitting perfectly in one direction, dislocations are seen to form in the other direction, Figure 5.3(b)-(e).

Scanning transmission electron microscopy (STEM)

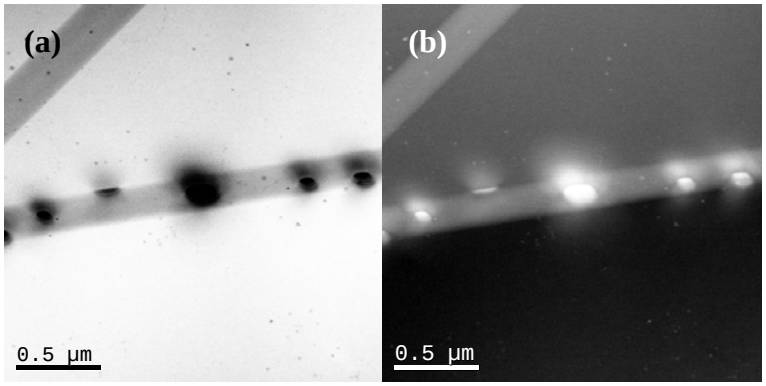

Figure 5.4. Bright field (a) and dark field (b) STEM images of copper precipitates in a grain boundary.

In STEM mode, the beam is focused to a small spot and is scanned over the sample in a raster. The BF detector is disk shaped and collects the unscattered electrons, while the DF detector is ring shaped and collects the scattered electrons. The BF and DF images obtained are complementary images, as can be observed from Figure 5.4. By changing the camera length, the angle of the detected electrons changes and the Z contrast is more evident. By using a high angle annular dark field detector (HAADF) combined with atomic resolution, individual heavy atoms can be recognized by Z contrast. A STEM image can be interpreted directly in contrast to the HRTEM image that is simulated [3,5,7].

X-ray energy dispersive spectroscopy (EDS)

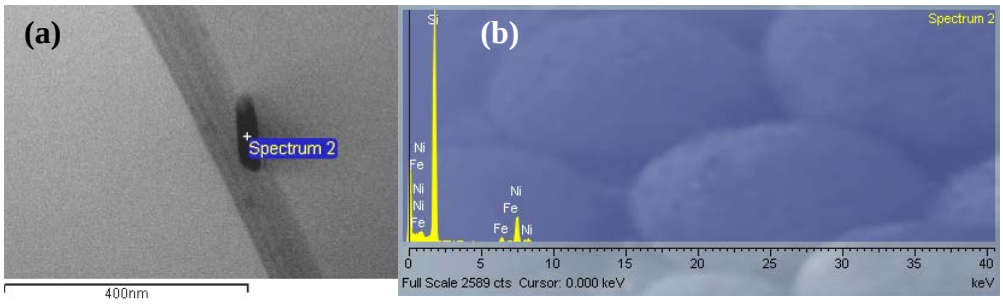

Figure 5.5. (a) Metallic precipitate in a grain boundary, (b) EDS spectrum from the precipitate shows that it contains iron and nickel in addition to silicon.

EDS is used to analyze the chemical composition of a sample, as shown in Figure 5.5, where a Ni-Fe silicide precipitate has been analyzed. When the electron beam hits the sample, some atoms are ionized and emit characteristic X-rays corresponding to the energy released from the electron transition. The electron transitions are specific for every element giving a fingerprint of the element. A combination of Si(Li) and Ge detectors can detect K_α lines of all elements from Be to U [5]. The sensitivity is lower for light elements than heavy elements. The relative heights of the peaks can be used to determine quantitatively the impurity level in the sample. By combining STEM and EDS, mapping of impurities can be performed. In STEM mode, a spectrum is created for every spot in the image, such that phase maps can be created.

TEM is the main technique used in most of the papers. Both plan view and cross-section samples have been used. Plan view samples were made by cutting a 3 mm disk using an ultrasonic disk cutter from an area of interest. The cross-section samples were made by gluing interesting surfaces face to face in to a 3 mm thick Al cylinder and cutting thin slices with a diamond saw. The disks were ground with SiC paper down to 30-50 μm thickness and ion milled with argon ions using a Gatan Ion Duo mill model 600, or a Gatan PIPS ion miller. Two different microscopes were used. A Phillips CM 30 operating at 200-300 kV, with LaB_6 filament and a resolution of 2.3 Å, was used for conventional microscopy, and electron diffraction. A JEOL 2010 F with field emission gun, (FEGTEM), operating at 200 kV, and a resolution of ~ 2 Å equipped with scanning TEM (STEM) and X-ray energy dispersive spectroscopy (EDS) detectors, was used for the high resolution imaging and chemical analysis. For STEM, a bright field or annular dark field detector was used in analytical mode with 0.7 nm spot size. An Oxford instruments EDS Si:Li detector was used for chemical analysis. INCA software was used for recording spectra and perform elemental mapping.

5.2 Scanning electron microscopy (SEM)

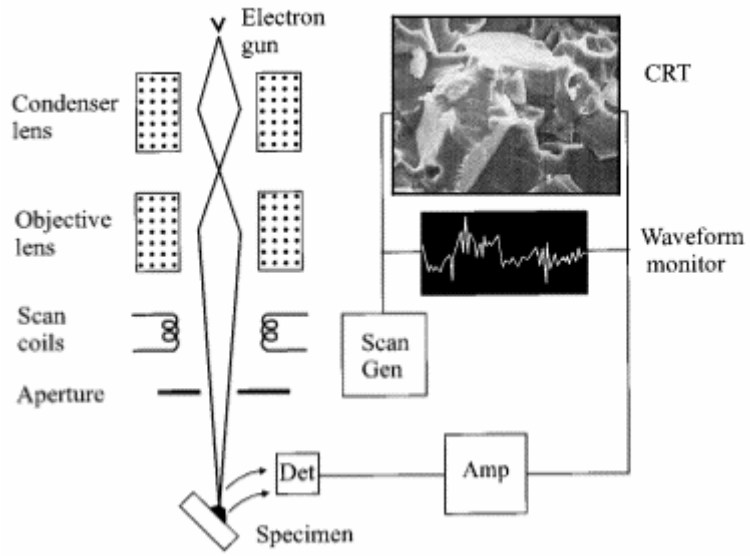

Figure 5.6. The beam path and generation of image in SEM [7].

SEM is used to study the morphology and chemical composition of surfaces. The beam path in a SEM is shown in Figure 5.6. In the SEM, electrons are emitted from the electron gun and accelerated by a potential field of 0.5-30 kV towards the sample surface. The resolution limit is typically a few nm. The lenses consist of magnetic fields that focus the beam onto the sample surface. A small probe is scanned over the sample surface in a raster. The electrons interact with the sample to produce secondary electrons (SE), back-scattered electrons (BSE), characteristic X-rays, cathodoluminescence and Auger electrons, as shown in the upper part of Figure 5.1. Detectors placed above the sample surface detect the different radiation. The resolution and surface sensitivity depend on the voltage used. In general, lower voltage increases the surface sensitivity and higher voltage increases the resolution [7-9].

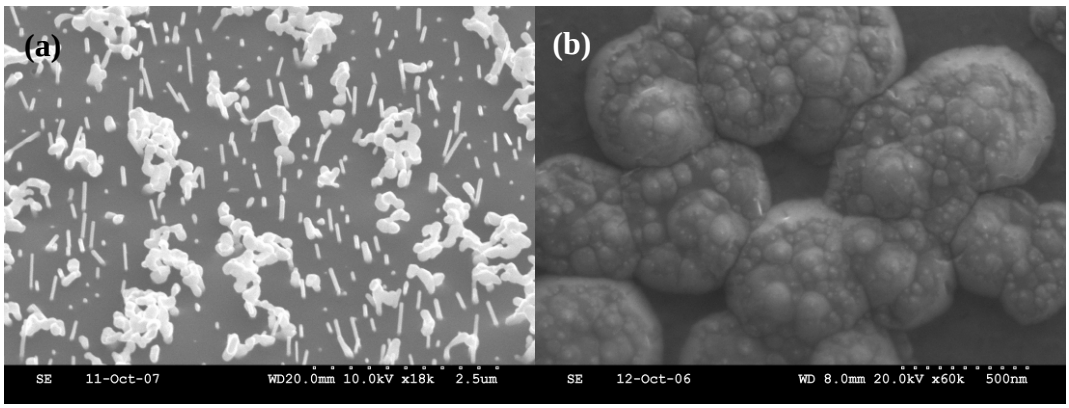

Figure 5.7. SEM secondary electron images of surface morphology of Si samples (a) SiW_2 whiskers and particles on the Si substrate surface, (b) Texturing after H plasma treatment, showing surface morphology.

The beam penetration depth in a sample depends on the voltage used, the crystal structure and the composition of the sample. Secondary electrons are emitted from the top surface layer, ~ 5-50 nm depth, and give information about the topography. An example on topographical contrast obtained using secondary electron detector is shown in Figure 5.7. BSE are elastically scattered by the sample, and their scattering angle depends on the lattice orientation and composition of the sample. They give rise to diffraction contrast, Z-contrast and topographic contrast. X-rays are emitted from the whole penetration depth and give the chemical composition of the sample [7-9].

An advantage of SEM over TEM is the much easier sample preparation. The dimensions of samples that can be studied are limited to the size of the sample chamber, but can be several cm. The sample surface needs to be clean and conducting or covered with conducting material to avoid charging.

Electron back-scattering diffraction (EBSD)

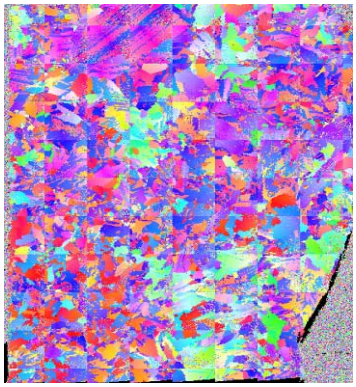

Figure 5.8. EBSD map of the small grained 5 x 5 cm wafer studied in paper 2. Every colour represents a different grain. Grains of similar orientation have similar colour in the map.

EBSD can be used to determine grain orientation, grain boundary misorientation and crystal structure of a sample, as shown in Figure 5.8. The technique is based on elastic Bragg scattering of electrons by the crystal lattice in the sample. Electrons that satisfy the Bragg condition for a plane are channeled and give rise to Kikuchi bands. The bands are located using Hough transform. Every point in the Kikuchi bands are transferred into the Hough space by the function

$$\rho = x \cos\theta + y \sin\theta, \text{ in the range } 0 \leq \theta \geq 180° \qquad (5.3)$$

A Kikuchi line gives rise to many curves that cross in a point, making a bright spot in the Hough space, $H(\rho, \theta)$. After transferring every pixel in the image, the Kikuchi lines can be recognized as bright spots and are used to index the diffraction pattern. For each point in the specimen an EBSD pattern is indexed and the orientation in the grain is calculated. The orientations from each point is stored and used to construct a crystal orientation map, where all grain boundaries are detected [9,10].

The surface morphology of the H^+ plasma treated and WSi_2 deposited + H radical treated Si surfaces in paper 4-7 and 8-9, respectively, was analyzed by a Hitachi s-4300SE scanning electron microscope (SEM) with Schottky emitter field emission gun operating at 5-20 kV. The working distance was set to 8-20 mm. For the EBSD map in paper 2, the sample was tilted 70°, a voltage of 20 kV and a camera length of 15 mm were used. The microscope is equipped with a secondary electron detector, solid state backscattered detector, Oxford EDS detector and Nordif EBSD detector. The image recording and analysis systems are Digitized images and Oxford INCA EDS and imaging system.

Electron beam induced current (EBIC)

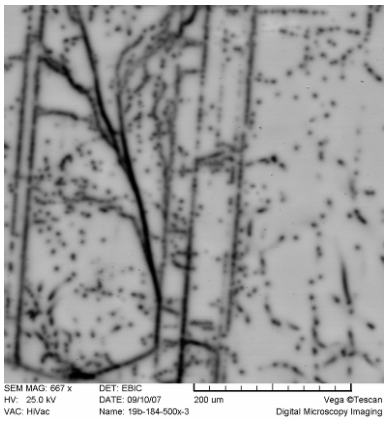

Figure 5.9. EBIC map of an area in the silicon wafer studied in paper 2, showing recombination active areas as dark contrast. This image was recorded at ~ 100 K.

For EBIC the sample needs to be covered by a thin transparent Schottky contact or contain a pn junction. The short circuit current, I_{sc} is amplified and displayed on a monitor, synchronized with the electron beam scan. The minority carriers induced by the electron beam, either recombine at a defect or are collected at the Schottky contact as current, the resulting signal being displayed on the monitor. Electronically active defects, or recombination active defects, reduce the current signal, giving dark contrast in the current image on the monitor, as shown in Figure 5.9. The recombination activity of a sample can be measured as a function of temperature by cooling down the sample with liquid nitrogen [11].

Defect contrast was measured as

$$C = \frac{I_b - I_d}{I_b} \tag{5.4}$$

where I_b is the bulk current and I_d is the current on the defect. The minimum contrast significantly measurable was estimated to be close to 0.2 % on polished samples.

For the EBIC measurements, a Tescan VEGA TS5136XM SEM with a tungsten filament was used. The beam current used allowed a measured current going through the wafer. The EBIC samples were first mechanically and then chemically polished with

CP4 (HF:HNO3:CH3COOH = 3:5:3 in volume ratio). Thereafter, Al Schottky contacts were realized by evaporating the metal under vacuum conditions of about 10-8 Pa. The resolution was limited to about 1 μm by the fixed working distance Z = 60 mm. The acceleration voltage used was 25 kV. The sample was cooled down to 90-100 K by use of liquid nitrogen before mapping.

5.3 Other techniques

5.2.1 *Dislocation density measurements*

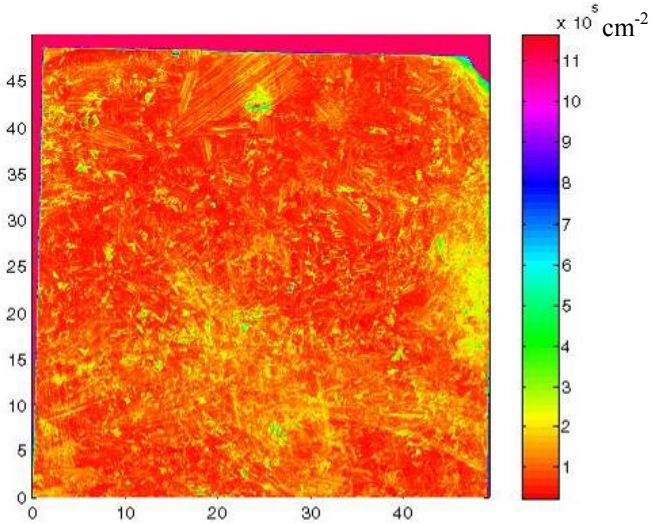

Figure 5.10. Dislocation density map of the 5 x 5 cm wafer studied in paper 2. Red areas have low dislocation density, while yellow and green areas have high dislocation density.

A dislocation map of a wafer is shown in Figure 5.10. A photovoltaic scanning system (PV-scan) was used to measure dislocation density. In this technique, the sample is placed under an integrating sphere and illuminated by a HeNe laser [12]. The etch pits created by Sopori etch solution [13] scatter the incoming light differently depending on their shape. Dislocation etch pits are U shaped, while grain boundary etch pits are V shaped. Grain boundaries reflect the light backwards with a small angle, while the etch pits from dislocations reflect the light diffusively to a cone with an angle of about 20° [14]. The light from the grain boundaries is allowed to emerge from the integrating sphere, while the light from the dislocations is captured. A map of the dislocation density is obtained. By calibrating the signal with reference signals, a numerical value of the dislocation density can be achieved [12].

A PV-scan delivered by GT Equipment Technologies Inc was used to measure dislocation density in paper 1. The samples were first mechanically ground down to 1 μm grade diamond paste, chemically polished and etched with Sopori etch ($36HF:15CH_3COOH:2HNO_3$) to reveal grain boundaries and dislocations [13]. A 630 nm HeNe laser was used to illuminate the defect etched sample [15].

5.2.2 *Atomic force microscopy (AFM)*

AFM measures the interaction force between a very sharp tip, usually of radius less than 50 nm in diameter, and the sample. The tip, attached to a cantilever, is scanned over the surface in a raster and a 3D image of the surface is created. In this way, surface topography, as well as physical properties of a surface, can be obtained [16,17]. Atomic resolution can be achieved by using an atomically sharp tip. An AFM can be operated in several modes, contact mode, non-contact mode and tapping mode. In addition, magnetic and charged tips can be used to measure the change of magnetic and electrical force on a sample [16-19].

In contact mode, the tip scans over the sample in contact with the surface. A repulsive force of 10^{-7}-10^{-11} N is used on the tip and the deflection of the cantilever is detected and applied in a feedback system. In non-contact mode, the tip is vibrated near its resonance frequency 10-100 nm above the surface and attractive Van der Waals forces acting between the tip and the sample surface are detected producing a topographic image of the surface [18]. In tapping mode, the tip oscillates on the surface close to the resonance frequency of the cantilever. The reduction in oscillation amplitude or phase due to surface roughness is detected [19]. Alternatively, changes in the vibrational frequency due to the force gradient can be detected.

The surface morphology of Si samples was analyzed by the AFM method using a Digital Instrument's Nanoscope Dim 3100 microscope. The AFM measurements were performed in tapping mode using commercial silicon tips, MikroMasch NSC35/AlBS, with a typical tip curvature radius of less than 10 nm. The following parameters were measured: (i) the root mean square (RMS) roughness (R_q), which gives the root mean square average of height deviations taken from the mean data plane within a given area, (ii) the mean roughness (R_a), which represents the arithmetic average of the absolute values of the surface height deviations measured from the mean plane; (iii) the difference in height between the highest and lowest points on the surface relative to the mean plane (h_{max}); (iv) the average differences of heights (h_{aver}) [20].

5.2.3 *Fourier transform infrared spectroscopy (FT-IR)*

FT-IR spectroscopy is used to chemically identify and quantify elements in a sample. During the analysis, infrared radiation is passed through the sample, some of the radiation is absorbed and the rest is transmitted, giving rise to an absorption or transmittance spectrum. Every molecule has its own fingerprint spectrum, such that the absorption peaks can be used to determine the concentrations of the different impurities. With a FT-IR spectrometer all frequencies are measured simultaneously making the recording time of a scan very fast. When measuring a sample, the background spectrum needs to be retracted [21].

In paper 1 and 3, FT-IR was used to measure interstitial dissolved oxygen and substitutionally dissolved carbon content in mechanically ground (6 μm diamond paste)

samples. The spectra were recorded in room temperature and the frequency range used was 4000 cm^{-1}- 400 cm^{-1}. The oxygen peak is located at ~ 1107 cm^{-1}, the carbon peak is located at ~ 605 cm^{-1} and the oxygen and carbon contents were measured in accordance with the ASTM standards [22,23].

5.2.4 *Raman*

Raman spectroscopy is used to study vibrational, rotational, and other low-frequency modes in a system. When the incident light is scattered inelastically due to interaction with molecules, it is called Raman scattering. Raman spectroscopy is based on measuring the energy shift of the incident photon beam on a sample that is inelastically scattered off the material [1]. The energy shift during such a scattering process is due to either the photon energy transfer to the lattice (i.e. phonon emission), or the absorption of a phonon by the photon. The intensity of light corresponding to Raman scattering process is weak, in the order of 10^{-5} % of the source, such that intense monochromatic light generated by a laser is commonly used in the process [2]. The Raman spectral peaks correspond to the frequencies of the vibrational modes and can be attributed to a particular molecular group or phase in the material studied [2].

Two different Raman setups have been used to study H bond formation in silicon. In Appendix B, Raman spectra were recorded with a multichannel spectrometer from Horiba (Jobin Yvon) model T 64000, employing a single monochromator with CCD detector, at room temperature, using 90° scattering geometry. The spectra were excited by a Milennia Pro diode-pumped (Nd:YVO_4 crystal) laser from Spectra-Physics (Model J 40) adjusted to give approximately 100 mW of the 532 nm line on the sample. A slit of 200 μm was used and the resolution used was 2 cm^{-1} resolution.

In paper 5, Raman measurements were carried out with a Dilor LABRAM Raman system, where a microscope is confocally coupled to a 300 mm focal length spectrograph. The excitation was supplied by an Ar^{+} ion laser (487.987 nm, 20 mW). The diameter of the focused laser spot on the samples surface was about 2 μm. The Raman spectra were collected at room temperature by a Peltier cooled CCD detector (collection time: 1200 s, averaging factor: 10). All spectra were normalized to the maximum of the optical Si phonon line at ~ 520 cm^{-1}, and the background luminescence was subtracted from the data.

5.2.5 *Lifetime*

The Quasi Steady State Photo Conductance Decay (QSSPC) technique is based on steady state conditions. When the generation and recombination rate of minority carriers are equal, the lifetime can be calculated from measurements of the injection level. The silicon wafer is illuminated by a long slowly decaying intensity light pulse such that the electrons and holes will have time to stabilize close to their equilibrium concentrations. The excess photoconductance generated by electrons and holes are measured by a coil in contact with the material [14,24]. The microwave photo-conductance decay method

(μPCD) measures the photoconductance decay transients after a very short light pulse from a light source by use of a microwave. The reflection of the microwave follows an exponential as the conductivity changes in the sample. The effective lifetime is obtained from the slope of the decay curve [24,25]. In Figure 5.11(a), a lifetime map of the wafer studied by other techniques in paper 2, is shown. An iron map, found by subtracting the lifetime before and after a short annealing that dissolves iron-boron pairs, is shown in Figure 5.11(b).

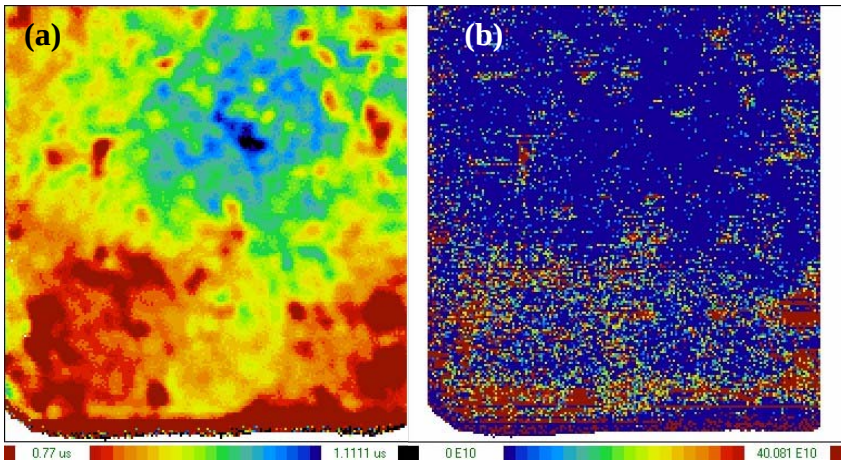

Figure 5.11. (a) Lifetime of the 5 x 5 cm wafer studied in paper 2, grown from metallurgical silicon measured by μW-PCD. Red color represents bad lifetime, blue color slightly better lifetime. (b) Corresponding iron map found by measuring the lifetime before and after a short annealing that dissolves iron-boron pairs. Not surprisingly, areas with the lowest lifetime were found to have the highest concentrations of iron.

Two methods of measuring lifetime in silicon have been used. In paper 1 and 3, the QSSPC technique was used for minority carrier lifetime determination [24]. In order to reduce the recombination velocity of the charge carriers at the surface, the samples were passivated by an iodine ethanol (IE) solution. The lifetime of the material was measured by quasi-steady state photo conductance (QSSPC) on passivated samples from the metallurgical ingot. A photographic lamp was used to illuminate the sample. In paper 5, the effective minority carrier lifetime was measured by the μ-PCD mapping system from Semilab. The surface of the silicon substrates was passivated by hydrogen termination by deposition of an a-Si:H layer on both sides at temperatures around 200 °C. The thickness of the a-Si:H layers was about 50 nm. Post deposition heat treatment was performed at 450 °C on a belt furnace in air for about 2 minutes.

5.2.6 *Glow discharge mass spectroscopy (GDMS)*

GDMS is a mass spectrometer with high resolution for chemical analysis and depth profiling of solid samples. The elemental concentration detection limit is very low, ~ ppb, and several elements can be analyzed at the same time. All elements in the periodic table, except from He and Ne can be measured with approximately equal sensitivity.

The Glow discharge is a low energy plasma created by inserting two electrodes, where the sample to be analyzed forms the cathode, in a cell with a low pressure (~ 0.1-1 Torr) gas, often Ar. A potential of 1 kV between the two electrodes, causes the gas to split into Ar^+ and e^-. Positive argon ions are accelerated towards the cathode (sample) surface, resulting in sputtering of the sample surface. Sputtered atoms and molecules are ionized in the plasma, and positive ions are extracted and accelerated into the mass spectrometer. The ions entering the mass spectrometer are separated due to their mass-to-charge and energy-to-charge and electrically detected by a photomultiplier or channeltron detector. The ratio between the signal intensities (counts per second) of the element and the matrix, i.e. IBR (Ion Beam Ratio), is used to quantify the element [26,27].

In paper 1, A Finnigan ELEMENT GD delivered by Thermo Electron Corporation was used to measure chemical composition of the ingot. The samples were lightly polished and cleaned in ethanol before analysis. The samples were sputtered 10 min before the measurement started, to remove surface contamination. The crater was ~ 8 mm in diameter [15].

5.2.7 *Secondary ion mass spectroscopy (SIMS)*

Secondary ion mass spectroscopy (SIMS) provides information of the depth distribution of elements at very low concentrations. A primary beam of ions, usually O^{2+}, Cs^+, Ar^+ or Ga^+, sputters the surface of a sample. A secondary beam of atoms, molecules, secondary scattered ions, electrons and photons from the sample, with energies between 0 and a few hundred eV, results from the sputtering. The secondary ions are separated in mass by a magnetic sector spectrometer, and subsequently collected by an electron multiplier detector. The amount of secondary ions detected per second versus time is monitored for each element. Knowing the primary ion beam current and the sputter rate, the conversion of the time scale into a depth scale can be calculated [28,29].

In appendix 1 and 2, SIMS was used for analysis of the hydrogen distribution in the Si samples upon ion implantation and plasma treatment. This was done using a CAMECA SIMS 7f instrument in negative mode with a 15 keV Cs^+ primary beam. The raw SIMS profiles were obtained as sputter time versus secondary ion intensity. The sputter time is related to depth and the conversion factor is determined by measuring the SIMS craters with a Dektak 8 surface stylus profilometer. The concentration calibrations for hydrogen were done using a $5x10^{15}$ cm^{-2} 150 keV $^+$ ion implanted Si reference sample. The depth resolution was 10-20 nm and detection limit for hydrogen was ~ 10^{18} cm^{-3}. A 10 µm spot was scanned over an area of 200 x 200 µm.

References

[1] D. Hull and D. J. Bacon; *Introduction to dislocations*, Butterworth-Heinemann, fourth edition (2001) and references therein.

[2] Yacobi, B. G. *Semiconductor Materials : An Introduction to Basic Principles,* Secaucus, NJ, USA: Kluwer Academic Publishers, 2002. p 197.

[3] K. Urban, , Science, **321**, 506 (2008)

[4] L. Houben, A. Thust and K. Urban, Ultramicroscopy **106**, 200 (2006)

[5] D. B. Williams, C. B. Carter, *Transmission Electron Microscopy* ,Plenum Press, New York (1996).

[6] *Innføring i transmisjon elektronmikroskopi*, J. K. Solberg and V. Hansen, Kompendium materialteknologi (2001)

[7] P. J. Goodhew, *Electron Microscopy and Analysis*, Taylor & Francis, Limited (2000)

[8] J. Hjelen, *Scanning electron-mikroscopi*, Metallurgisk institutt, NTH (1989)

[9] J. Goldstein, D. Newbury, D. Joy, C. Lyman, P. Echlin, E. Lifshin, L. Sawyer and J. Michael, *Scanning electron microscopy and X-ray microanalysis*, Kluver Academic/Plenum publisher, third edition (2003)

[10] F. J. Humpreys, J. Mater. Sci. **36**, 3833 (2001)

[11] M. Acciarri, oral precentation, PV mini conference, Trondheim, 2007

[12] B. L. Sopori, R. Murphy and C. Marshal, Proceedings of the 23rd IEEE Photovoltaic specialist conference, Louesville, USA, p. 190 (1993)

[13] B. L. Sopori, J. Electrochem. Soc. **131**, 667 (1984)

[14] Gaute Stokkan, *Characterisation of multicrystalline silicon solar cells; Development of characterization method for the combined effect of dislocations and grain boundaries on the minority carrier lifetime*, PhD thesis, NTNU (2004)

[15] R. Kvande, Incorporation of impurities during directional solidification of multicrystalline silicon for solar cells, PhD thesis, 2008

[16] Paul West, *Introduction to Atomic Force Microscopy: Theory, Practice, Applications*, AFM University (2006) (afmuniversity.org)

[17] G. Binning, C. F. Quate and C. Gerber, Phys. Rev. Lett. 56, 930 (1986)

[18] D. Rugar and P. Hansma, Physics Today, 31, (October 1990)

[19] Q. Zhong, D. Inniss, K. Kjoller and V. B Elings, Surface Sci. Lett. **290**, L688 (1993)

[20] *NanoScope Command Reference Manual*, DI/Veeco Metrology Group Inc (2001).

[21] ThermoNicolet, An introduction to Fourier Transform Infrared spectrometry, P/N 169-707500 2/01

[22] Substitutional carbon; ASTM, F1391.93

[23] Interstitial oxygen; ASTM F1188 93a

[24] R. A. Sinton, A Cuevas and M. Stuckings, Proc. 25th IEEE Photovoltaic specialists conference, p. 457 (1996)

[25] Stefan Rein, *Lifetime Spectroscopy: A Method of Defect Characterization in Silicon for Photovoltaic Applications*, Springer (2005)

[24] R. A. Sinton, A Cuevas and M. Stuckings, Proc. 25th IEEE Photovoltaic specialists conference, p. 457 (1996)

[26] M. Betti and L. Aldave de la Heras, Spectroscopy Europe **15/3**, 15(2003)

[27] J. W. Coburn, E. Taglauer and Eric Kay, J. Appl. Phys. **45**, 1779 (1974)

[28] T. Höchbauer, *On the mechanisms of hydrogen implantation induced silicon surface layer cleavage*, PhD thesis, Philipps-Universität Marburg (2001) and references therein

[29] C. A. Evans, *Thin Solid Films,* **19**, 11 (1973)

II. Papers

Part 1.

Studies of multicrystalline silicon grown from metallurgical feedstock

Paper 1

TEM studies of oxide and metal silicide precipitation on structural defects in multicrystalline silicon grown from metallurgical feedstock

(To be submitted)

Is not included due to copyright

Paper 2

EBIC, EBSD and TEM study of grain boundaries in multicrystalline silicon cast from metallurgical feedstock

(Proceedings of the 33rd IEEE Photovoltaic Specialists Conference, San Diego, USA, (2008))

EBIC, EBSD AND TEM STUDY OF GRAIN BOUNDARIES IN MULTICRYSTALLINE SILICON CAST FROM METALLURGICAL FEEDSTOCK

H. Nordmark[1], M. Di Sabatino[2], M. Acciarri[3], J. Libal[3], S. Binetti[3], E. J. Øvrelid[2], J. C. Walmsley[1, 2] and R. Holmestad[1]

[1]Dept of Physics, NTNU, NO-7491 Trondheim, Norway
[2] SINTEF Materials and Chemistry, NO-7465 Trondheim, Norway
[3] Universitá di Milano-Bicocca(UNIMIB), Dept. of Materials Science, via Cozzi 53, 20125 Milano, Italy

ABSTRACT

Grain boundaries in multicrystalline silicon material grown from metallurgical feedstock, were investigated in detail using Electron Beam Induced Current (EBIC), Electron Back-Scattered Diffraction (EBSD) and Transmission Electron Microscopy (TEM) techniques. The EBSD analysis showed that small angle grain boundaries, with misorientation angles lower than 2°, gave high EBIC contrast, i.e., high recombination activity. EBIC combined with TEM showed that at low temperatures, silicon oxide was found to be recombination centers both at grain boundaries and on decorated dislocations in the bulk. The grain boundaries containing multi-metallic silicides were found to have random misorientations and showed strong contrast in the EBIC image. Clean twins showed less or no contrast in the EBIC image. The metallic precipitates observed in the sample contain mainly nickel silicide with an iron rich core.

INTRODUCTION

More than 50% of the solar cells produced today are made from multicrystalline (mc) silicon. It is well known that mc silicon solar cells have lower efficiency than monocrystalline silicon solar cells because the higher levels of impurities and structural defects that are present act as recombination centers. From the literature [1-3], it is known that recombination activity depends on grain boundary character and contamination. While grain boundaries in clean samples show very low recombination activity, almost independent of misorientation and temperature, the recombination activity increases with contamination level. Random and high-Σ grain boundaries show stronger Electron Beam Induced Current (EBIC) contrast than low-Σ grain boundaries [1]. Small angle grain boundaries, with a tilt angle between 0 and 10° show weak EBIC contrast at room temperature and strong contrast at low temperature [2,3]. EBIC contrast has been found to decrease with increasing temperature, showing a minimum at 250 K, and then increase with further increase in temperature [4]. This temperature dependence has been attributed to two types of recombination processes; i) a shallow level associated with an inherent grain boundary structure and ii) a deep level associated with impurities segregated at grain boundaries [4]. In addition, irregularities like boundary steps, give contrast variation in the EBIC signal along grain boundaries [4]. The recombination activity of the grain boundaries is also found to vary with the ingot position. Grain boundaries in the top and bottom of an ingot showed strongest contrast due to their higher iron contamination level than the middle of the cast [5,6]. In iron contaminated samples, small angle grain boundaries show stronger contrast than low-Σ-grain boundaries and random grain boundaries, indicating that their boundary dislocation structures act as effective gettering sites for iron [2,3]. Combination of Electron Back-Scattered Diffraction (EBSD) and synchrotron–based analytical microprobe techniques have shown that metal silicide precipitates are most often detected in random grain boundaries [7]. Oxygen-related defects have weak recombination activity at 300 K, but become strongly active upon cooling to 80K [8]. Stacking faults, associated with oxide precipitates, were found to be recombination active only at temperatures below 100 K, while the bounding Frank partial dislocations were found to be active up to 20 K [9].

Ihlal et. al [10] studied, in 1994, copper contamination in a Si bicrystal by EBIC and Transmission Electron Microscopy (TEM) and found that the EBIC contrast was mainly attributable to Cu_3Si precipitates, although oxygen also had to be taken into account. The increase of the EBIC contrast with temperature and its nature, discontinuous or uniform, was found to be controlled by the precipitate density at the grain boundary [10]. Precipitate colonies containing the fast diffusing elements Ni and Fe, were found to be the origin of electrical activity in the grain boundary of a silicon bicrystal after annealing [11].

Transition metals are known to form silicides in silicon. During solidification of the cast, multi-metallic silicides form at high temperatures, while single-metallic silicides form at lower temperatures [12].

In the present work, defect-rich areas in mc silicon cast materials were studied in detail by use of EBIC, EBSD and TEM. EBIC was used to identify electrically active defects in the material, such as grain boundaries and dislocations. EBSD was used to determine grain orientations and grain boundary misorientation in the

same samples. To correlate the EBIC map with the microstructure, the samples had to be carefully thinned, and the grain boundaries examined in TEM. The type and nature of the precipitates observed in the grain boundaries was carefully examined by use of scanning TEM (STEM) in combination with x-ray Energy Dispersive Spectroscopy (EDS). The combination of EBIC, EBSD and TEM is a powerful tool in relating recombination activity with grain misorientation and contamination in the grain boundaries. Moreover, the combination of these techniques in a heavily contaminated material can give insight into the understanding of recombination processes at extended defects.

EXPERIMENTAL

Silicon was made by reduction of high purity quartz. The mc-Si ingot was produced in a directional solidification lab scale furnace with no further refining steps. No doping elements were added. The charge material was approximately 12 kg metallurgical poly-crystalline silicon, producing an ingot of 250 mm diameter and 100 mm height. The doping elements present (boron, phosphorous and aluminium) have different segregation coefficients, such that the solidified ingot was p-type in the bottom and n-type at the top 10 mm [13]. A 50x50 mm, small-grained, wafer positioned 25% from the bottom was cut into 10x10 mm samples. Resistivity in this ingot part was about 5 Ωcm.

For the EBIC measurements, a Tescan VEGA TS5136XM SEM with a tungsten filament was used. The beam current used allowed a measured current going through the wafer in the order of nA. Defect contrast was measured as $C = (I_b - I_d)/I_b$ where I_b is the bulk current and I_d is the current on the defect. In our set-up, the minimum contrast significantly measurable has been estimated to be close to 0.2% on polished samples. The resolution was limited to about 1 µm by the fixed working distance Z = 60 mm. The acceleration voltage used was 25 kV. The sample was cooled down to 90-100 K by use of liquid nitrogen before mapping. The EBIC samples were first mechanically and then chemically polished with CP4 (HF:HNO3:CH3COOH = 3:5:3 in volume ratio). Thereafter, Al Schottky contacts were realised by evaporating the metal under vacuum conditions of about 10^{-8} Pa.

The Hall mobility (ASTM F76-88) was determined at room temperature (magnetic field of 5000 Gauss) using van der Pauw geometry on samples already prepared for EBIC measurements. Ohmic contacts were obtained by depositing InGa past on the four sample corners. The Quasi Steady-State Photoconductance Decay (QSSPC) technique was used for lifetime determination. In order to reduce the recombination velocity of the charge carriers at the surface, the samples were passivated by an iodine ethanol (IE) solution.

Finally, the interstitial oxygen $[O]_i$ and substitutional carbon $[C]_s$ content was determined by Fourier Transform InfraRed (FTIR) spectroscopy in the 400-4000 cm^{-1} range, at room temperature (ASTM, F1391.93 ; ASTM F1188 93a).

To perform EBSD-analysis a Hitachi FE-SEM was used. The sample was tilted to 70 °C, the acceleration voltage used 20 kV and the working distance was 15 mm.

To make TEM samples, a 3 mm disc, from an area selected on the basis of EBIC and EBSD observations, was cut with ultrasonic disk cutter, ground, dimpled and ion milled with argon ions by use of a Gatan PIPS, until a small hole appeared close to the area of interest. The interesting area was carefully thinned using low voltage and low incidence angle. At an incidence angle of 2.5° and voltage of 2.5 kV milling from above, a milling rate of approximately 2-3 nm/minute was observed. A Phillips CM 30 TEM operating at 300 kV was used for low and medium resolution bright field imaging and a JEOL 2010F TEM microscope operating at 200 kV equipped with scanning TEM (STEM) and X-ray Energy Dispersive Spectroscopy (EDS) systems was used for the high resolution imaging and chemical analysis.

RESULTS AND DISCUSSION

The material analyzed in this study is characterized by low lifetime and low Hall mobility values, 1µs and 120 $eVcm^{-2}s^{-1}$, respectively. These poor electrical properties are consequence of defects and the high impurity density due to the use of a metallurgical feedstock. Both due to the feedstock used and to the small ingot dimension, high content of oxygen and carbon in respect to standard multicrystalline silicon was found ([O] = 23 ppma and [C] = 8 ppma). Information about defect nature came from microscopic analysis.

EBIC maps collected at room temperature and 90K are shown in figure 1. In these maps, highly recombination active defected areas (arrows) are clearly evident. Areas with dark EBIC contrast in the image, correspond to areas with high recombination activity. At 100 K, the EBIC contrast of the measured dislocations was typically around 20%, while the contrast in the most recombination active grain boundaries was typically 50-60%.

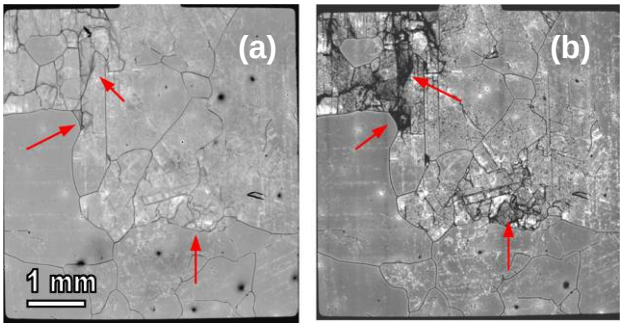

Fig. 1. EBIC maps collected at 300K (a) and 90K (b) showing recombination active defect areas (arrows).

In order to obtain more information about defects responsible of the low electronic material quality, EBIC and EBSD analysis were performed on the same area in the selected samples.

Figure 2 shows an EBIC map collected at 100 K (a), and a corresponding EBSD map, (b). The arrow to the dotted line points out a possible small angle grain boundary (< 2°) with high recombination activity observed in EBIC, not observed in the EBSD map where the grain boundary misorientation angle detection level was set to 2°. Σ3, Σ9 and Σ27 grain boundaries are marked on the map with black, red and green lines respectively. The other grain boundaries are randomly oriented. The misorientation angle is given in the figure for some of the boundaries.

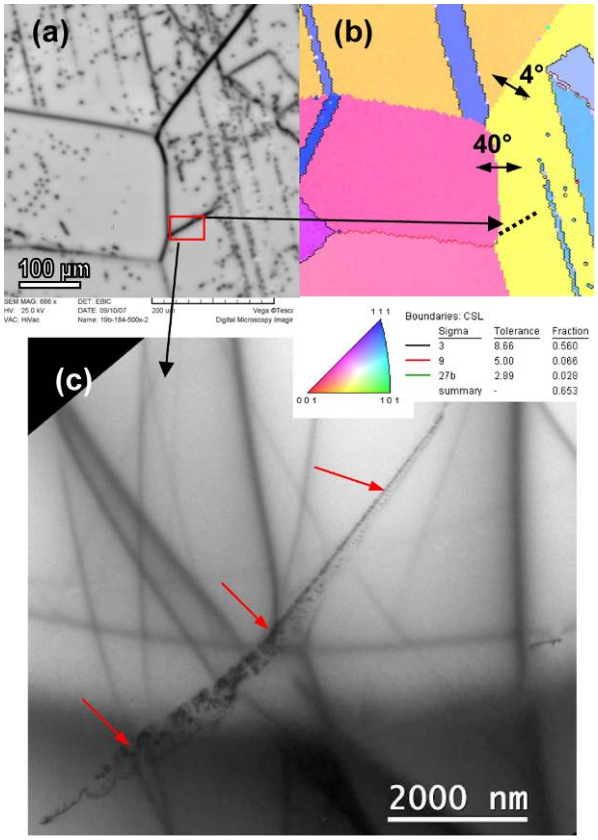

Fig. 2. EBIC, EBSD and TEM images from one area in the sample. 1(a) EBIC map at T = 100 K of the recombination activity of the extended defects in the selected sample. High contrast (dark) areas have high recombination activity, (b) EBSD map from the same area indicating grain orientation and grain boundary misorientation. Σ grain boundaries are indicated on the map, (c) The area from the rectangle in (a) shown in fine details in the TEM reveals a large climbing dislocation leaving oxide-precipitates in its path.

A TEM image from the area inside the red rectangle in the EBIC map is shown in Figure 2(c). The curved dark line running from the lower left corner towards the upper right corner is a climbing dislocation line (arrows). Other dark lines are bend contours in the sample. The dislocation, heavily contaminated with silicon oxide precipitates, correlates with the position of the small angle grain boundary in the EBIC map. Sub grain boundaries or very low angle grain boundaries, are known to consist of an array of dislocation lines. In the TEM sample only part of one dislocation line is present because the rest of the dislocation array was thinned away in the sample preparation process.

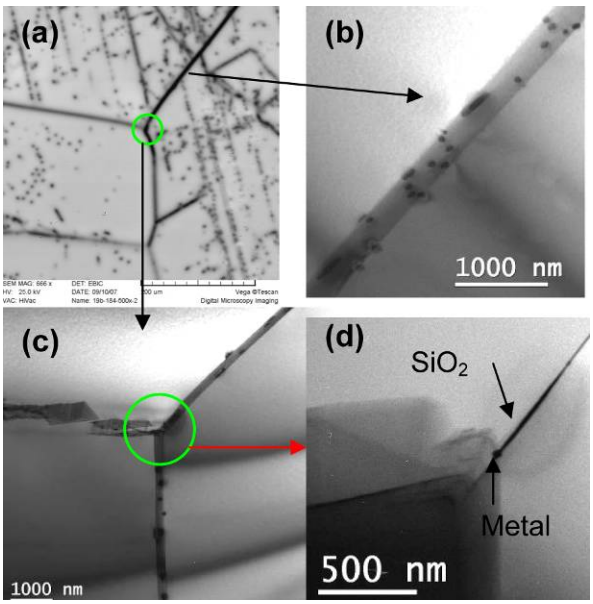

Fig. 3. EBIC with corresponding TEM images. (a) The same EBIC map as in figure 1. The green circle marks a triple point. (b) Numerous oxide precipitates were observed in the grain boundaries. c) Triple point enlarged. (d) A small metallic precipitate can be observed in the triple point nucleated nearby a SiO_2 precipitate.

The triple point encircled in Figure 3(a) was found to be particularly interesting because of a high contrast (dark) grain boundary meeting a lower contrast grain boundary from the left. It was assumed that the former might contain metallic silicides. Figure 3(c) and d) show this triple point in detail. As can be observed, both the upper and lower grain boundaries are heavily contaminated with oxides, while the stepped grain boundary at the left is less contaminated. The upper grain boundary from a thicker part of the sample is shown in Figure 3(b). All the dark features in the grain boundary are silicon oxide precipitates. In figure 3(d), a small metallic precipitate can be observed at the edge of a silicon oxide precipitate.

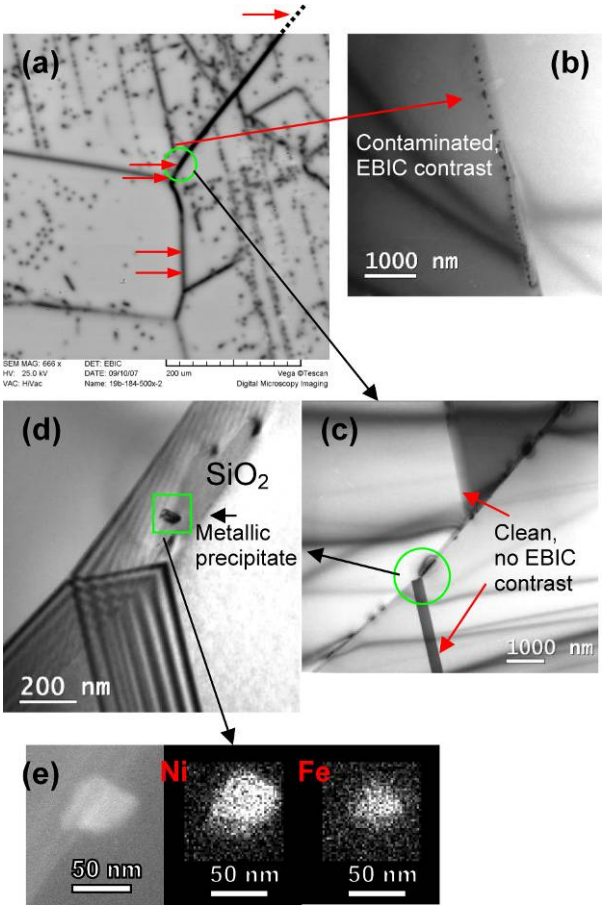

Fig. 4. (a) EBIC map of the selected area. The red arrows indicate positions of observed metal silicides, (b) Twin boundary heavily contaminated with oxides that showed moderate contrast in the EBIC map, (c) Enlarged image of the area inside the green circle in (a). Clean twins show no recombination activity in the EBIC map, (d) Enlarged TEM image of the grain boundary triple point, marked by a green circle in (c). A small metallic precipitate can be observed at the edge of a silicon oxide platelet, (e) EDS-maps of the metallic precipitate show that in addition to silicon, the precipitate contains mainly nickel, with an iron rich core.

Several metallic silicides were observed in the grain boundaries with strong EBIC contrast, as indicated in Figure 4(a) (red arrows). In Figure 4(b) a TEM-image of a contaminated part of the upper twin is shown. Figure (c) shows an enlarged image of the area inside the green circle in figure 4(a). Two twins are seen to initiate from the grain boundary. Since the twins are almost clean of impurities, no contrast can be observed in the EBIC image. Metallic precipitates were found only in random grain boundaries and small angle grain boundaries, most frequently in triple points. Close to the start of the lower twin, a small metallic precipitate is observed on the edge of a large silicon oxide precipitate (the area of uniform contrast in the grain boundary). EDS-mapping of the metal silicide is shown in Figure 4(e). The precipitate contains nickel and a lower level of iron, in addition to silicon.

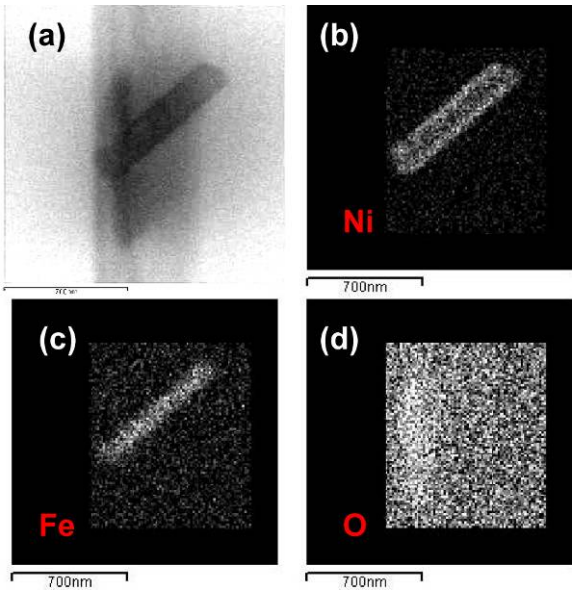

Fig. 5. (a) Bright field image of a rod shaped metallic silicide precipitate on an oxide platelet precipitate. EDS maps show that, in addition to silicon, the metallic precipitate contains mostly nickel (b) with an iron-rich core (c), nucleated at the edge of an oxide platelet precipitate (d).

All multi-metallic precipitates observed in the sample were found to consist of nickel silicide with an iron rich core. Because of the very low misfit of the $NiSi_2$ lattice with the silicon structure, only about 0.4 % [20], the precipitates are almost coherent with the silicon lattice. In Figure 5, a rod shaped metallic silicide is found to consist of an iron cylinder enclosed by nickel. At the edge of the precipitate the Fe/Ni ratio was found to be about 0.25, while in the core the ratio is about 1.6. The overall Fe/Ni ratio is about 0.60. Why the iron tends to cluster in the middle of the precipitate is still an open question. It is well known that iron has a high nucleation barrier in silicon and remains in solid solution, interstitially dissolved or as iron–boron complexes [14]. EBIC studies of iron contaminated samples have shown that grain boundaries and dislocations getter iron during annealing [2,3]. Shen et al. [15] studied the effect of iron contamination on oxygen precipitation in Czochralski silicon, where no iron silicide precipitates were observed in the contaminated samples by TEM. Still, EBIC measurements showed that the oxygen related defects were recombination active at room temperature, which indicates that they contained unprecipitated iron [15]. However, Buonassisi et al. [19] have reported that a certain annealing can promote iron

precipitation [19]. Furthermore, iron is found to form FeSi or $FeSi_2$ precipitates after iron contamination followed by slow cooling in a silicon bicrystal [5]. After rapid cooling, evidence for segregation of Fe is found by EBIC [5].

In this study no single iron silicide precipitates were observed, instead high concentrations of iron are detected in nickel rich precipitates or multi metallic silicides, consistent with other recent studies [12,15-18]. $NiSi_2$-precipitates seem to getter iron effectively. Multi-metallic silicides have reduced lattice mismatch and are therefore more stable and energetically favorable than single metals [16]. One possible explanation can be the liquid droplet theory [17]. The iron solubility in solid $NiSi_2$ is probably lower than in the liquid droplet, such that during solidification of the droplet, iron is segregated towards the middle of the precipitate, forming an iron rich core. Another explanation might be that only a small amount of iron atoms can fit into the $NiSi_2$ lattice. When the concentration increases above the solubility limit of iron in the $NiSi_2$ structure, iron starts clustering in the core of the precipitate. Instead of going to the edges like the copper nodules [12,16-18], iron' s high nucleation barrier in silicon, which probably is lowered in $NiSi_2$, forces it to cluster inside the $NiSi_2$ precipitate.

Figure 6 shows some of the oxide configurations observed in the sample. In Figure 6(a), a platelet SiO_2 precipitate is shown. This kind of precipitate was common in all grain boundaries except for Σ3 twin boundaries. The size varies from tens of nm to a few hundred nm, as shown in Figure 2(b). Figure 6(b) shows oxide precipitation in the bulk. In the upper left corner a climbing dislocation can be observed, leaving small oxide precipitates behind. In the lower right corner, a large bulk precipitate (arrow) can be observed. Dislocations initiate from the precipitate. The large volume expansion associated with forming an oxide can be released both by emitting silicon self interstitials and by initiating dislocations [22]. The small SiO_2 precipitates in the upper left corner that nucleated on a dislocation, emitted silicon self-interstitials while growing, resulting in climb of the dislocation. From the larger oxide in the lower right corner, dislocations are initiated because emitting silicon interstitials were not effective enough in removing the volume extraction [22]. Such dislocation clusters in the bulk or on twins/stacking faults most probably correspond to the medium dark contrast spots in the intragranular area of the EBIC map. In Figure 6(c) a twin structure is shown (Twins are marked by double arrows). All precipitates in the image including the rod shaped precipitate with darker features at its ends (blue arrow) in the upper right corner were found to contain oxygen.

In this study, all dislocations and most of the grain boundaries were found to contain silicon oxide precipitates. Only a few coherent twins and stacking faults were clean. Möller et. al. [21] found that oxygen precipitation is enhanced in mc silicon because of higher density of nucleation centers, compared to Cz silicon. Oxygen precipitates at dislocations and grain boundaries when there is sufficient time to diffuse to these defects [21]. Also transition metals can enhance oxygen precipitation in Cz silicon [15,22]. Probably all these factors together with the extremely high oxygen content observed in this material [17] are needed to explain the heavily oxide contamination observed.

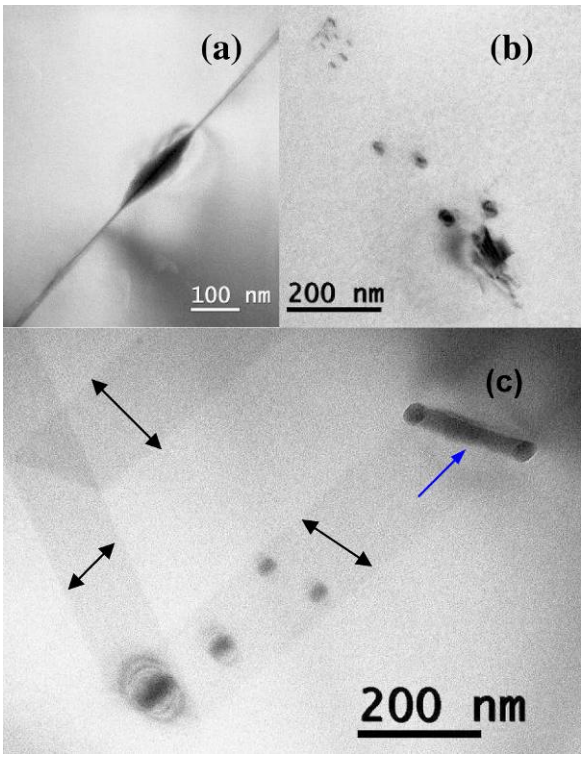

Fig. 6. SiO_2 precipitates in random grain boundary (a), dislocations (b), stacking fault/twin structure (c)

The results obtained in this study show that both oxides and metallic silicides are recombination centers at low temperatures. All the metallic precipitates were observed on small angle and random grain boundaries, consistent with Buonassisi [7] and Chen et al. [1-3]. Moreover, the results show that only a few metallic silicides were observed to be associated with oxide precipitates. EDS analysis did not detect any iron in the oxide precipitates. All observed precipitated iron was detected in Ni-rich precipitates. These results suggest that $NiSi_2$ seems to be the preferred gettering site for iron, rather than the oxide precipitates. Due to the TEM sample size limitation, only small volumes in thin samples could be studied. The EBIC contrast of grain boundaries is based on much thicker samples, several μm compared to ~ 0.5 μm for the thickest part of the TEM samples. Therefore, a higher number of precipitates contribute to the contrast in the EBIC map, compared to the observations done by TEM. However, this study gives an indication of the correlation between EBIC contrast and impurity level of the grain

boundaries and also shows the power in combining several characterization methods.

CONCLUSION

The combination of EBIC, EBSD and TEM has proven to be a very powerful tool in relating recombination activity with grain misorientation and precipitation of impurities at grain boundaries and dislocations. EBSD analysis showed that grain boundaries with misorientation angle lower than 5° gave high EBIC contrast, i.e., high recombination activity. At low temperatures, silicon oxide was found to be recombination centers both at grain boundaries and on decorated dislocations in the bulk. The grain boundaries that contained multi-metallic silicides were found to have random orientation and showed strong EBIC contrast. Clean twins showed no contrast in the EBIC image. STEM in combination with EDS mapping showed that most of the small metallic precipitates observed in addition to silicon, mainly contain nickel with iron rich core and small additions of copper and cobalt.

REFERENCES

[1] J. Chen, T. Sekiguchi, D. Yang, F. Yin, K. Kido and S. Tsurekawa, J. Appl. Phys. **96**, 5490 (2004)

[2] J. Chen, T. Sekiguchi, R. Xie, P. Ahmet, T. Chikyo, D. Yang, S. Ito and F. Yin, Scripta materialia **52,** 1211 (2005)

[3] J. Chen and T. Sekiguchi, Jpn. J. Appl. Phys. **46**, 6489 (2007)

[4] Z.-J. Wang, S. Tsurekawa, K. Ikeda, T. Sekiguchi and T. Watanabe, Interface Sci. **7**, 197 (1999)

[5] J. Chen, T. Sekiguchi, S. Nara and D. Yang, J. Phys.: Condens. Matter **16,** S211 (2004)

[6] M. Acciarri , S. Binetti , A. Le Donne, S. Marchionna, M. Vimercati, J. Libal, R Kopecek, K. Wambach Prog. Photovolt. Res. Appl. **15,** 375–386 (2007)

[7] T. Buonassisi, A. A. Istratov, M. D. Pickett, M. A. Marcus, T. F. Cizek and E. R. Weber, Appl. Phys. Lett. **89**, 042102 (2006)

[8] W. Seifert, M. Kittler and J. Vanhellemont, Matr. Sci. Eng. B **42**, 260-264 (1996)

[9] T. Sekiguchi, B. Chen, T. Watanabe and K. Sumino, Mat. Sci. Eng. B **42**, 235 (1996)

[10] A. Ihlal and G. Nouet, Phys. Stat. Sol. A, **141**, pp.81-92, (1994)

[11] J.-L Maurice and C. Colliex, Appl. Phys. Lett. **55**, pp 241-243 (1989)

[12] T. Buonassisi, M. Heuer, A. A. Istratov, M. D. Picett, M. A. Marcus, B. Lai, Z Cai, S. M. Heald, E. R. Weber, Acta Materialia, **55**, 6119-6126 (2007).

[13] M. Di Sabatino, S. Binetti, E. Øvrelid, J. Libal, M. Acciarri, Proceedings of the 22st European Photovoltaic Solar Energy Conference, pp (2007)

[14] D. MacDonald, T. Roth, L. J. Geerligs and A. Cuevas, Solid State Phenomena 1**08-109** (2005) 519-523

[15] B. Chen, J. Jablonski, T. Sekiguchi and K. Sumino, Jpn. J. Appl. Phys. **35**, 4187 (1996)

[16] M. Heuer, T. Buonassisi, A. A. Istraov, M. D. Pickett, M. A. Marcus, A. M. Minor and E. R. Weber, J. Appl. Phys. **101**, 123510 (2007)

[17] H. Nordmark, M. Di Sabatino, E. Øvrelid, J. C. Walmsley and R. Holmestad, submitted

[18] M. Heuer, T. Buonassisi, M. A. Marcus, A. A. Istraov, M. D. Pickett, Tomohiro Shibata and E. R. Weber, Phys. Rew. B **73**, 235204 (2006)

[19] T. Buonassisi, M. D. Pickett and R. Sveeney, NREL Workshop on crystalline silicon PV proceedings (2007)

[20] X. Portier and R. Rizk, Phys. Stat. Sol. A **155**, 125 (1996)

[21] H. J. Möller, L. Long, M. Werner and D. Yang, Phys. Stat. Sol. (a) **171**, 175 (1999)

[22] Z. Xi, D. Yang, J. Chen, J. Xu, Y. Ji, D. Que and H. J. Möller, Semicond. Sci. Technol. **19**, 299-305 (2004)

Paper 3

Study of defects and impurities in multicrystalline silicon grown from metallurgical silicon feedstock

(Accepted for publication in Materials Science and Engineering B)

Materials Science and Engineering B xxx (2008) xxx–xxx

Contents lists available at ScienceDirect

Materials Science and Engineering B

journal homepage: www.elsevier.com/locate/mseb

Study of defects and impurities in multicrystalline silicon grown from metallurgical silicon feedstock

S. Binetti[a,*], J. Libal[a], M. Acciarri[a], M. Di Sabatino[b], H. Nordmark[c], E.J. Øvrelid[b], J.C. Walmsley[b,c], R. Holmestad[c]

[a] University of Milano Bicocca, Department of Materials Science, via Cozzi 53, 20125 Milano, Italy
[b] SINTEF Materials and Chemistry, A. Getz v. 2B, 7465 Trondheim, Norway
[c] Department of Physics, NTNU, NO-7491 Trondheim, Norway

ARTICLE INFO

Article history:
Received 29 April 2008
Received in revised form 10 May 2008
Accepted 13 May 2008

Keywords:
Metallurgical silicon
Impurities
Gettering
Lifetime
EBIC
Photoluminescence

ABSTRACT

Nowadays the photovoltaic (PV) market suffers the severe shortage of silicon. One possible solution is to produce SoG-Si via a direct metallurgical route, followed by a final casting step. The use of such lower quality materials in solar cell production depends on the possibility of improving the electrical quality during the cell processing and requires a deep understanding of the interaction between defects. The aim of this work is to study the electrical properties and the minority charge carrier recombination behaviour of extended defects in a mc-Si ingot grown from metallurgical Si produced directly by carbothermic reduction of very pure quartz and carbon. The combined application of photoluminescence, infrared spectroscopy, electron beam induced current technique and transmission electron microscopy succeeded in identifying oxygen precipitates, decorated grain boundaries and dislocations as the defects which limit the quality of the metallurgical mc-Si and, therefore, the efficiency of the related solar cells.

1. Introduction

The increasing interest in renewable energy sources with a low environmental impact has given rise to a rapid growth of the photovoltaic (PV) industry. Up to now, the dominant semiconductor material used in PV is silicon and it is expected that silicon will play a fundamental role at least for the next decade. As the electronics sector recovers, and the requirements of the PV industry expand, there has been an increasing need for a dedicated supply of silicon. On the other hand, the severe shortage of the silicon used in the systems threatens to dampen the PV market's growth. Therefore, a new supply of solar grade silicon (SoG-Si) is crucial. One possible solution is to produce SoG-Si via a direct metallurgical route, followed by a final casting step. The metallurgical grade silicon made by direct reduction of quartz and carbon black is about 98.5% pure [1], i.e. a purity far from the 8 N pure silicon currently used in PV industry. The possibility of using such contaminated material in solar cell production depends on the following factors:

- using extra pure quartz in order to start with a higher quality material;
- improving the electrical quality during the cell processing;
- develop of new device process with less dependence on the quality of the material, i.e., on the diffusion length and on dopant/type.

The possibility of improving the electrical quality before or during the cell process requires a deep understanding of the type and concentration of impurity and defect, the presence of complex and cluster, the effect of impurity segregation process on the electrical activity of extended defects, as the solar cell efficiencies attainable with mc-solar grade Si are determined by all these material properties.

This work deals with a complete characterization of the electrical properties and the minority charge carrier recombination behaviour of extended defects in mc-Si ingots grown from metallurgical Si, produced directly by carbothermic reduction of very pure quartz and carbon without subsequent purification processes. The aim of the work is to test the feasibility of using such material in solar cell standard device process and to show how a combined application of different techniques succeeded in the identification of the nature of the defects which can limit the efficiency of the final solar cells.

* Corresponding author. Tel.: +39 0264485177; fax: +39 0264485400.
E-mail address: simona.binetti@unimib.it (S. Binetti).

0921-5107/$ – see front matter © 2008 Elsevier B.V. All rights reserved.
doi:10.1016/j.mseb.2008.05.013

Please cite this article in press as: S. Binetti, et al., Mater. Sci. Eng. B (2008), doi:10.1016/j.mseb.2008.05.013

2. Experimental details

The silicon feedstock used has been produced by direct reduction of extra pure quartz and carbon black. After tapping from the reduction furnace, the material was cooled down, etched and cleaned with DI water. The mc-Si ingot was made in a directional solidification lab scale furnace, without any subsequent purification processes. The resulting ingot (diameter 250 mm, height 120 mm, 12 kg) was cut into wafers after a single crystallization step. Details of the furnace and casting experiment were previously given [2]. The lifetime of minority carriers was determined using the quasi-steady-state photoconductance technique (QSSPC) [3]. Before measuring the as-grown samples have been subjected to a polishing etch containing HNO_3, HF and CH_3COOH and subsequent surface clean by H_2O_2:H_2SO_4 = 1:4, followed by an HF-Dip. The surfaces of the samples were passivated by an iodine ethanol (IE) solution [4].

The resistivity values were determined at various positions in each wafer and along the ingot height using the 4-point-probe technique [5]. The local recombination activity of extended defects was measured by EBIC at 300 K and down to 100 K. The photoluminescence (PL) spectra were recorded at 14 K with a spectral resolution of 6.6 nm. Details about sample preparation, PL and EBIC techniques are reported in [6]. Finally, the interstitial oxygen [O]i and substitutional carbon [C]s concentrations were measured by Fourier transform infrared (FTIR) spectroscopy [7]. The total oxygen concentration was carried out by inert gas fusion method by LECO [8]. In order to test the well-known gettering effect of the phosphorus diffusion step [9,10] on such solar grade silicon, a P-diffusion with $POCl_3$ in an open-tube furnace was carried out on different wafers. The doped regions were subsequently removed from the samples to carry out lifetime, EBIC and PL measurements. Transmission Electron Microscope (TEM) was used for the high resolution imaging and chemical analysis of precipitates. Experimental details in [11].

3. Results and discussion

Table 1 shows the main properties of the selected wafers from different heights of the ingot (where nr 1 indicates a wafer close to the top while nr 6 close to the bottom of the ingot). The minority carrier-lifetime values in the investigated material are much lower than in standard mc-Si, as one may expect due to a higher concentration of metallic impurities. According to the glow discharge mass spectrometry (GDMS) analysis Al and Fe concentrations were about 1.18 and 0.09 ppmw (at 88 mm from the bottom), respectively and the concentrations of other metallic elements such as Cu, Ni and Ti, were less than 50 ppbw [12,13]. As no doping elements were added during the solidification, and as the doping elements (B, Al, P) present have different segregation coefficient, the resulting ingot was n-type in a small fraction of the top and p-type in the bottom part of the ingot. As can be seen from Table 1, the interstitial oxygen concentration is higher than in a standard mc-Si [6,14]. The

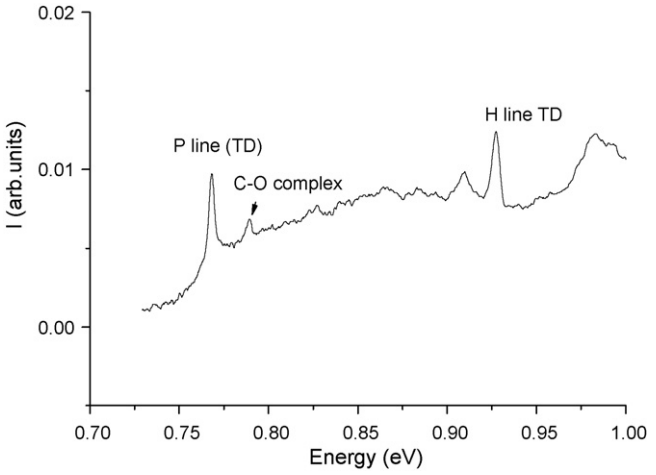

Fig. 1. Typical PL spectrum collected at T = 12 K and P = 6 W/cm^2.

LECO analysis carried out on the feedstock chunks revealed a total oxygen concentration of about 30 ppmw indicated that one of the major oxygen source is the feedstock itself. This can be explained, by an oxidation process that occurs during the tapping into vessel of the liquid silicon, carried out in air and at high temperature. As the tapping is a discontinuous process, silicon dioxide interface layers can be formed in silicon, becoming an oxygen source during the solidification process.

A typical PL spectrum of the as-grown samples, in the low energy range, is plotted in Fig. 1 and it shows the presence of a peak at approximately 0.77 eV, usually labeled as P line, together with two signals at approximately 0.91 and 0.93 eV, respectively (labeled as H lines) [15,16]. These lines are related to the presence of C–O complex and nuclei of SiO_x, known as old thermal donors (OTD). As the P line luminescence should be related to a transition from a thermal donors (TD) bound excitation level to a deep level corresponding to the C–O complexes [17,18] it could be responsible for a decrease of the minority carrier-lifetime. Evidence was given that thermal donors decrease the minority charge carrier-lifetime in solar grade monocrystalline silicon [14]. While the PL analysis revealed the presence of silicon dioxide nuclei, the presence of silicon dioxide precipitates have been identified by TEM analysis. SiO_2 precipitates were commonly observed in grain boundaries and almost all dislocations were heavily decorated by oxygen precipitates as shown in Fig. 2.

From the EBIC measurements (see Fig. 3), it is evident that, independently by the ingot position, the material is characterised by a high density of active extended defects also at room temperature. In the EBIC maps at 300 K, "bright" denuded zone at GBs are easily visible. This effect is typical of high-contaminated materials and it is due to segregation of metallic impurities at defects [19,20]. Even though the EBIC measurements have no statistical meaning, as the maps are performed on small selected areas of each sample, we

Table 1
Sample designations, positions of the wafers in the ingot, resistivity, lifetime, interstitial oxygen and substitutional carbon concentration

Wafer#	Position from bottom (mm)	Resistivity (Ω cm)		Lifetime (μs)	O_i (ppma)	C_s (ppma)
6-2	16	3.9 (±1.6)	p	1	23.1 (±1.3)	4 (±0.3)
5-2	28	4.6 (±1.6)	p	1	25 (±1.4)	4 (±1.7)
4-2	40	4.2 (±2.5)	p	0.9	27.2 (±2.6)	10 (±0.5)
3-2	52	3.6 (±1.8)	p	1.1	25.6 (±4)	8.8 (±1.6)
2-2	64	4.4 (±3.1)	p	1	24.8 (±3)	7.6 (±2)
1-2	76	4.5 (±4.4)	n	3.2	25 (±3)	12 (±2)

The high standard deviation of average resistivity values measured on different points into a single wafers are related to grain boundaries effect. Lifetime values have been calculated with an excess carriers density between 7×10^{13} and 5×10^{14} cm^{-3}. Note that numerical designations are used in the text and figures.

Please cite this article in press as: S. Binetti, et al., Mater. Sci. Eng. B (2008), doi:10.1016/j.mseb.2008.05.013

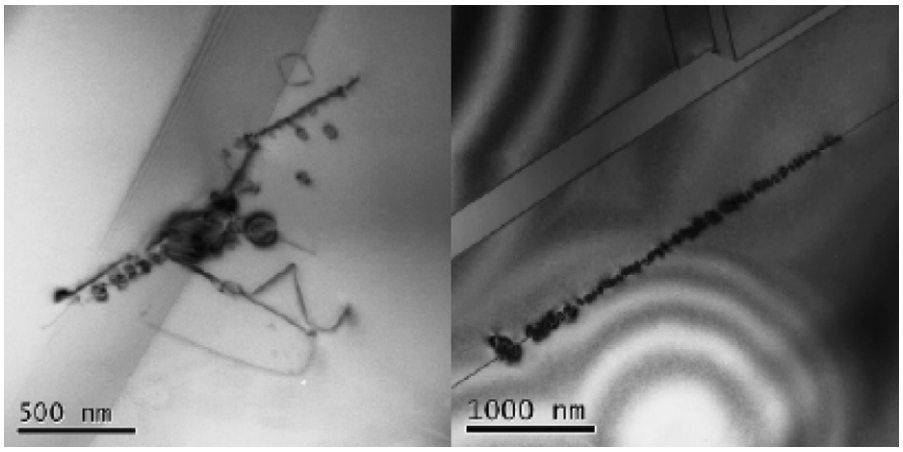

Fig. 2. SiO_2 precipitates located on a dislocation in a grain boundary (left) and SiO_2 platelets edge on in a twin boundary (right).

saw that the density of bright spots is higher in the top part of the ingots. Furthermore, the average EBIC contrast measured is relatively high (about 30% at RT) and can be also due to the presence of metallic precipitates, confirmed by TEM analysis carried out on the same material [21]. The presence of precipitates is confirmed by the behaviour of contrast versus *T*: at low temperature the GBs contrast slightly decreases (at about 20%). This effect has been explained on the basis of the Shockley–Read–Hall theory [20] with the presence of a high density of deep levels at the GBs as a consequences of metallic decoration and precipitation.

The effect of the P-diffusion step on the lifetime is reported in Fig. 4. It could be observed that an increase was obtained only for the top part of the ingot. The non-increase of lifetime in other part of the ingot is related to a non-sufficient effectiveness of gettering P-diffusion step on these wafers. As the type of metallic impurities is the same along the ingot, this can be only due to a difference in

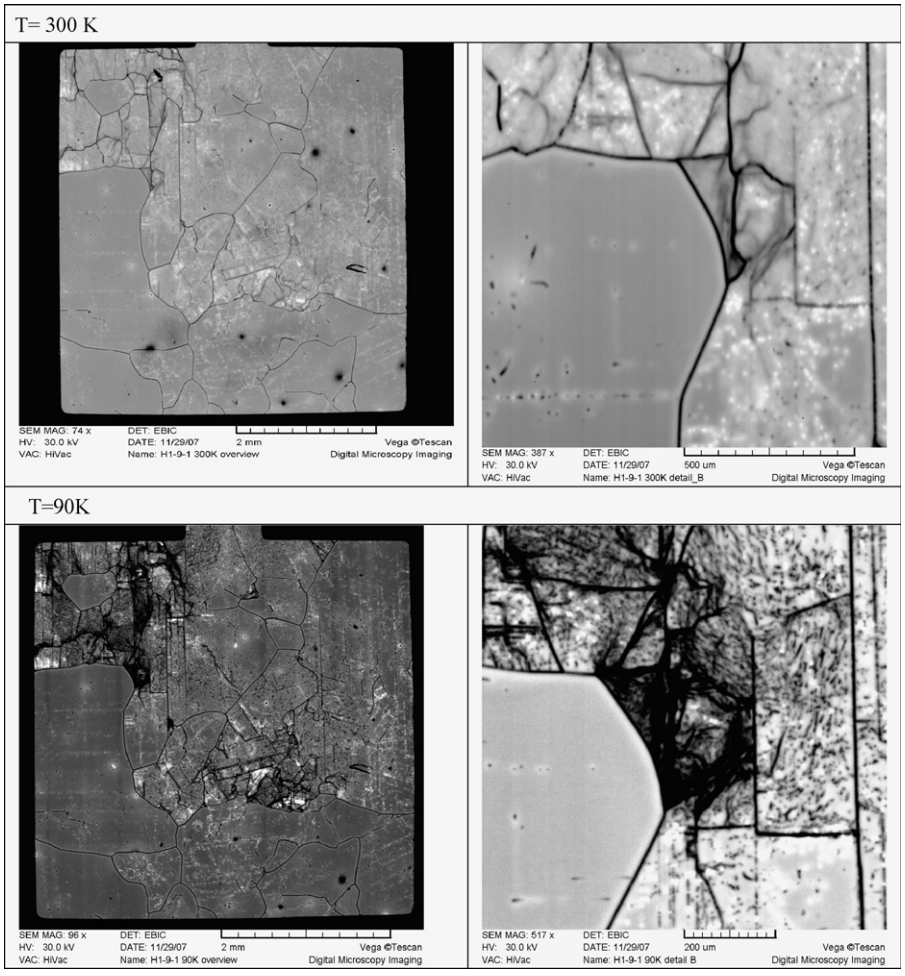

Fig. 3. Low magnification EBIC maps collected at 300 and 90 K for sample #2-2 (left) and high magnification EBIC maps collected at 300 and 90 K for the same sample (right).

Please cite this article in press as: S. Binetti, et al., Mater. Sci. Eng. B (2008), doi:10.1016/j.mseb.2008.05.013

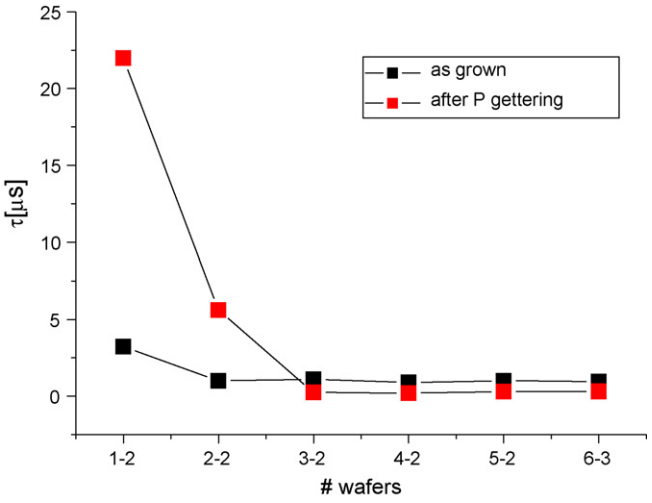

Fig. 4. Change in lifetime along the ingot due to the solar cell processing steps of P-diffusion (sample #1-2 is n-type).

concentration or a difference in extended defects density. The difference in concentration of metallic impurities along the ingot can explain the higher improvement of the top part as already observed in literature but not the constant low lifetime from wafer #3.2 to the bottom part of the ingot. On the one hand, EBSD measurements showed that the grains in the top of the ingot (1-3 to 3-3) are rather large (≈5–20 mm) whereas they are small in the bottom of the ingot (sample 4-3 to 6-3, <1 mm), however, it is not small enough to limit the lifetime to the low values found in these samples after P-gettering. However, EBIC measurements on this material showed that often small grains feature a much higher dislocation density than larger grains do. This problem will be certainly resolved when growing industrial size ingot.

On the other hand, the PL spectra on gettered sample indicate a disappearance of bands associated to nuclei of precipitates, but the interstitial oxygen concentration does not increase indicating the formation of precipitates during the P-diffusion.

According to EBIC, TEM and PL results, it can be inferred that, besides a high dislocation density in the bottom part of the ingot, the main factor responsible of the low quality wafers after the gettering is the presence of high density of oxygen precipitates sometimes decorated with metals. This confirms also that the impurities present in the form of precipitates (oxides and silicides) can not be gettered out by P-diffusion step as already observed in [22].

4. Conclusions

An important aspect pointed out by this work is that the presence of a high oxygen concentration, should be taken into account when using such solar grade silicon for solar cell production. The presence of silicon dioxide precipitates should be avoided. First of all because they show strong recombination activity as verified in monocrystalline silicon [23] but mainly because they can act as internal gettering sink during the solidification step and device processes. The possibility of using solar grade silicon directly solidified from metallurgical one is not so far and depends mainly on the control of the precipitation process during crystallization (i.e. optimizing the temperature profiles) and on post-solidification annealing able to reduce the density of oxygen or oxygen-containing defect centres. The dissolved metallic impurities are largely getterable by a P-diffusion step and are, therefore, not so harmful for the electrical properties of the material at the end of the solar cell process. PC1D simulations [24] using the carrier-lifetimes measured in wafer #1-2 and # 2-2 after gettering showed that solar cell with efficiency of 12.4 and 13.9%, respectively, could be obtained. Taking into account the high actual cost of Si feedstock which leads to a contribution of up to 60% to the total module cost, the solar cell manufacturers are forced to make a compromise between cost and performance. Consequently, obtaining efficiencies around 12% with a pure metallurgical silicon could be acceptable.

Acknowledgments

The authors thank Thomas Buck for having performed $POCl_3$ diffusion. The financial support of EU project FOXY (contract number 019811) is gratefully acknowledged.

References

[1] B. Ceccaroli, O. Lohne, in: A. Luque, S. Hegedus (Eds.), Handbook of Photovoltaic Science and Engineering, John Wiley & Sons, England, 2003, pp. 153–204.
[2] E.A. Meese, E.J. Øvrelid, H. Laux, M. M'Hamdi, Proceedings of the 20th European Photovoltaic Solar Energy Conference, 2005, pp. 909–913.
[3] R.A. Sinton, A. Cuevas, M. Stuckings, Proceedings of the 25th IEEE Photovoltaic Specialists Conference, 1996, pp. 457–460.
[4] T.S. Horányi, T. Pavelka und, P. Tüttö, Appl. Surf. Sci. 63 (1993) 306–311.
[5] ASTM F43-93, 1996.
[6] M. Acciarri, S. Binetti, A. Le Donne, S. Marchionna, M. Vimercati, J. Libal, R. Kopecek, K. Wambach, Prog. Photovolt. Res. Appl. 15 (2007) 375–386.
[7] ASTM, F1391.93; ASTM F1188 93a.
[8] LECO Corporation, Application Bulletin (1991).
[9] I. Perichaud, Sol. Energy Mater. Sol. Cells 72 (2002) 315–326.
[10] M. Sheoran, A. Upadhyaya, A. Rohatgi, Solid State Electron. 52 (2008) 612–617.
[11] H. Nordmark, M. Di Sabatino, E.J. Øvrelid, J.C. Walmsley, R. Holmestad, Proceedings of the 22th European Photovoltaic Solar Energy Conference, vol. I, 2007, pp. 1710–1714.
[12] M. Di Sabatino, A.L. Dons, J. Hinrichs, O. Lohne, L. Arnberg, Proceedings of the 22nd European Photovoltaic Solar Energy Conference, 2007, pp. 271–275.
[13] M. Di Sabatino, S. Binetti, E.J. Øvrelid, M. Acciarri, J. Libal, Proceedings of the 22nd European Photovoltaic Solar Energy Conference, 2007, pp. 883–888.
[14] C. Hassler, H.U. Hofs, W. Koch, G. Stollwerck, A. Muller, D. Karg, G. Pensl, Mater. Sci. Eng. B 71 (2000) 39–46.
[15] G. Davies, Phys. Rep. 176 (1989) 83–188.
[16] W. Kürner, R. Sauer, A. Dornen, K. Thonke, Phys. Rev. B 39 (1989) 13327–13337.
[17] S. Pizzini, S. Binetti, E. Leoni, A. Le Donne, M. Acciarri, A. Castaldini, MRS Symp. Proc. 692 (2002) 275–281.
[18] J. Weber, H.J. Queisser, MRS Symp. Proc. 59 (1986) 147–152.
[19] M. Kittler, W. Seifert, Mater. Sci. Eng. B42 (1996) 8–13.
[20] J. Chen, T. Sekiguchi, D. Yang, F. Yin, K. Kido, S. Tsurekawa, J. Appl. Phys. 96 (2004) 5490–5495.
[21] H. Nordmark, M. Di Sabatino, M. Acciarri, J. Libal, S. Binetti, E.J. Øvrelid, J.C. Walmsley, R. Holmestad, Proceedings of the 33rd IEEE Photovoltaic Specialists Conference, 2008, in press.
[22] M. Sheoran, A. Upadhyaya, A. Rohatagi, Solid State Electron. 52 (2008) 612–617.
[23] A. Borghesi, B. Pivac, A. Sassella, A. Stella, J. Appl. Phys. 77 (1995) 4169–4244.
[24] P. Basore, P.D.A. Clugston, PC1D v.5.9, University of New South Wales (2003).

Please cite this article in press as: S. Binetti, et al., Mater. Sci. Eng. B (2008), doi:10.1016/j.mseb.2008.05.013

Part 2.

Studies of hydrogen defect formation in silicon

Paper 4

Evolution of hydrogen induced defects during annealing of plasma treated Czochralski silicon

(*Nuclear Instruments and Methods in Physics Research B* ***253****, p 176-181 (2006))*

Available online at www.sciencedirect.com
ScienceDirect
Nuclear Instruments and Methods in Physics Research B 253 (2006) 176–181
NIM B
Beam Interactions with Materials & Atoms
www.elsevier.com/locate/nimb

Evolution of hydrogen induced defects during annealing of plasma treated Czochralski silicon

Heidi Nordmark [a,*], Alexander Ulyashin [b], John C. Walmsley [a,c], Bård Tøtdal [a], Randi Holmestad [a]

[a] Department of Physics, NTNU, N-7491 Trondheim, Norway
[b] Department of Physics, University of Oslo, N-0316 Oslo, Norway
[c] SINTEF Materials and Chemistry, N-7465 Trondheim, Norway

Available online 7 November 2006

Abstract

Transmission electron microscopy (TEM) and atomic force microscopy (AFM) are used to study the temperature evolution of hydrogen plasma induced defects in silicon. Hydrogen plasma treated n- and p-doped Czochralski silicon samples were annealed at temperatures between 200 and 1000 °C for up to 10 h in air. Platelets are formed on {1 1 1} and {1 0 0} crystallographic planes. The structural defects are similar in n-type and p-type material. Small defects at the surface anneal out at temperatures above 400 °C and {1 1 1} platelets start to dissolve above 500 °C, except in highly p-doped samples where the platelets are stable up to 600 °C. The hydrogen penetrates deeper into a low doped than a high doped sample, resulting in platelet formation deeper into the sample. At annealing temperatures above 800 °C, an amorphous oxide layer forms at the surface of the sample. New platelets form after 1 h annealing at 1000 °C. The roughest surface is found in highly n-doped samples, hydrogenated at high plasma frequency for long exposure times. For high annealing temperatures the roughness decreases.

PACS: 61.72.Tt; 61.72.Qq; 61.72.Nn

Keywords: TEM; AFM; Hydrogen; Silicon

1. Introduction

The behaviour of hydrogen in silicon has been studied intensively for more than 20 years, motivated in particular by its ability to provide: (i) suppressing carrier traps by passivation of dangling bonds and (ii) thin Si layer "hydrogen knife" exfoliation [1]. It has been shown recently that a combination of low dose implantation and hydrogenation can be used instead of high dose hydrogen implantation to achieve exfoliation of thin Si layers [2,3]. In these processes hydrogen causes the formation of extended structural defects in the Si lattice, stacking faults, dislocation loops, hydrogen bubbles and platelets. Such defects are not desirable imperfections in the Si bulk, but they are responsible for the hydrogen initiated exfoliation process, caused by the growth and coalescence of these defects into cracks. It is well established that heavy hydrogenation of un-implanted Si also leads to the formation of structural defects [4,5].

The structural defects introduced by hydrogen depend on the type of silicon, conductivity, doping level and hydrogenation conditions [6]. While much work has already been done on hydrogenated Czochralski (Cz) silicon [2,4,5,7–9], a systematic investigation of the temperature evolution of hydrogen initiated structural defects is lacking. In particular, it is important to investigate the influence of the doping level, type of doping, plasma frequency and the time of hydrogenation on defect formation.

* Corresponding author. Tel.: +47 73593198; fax: +47 73597710.
E-mail address: heidi.nordmark@ntnu.no (H. Nordmark).

0168-583X/$ - see front matter © 2006 Elsevier B.V. All rights reserved.
doi:10.1016/j.nimb.2006.10.043

The purpose of such investigations is to accumulate knowledge concerning the formation and evolution of H-related defects. In this paper TEM and AFM are used to study the formation and temperature evolution of hydrogen plasma induced structural defects in n- and p-doped Cz silicon samples, which have different doping levels.

2. Experimental

Phosphorus-doped n-type and boron-doped p-type [0 0 1]-oriented Cz silicon wafers with resistivities: (i) 1.8–2.6 Ω cm and 0.005–0.018 Ω cm for the n-type and (ii) 1–10 Ω cm and 10–20 Ω cm for the p-type silicon were used. Table 1 shows the sample processing details.

Hydrogen plasma treatments of all wafers were done in a plasma enhanced chemical vapor deposition (PECVD) setup for between 0.5 and 2 h at a frequency of 13.56 or 110 MHz, a power of 50 W and a hydrogen flux of 200 sccm. The wafer temperature was ~250 °C. Subsequent annealing was performed on ~1 × 1 cm samples at temperatures between 200 and 1000 °C for 1 and 10 h in a furnace in air followed by a rapid cooling.

A cross-section sample was prepared for TEM study from each annealing condition. The samples were prepared by mechanical polishing down to a thickness of about 10 μm in the middle of the 3 mm disk and thinned to electron transparency using a Gatan PIPS ion mill. The TEM-observations were performed using a Phillips CM30 operating at 300 kV or a JEOL 2010 F operating at 200 kV. The cross-section direction used for observations was (1 1 0).

The surface morphology of Si samples was analyzed by AFM using a Digital Instrument Nanoscope Dim 3100 microscope. The AFM-measurements were performed in tapping mode using commercial silicon tips (MikroMasch NSC35/AlBS) with a typical tip curvature radius of less than 10 nm.

3. Results and discussion

A summary of the TEM- and AFM-observations is given in Tables 2 and 3. The mean platelet diameter is seen to increase with temperature for most samples. The increase in diameter is mostly due to the smallest platelets dissolving. Formation depth is given as the deepest platelet location found in the investigated samples. It is found to be largest and increase slightly for low doped samples, S1 and S5, while being almost constant for high doped samples, S2 and S4. The density, only given qualitatively, was found to decrease for all samples at temperatures above 400 °C. The Roughness (R_q) gives the root mean square average of height deviations taken from the mean data plane within a given area [10]. The roughness is seen to decrease for all samples at high annealing temperatures.

Fig. 1(a)–(c) show the microstructure in S5, S2 and S3. Note the difference in scale between the pictures. At the surface, a plasma defect layer of about 100 nm thickness can be observed in all samples. The damage layer consists of differently sized pyramids and other defects like stacking faults, hydrogen induced platelets and dislocation loops. The pyramidal surface morphology is due to the direct plasma beam etching and is most prominent where the platelets intersect the surface [12]. Most of the platelets are formed in the subsurface layer. All five samples contain both {1 1 1} and {1 0 0} platelets, but the {1 1 1} platelets

Table 1
Processing parameters and plasma treatment of the samples

Sample label	Doping		Hydrogen plasma treatment			
	Type	Resistivity (Ω cm)	Time (h)	Temperature (°C)	Power (W)	Frequency (MHz)
S1	n	1.8–2.6	1	250	50	110
S2	n	0.005–0.018	1	250	50	110
S3	n	1.8–2.6	2	250	50	13.56
S4	p	1–10	0.5	250	50	110
S5	p	10–20	1	250	50	110

Table 3
Roughness found by AFM-measurements

Sample	Roughness R_q (nm) in 1 × 1 μm samples				
	As-exposed	500 °C/1 h	500 °C/10 h	600 °C/1 h	800 °C/1 h
S1	10.81	44.31	25.59	20.72	26.37
S2	25.93	33.49	27.47	16.29	31.15
S3	7.73	6.59	1.51	1.18	0.93
S4	12.53	7.14	6.98	7.94	9.13
S5	6.77	10.52	11.52	7.08	6.33

Table 2
Mean platelet diameter, deepest platelet formation depth and density in the samples observed by TEM

Sample	Diameter (nm)			Formation depth (μm)			Density		
	RT	400 °C	500 °C	RT	400 °C	500 °C	RT	400 °C	500 °C
S1	80	205	440 (large) 170 (small)	3	4.4	6	Low	Low	Low
S2	500 (large) 40 (small)	143	200	1.5	1.7	1.1	Low	Low	Low
S3	16	18	20	0.5	0.3	0.4	High	Medium	Low
S4	125	108	175	0.5	0.5	0.55	Medium	Medium	Medium
S5	95	90	85	1.7	2.7	2	Low	Low	Low

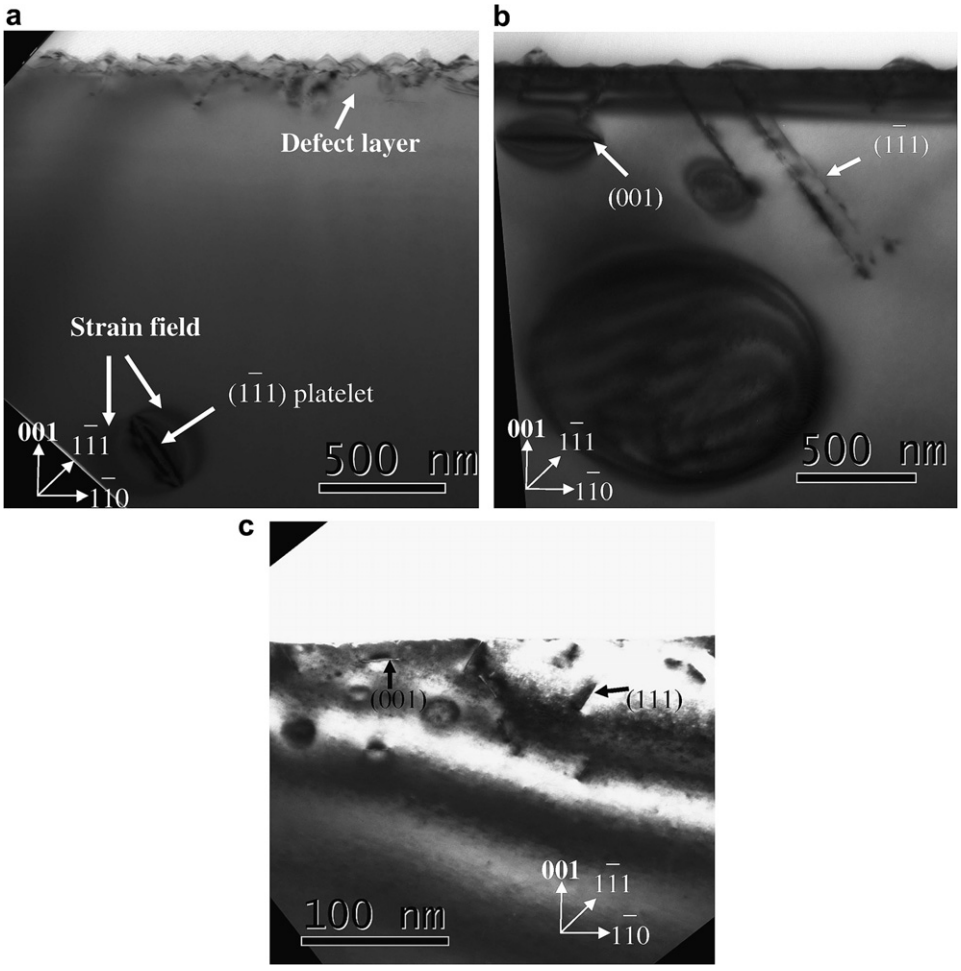

Fig. 1. TEM images showing the defects in low temperature annealed samples. (a) Direct plasma surface layer and a large platelet, ~300 nm, formed deep into S5, ~2 μm. (b) Defects and large platelets formed in S2. (c) High density of small platelets, ~ 20 nm, formed close to the surface, ~0.4 μm, in S3, annealed at 400 °C for 10 h.

dominate significantly, as expected for hydrogenated samples [11].

Fig. 1(a) shows low p-doped S5. A large platelet, ~0.3 μm, is formed deep into the silicon. Low n-doped S1 is similar, except for higher density of platelets formed deep into the silicon, up to 6.5 μm from the surface. At the surface a damage layer containing stacking faults, dislocations and small platelets is found. Fig. 1(b) shows high n-doped S2, with platelets up to 1.5 μm in diameter, extending ~2 μm into the wafer. High p-doped S4 is similar, except that the platelets are smaller, ~100–500 nm, and form up to 0.5 μm into the wafer.

S3 contains a high density of small platelets and other defects, ~20 nm, formed up to a depth of 0.5 μm from the surface, as illustrated in Fig. 1(c). The density is largest at the surface and decreases gradually with depth.

Fig. 2(a) shows an AFM surface topography plot of S2 after plasma exposure. A pyramidal surface morphology is very clearly. The surface of S1 and S5 has almost the same morphology. Fig. 2(b) shows an AFM-picture from S3. S4 is similar. The surface shape does not change much during annealing, although Table 3 shows that the roughness generally decrease with temperature and annealing time for most samples.

From the images in Figs. 1 and 2, together with Table 2 and 3, it is seen that in the low doped S1 and S5 the hydrogen penetrates further into the samples than in the higher doped samples S2 and S4. The platelet density is expected to be higher in p-doped than in n-doped material [4], but it is hard to see any difference in the investigated samples. It is well known that hydrogen can interact with dopants, creating boron–hydrogen and phosphorous–hydrogen species, that are stable up to 160 °C [6]. This is the probable reason that hydrogen penetrates less in the highly doped samples. Longer hydrogen plasma exposure times lead to growth of the platelets and reduction of hydrogen diffusivity [7]. Large platelets grow faster than small ones [7]. The double plasma exposure time is probably one of the main reasons that the platelets are larger in S2 than in S4. The very small platelets found in S3 compared to S1 must be due to the much lower plasma frequency used for this sample since the other parameters are the same. The surface of S3 is less etched by the less energetic hydrogen plasma that contains fewer monoatomic species, despite the longer exposure time. The short plasma

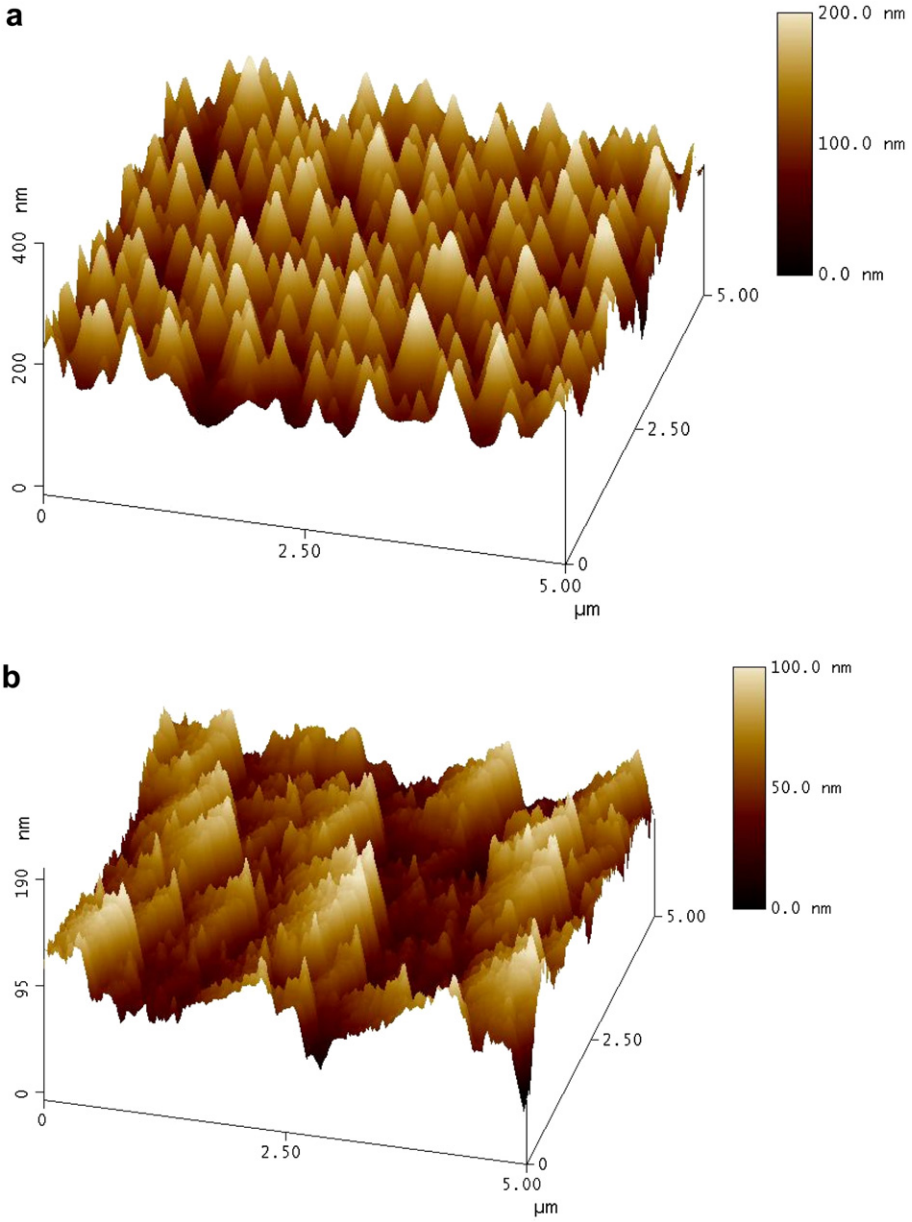

Fig. 2. AFM-pictures showing the pyramidal surface structure of the plasma etched wafers. (a) Surface structure of S2 before annealing, having the most prominent pyramids. S1 and S5 have almost similar structure, (b) The less etched surface of S3 before annealing.

exposure time of S4 is probably the reason for the similarity between the surface morphology of S3 and S4. Surface pyramids were most prominent in the highly doped S2. Earlier experiments also found that the roughness depends on the doping and orientation of the substrate [5], as well as the plasma frequency [12].

The microstructure in all samples is stable up to 400 °C. At 500 °C the smallest defects in the surface damage layer of the samples disappear, probably due to Ostwald ripening. In S3, the density decreases above 400 °C, and the small platelets deepest into the sample disappear. Earlier experiments on similar materials, have shown that the hydrogen in the plasma surface damage layer is stable up to 400 °C [9].

At 600 °C almost all {1 1 1} platelets start to dissolve in all samples, except for S4. Fig. 3(a) shows partly dissolved {1 1 1} platelets and unchanged {1 0 0} platelets in S5. Almost all platelets in S3 are annealed out. Fig. 3(b) shows a circular partly dissolved platelet in S1 annealed at 800 °C for 1 h. The circular platelets formed deep into the material are replaced by dislocation loops, containing voids that grow due to Ostwald ripening [13], while the defects formed close to the surface transform into dislocation loops, small blisters, or collapse into a ring of small circular defects. The low density {1 0 0} platelets are unchanged to over 600 °C. Earlier experiments have shown that below 500 °C the {1 1 1} platelets dominate, while above 500 °C the {1 0 0}

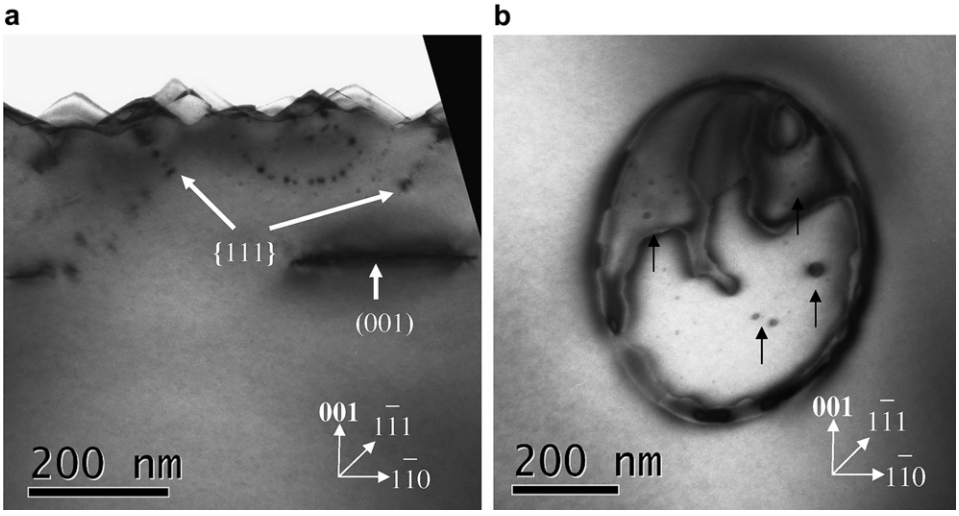

Fig. 3. (a) Stable (1 0 0) platelets parallel to the surface and partly dissolved (1 1 1) platelets in S5 annealed for 10 h at 600 °C. (b) Partly dissolved platelet in S1 annealed for 800 °C for 1 h. Notice the small voids (arrows) inside the platelet and the boundary dislocations.

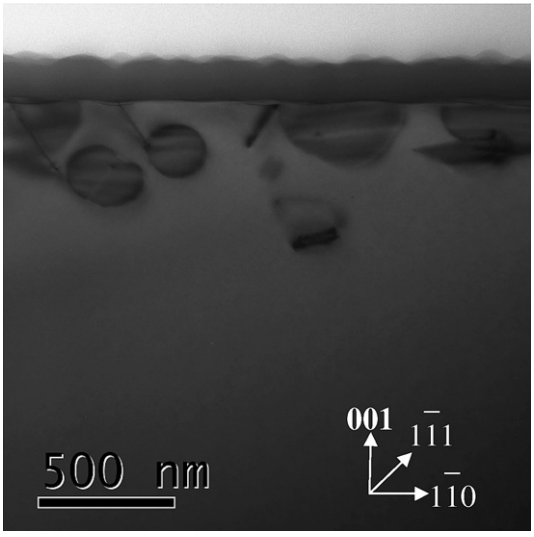

Fig. 4. New platelets formed in S4, annealed at 1000 °C for 1 h. Notice the thick oxide layer formed at the surface.

platelets dominate [4]. Hydrogen in n-type silicon is less stable than in p-type silicon [4]. This is probably the reason for the total dissolution of the small platelets in the n-doped S3. This can also explain the stable platelets in S4, which is highly p-doped. Earlier Raman experiments have also shown that the surface plasma damage layer mostly consists of Si–H bonding, while the H_2 molecules mostly are found in the subsurface or platelet layer [9]. The Si–H bonds are released at temperatures above 400 °C. H_2 molecules are released after 10 min annealing at 600 °C leaving empty voids [9]. After 1 h annealing at 700 °C also the {1 1 1} platelets in S4 start to dissolve. At 800 °C the partly dissolved defects are still visible in all samples except S3.

After 1 h annealing at 1000 °C in air, a blue amorphous oxide layer has formed at the surface of the samples, and new defects have formed. Fig. 4 shows new platelets formed in S4 annealed for 1 h at 1000 °C with a similar microstructure as in Fig. 1(a)–(c). In S1 (picture not shown here), the new defects form within ~0.5 μm from the surface, while the platelets formed deep into S1 are still partly dissolved. Oxygen from the surface is likely to have diffused into the silicon, forming SiO_2 defects. Further investigation is needed to confirm this.

4. Conclusion

The temperature evolution of hydrogen plasma induced structural defects of hydrogen plasma treated (~250 °C) n- and p-doped Cz silicon samples with various type of doping, doping level, plasma frequency and hydrogenation time have been studied. In low doped samples, defects were found to form deeper than for highly doped samples. Platelets formed deep into the sample were found to be more stable than platelets formed close to the surface. The defects in highly p-doped samples were found to be the most stable at elevated temperatures. The plasma frequencies and hydrogenation time are important factors for determining the size and formation depth of the platelets. Low plasma frequency and short hydrogenation times form small platelets and other defects close to the surface. The mean platelet diameter increases and the density decreases at elevated temperatures due to Ostwald ripening. The dominating {1 1 1} platelets start to dissolve at 500 °C. The low density {1 0 0} platelets are stable to temperatures above 600 °C. The smallest platelets, <50 nm, close to the surface, start to disappear at 500 °C, while the large ones decompose into several parts or collapse into dislocation loops. For annealing temperatures above 800 °C in air, an amorphous oxide layer forms at the surface of the samples and new platelets form at 1000 °C. AFM-measurements show that the roughness depends on both doping type and level and the plasma frequency in

addition to exposure time. The roughness reduces at elevated temperatures in most samples. The surface pyramid become rounded off for very high annealing temperatures due to the amorphous oxide layer forming on the top surface.

References

[1] M. Bruel, B. Aspar, A.-J. Auberton-Hervé, Jpn. J. Appl. Phys. 36 (1997) 1636.
[2] A.Y. Usenko, A.G. Ulyashin, Jpn. J. Appl. Phys. 41 (2002) 5021.
[3] P. Chen, P.K. Chu, T. Hörchbauer, J.-K. Lee, M. Nastasi, D. Buca, S. Manti, R. Loo, M. Caymax, T. Alford, J.W. Mayer, N.D. Theodore, M. Cai, B. Schmidt, S.S. Lau, Appl. Phys. Lett. 86 (2005) 031904.
[4] R. Job, M.-F. Beaufort, J.-F. Barbot, A.G. Ulyashin, W.R. Fahrner, Mat. Res. Soc. Symp. Proc. 719 (2002) 217.
[5] A.G. Ulyashin, R. Job, W.R. Fahrner, O. Richard, H. Bender, C. Claeys, E. Simoen, D. Grambole, J. Phys. Condens. Mat. 14 (2002) 13037.
[6] J. Pearton, W. Corbett, M. Stavola, Hydrogen in Crystalline Semiconductors, Springer-Verlag, 1992, p. 63.
[7] Y.L. Huang, Y. Ma, R. Job, W.R. Fahrner, Appl. Phys. Lett. 86 (2005) 131911.
[8] R. Job, Y. Ma, Y.-L. Huang, A.G. Ulyashin, W.R. Fahrner, M.-F. Beaufort, J.-F. Barbot, Solid State Phen. 95–96 (2004) 141.
[9] A.G. Ulyashin, R. Job, W.R. Fahrner, D. Grambole, F. Herrmann, Solid State Phen. 82–84 (2002) 315.
[10] NanoScope Command Reference Manual, DI/Veeco Metrology Group Inc. (2001).
[11] F.A. Reboredo, M. Ferconi, S.T. Pantelides, Phys. Rev. Lett. 82 (1999) 4870.
[12] K.-H. Hwang, E. Yoon, K.-W. Whang, J.Y. Lee, Appl. Phys. Lett. 67 (1995) 3590.
[13] M.F. Beufort, H. Garem, J. Lépinoux, Philos. Mag. A 69 (5) (1994) 881.

Paper 5

The Temperature Evolution of the Hydrogen Plasma Induced Structural Defects in Crystalline Silicon

(Solid State Phenomena Vol. 131-133, p. 315-320 (2008))

Is not included due to copyright

Paper 6

TEM study of hydrogen defect formation at extended defects in hydrogen plasma treated polished and as cut multicrystalline silicon

(*Accepted for publication in Journal of Applied Physics (December 2008))*

TEM study of hydrogen defect formation at extended defects in hydrogen plasma treated multicrystalline silicon

Heidi Nordmark[1], Alexander Ulyashin[2], John C. Walmsley[1,3] and Randi Holmestad[1,a)]

[1] Dept of Physics, Norwegian University of Science and Technology (NTNU), NO-7491 Trondheim, Norway
[2] SINTEF Materials and Chemistry, P.O. Box 124 Blindern, NO-0314 Oslo, Norway
[3] SINTEF Materials and Chemistry, NO-7465 Trondheim, Norway

(Accepted for publication in Journal of Applied Physics)

Hydrogenation of multicrystalline silicon for solar cell applications is considered to be an effective method of increasing the lifetime by passivating defects and impurities. Hydrogen plasma treated, as-cut and chemically etched, multicrystalline silicon samples have been studied by electron microscopy in order to investigate hydrogen defect formation at extended bulk defects. In chemically etched samples, the texture of the surface after hydrogen plasma treatment differs between different grains depending on grain orientation. In as-cut samples, hydrogen induced defects are formed on sawing defects, that extend up to ~ 5 μm below the Si surface. Intra-granular defects are also observed in the ~ 1 μm subsurface region. The density of defects is higher in as-cut samples than in chemically etched samples and the size of the defects increases with depth. Hydrogen induced structural defects on bulk dislocations and on dislocations in twin grain boundaries and stacking faults are found several μm below the sample surface. It is concluded that: (i) the passivation efficiency of multicrystalline silicon substrates after H plasma treatment can be limited by the formation of hydrogen induced structural defects and that (ii) such defects can be used to getter unwanted impurities upon high temperature processing of the Si wafers.

I. INTRODUCTION

Hydrogenation is considered to be an effective method for improving properties of low cost silicon used for solar cell applications, by passivating defects and increasing the minority carrier diffusion length[1]. However, it is well known that hydrogen initiated structural defect formation in the subsurface region, up to ~ 1 μm below the surface, may occur, especially if direct plasma treatments are employed[2]. The H induced defects arise from the low solubility of hydrogen in silicon[4] which leads to the interaction of H atoms with dopants, impurities and defects, and, for high concentrations, H induced structural defect formation[3]. Such defects are active recombination sites and can reduce the effectiveness of the hydrogenation. To avoid H induced structural defect formation on the hydrogen plasma treated Si surfaces, a microwave remote hydrogen plasma technique is often used. However, the electrical properties of multicrystalline (mc) Si materials are still poorer than those of monocrystalline silicon[3]. Thus, hydrogenation of low-cost Si substrates can not provide complete "recovery" of the material.

Direct hydrogen plasma treatment of Czochralski (Cz) Si can be regarded as a promising non-toxic method to texture silicon surfaces. The plasma etches and redeposits Si on the surface, building up cones or pyramids with {211} lateral surfaces[5], consisting of small

a) Corresponding author: Randi.Holmestad@ntnu.no

{111} facets[6]. It has been found that the surface morphology differs for (001) and (111) oriented wafers[7]. Surface roughness is strongly related to {111} platelet defects in the Si subsurface region and subsequent preferential etching at positions where these intersect the Si surface[6].

Hydrogen induced defects in silicon have large strain fields. In platelet defects Si-Si bonds are broken and Si-H_x bonds are formed, resulting in a dilation of the silicon lattice by 20%-30%[8]. Small hydrogen gas filled bubbles are located within the platelets. Multicrystalline silicon contains extended defects, such as grain boundaries and dislocations, which lower the hydrogen defect nucleation barrier. Dislocations are effective at absorbing both vacancies and self-interstitials by climb. They play an important role in the precipitation of Cu_3Si, which has a large volume misfit with the silicon lattice[9]. In particular, it is shown that vacancies from silicon implantation act as trapping centers that block the diffusion of hydrogen deeper into the bulk during subsequent plasma treatment[10]. Random geometry grain boundaries and dislocations with excess vacancies are, therefore, expected to be the preferred nucleation sites for hydrogen induced defects in mc silicon. Despite this, in remote plasma hydrogenation studies Nickel et al.[11] found that in mc Si there was no evidence for either preferred nucleation of platelets at or penetration of platelets through the grain boundaries. No platelets were found within a distance of 40 nm from the grain boundaries.

The behavior of hydrogen is of technological importance. For example hydrogen initiated structural defect formation is a crucial process for the exfoliation of thin Si layers that are used commercially in the semiconductor industry and provides a potential method for cutting thinner silicon wafers from bulk ingots[12-14]. About 50% of the solar cell wafers produced today are made from mc silicon[15], therefore it is important to study hydrogen induced defects also in such material. Another important motivation for this work is that structural defects formed by H implantation can be considered as suitable gettering sites for the removal of unwanted impurities[16], and thereby might improve the minority carrier lifetime of the material.

For surface texturing, diffusion blocking and exfoliation, it is important to study the effects of grain boundaries and dislocations on hydrogen defect formation in mc Si material and compare it with detailed investigations of hydrogen defect formation in Cz Si substrates heavily hydrogenated using H^+ plasma treatments[17-21]. While many studies have focused on platelet formation in n- and p-type monocrystalline Si, very few have studied the influence of extended defects, like dislocations, stacking faults and twins on hydrogen induced defect formation in mc silicon. Even fewer, if any, have studied hydrogen plasma treated, as-cut, mc material. This is important for getting a better understanding of the interaction between hydrogen and extended defects and in learning more about the impact of different grain orientations on hydrogen defect formation. In this work, the microstructure of chemically etched and as-cut mc silicon wafers after H^+ plasma treatment is studied in detail. The surface morphology of the different grain orientations is studied together with the interaction between the hydrogen related defects and the structural bulk defects of chemically etched and as-cut mc silicon samples.

II. EXPERIMENTAL

Two ~ 10 Ωcm boron doped mc Si wafers, one as-cut and one chemically etched with CP133 ($HF:3CH_3COOH:3HNO_3$) for 15 minutes, were studied. During etching a 20 μm surface layer was removed from both sides of the wafer. This is sufficient to remove all structural defects originated from wafer cutting. Polished Cz silicon wafers with resistivity ~ 10 and 10-20 Ωcm p type and 1.8-2.6 Ωcm n type silicon were used as reference samples. All samples were hydrogenated in a plasma enhanced chemical vapor deposition (PECVD) system for about 1 hour at a frequency of 110 MHz, a power of 50 W and a hydrogen flux of 200 sccm at a

temperature of ~ 250 °C. The as-cut and chemically etched mc samples were post annealed at 450 °C for about 10 hours. P and n type reference samples were post annealed between 200 and 1000 °C for one hour.

Secondary ion mass spectroscopy (SIMS) was used for analysis of the hydrogen distribution in the reference Cz Si sample after plasma treatment. A CAMECA ims 7f instrument operating in negative mode with a 15 keV Cs^+ primary beam was used. The raw SIMS profiles were obtained as sputter time versus secondary ion intensity. The sputter time is related to depth and the conversion factor was determined by measuring the SIMS craters with a Dektak 8 surface stylus profilometer. The concentration calibration for hydrogen was made using a $5x10^{15}$ cm^{-2} 150 keV $^+$ ion implanted Si reference sample. The detection limit for hydrogen atoms for this analysis was ~ 10^{18} cm^{-3}.

Surface morphology of the Si surface was analyzed by a Hitachi S-4300SE scanning electron microscope (SEM) operating at 15 kV. Cross-section transmission electron microscopy (TEM) samples were prepared by mechanical polishing down to a thickness of about 10 µm in the middle of the 3 mm disk and thinning to electron transparency using a Gatan PIPS ion mill. TEM observations were made using a Philips CM30 operating at 300 kV and JEOL 2010F operating at 200 kV, equipped with scanning TEM (STEM) and X-ray energy dispersive spectroscopy (EDS) detectors.

III. RESULTS AND DISCUSSION

Figure 1 shows the SIMS depth profile of hydrogen in the reference H plasma treated polished p-type Cz Si sample. At and just below the surface, the hydrogen concentration is almost $5x10^{20}$ cm^{-3}, or about 1 at %. It gradually decreases to about $5x10^{18}$ cm^{-3}, or 0.01 at %, 0.5 µm below the surface. It can be concluded that, upon H plasma treatment, hydrogen saturates the Si subsurface region at a concentration much higher than the H solubility limit at the hydrogenation temperature[4] (~ 10^6 cm^{-3}). Thus, one can expect that hydrogen may form precipitates and introduce structural defects[12-14,17-21].

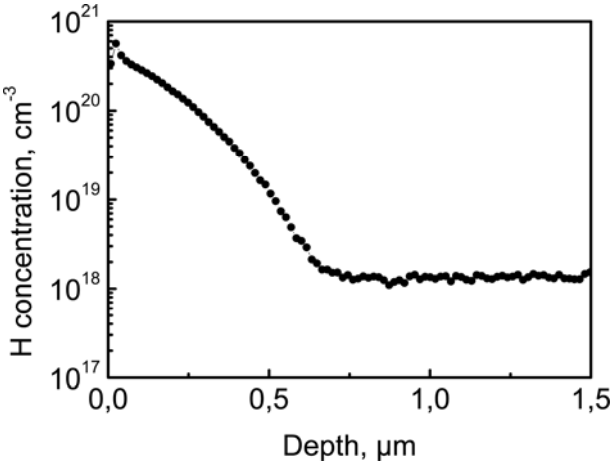

FIG. 1. SIMS profile of hydrogen in hydrogenated Cz Si p-type sample.

A. Surface morphology

Hydrogen diffusion into the Si subsurface region from the direct plasma treatment, is accompanied by a surface texturing arising from the etching of Si by H^+ ions. The SEM images in Figure 2 compare the surface morphology of the H plasma treated Cz Si and chemically etched mc Si samples. Figures 2(a) and 2(b) have the same magnification and show the cones formed in the reference Cz [001] oriented sample and a grain from the chemically etched mc Si sample, oriented away from [001], respectively. The cones in Figure 2(b) are larger and tilted compared those in Figure 2(a).

The surface morphology differs significantly between grains in different orientations in plasma treated, chemically etched, mc Si, from almost smooth to almost fully covered with cones as shown in Figure 3. In some grains the density of cones is high in the center, while the density close to the grain boundaries is low. In other grains the opposite is observed. The area close to a grain boundary is often free of cones. The cones are tilted in most of the grains in the etched mc sample. The different surface morphologies for the different grain orientations are consistent with what has been observed after

a similar texturing process was applied to Cz Si substrates with different orientations[7].

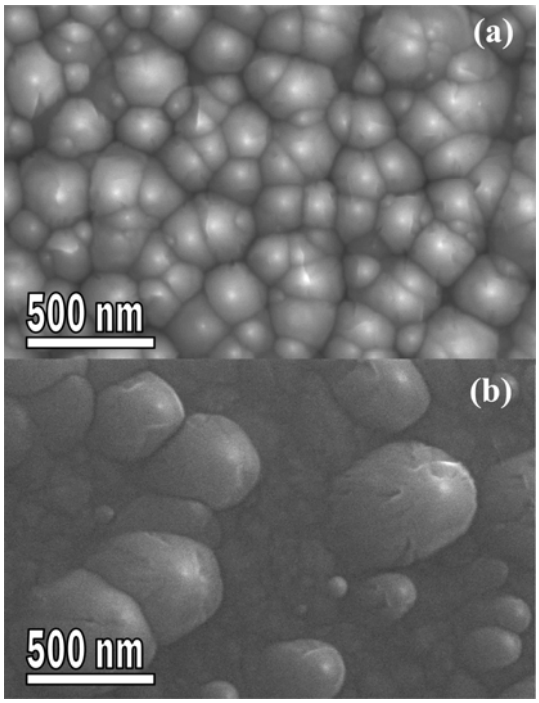

FIG. 2. SEM image of the surface morphology of 1 Ωcm p-type hydrogen plasma treated samples. (a) [001] oriented reference Cz Si wafer, (b) tilted cones in a grain ≠ [001] in a chemically etched mc Si sample.

Figure 3(a) shows a grain boundary triple point in the chemically etched sample. The density of surface cones differs from grain to grain and also within a grain. Small height differences between adjacent grains can be observed after chemical etching. The arrows indicate cones formed on the resulting new inclined surfaces of the grain boundaries. The broad, cone-free, band (double-headed arrow) in the upper grain, close to the grain boundary, might be tilted relative to the grain surface. The lower left grain in the image is free from cones, but small defects can be observed on its surface.

Figures 3(b) and 3(c) show a grain boundary in the chemically etched mc Si wafer in more detail. In Figure 3(b), rows of cones running from the grain boundary can be seen. These might be due to scratches, stacking faults or dislocations in the original surface. Figure 3(c) shows several cones that terminate in the grain boundary. Smaller defects, often showing a triangular morphology (arrows), are also present. These probably represent surface images of the hydrogen induced bulk defects located in the subsurface layer, which are described in the section below. Similar small defects can also be located on grain surfaces without cones, indicating the presence of H-related defects in these grains also.

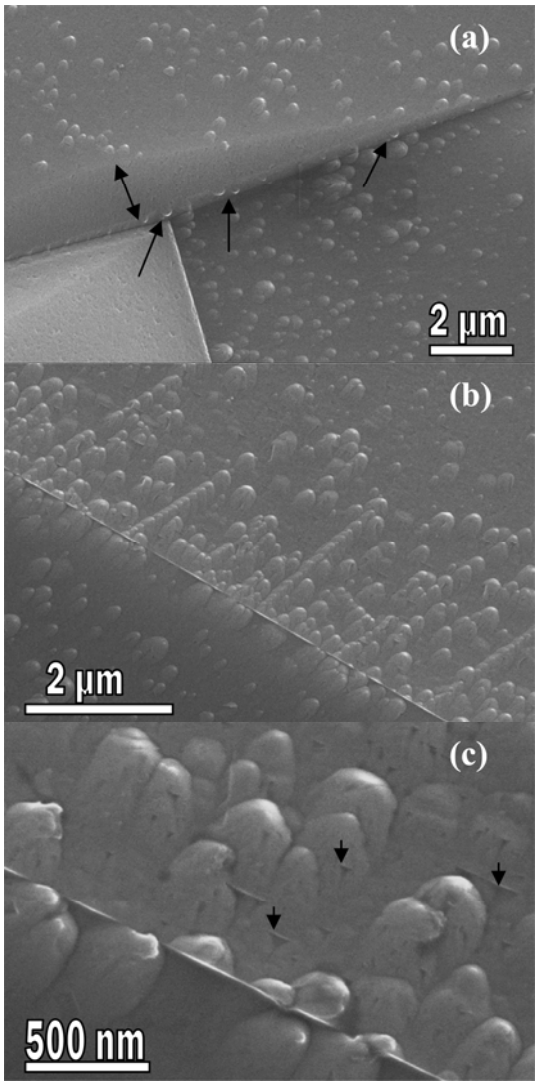

FIG. 3. SEM images of chemically etched and hydrogen plasma treated mc Si surfaces. (a) Shows a grain boundary triple point. The surface roughness differs between the different grains. (b) At certain locations the cones tend to line up in rows normal to the grain boundary. (c) The cones do not extend across a grain boundary. Smaller defects on the surface of the cones are visible (arrows).

No significant difference of surface morphology between the differently oriented grains in the as-cut mc sample was observed. This is because of the very rough surface produced by sawing, ~ µm compared to ~ 100 nm after H plasma treatment, with numerous cracks and defects that dominate the surface morphology of this sample.

B. Hydrogen induced bulk defects

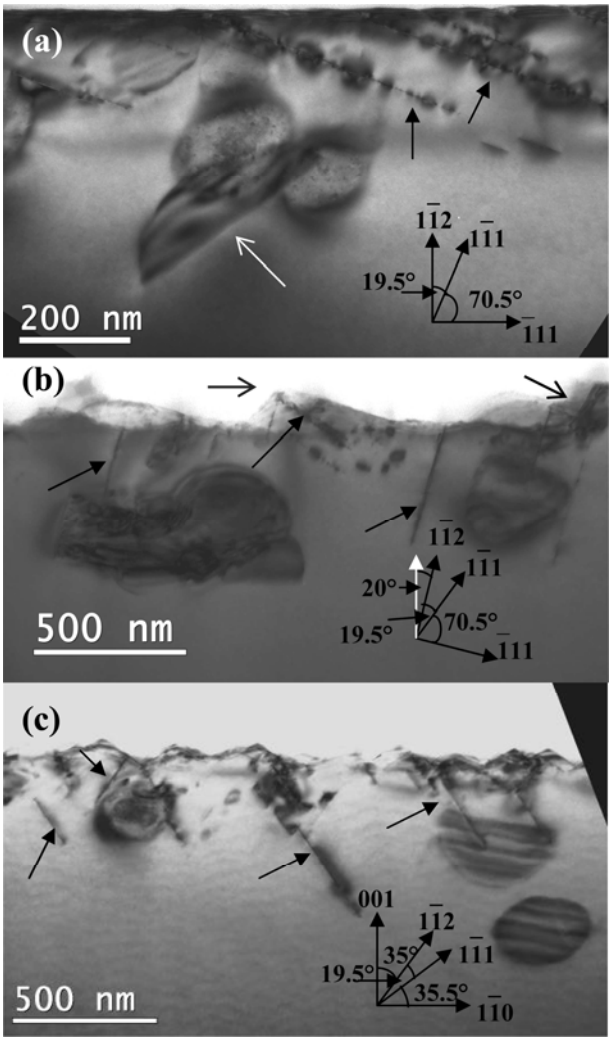

FIG. 4. TEM bright field images showing the surfaces of chemically etched mc Si and Cz reference cross-section orientation after plasma treatment. The images are aligned so that the surface is horizontal. (a) [1-12] oriented grain in mc Si sample without surface cones, (b) mc Si sample showing defects in the subsurface and tilted cones on the surface. (c) [100] oriented Cz sample with symmetrical surface cones.

Both surface morphology and hydrogen induced defect formation in the subsurface after plasma treatment can be studied in cross-section TEM samples. Figure 4(a) shows a grain in a chemically etched mc Si sample without surface cones where the surface is almost flat. Figure 4(b) shows tilted cones on a grain in the chemically etched mc Si, while Figure 4(c) shows cones on a [001] oriented Cz Si sample, for reference. This is the same sample as in Figure 2(a). The microstructure is similar in all samples except from the differences arising from different grain orientations. A high density of H initiated platelet defects can be observed in the subsurface region. The orientation of the surface cones and the {111} and {100} platelet defects differs relative to the wafer surface, as indicated in Figures 4(a)-(c). Crystallographic directions are indicated in the figures and the sample surface is oriented horizontally in all images. The lateral surfaces of the cones are {112}, which makes an angle of 35° with the surface normal in a [001] oriented grain[5]. The angle between [001] and a {111} platelet is ~ 55° and the angle between a (-111) platelet and a (1-11) platelet is ~ 70.5°, while the angle between [1-11] and [1-12] is 19.5°. In Figure 4 (a) the surface normal is seen to be close to [1-12] because the angle between the surface normal and the {111} platelets (arrows) is ~ 21°. The white arrow indicates a {100} platelet, which makes an angle of 35° with the surface normal. In Figure 4 (b) the surface cones are tilted (open arrow head). The angles between the lateral surface of the tilted cones and the {111} platelets, were found to be ~ 20° and ~ 90°, which confirms that the tilted cones also have lateral surfaces of {211}.

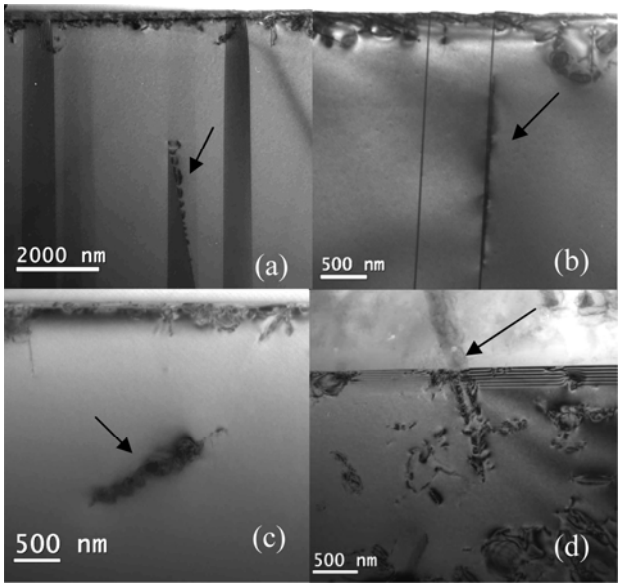

FIG. 5. TEM images showing hydrogen induced defects observed on pre-existing defects deep below the surface in chemically etched mc Si cross-section orientation after plasma treatment. (a) Platelet defects on a dislocation in an inclined twin boundary/stacking fault, (b) platelet defects on a dislocation in a twin boundary/stacking fault tilted edge on, (c) hydrogen induced defects at a dislocation (arrows), (d) Plane view TEM bright field image, showing no preferred nucleation at a grain

boundary and rows of platelet defects (arrows) probably arising from surface scratches or dislocations.

In Figures 5(a)-(c) hydrogen induced defect formation is seen to occur both in the subsurface of the mc samples and on extended defects in the bulk. Figures 5(a) and (b) show hydrogen induced platelet defects in twin boundaries and stacking faults in the chemically etched mc Si sample. To form such defects in a deep subsurface region, hydrogen has to diffuse from the surface to dislocations in the twin boundaries/stacking faults (arrow, Figures 5(a) and (b)). It can be seen that the dislocation free twin boundaries and stacking faults in the same images are not affected by the H initiated structural defect formation. Hydrogen induced platelets are seen to form on a bulk dislocation in Figure 5(c) (arrows). H-related defects can be observed several μm deep below surfaces at extended defects, predominantly on dislocations, in such samples, compared to about 0.5 μm in Cz Si H^+ treated in a similar way. This suggests that such defects, act as preferred nucleation sites by lowering the nucleation barrier for hydrogen defect formation in mc samples. The diffusion of hydrogen in silicon has been found to be highest for undoped, defect free silicon $D_{H+} = 9.4\text{x}10^{-3}\exp(-0.48\ eV/kT)$ and decreases 2-6 orders of magnitude when dopants, impurities and point defects are present, because the defects captures H atoms[22]. In mc Si, hydrogen was found to penetrate deeper along dislocation arrays than in grain boundaries and twins, resulting in a diffusion of one and 2-3 orders of magnitude lower than for defect free Cz Si, respectively[22]. Figure 5(d) shows a TEM plan view image of the H plasma treated chemically etched mc Si sample. The grain boundary in the image is not preferentially decorated with platelets. Since the silicon surface is preferentially etched at the {111} platelet positions[6], an explanation for the rows of dense nucleated platelets (arrow) observed in the image could be that they have formed at the same positions as the surface cone rows in Figure 3(b). Scratches on the surface or dislocations are probable nucleation sites for the platelets at these positions.

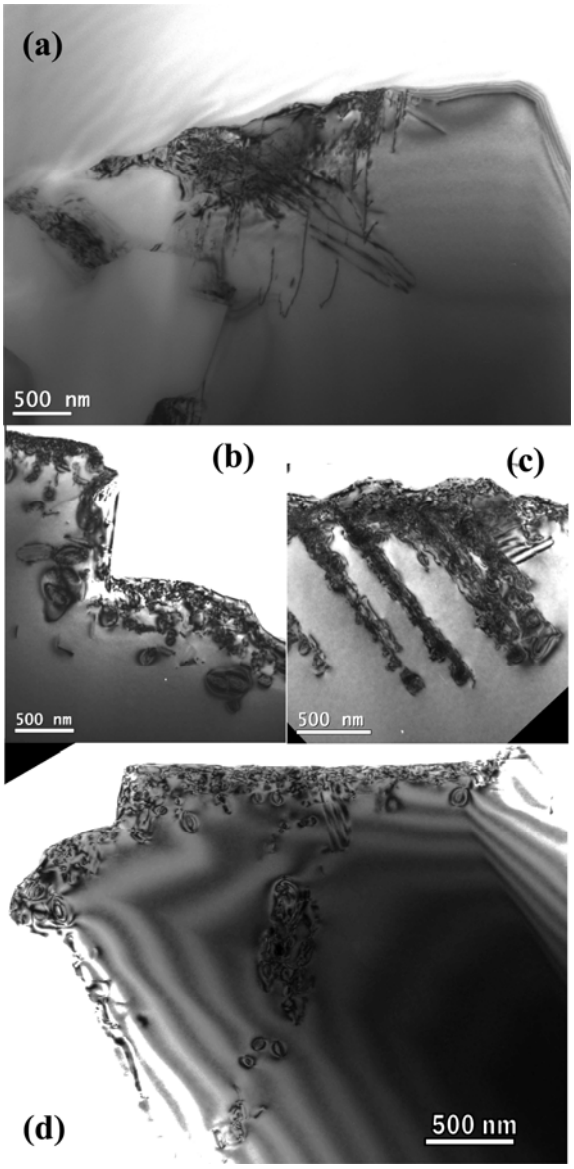

FIG. 6. Cross-section TEM images showing defects in as-cut sample before and after H^+ plasma treatment. (a) Structural defects in as-cut mc Si samples, (b) Hydrogen induced defects in an as-cut mc Si sample after H plasma treatment. The surface is rough on a μm scale, (c) and (d) the hydrogen diffuses to defects from the sawing process in the sample, forming structural defects.

Figure 6 shows TEM images of hydrogen structural defects in the as-cut mc Si sample. From Figure 6(a), which shows the surface before plasma treatment, it can be seen that the sawing process creates a defect zone, extending several μm into the bulk. A high density of cracks and dislocations are present. These are expected to be preferred nucleation sites for hydrogen containing defects and during solar cell fabrication. They are removed by etching. Figure 6(b) shows the subsurface region in the as-cut mc Si sample after H^+ plasma treatment.

It can be observed that a high density of hydrogen induced defects has also formed in the subsurface in this case. Further, it can be seen that hydrogen related platelets formed far into the sample bulk are larger than the platelets formed close to the surface.

Figures 6(c) and 6(d) show hydrogen induced defects formed deep into the subsurface region of the sample. The results confirm that extended defects in silicon getter the hydrogen, which diffuses from the plasma treated surface deep into the bulk of the Si sample, in agreement with earlier observations of hydrogen gettering by defect layers formed by ion implantation[10,13,20,23]. Structural defects in mc Si samples act as trap centers for the in-diffused hydrogen during the hydrogenation process in the same way as buried defect layers are initiated by ion implantation. In Figure 6b-d, it appears that the platelets close to the surface originate from the sawing defects and that these can getter hydrogen atoms. The platelets grow larger when they are nucleated deeper below the surface where fewer nucleation sites are available.

Figure 7(a) shows an example of platelet defects containing hydrogen gas bubbles, observed about 1 μm below the surface, in the as-cut mc Si sample after H plasma treatment. We have observed similar hydrogen gas containing bubbles inside platelets in H^+ plasma treated Cz Si samples[18,21]. Formation of such defects explains results of Raman investigation on Si samples heavily saturated by hydrogen, in which nearly free hydrogen molecules were observed for both monocrystalline[7] and mc[24] materials after H plasma treatments. Figures 7(b) and (c) show the remains of a {100} platelet after 1 hour annealing at 900 °C in a 10-20 Ωcm p type Cz Si sample, edge on and in plan view respectively. The hydrogen has diffused out of the bubbles and only spherical voids remain, lying in the plane of the original defect. The voids were found to have dark contrast and the H_2 containing bubbles appear bright in the images. This is probably due to diffraction contrast or different focus conditions. In Figure 7(b), the two dark lines on each side of the voids (arrows) are part of the boundary dislocation of the platelet defect, which was truncated during ion milling. When observing a platelet edge on, the voids line up in a row. In Figure 7(c),which shows the same platelet face on, the voids form a disk.

C. Segregation of impurities

Implantation related damage, such as structural defects and voids in silicon are known to getter Cu[25-27]. Earlier studies have shown that, after one hour annealing in air at 1000 °C, platelets containing oxygen are formed on the remnants of the hydrogen platelets[9,11].

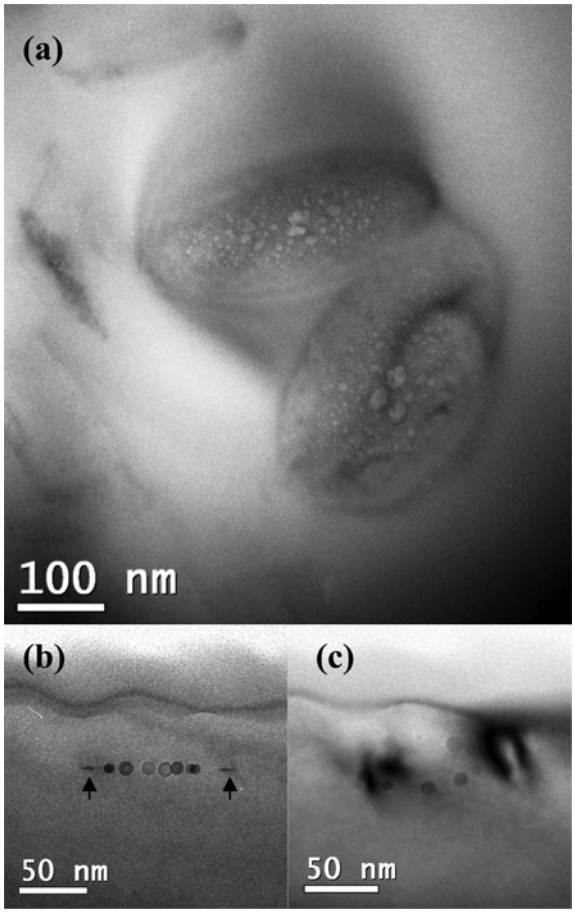

FIG. 7. Temperature evolution of hydrogen bubbles in platelets. (a) TEM bright field image of hydrogen gas filled bubbles observed in platelets 1 μm below the surface region of the as-cut mc Si sample. Spherical voids observed after 1 hour annealing at 900 °C in a {100} platelet tilted edge on, (b), and face on, (c).

Figure 8 shows n type Cz Si after annealing for one hour at 1000 °C. Figure 8(a) is a bright field STEM image showing oxygen containing platelets. Cz Si contains ~10^{17}-10^{18} cm^{-3} oxygen

that are mobile at high annealing temperatures. In addition, since the annealing was done in air, the oxygen might have diffused into the sample.

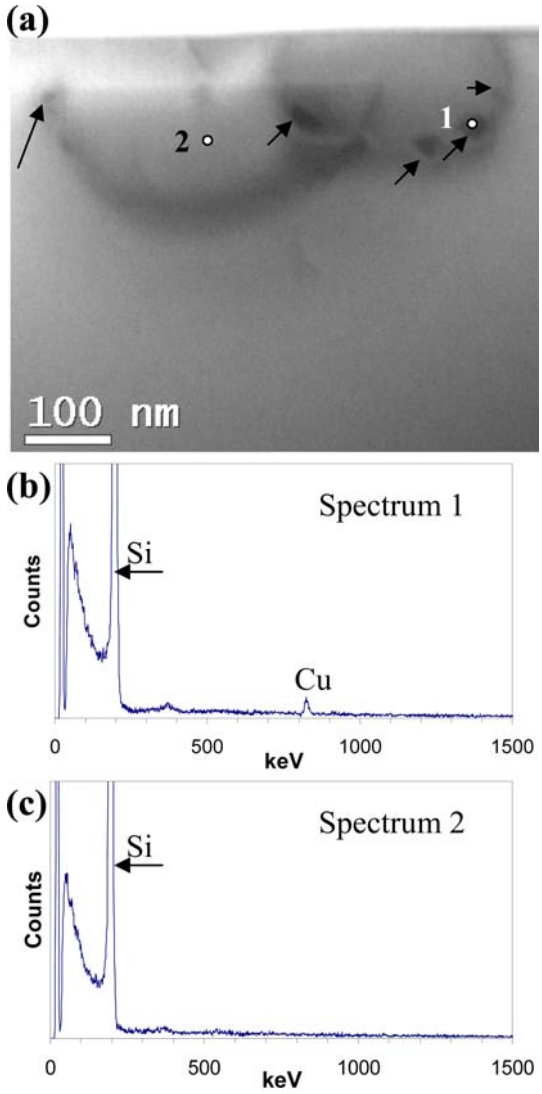

FIG. 8. Showing evidence of oxygen platelet formation and Cu segregation at the hydrogen platelet positions after 1 hour annealing at 1000 °C, of n type hydrogen plasma treated material. (a) STEM bright field image of H plasma treated sample. Oxide platelets have formed at the remnants of the H induced platelets. Cu has segregated to defects in the platelets, probably the voids (arrows), (b) EDS spectrum from a Cu-rich defect, (c) EDS spectrum from a platelet.

Figures 8(b) and 8(c) show EDS spectra from the dark features on the platelet and the bulk of the platelets, respectively. Spectrum 1 shows that the dark spots contain Cu. In spectrum 2, from the middle of a platelet, no Cu was detected. The shape and contrast of the dark Cu containing defects are similar to the voids shown in Figure 7(c). This show that defects from H^+ plasma treatments can getter metallic impurities in the same way as implantation-related defects. No oxygen peak is visible in the spectra. This is because the platelets are only a few atomic layers thick and give a very weak EDS signal. Spectra from platelet defects oriented edge on however, showed small oxygen peaks indicating a segregation/gettering process of oxygen by these structural defects. Similar oxygen segregation has been observed in implantation induced defects [28,29].

V. CONCLUSIONS

After plasma hydrogenation, a hydrogen content of 1%, well above the solubility limit, was measured by SIMS in the very close subsurface in p-type Cz Si. This supersaturation of monoatomic hydrogen led to hydrogen defect formation in the subsurface of both the Cz and as-cut and chemically etched mc Si. In the chemically etched mc Si sample, different grain orientations showed different surface roughness after H plasma treatment. However the density of H induced defects in the subsurface was constant for all investigated grains. Grain surfaces oriented close to {112}, were found to have an almost smooth surface, while grains oriented close to {100}, showed large, symmetrical, cones oriented parallel to the surface normal. Other grain orientations showed tilted surface cones. In mc Si, additional H-related defects were observed on extended defects, several µm deeper into the bulk than in similarly treated Cz silicon. Dislocations in the bulk or in twins/stacking faults seem to be the preferred nucleation/gettering sites for the hydrogen induced defects in mc silicon. No hydrogen induced defects were observed on dislocation free twins/stacking faults.

In the as-cut mc Si sample, no difference in the surface etching was observed between differently oriented grains because of the rough surface from sawing. Extended defects from the sawing process were shown to getter hydrogen effectively and H-related defect formation was found to depend strongly on available nucleation sites. The density of hydrogen induced defects was found to be higher in as-cut samples, with

numerous sawing defects, than in the Cz reference and chemically etched mc Si samples.

The hydrogen induced defects nucleated on extended defects were found to be similar to defects seen in Cz Si. They contain hydrogen bubbles that evolve during post annealing. After annealing at 1000 °C in air, evidence for oxygen and in some cases Cu segregation to the remnants of the H induced platelets have been observed, which indicates that such H induced defects can be used to remove unwanted impurities from the bulk of the Si wafer. Moreover, these structural defects could be used to prevent penetration of impurities from the ambient atmosphere, for example, during high temperature heat treatments occuring during gettering processes, which are widely used for the low-cost Si based solar cells fabrication. Further investigations of this phenomenon are in progress.

ACKNOWLEDGEMENTS

NTNU and the Norwegian Research Council are gratefully acknowledged for financial support. University of Oslo is acknowledged for SIMS measurements.

[1]S. Darwiche, M. Nikravech, D. Morvan, J. Amouroux and D. Ballutaud, Sol. Energy Mater. Sol. Cells **91**, 195 (2007)
[2]S. J. Pearton, J. W. Corbett and T. S. Shi, Appl. Phys. A **43**, 153 (1987)
[3]G. Hahn, P. Geiger, D. Sontag, P. Fath, E. Bucher, Sol. Energy Mater. Sol. Cells **74**, 57 (2002)
[4]A. Van Wieringen and N. Warmoltz, Physica **22**, 849 (1956)
[5]M. Bruel, B. Aspar and A.-J. Auberton-Hervé, Jpn. J. Appl. Phys. **36**, 1636 (1997)
[6]A. Y. Usenko and A. G. Ulyashin, Jpn. J. Appl. Phys. **41**, 5021 (2002)
[7]P. Chen, P. K. Chu, T. Höchbauer, J.-K. Lee, M. Nastasi, D. Buca, S. Mantl, R. Loo, M. Caymax, T. Alford, J. W. Mayer, N. D. Theodore, M. Cai, B. Schmidt, and S. S. Lau, Appl. Phys. Lett. **86**, 031904 (2005)
[8]C. Ghica, L. C. Nistor, H. Bender, O. Richard, G. Van Tendeloo and A. Ulyashin, Phil. Mag. **86**, 5137 (2006)
[9]H. Nordmark, A. Ulyashin**,** J. C. Walmsley, B. Tøtdal and R. Holmestad, Nucl. Instrum. Methods Phys. Res. B. **253**, 176 (2006)
[10]C. Ghica, L. C. Nistor, H. Bender, O. Richard, G. Van Tendeloo and A. Ulyashin, J. Phys.D **40**, 395 (2007)
[11]H. Nordmark, A. G. Ulyashin, J. C. Walmsley and R. Holmestad, Solid State Phenomena **131-133**, 309 (2008)
[12]H. Nordmark, A. Ulyashin, J. C. Walmsley, A. Holt and R. Holmestad, Solid State Phenomena **131-133**, 315 (2008)
[13]H. Kumano, T. Sasaki and H. Soyama, Appl. Phys. Lett. **85**, 3935 (2004)
[14]S. Muto, S. Takeda and M. Hirata, J. Appl. Phys. **70**, 3505 (1991)
[15]H. Matsuo, R. B. Ganesh, S. Nakano, L. Liu, K. Arafune, Y. Ohshita, M. Yamaguchi, and K. Kakimoto, J. Cryst. Growth **310**, 2204 (2008)
[16]M Seibt, V. Kveder, W. Shröter and O.Voß, Phys. Stat. Sol. (a) **202**, 911 (2005)
[17]A. G. Ulyashin, J. S. Christensen, B. G. Svensson, R. Kogler and W. Skorupa, Nucl. Instrum. Methods: Phys. Res. B **253**, 126 (2006)
[18]N. H. Nickel, G. B. Anderson, N. M, Johnson and J. Walker, Phys. Rev. B **62**, 8012 (2000)
[19]M. Ishii, K. Nakashima, I Tajima, and M. Yamamoto, Jpn. J. Appl. Phys. **31**, 4422 (1992)
[20]K.-H. Hwang E. Yoon, K.-W. Whang and J. Y. Lee, J. Electrochem. Soc. **144**, 335 (1997)
[21]A. G. Ulyashin, R. Job, W. R. Fahrner, O. Richard, H. Bender, C. Claeys, E. Simoen, D. Grambole, J. Phys.: Cond. Matter. **14**, 13037 (2002)
[22]Christopher E. Dub and Jack I. Hanoka, *proceedings of the 31 st Photovoltaic Specialists Conference proceedings* (IEEE, Florida, USA 2005), p. 883
[23]A. G. Ulyashin, A. I. Ivanov, R. Job, W. R. Fahrner, F. F. Komarov and A.V. Frantskevich, Mater. Sci. Eng. B **73**, 64 (2000)

[24]A. Ulyashin, M. Scherff, R. Hussein, M. Gao, R. Job and W. R. Fahrner, Sol. Energy Mater. Sol. Cells **74**, 195 (2002)
[25]H. Kumano, T. Sasaki, H. Soyama, Appl. Phys. Lett. **85**, 3935 (2004).
[26]M. Zhang, C. Lin, X. Duo, Z. Lin, Z. Zhou, J. Appl. Phys. **85**, 94 (1999)
[27]A. Peeva, P. F. P. Fichtner, D. L.da Silva, M. Behar, R. koegler, W. Skorupa, J. Appl. Phys. **91**, 69 (2002)
[28]A. G. Ulyashin, Y. A. Bumay, W. R. Fahrner, A. I. Ivannov, R. Job, L. Palmetshofer, MRS Symposium Proceedings Series **469**, 95 (1997)
[29]R. Job, A. G. Ulyashin, W. R. Fahrner, A. I. Ivanov, L. Palmetshofer, Appl. Phys. A **72,** 325
(2001)

Paper 7

A comparative analysis of structural defect formation in Si^+ implanted and then plasma hydrogenated and in H^+ implanted crystalline silicon

(Solid State Phenomena Vol. 131-133, p. 309-314 (2008))

Is not included due to copyright

Part 3.

Surface texturing and silicon whiskers growth using tungsten hot filament reactor

Paper 8

Silicon whisker growth using hot filament reactor with hydrogen as source gas

(Japanese Journal of Applied Physics, Vol. 47, No. 6, pp. 4807–4809 (2008))

Is not included due to copyright

Paper 9

Si substrates texturing and vapour-solid-solid Si nano-whiskers growth using pure hydrogen as source gas

(*Accepted for publication in Journal of Applied Physics (January 2009))*

Si substrates texturing and vapour-solid-solid Si nano-whiskers growth using pure hydrogen as source gas

H. Nordmark[1], H. Nagayoshi[2], N. Matsumoto[3], S. Nishimura[3] and K. Terashima[3], C. D. Marioara[4], J. C. Walmsley[4,1], R. Holmestad[1,a)] and A. Ulyashin[5]

[1]Department of Physics, NTNU, NO-7491 Trondheim, Norway
[2]Tokyo National College of Technology, 1220-2, Kunugida-machi, Hachioji, Tokyo, Japan
[3]Shonan Institute of Technology, 1-1-25, Nishikaigan, Tsujido, Fujisawa, Kanagawa, Japan
[4]SINTEF Materials and Chemistry, NO-7465 Trondheim, Norway
[5]SINTEF Materials and Chemistry, Forskningsveien 1, P.O. Box 124 Blindern, NO-0314 Oslo

(Accepted for publication in Journal of Applied Physics)

Scanning and transmission electron microscopy have been used to study silicon substrate texturing and whiskers growth on Si substrates using pure hydrogen source gas in a tungsten hot filament reactor. Substrate texturing in the nm-μm range of mono- and as-cut multicrystalline silicon, independent of grain orientation, was observed after deposition of WSi_2 particles that acted as a mask for subsequent hydrogen radical etching. For a specific experimental condition, simultaneous surface texturing and Si whisker growth was observed. The whiskers formed via vapour-solid-solid growth in which the deposited WSi_2 particles acted as catalysts for a subsequent metal induced layer exchange process well below the eutectic temperature. In this process SiH_x species, formed due to the etching of the substrate by the H radicals, diffuse through the metal particles leading to growth of crystalline Si whiskers via metal-induced solid phase crystallisation. High resolution transmission electron microscopy, electron diffraction and X-ray energy dispersive spectroscopy were used to study the WSi_2 particles and the structure of the Si substrates in detail. It is established that Si whiskers are partly crystalline and partly amorphous, consisting of pure Si with WSi_2 particles on their tips as well as incorporated into their structure. Both texturing of mc Si and whiskers growth have potential for within solar cells applications. Si whiskers also in addition promise applications as electronic or photonic components.

I. INTRODUCTION

In recent years the interest for silicon nanostructures has exploded. Several different structures and growth methods have been developed. Silicon nanowhiskers/wires/rods and nanotubes have wide applications within photonics and nanoelectronics. Silicon nanowire (SiNW) technology is particularly important because silicon-based nanoelectronics is compatible with silicon-based microelectronics. SiNW also have applications within nanosensors, nanospintronics, nanomedicine and nanobiology[1-6].

Because of the SiNWs narrow size, their electrical and optical properties differ from silicon bulk properties. For diameters less than 3 nm, quantum effects occur. In contrast to bulk silicon that is a poor light emitter, narrow SiNW show promising properties as light emitting devices[1]. As the SiNW gets narrower, the emitted light shifts from red to blue[1]. The band gap has been found to increase from 1.1 eV to 3.5 eV when the diameter is decreased from 7

a) Corresponding author: Randi.Holmestad@ntnu.no

nm to 1.3 nm[7]. Si whiskers with p-n junctions (as well as nanorods/whiskers which are composed of several materials), may provide a solution for fabrication of higher efficiency solar cells than those based on conventional planar p-n junction geometry[8-10].

The two main methods of growing SiNW[1] are Vapour-Liquid-Solid (VLS)[11] growth and Oxide-Assisted Growth (OAG)[12]. In the case of VLS, small liquid metal droplets, such as gold, work as catalysts for growth at the solid liquid interface between the droplet and the silicon substrate. Silicon from a gaseous source is dissolved into the liquid metal droplet. A low-temperature eutectic liquid, supersaturated with silicon, forms and crystalline silicon precipitates out from the droplet[11,13-15]. A variant of this method is vapour-solid-solid (VSS) growth, a similar low-temperature process that can occur at temperatures well below the eutectic temperature of the catalyst particles. This method is similar to a metal induced layer exchange (MILE) process[16,17] followed by metal-induced solid-phase crystallization (SPC)[18,19], where amorphous silicon is deposited on top of a metal film on a substrate, for example aluminium film deposited on a glass substrate. The amorphous silicon dissolves in the metal film, diffuses through it during annealing below the eutectic temperature, forming crystalline silicon nucleus on the substrate that grows, resulting in a thin polycrystalline Si film confined at the interface between the metal film and the substrate. Growth of SiNW by the VSS method has been reported previously with Al catalyst particles[20], Ti forming $TiSi_2$ islands[21,22] and Cu catalyst particles[23].

It is necessary to note that Si whisker growth can be considered as a nano-scale texturing of Si substrates, which is important in case of some specific applications, in particular for solar cells, and can be combined as in this case, with the coarser texturing of the substrates on a micron-scale. Indeed, lack of a low cost texturing method is one of the limiting factors for the processing of low cost, high efficiency, Si based solar cells. Texturing of the front surface reduces optical losses, thereby increasing the efficiency of the solar cell[24,25]. For monocrystalline silicon, alkaline etchants, KOH and NaOH, are generally used to form randomly distributed pyramids on (100) oriented wafers. These etchants are anisotropic with respect to grain orientation and cannot be used for mc Si. Various methods such as acidic etching, mechanical grooving, reactive ion etching and laser texturing have received recent attention for mc Si texturing[26-32]. Most of these methods cannot be regarded as low cost candidates for industrial applications, thus, development of a low cost texturing method still is required. The tungsten hot filament reactor can be used to texture the surface of silicon substrates on a micron-scale, as proved in earlier publications[33-35]. The power of this method is that it can texture all grain orientations, and can therefore also be used for mc Si, in contrast to pure hydrogen plasma treatment[36-46], where texturing depends on grain orientation and hydrogen induced structural defects form in the bulk [36-46]. In the tungsten hot filament case, the high temperature, ~800°C (in contrast to ~250°C for H plasma treatments used in [41-45]), prevents hydrogen defect formation in the bulk. However, the mask of deposited tungsten silicide particles on the surface needs to be removed after the etching if a clean textured Si surface is needed.

In a recent paper[47], we described the growth mechanism and physical structure of Si whiskers grown on a Si substrate using a tungsten hot filament CVD reactor with hydrogen as the source gas. We found that growth occurred without any deposition of metal droplets prior to the hydrogen radical treatment of the silicon substrate. In the first step of the process, atomic hydrogen etched the silicon surface, forming SiH_4 species that reacted with tungsten from the filament, which is also etched by hydrogen radicals. As a result, silicide particles were deposited onto the Si substrate surface. Whiskers then grew onto the substrate due to the interaction of silicon hydrides with the particles and subsequent precipitation of saturated Si. The whiskers were found to have tungsten silicide particles on their tip, indicating the VSS growth

mechanism, since the process temperature is well below the eutectic temperature of the tungsten silicide.

Table 1. Experimental conditions

Condition	(i) WSi_2 deposition	(ii) Si texturing	(iii) Si whisker growth
H_2 flow rate (sccm)	30	250	30
Pressure (Torr)	0.3	1	10
Filament current (A)	24	22	22
Furnace temperature (°C)	800	800	800
Time (s)	20	1800	1800
Filament to substrate distance (mm)	15	7-15	7

In this paper we demonstrate that nano- and micro-scale texturing of a Si substrate can be done in one process in a tungsten hot filament reactor upon using only pure hydrogen flow. By changing experimental parameters, different surface texturing and/or whiskers growth results, table 1. High resolution transmission electron microscopy (HRTEM) is used to study the whisker structures and the interface between the deposited silicon tungsten phase and the substrate in detail. Electron diffraction is used to verify the WSi_2 phase and scanning TEM (STEM) in combination with X-ray energy dispersive spectroscopy (EDS) is applied to map the different phases and point out the presence of tungsten silicide particles in the whisker structure.

II. EXPERIMENTAL

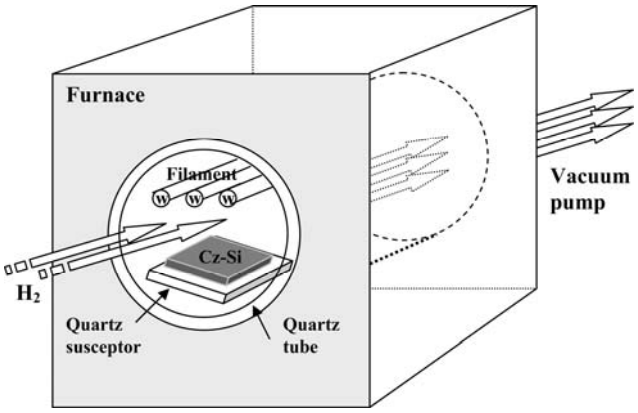

FIG. 1. Experimental setup for the tungsten hot filament reactor[18]. Hydrogen gas is pumped through the furnace quartz tube and is decomposed to reactive atomic hydrogen by the tungsten filament. A vacuum pump evacuates the chamber.

Figure 1 shows the experimental setup. The reactor is enclosed in a furnace that holds 800 °C. Tungsten filaments are positioned above the substrate and heated to 1200 °C in order to decompose hydrogen molecules. More details can be found elsewhere [33,34]. The substrates used were, polished p-type, 10 Ωcm Czochralski (CZ) (100) silicon wafer for whiskers growth and polished n and p type 10 Ωcm Cz Si and as-cut multicrystalline (mc) Si for texture etching. The native oxide was removed from the substrate surface using a 5% of HF solution. The reactor was operated under two of three experimental conditions, Table 1, (i) initial deposition of tungsten silicide particles on the Si substrate (Fig.2a), followed by (ii) substrate texturing (Fig. 2b) or (iii) simultaneous substrate texturing and Si whisker growth (Fig.2c). Experimental parameters are shown in Table 1.

Figure 2 visualizes schematically the processes of hydrogen radical interaction with the Si surface and a tungsten hot wire, substrate texturing and final Si whiskers growth. Fig.2a illustrates atomic hydrogen etching the substrate surface by breaking Si-Si bonds, forming SiH_x-species. Moreover it can be supposed that H radicals as well as the SiH_x species react with the tungsten filament, etching and leading to the formation of tungsten silicides, which are shown as black spheres at the Si-substrate surface in Fig.2. By reducing the filament current, to stop further deposition of tungsten, substrate texturing can be achieved with the tungsten silicide particles masking the substrate, Fig. 2b. To obtain whisker growth (light grey threads terminated with black spheres) as illustrated in

Fig. 2c, long residence time of the source gas and low H_2 flow rate with high pressure were needed. The filament-to-substrate distance was reduced to 7 mm to grow whiskers.

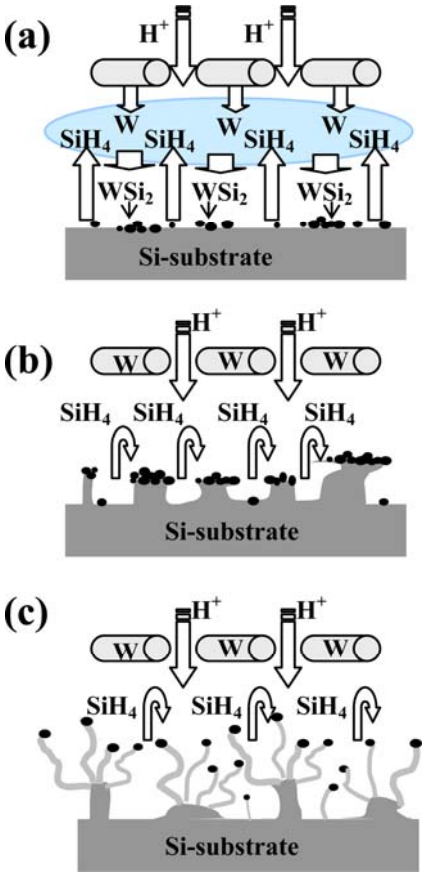

FIG. 2. A model of whiskers growth on the silicon surface. Black spheres represents WSi_2 particles, grey curved lines on the silicon substrate are the whiskers and the arrows represents the gas flow in the system. (a) Particle deposition, (b) Surface texturing with particles acting as a mask, (c) Silicon whiskers growth.

A Hitachi S-4300SE field emission scanning electron microscope (SEM), operating at 10 kV, was used to study the surface morphology. Cross-section samples were prepared for TEM studies by argon ion milling using a Gatan PIPS. A Phillips CM30 microscope operating at 300 kV was used for conventional TEM and electron diffraction. A JEOL 2010F, operating at 200kV, equipped with an Oxford Instruments INCA x-ray detector, was used for HRTEM, STEM and EDS analysis.

III. RESULTS

A. Texturing and the tungsten silicide phase

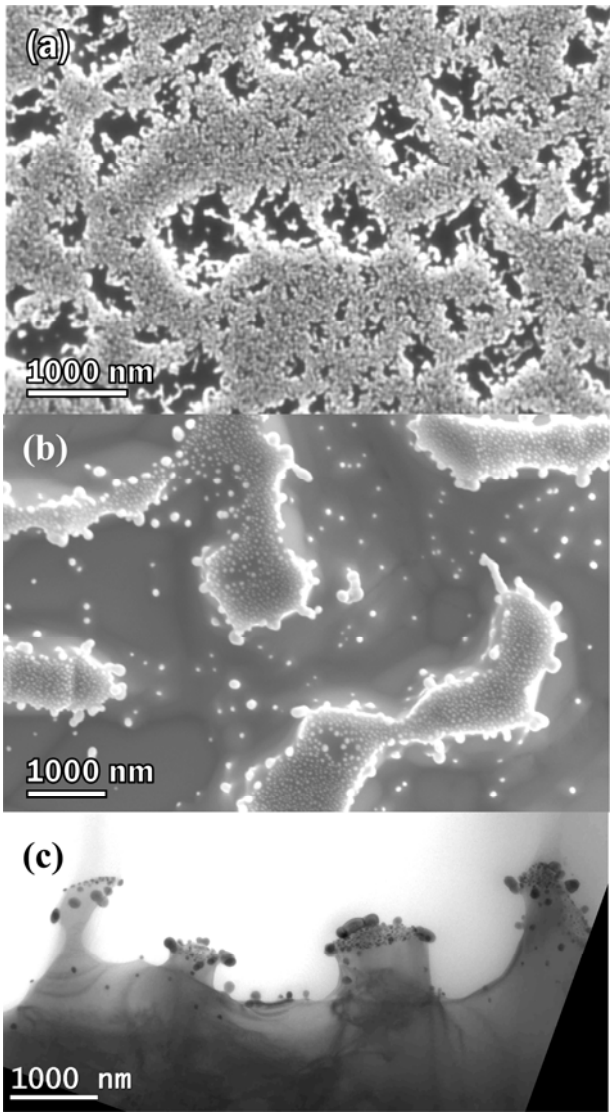

FIG. 3. Particle deposition and hydrogen radical etching of silicon substrates, (a) SEM image after 20 second particle deposition on the silicon substrate. Tungsten silicide particles show bright contrast. (b) SEM image after 20 second particle deposition and subsequent hydrogen radical etching of mc Si. Most particles are seen to cluster together. Tungsten silicide particles show bright contrast. (c) Cross-section TEM bright field image of the textured sample in (b). Tungsten silicide particles show dark contrast.

Fig. 3a shows a SEM image of tungsten silicide particles after 20 seconds deposition time on the silicon substrate produced in condition (i) in Table 1. The particles are seen to cluster together and cover most of the surface. Single particles are 20-50 nm in diameter. After hydrogen radical etching, experimental condition (ii), the structure in Fig. 3b resulted for as cut multicrystalline silicon. The particles

are not evenly distributed on the surface. Some are isolated, but most are present in clusters. Fig. 3c shows a cross-section TEM image of the surface texturing observed after etching. The clustered particles are observed on Si islands, separated by grooves left where the particle density is lower. The particles act as a mask against hydrogen radical etching, protecting the surface below. Both monocrystalline and multicrystalline substrates showed similar µm-sale texturing. Hydrogen radical etching without particles resulted in texturing on a scale of less than 100 nm[33]. Reflectance spectra show less than 1% reflectance after V-grove surface texturing by this method[33]. The advantage of this method is that all grains obtain the same surface texturing. However, a method of removing particles is needed before the substrates can be used for solar cell applications. Although tungsten form deep levels in silicon, its diffusivity in silicon is very low, on the order of boron and phosphorous diffusivity[48]. In this case tungsten silicide is evaporated on to the silicon surface, which may make diffusion of tungsten into the Si bulk even slower[49]. In our case 30 minutes annealing at 800 °C is used, which is not sufficient for the tungsten to diffuse deep into the silicon. As a result tungsten only react with the surface layer of the samples and the substrate was found in [33] to easily be cleaned after an acid rinse ($HF+HNO_3$), which removed all particles after 5 seconds[33].

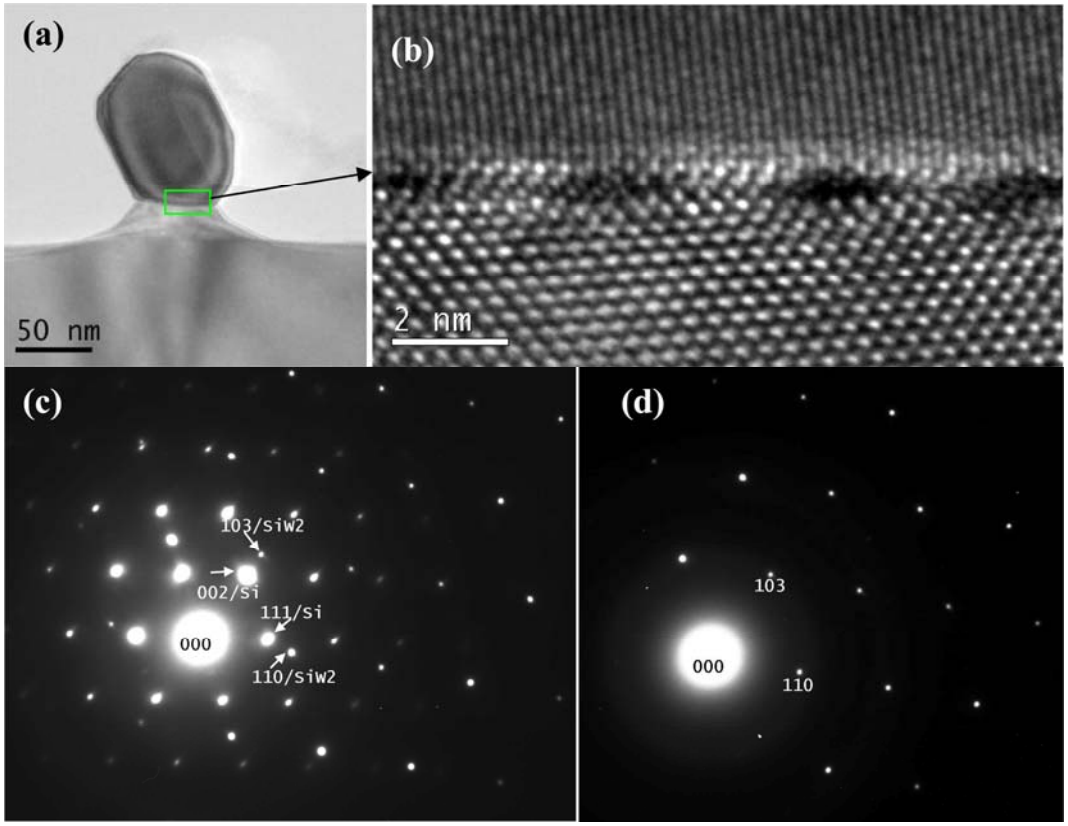

FIG. 4. Analysis of tungsten silicide particles. (a) TEM and b) HRTEM image of the interface between the tungsten silicide and the silicon substrate after H radical treatment. (c) Diffraction pattern showing Si [-110] zone axis superimposed on a [-331] zone axis from the WSi_2 phase. (d) Indexed diffraction pattern from the [-331] zone axis of the WSi_2 phase

HRTEM was used to study the interface between the silicon substrate and the tungsten silicide particles after texturing in detail. Silicide diffraction pattern spacings were measured, using Si {110} zone axis as a reference and the results were compared with known W-Si structures[50]. The tetragonal WSi_2-phase with lattice parameters a = b = 3.211 Å and c = 7.868 Å was found to match the diffraction patterns from the particles. Figure 4a shows a particle that is adhering to a mound on the Si substrate. Fig. 4b is an enlarged image of the rectangular

area marked in Fig. 4a. The tungsten silicide phase was found to be crystalline as can be observed from the lattice image in Fig. 4b. The dark-bright contrast and the orientation relationship at the interface indicate some strain between the two phases. A diffraction pattern of a similarly oriented particle superimposed on silicon [110] zone axis is shown in Fig. 4c. In Fig. 4d the diffraction pattern from the [-331] zone axis in the particle is indexed. The two lattices are semi coherent and some lattice planes continue through the interface. The orientation relationship from this particle was found to be $(002)_{Si} \| (103)_{WSi2}$ and $[-110]_{Si} \| [-331]_{WSi2}$.

B. Silicon whiskers

Si whiskers were grown under condition (iii) in Table 1. Figure 5a shows a SEM image of the Si whiskers grown on the substrate. As can be observed from this figure, the whiskers are not homogenously distributed on the surface, but associated with the silicide-covered mounds. The presence of the mounds indicates that the H radical texturing process of the Si substrate takes place also under condition (iii), in parallel with whisker growth. The silicon source for the whisker growth is the Si substrate itself. All parts of the silicon substrate that are not covered with tungsten silicide particles are etched during the whisker growth process, and then re-deposited, but not homogeneously, on the Si surface, resulting in a V-groove texturing in addition to the whisker growth. The bright dots on some of the whisker tips in Fig. 5a, are tungsten silicide particles. Sometimes the particles were also incorporated in the whisker structures. The particles could be recognized by recording a corresponding image using back-scattered electrons where the heavier phase shows bright contrast. In the secondary electron images shown, both the whiskers and silicide particles can be seen clearly. The inset to the right shows an enlarged image of an almost straight whisker with WSi_2 particle on its tip (arrow). This indicates the VSS growth mechanism for the Si whiskers, whose diameters range from about 10 to about 50 nm. Figure 5b shows a cross-section TEM image of whiskers grown on Si islands. A single whisker bundle on a silicon island is shown in Fig. 5c.

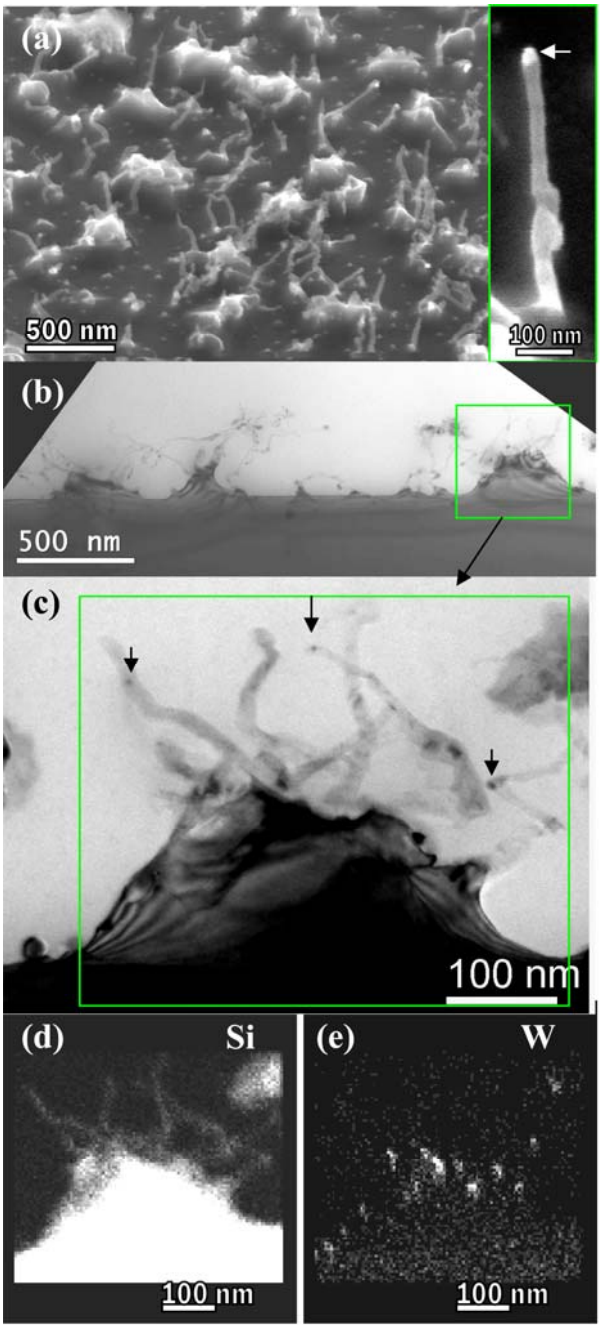

FIG. 5. Silicon whiskers. (a) SEM image of silicon whiskers, substrate is tilted 50°. Enlarged image of a whisker with a WSi_2 particle on its tip (arrow) is shown flush mounted to the right, (b) TEM images of silicon whiskers. (c) Enlarged image of an island with whiskers and corresponding EDS elemental maps of (d) silicon and (e) tungsten.

The whiskers do not grow straight, but with a zigzag morphology. This might be a result of defects in the structure or incorporation of tungsten particles as indicated with arrows in Fig. 5c. EDS elemental maps from the area defined by the rectangle in Fig. 5c, are shown in

Fig. 5d and Fig. 5e, for silicon and tungsten, respectively. The whiskers are found to consist of silicon, while the particles in addition contain tungsten and sometimes iron (EDS map not shown). Not all of the particles indicated in Fig. 5c show up in the tungsten map in Fig. 5e, because they are too small to give a strong signal. The sample also drifted slightly during the analysis. The smallest particles were identified as silicides by recording individual spectra with the beam positioned at their locations.

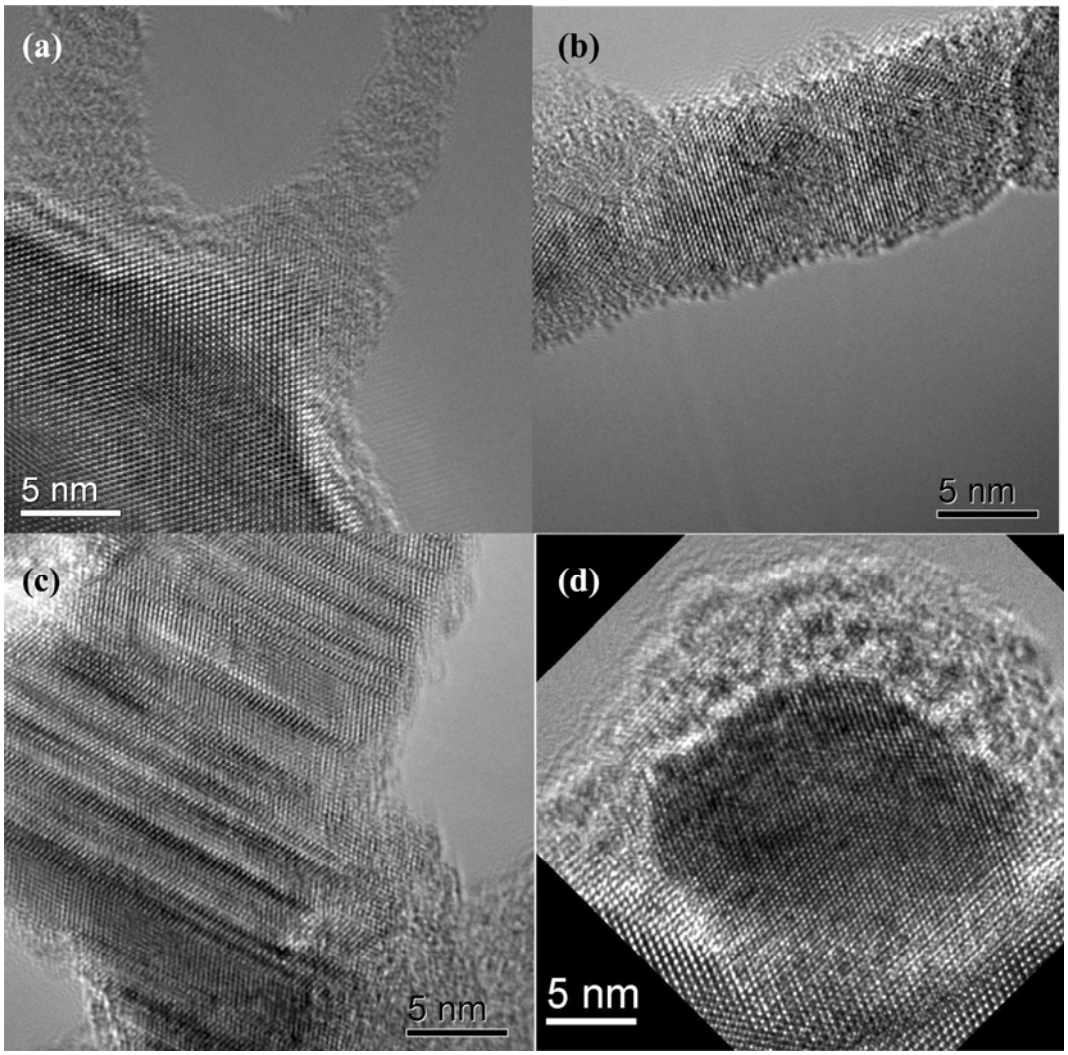

FIG. 6. High resolution images of the whiskers structure. (a) Very thin amorphous whiskers grown on the silicon substrate, (b) Thin crystalline whisker, (c) Stacking fault/twin structure of whisker close to a {110} zone axis, (d) Crystalline WSi_2 particle (zone axis (-331)) embedded in the Si substrate tilted to zone axis (110).

HRTEM-images of different parts of several Si whiskers are shown in Fig. 6. The size and orientation of individual whiskers vary. Fig. 6a shows very thin amorphous whiskers grown from an island on the substrate. A thin, mostly crystalline, whisker is observed in Fig. 6b. In Fig.6c, a twinning/stacking fault structure in a whisker can be observed. The whisker is oriented close to the silicon [110] zone axis. The faults lie along traces of

(1-11) planes. Fig. 6d shows a TEM image of a crystalline particle on the silicon surface after whisker growth. HREM pattern from the particle was calibrated with the known silicon matrix [110] zone axis, and identified as the same WSi_2 phase as in the deposited particles. In this case, the zone axis was found to be [-331], the same

zone axis as indexed in Fig. 4d. In Fig. 7a, a partly crystalline and partly amorphous whisker can be observed. The EDS spectrum from this whisker, shown in Fig. 7c, shows the presence only of silicon. During ion milling, thin crystalline structures can be damaged by the ion beam. Therefore it is not excluded that the entire whisker was crystalline before the sample preparation. WSi_2 particles were also found to be embedded in the whiskers structure, as shown in Fig. 7b. The EDS spectrum of the embedded particle, Fig. 7d, confirms that it contains tungsten. As mentioned, the small silicide particles were often observed at bends in whiskers.

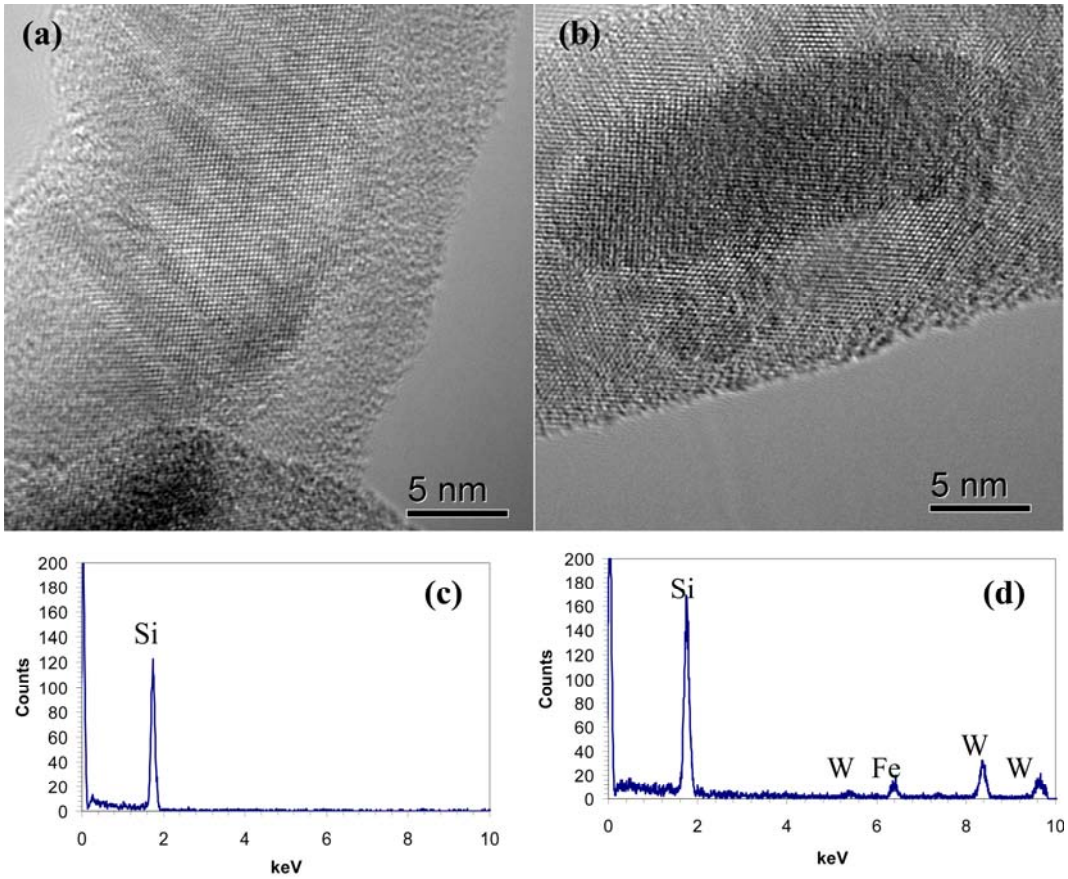

FIG. 7. Chemical analysis of whiskers. (a) Thick, partly-crystalline and partly-amorphous silicon whisker, (b) Crystalline WSi_2 particle incorporated in the structure, (c) EDS-spectrum from the whisker in (a), showing only silicon, (d) EDS-spectrum from the particle in (b), showing silicon, tungsten and iron.

Some of the embedded particles were found to contain iron. For a few catalyst particles, a W-Fe ratio as high as 2:1 was observed. Only silicon, tungsten and hydrogen are involved in the process under investigation and the experimental set up does not have any iron-containing components. Iron was not detected in the silicon part of the whiskers which suggests that it was not due to secondary excitation of the sample holder or TEM column. One possible source is impurities in the H_2 gas. Multi-metal silicides are more stable than single metal silicides[51] and can getter iron effectively[51,52]. The high substrate temperature used during H radical treatment might allowed iron to diffuse into the WSi_2 particles.

The obtained experimental results clearly show that the Si whiskers are more stable than the bulk Si surface against hydrogen radical attack. We can only speculate about the reason for this at the present stage, and it is probably related to the observed amorphous subsurface part of the whiskers. All of the depicted whiskers in the HRTEM images in Fig. 6 and 7 are seen to be amorphous on their edges. It can be assumed that the amorphous subsurface part of each whisker is highly saturated by hydrogen as a

result of segregation during the crystallisation of the Si whisker bulk and incorporation of hydrogen from the H radical ambient. The resulting, highly stable, a-Si:H structure protects the silicon whisker structure against H radical etching. It is also possible that native oxygen, which is not detectable by the EDS, is included into the resistant subsurface amorphous layer. As a result, the whiskers are stable on the surface, as observed from Fig. 5.

During VSS growth, the tungsten silicide particles act as catalysts for the whisker growth in the same way as the metal particles in the standard MILE process[16]. Indeed, since the processing temperature used (~ 800 ºC) is far below the WSi_2 eutectic temperature (1390 ºC[53]), the MILE process is followed by whiskers growth and metal-induced SPC[18,19]. In our case whiskers result since the metal layer consists of distinct metal particles instead of a continuous surface film. The silicon islands result from the hydrogen radical etching, which also constitute the amorphous Si source for the MILE and SPC processes. In this case only substrate texturing, without any additional growth of a Si layer, occurs upon whisker formation on the Si substrate, in contrast to the case of a molecular beam epitaxy based silicon nanowires growth[54].

As for conventional VLS growth[1,11,13-15], the diameter of the whiskers grown by the VSS method observed in this study depends on the size of the deposited particles. This means that by shortening the deposition time for the WSi_2 catalyst particles, even thinner whiskers than 10 nm can probably be grown, and might reach the dimensions where quantum effects will occur. It is also likely that this approach can be applied using other catalysts than WSi_2, like $TiSi_2$ that can be used to grow whiskers in a similar way[21,22]. Controlling the size, growth direction and morphology might be a challenge. For solar cell applications the whiskers grown in this study are not suited since they contain W, which even at very low concentrations (above 1.2×10^{12} cm^{-3})[55] forms deep levels in silicon. By optimising the whiskers growth process, defect free whiskers suited for solar cells might be grown. Zigzag growth has also been observed for the SiNW grown on $TiSi_2$ islands[21,22] using SiH_4 or SiH_2Cl_2 as source gas, where no H-radicals etching of the substrate took place. This suggests that attack from hydrogen radicals probably does not primarily influence the growth of the whiskers in our case. In the $TiSi_2$ catalyst work[21,22], particles were only observed at the tip of the wires and sometimes at their base but never incorporated in the structure, as in our case. The change in growth directions for the $TiSi_2$ case was found to be due to defect formation in the whiskers structure[21,22]. In our case we also observed change of growth direction at positions where metal silicide particles are incorporated in the structure. In the case of VSS growth using Al particles as catalysts[20], the resulting SiNW grow normal to the (111) surface with a conical morphology and no particles were incorporated in the structure. In the Cu catalyst case, the morphology of the nanowires was found to depend on substrate temperature[23]. While thick defect-free wires could be grown at 500-550°C, thinner wires with defects and alternating diamond-wurtzite structure could be grown at higher temperatures, 600-650°C[23]. Such features could probably also be realized by our setup by choosing specific experimental conditions. More experiments are necessary to find the optimal experimental conditions for whiskers growth in the heated tungsten filament case.

The incorporation of WSi_2 particles during growth observed in this study can be due to several reasons: (i) during growth a small tungsten silicide particle became detached from the larger particle from which the whisker was growing. As a result the whiskers diameter might change as can be observed for some of the whiskers in Fig.5c. (ii) small particles are deposited on the whiskers and sink into the structure due to a lateral VSS growth process as observed for gold particles during VLS growth[56], (iii) during growth tungsten might diffuse to lattice defects in the silicon whiskers forming precipitates. Such particles are often observed at positions where the growth direction changes as pointed out by arrows in Fig. 5c.

V. CONCLUSIONS

We have described a method to texture silicon surfaces by using a hot tungsten filament reactor and only hydrogen as source gas. In the process a tungsten particle mask is used to shield part of the silicon surface from hydrogen radical etching, such that a V grove texturing of the surface results. The power of this method is that the texturing is independent of grain orientation and therefore has potential in texturing both mono- and multicrystalline silicon as well as as-cut silicon. Furthermore the high processing temperature prohibits hydrogen defects from forming in the silicon subsurface, which is a well-known problem when using H-plasma treatment to texture surfaces.

For a specific experimental condition simultaneous μm surface texturing and silicon nano-whiskers growth on the surface was observed using this setup. In the process, tungsten silicide particles act as catalyst particles and SiH_x species etched from the silicon surface by the hydrogen radicals act as silicon source for vapour-solid-solid growth of whiskers. Our experimental results show that the Si whiskers are more stable than the bulk Si surface against hydrogen radical attack. Moreover, Si whiskers were found to be partly crystalline and partly amorphous and consisted of several links and bends connected together by crystalline WSi_2 particles. The diameter of the Si whiskers depends on the deposited particle sizes, ranging from about 10 to about 50 nm. The tungsten silicide phase, including the deposited particles and particles embedded in the Si whisker structure, were identified as the tetragonal WSi_2 phase.

It is concluded that by using a hot filament reactor with only hydrogen as a source gas, and a Si substrate, it is possible to realize the following processes: (i) deposition of tungsten silicide particles on the Si surface, (ii) texturing of the Si surface and (iii) growth of Si whiskers on top of the textured Si surface without any additional technological steps.

ACKNOWLEDGEMENTS

NTNU and the Norwegian Research Council are gratefully acknowledged for financial support.

[1] B. K. Teo and X. H. Sun, Chem. Rev. **107**, 1454 (2007) and references therein

[2] Y. Xia, P. Yang, Y. Sun, Y. Wu, B. Mayers, B. Gates, Y. Yin, F. Kim and H. Yan, Adv. Mater. **15, 353** (2003)

[3] V. Schmidt, H. Riel, S. Senz, S. Karg, W. Riess and U. Gösele, Small **2, 85** (2006)

[4] J. Goldberger, A.I. Hochbaum, R. Fan and P. Yang, Nano Lett. **6, 973** (2006)

[5] J.-F. Hsu, B.-R. Huang, C.-S. Huang and H.-L. Chen, Jpn. J. Appl. Phys. **44, 2626** (2005)

[6] J.A. Streifer, H. Kim, B.M. Nichols and R.J. Hamers, Nanotechnology **16, 1868** (2005)

[7] D. D. D. Ma, C. S. Lee, F. C. K. Au, S. Y. Tong, S. T. Lee, Science, **299**, 1874 (2003)

[8] J. Goldberger, R.R. He, Y.F. Zhang, S.W. Lee, H.Q. Yan, H.J. Choi, and P.D. Yang, Nature **422**, 599 (2003).

[9] B.M. Kayes, H.A. Atwater, and N.S. Lewis, J. Appl. Phys. **97**, 114302 (2005)

[10] L. Tsakalakos, J. Balch, J. Fronheiser, B. A. Korevaar, O. Sulima and J. Rand, Appl. Phys. Lett. **91**, 233117 (2007)

[11] Wagner, R. S. Appl. Phys. Lett. **4**, 89 (1964)

[12] Wang, N.; Tang, Y. H.; Zhang, Y. F.; Lee, C. S.; Lee, S. T. Phys. Rev. B **58**, R16024 (1998)

[13] R. S. Wagner, W. C. Ellis, K. Jackson, and S. M. Arnold, J. Appl. Phys. **35**, 2993 (1964)

[14] E. I. Givargizov, J. Cryst. Growth **31**, 20 (1975)

[15] Alfredo M. Morales and Charles M. Lieber, Science **279**, 208 (1998)

[16] O. Nast, S. Brehme, D.H. Neuhaus, S.R. Wenham, IEEE Trans. Electron dev. **46**, 2062 (1999)

[17] P.I. Widenborg, A.G. Aberle, J. Cryst. Growth. **242**, 270 (2002)

[18] T.J. Konno, R. Sinclair, Phil. Mag. B **66**, 749 (1992)

[19] P.I. Widenborg, A. Straub, A.G. Aberle, J Cryst. Growth **276**, 19 (2005)

[20] T. J. Konno and R. Sinclair, Mater. Sci. Eng. A **179/180** 426 (1994)

[20] Y. Wang, V. Schmidt, S. Senz and U. Gösele, Nature nanotechnology, **1**, 186 (2006)

[21] T. I. Kamins, R. Stanley Williams, Y. Chen, Y.-L. Chang, and Y. A. Chang, Appl. Phys. Lett. **76**, 562 (2000)

[22] T. I. Kamins, R. Stanley Williams, D. P. Basile, T. Hesjedal and J. S. Harris, J. Appl. Phys. **89**, 1008 (2001)

[23] J. Arbiol, B. Kalache, P. R. i Cabarrocas, J. R. Morante and A. F. i Morral, Nanotechnology **18**, 305606 (2007)

[24] J. Zhao, A. Wang and M. A. Green, *Proceedings of 21st IEEE Photo voltaic solar cell conference*, 333 (1991)

[25] M. A. Green, *Solar cells: Operating principles, technology and system applications*, Kensington : University of New South Wales (1998)

[26] J. Nijs, S. Sivoththaman, J. Szlufcik, K. De Clercq, F. Duerinckx, E. Van Kerschaever, R. Einhaus, J. Poortmans, T. Vermeulen and R. Mertens, Sol. Energy Mater. Sol. Cells **48, 199** (1997)
[27] D.H. Macdonald, A. Cuevas, M.J. Kerr, C. Samundsett, D. Ruby, S. Winderbaum and A. Leo, Solar Energy **76**, 277 (2004)
[28] U. Gangopadhyay, S.K. Dhungel, P.K. Basu, S.K. Dutta, H. Saha and J. Yi, Sol. Energy Mater. Sol. Cells, **91**, 285 (2007)
[29] P. Fath, C. Borst, C. Zechner, E. Bucher, G. Willeke, S. Narayanan, Solar Energy Materials and Solar Cells, **48**, 229 (1997)
[30] Y. Inomata, K. Fukui and K. Shirasawa, Sol. Energy Mater. Sol. Cells, **48**, 237 (1997)
[31] G. Kumaravelu , M. M. Alkaisi , A. Bittar , D. Macdonald and J. Zhao, Curr. Appl. Phys. **4**, 108 (2004)
[32] L.A. Dobrzański, A. Drygała, K. Gołombek, P. Panek, E. Bielańska and P. Zięba, J. Mat. Proc. Tech. **201**, 291 (2008)
[33] H. Nagayoshi, S. Nishimura, K. Treashima, and K. Konno, Jpn. J. Appl. Phys. **44**, 7839 (2005)
[34] H. NAGAYOSHI, S. NISHIMURA, K. TERASHIMA, AND A. ULYASHIN, *PROC. WCPEC-4, IEEE*, 1411 (2006)
[35] H.Nordmark, H. Nagaoyshi, K. Terashima, S. Nishimura, J.C. Walmsley, R. Holmestad, and A. Ulyashin, *Proceedings 22nd European Photovoltaic Solar Energy Conference, Milan, Italy*, 1686 (2007)
[36] K.-H. Hwang, E. Yoon, K.-W. Whang and J. Y. Lee, Appl. Phys. Lett. **67**, 3590 (1995)
[37] K.-H. Hwang, E. Yoon, K.-W. Whang and J. Y. Lee, J. Electrochem. Sos. **144**, 335 (1997)
[38] I. Solomon, B. Drévillon, H. Shirai and N. Layadi, J. Non-Cryst. Sol. **164-166**, 989 (1993)
[39] M. Ishii, K. Nakashima, I. Tajima and M. Yamamoto, Jpn. J. Appl. Phys. **31**, 4422 (1992)
[40] Y. L. Huang, Y. Ma, R. Job, M. Sherff, W. R. Fahrner, H. G. Shi, D. S. Xue and M.-L. David, J. Electrochem. Sos. **152**, C600 (2005)
[41] A. G. Ulyashin, R. Job, W.R. Fahrner, O. Richard, H. Bender, C. Claeys, E. Simoen, and D. Grambole, J. Phys.: Cond. Mat. **14**, 13037 (2002)
[42] C. Ghica, L. C. Nistor, H. Bender, O. Richard, G. Van Tendeloo, and A. Ulyashin, Phil. Mag. **86**, 5137 (2006)
[43] H. Nordmark, A. Ulyashin, J.C. Walmsley, B.Tøtdal, and R. Holmestad, Nucl. Instr. Meth. Phys. Res. B. **253**, 176 (2006)
[44] C. Ghica, L. C. Nistor, H. Bender, O. Richard, G. Van Tendeloo, and A. Ulyashin, J. Phys. D **40**, 395 (2007)
[45] H. Nordmark, A.Ulyashin, J.C. Walmsley, A. Holt, and R. Holmestad, Sol. State Phen. **131-133**, 315 (2008)
[46] H. Nordmark, A. Ulyashin, J. C. Walmsley and R. Holmestad, J. Appl. Phys. (submitted).
[47] H. Nagayoshi, H. Nordmark, N. Matsumoto, S. Nishimura, K. Terashima, J.C. Walmsley, R. Holmestad, and A. Ulyashin, Jpn. J. Appl. Phys. **47**, 4807 (2008)
[48] D. Cali, C. M. Cammaleri and V. Raineri, Mater. Sci. Semicond. Proc. **4**, 19 (2001)
[49] G. M. Voronkova, V. V. Zuev, A. D. Kiryukhin and K. V. Yakubovskii, Russian Phys. J. **39**, 430 (1996)
[50] Powder diffraction file, Inorganic phases, Sets 1-44, International centre for diffraction data (ICCD) (1994)
[51] M. Heuer, T. Buonassisi, A. A. Istratov and M. D. Pickett, J. Appl. Phys **101**, 123510 (2007)
[52] H. Nordmark, M. Di. Sabatino, E. J. Øvrelid, J. C. Walmsley, P. Manshanden, L. J. Geerligs R. Holmestad, J. Appl. Phys. (submitted).
[53] L.Fu, F. Gromball, C. Groth, K. Ong, N. Linke, J. Muller, Matr. Sci. Eng. B **136**, 87 (2007)
[54] J. Bauer, F. Fleischer, O. Breitenstein, L. Schubert, P. Werner, U. Gosele and M. Zacharias, Appl. Phys. Lett. **90**, 012105 (2007)
[55] J. R. Davis, A. Rohatgi, R. Hopkins, P. Blais, P. Rai-Choudhury, J. McCormick and H. C. Mollenkopf, IEEE Trans. Electron. Devices **27**, 677 (1980)
[56] C. P. Li, N. Wang, S. P. Wong, C. S. Lee, T. S. Lee and B. K. J. Teo, Phys. Chem. B **106**, 6980 (2002).

III. Unpublished results

Appendix A:

TEM-study of impurities in the red-zone of a mc Si ingot with intentional 100 ppm Ca and unintentionally Cu contamination

H. Nordmark[a], J. C. Walmsley[b], E. Olsen[b], E. J. Øvrelid[b] and R. Holmestad[a]

[a)]Dept of Physics, NTNU, NO-7491 Trondheim, Norway
[b)]SINTEF Materials and Chemistry, NO-7465 Trondheim, Norway

Top and bottom samples of a p-type ingot solidified from conventional solar grade poly-silicon have been studied by transmission electron microscopy (TEM) techniques. Transition metal precipitates were observed in grain boundaries and identified with scanning TEM (STEM) in combination with X-ray energy dispersive spectroscopy (EDS). Disc shaped Cu_3Si precipitates were frequently observed in grain boundaries and at positions where stacking faults/twins initiated from the grain boundary. Also multi-metallic iron-rich precipitates, a large multi-metallic cluster containing Cu_3Si precipitates and a Ni-Fe coprecipitate were observed in one sample. The multiplatelet defects observed probably contain oxygen. The intention was to study Ca containing precipitates, but none was observed in the samples.

After casting, the top, bottom and the sides of an ingot are cut away due to poor lifetime properties. These parts are called red-zone because of their red colour in the lifetime map. During solidification, most impurities are segregated towards the top, such that the top cut is very contaminated. Side cuts and the bottom cut contain contamination from the crucible and coating, in particular iron. The oxygen content is highest in the bottom of an ingot because it has a segregation coefficient higher than 1 [1]. Transition metals are well known to form silicides in silicon. $FeSi_2$, $NiSi_2$ and Cu_3Si are the common silicide phases for Fe, Ni and Cu, respectively.

The boron doped, 1.2 Ωcm ingot was cast in a pilot furnace from commercial poly-silicon with standard crucible and Si_3Ni_4 coating [1, 2]. After solidification, the ingot was annealed for 1 hour at 1100 °C and was then slowly cooled to room temperature [2]. 100 ppm Ca was added to the melt. During the solidification, electrical arcing between the heating element and the outer graphite crucible liner led to the formation of Cu vapor [2], which probably caused the Cu contamination. The ingot was about 12 kg, 250 mm in diameter and 100 mm in height. Several 3 mm discs containing grain boundaries were punched out by an ultrasonic disc cutter, ground with SiC paper down to 30-50 μm thickness, and ion milled with argon ions using a Gatan Ion Duo mill model 600. A Philips CM30 TEM operating at 300 kV was used for medium resolution bright field imaging and a JEOL 2010F TEM operating at 200 kV, equipped with scanning TEM (STEM) and X-ray energy dispersive spectroscopy (EDS) detectors, was used for the high resolution imaging and chemical analysis. For STEM, a bright field or annular dark field detector was used in analytical mode with 0.7 nm spot size. An Oxford instruments EDS Si:Li detector was used for chemical analysis. INCA software was used for recording spectra and perform elemental mapping.

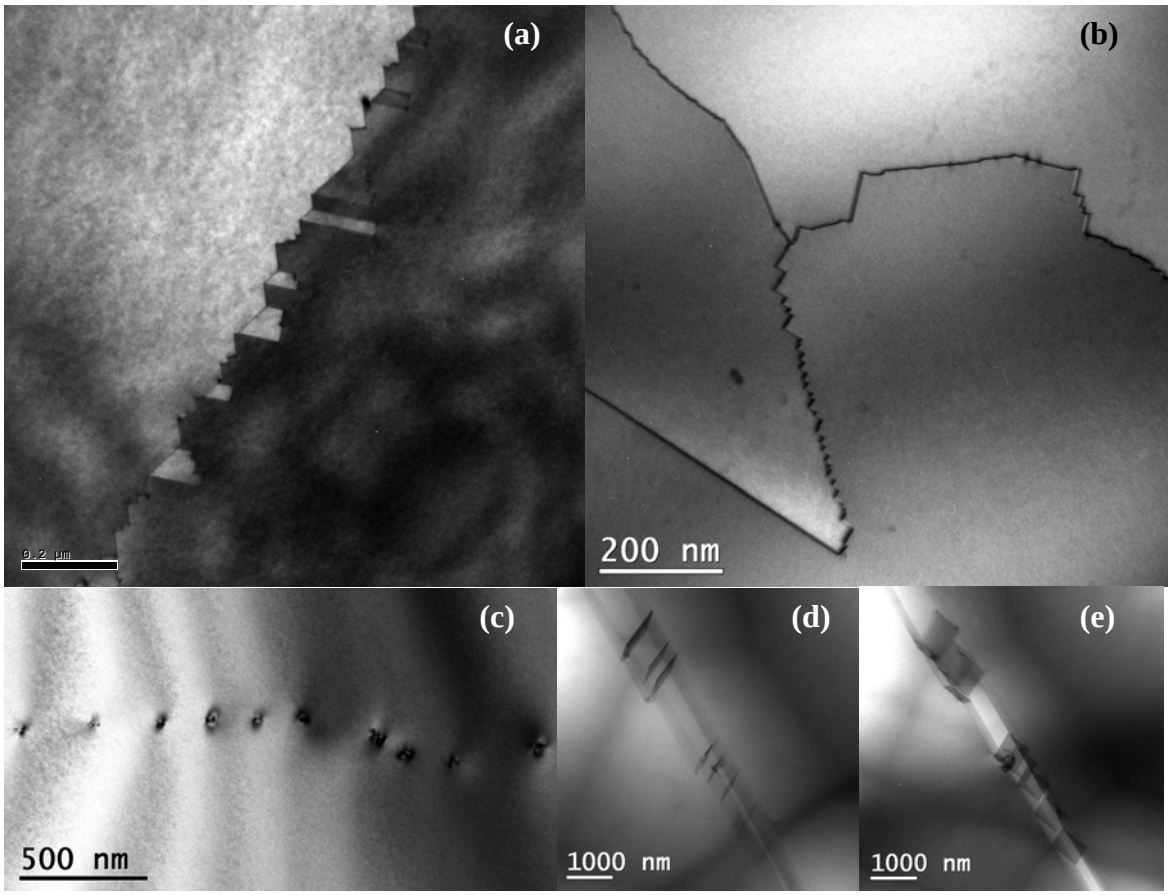

Figure 1. The grain structure in the bottom of the cast is dominated by small grains with steps (a) and (b), subgrains consisting of a row of dislocations (c), and stacking faults/twin structures (d) and (e).

Iron rich-precipitates

Iron has a very high precipitation barrier in silicon [3]. Even though the solubility of iron in silicon at room temperature is very low, ~ 10^{-24} cm^{-3}, concentrations of 10^{12}-10^{14} cm^{-3} interstitially dissolved iron paired with boron has been detected in p type silicon [4]. $FeSi_2$ precipitates have been found to form at temperatures of 500-600 °C and to dissolve at higher temperatures [5]. The iron-rich precipitates shown in Figure 2 and 3, were formed during the slow cooling of the solidified ingot. Iron has previously been detected in multi-metallic precipitates, frequently coprecipitated with nickel and copper [6-10]. The iron precipitates observed in this study are associated with strain and dislocation formation due to lattice mismatch or different thermal expansion coefficients. From the EDS analysis in Figure 3, the precipitates are found to consist of mainly Fe and small amounts of Ni in addition to silicon.

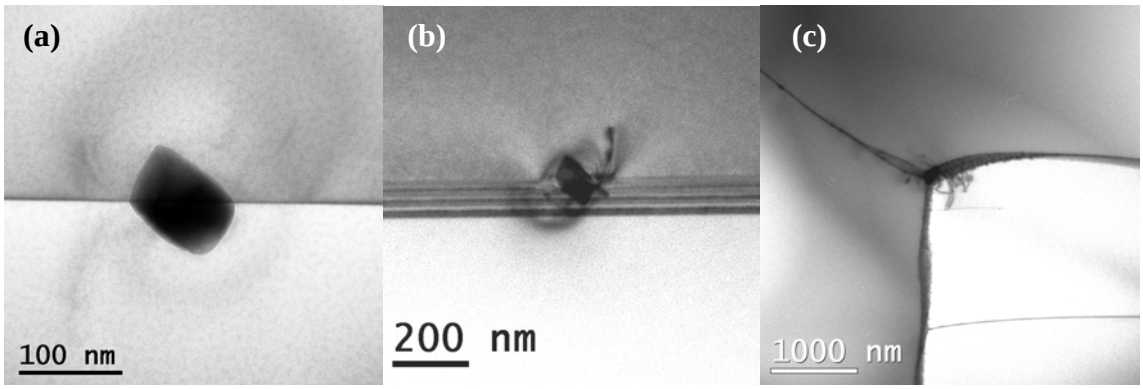

Figure 2. Iron-rich precipitates observed in grain boundaries. The precipitates cause a lot of strain as can be observed from the induced dislocations around the precipitates. (a) Grain boundary tilted edge on, (b) The Fe-rich precipitate tilted such that its dislocations are visible, (c) Fe-rich precipitate formed in a grain boundary triplet point.

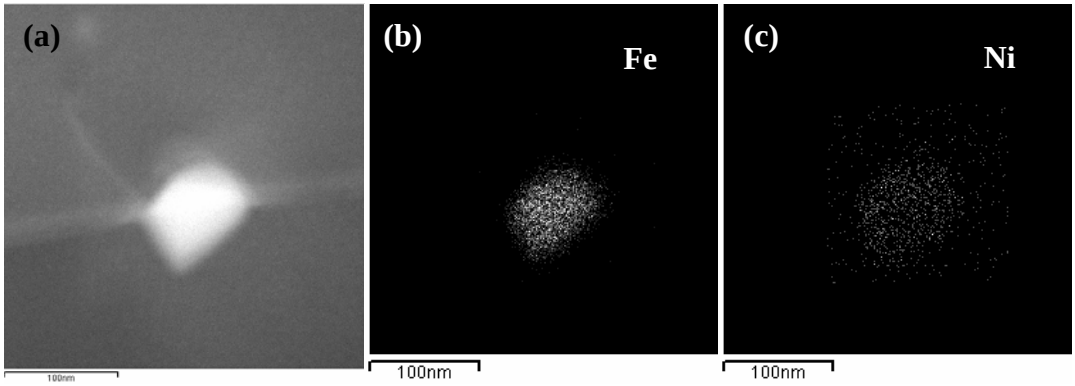

Figure 3. (a) Iron-rich precipitate consisting mainly of iron, (b), and small amounts of nickel, (c), in addition to silicon.

Copper silicide precipitates

Two types of copper silicide precipitates were observed in grain boundaries, disk shaped colonies, as shown in Figure 4, and solid disk shaped precipitates, as shown in Figure 5. Both types of precipitates have previously been observed in the grain boundary of a $\Sigma = 25$ bicrystal [11]. The strong STEM contrast of the precipitates in Figure 5(a) and (b), is mainly due to Z-contrast and the more diffuse contrast surrounding the precipitates is due to strain contrast. The small dots in the images, are due to surface contamination. Strong strain fields are evident around the precipitates in Figure 5(c). The strain fields arise because of the large volume extraction of 150 % associated with Cu_3Si precipitates formation [12].

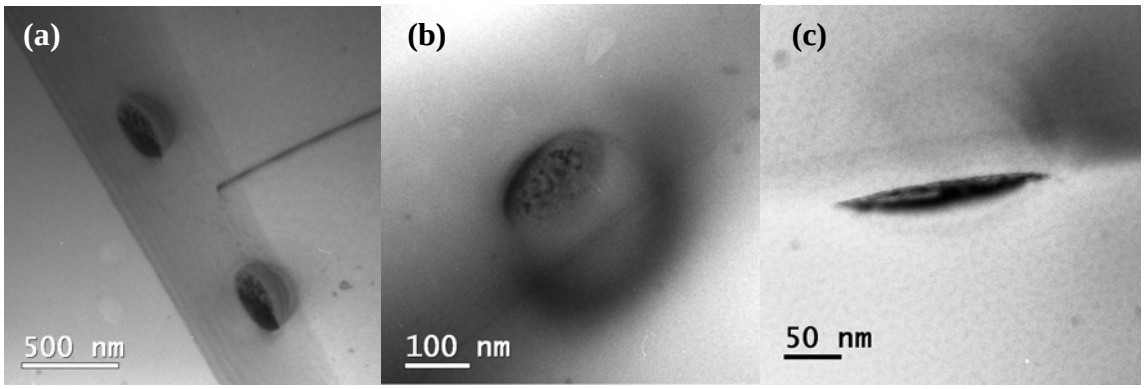

Figure 4. Disc shaped colony precipitates observed in grain boundaries.

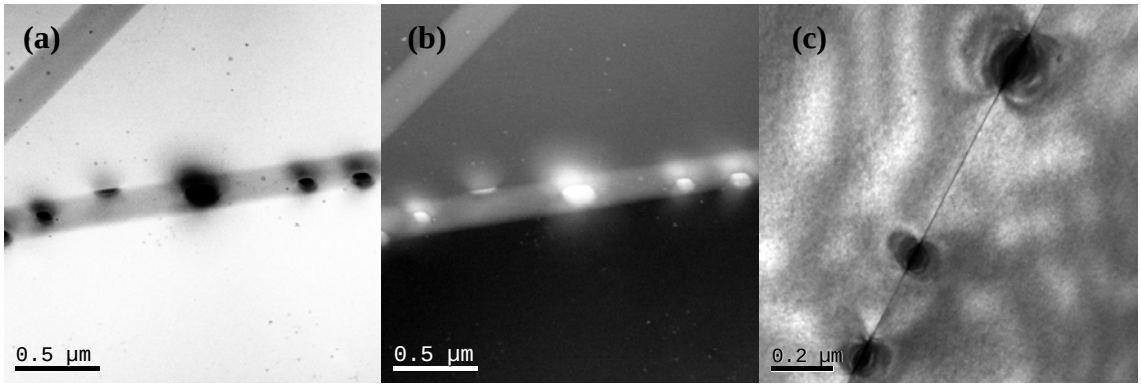

Figure 5. Disk shaped copper-rich platelets in a grain boundary. (a) Bright field STEM, (b) Dark field STEM, (c) Bright field TEM.

Copper precipitates were also frequently observed at positions where twins or stacking faults initiated from or ended in a grain boundary (arrows), as shown in Figure 6 and 7. The precipitates were found to contain Cu in addition to Si, as shown in figure 8.

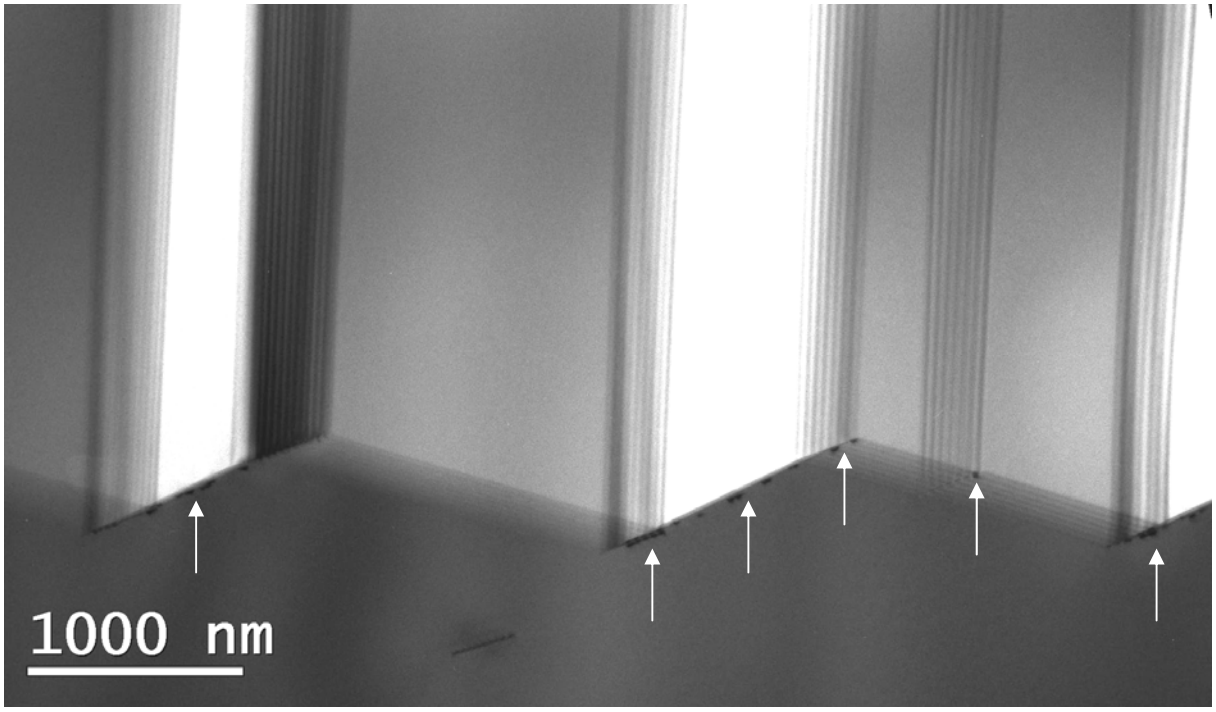

Figure 6. Stacking fault/twinning structure initiated at grain boundary steps. Notice the Cu-contamination at the interface between the stacking faults/twins and the grain boundary.

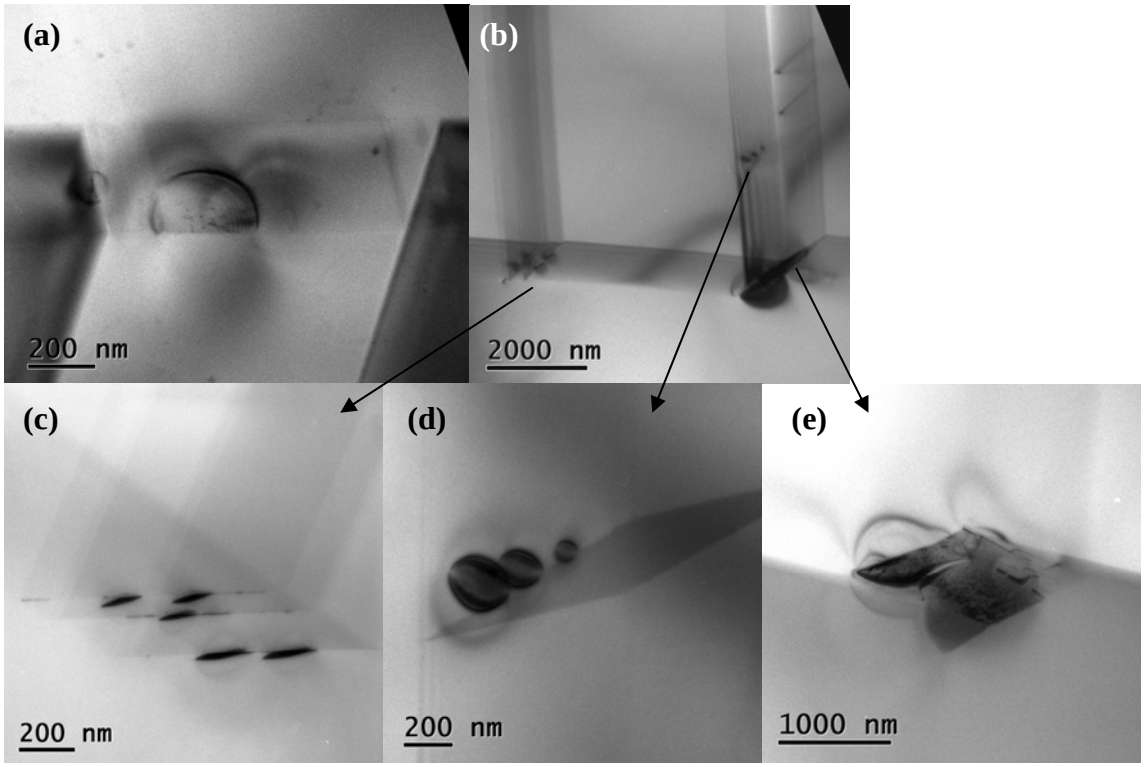

Figure 7. At the interface between the grain boundary and the stacking faults/twins several Cu platelet precipitates have formed.

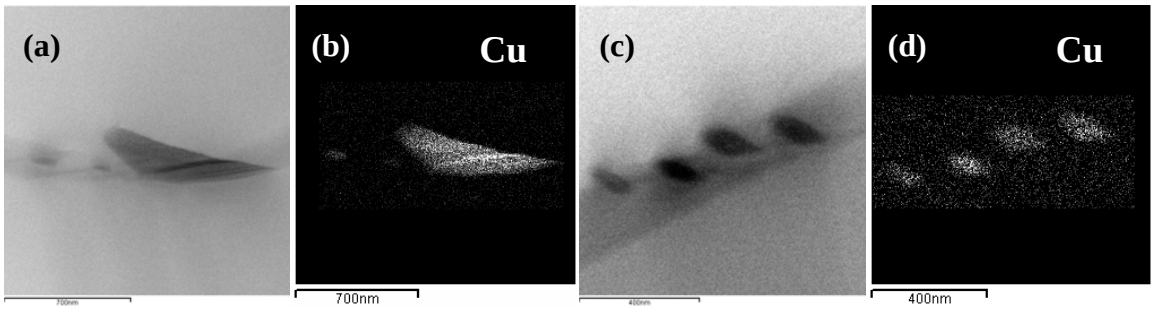

Figure 8. EDS-analysis of precipitates, (a) and (c), show that the defects contain copper, (b) and (d), in addition to silicon.

Multi-metallic clusters

Multi-metallic precipitates consisting of Cu and Ni were observed in ref [13]. Recently, multi metallic clusters containing Cu, Fe, and Ni have been observed and analysed with synchrotron X-ray and TEM [10, 14-15]. In Figure 9, a multi metallic cluster consisting of Cu_3Si precipitates and a Ni-Fe rich platelet precipitate can be observed.

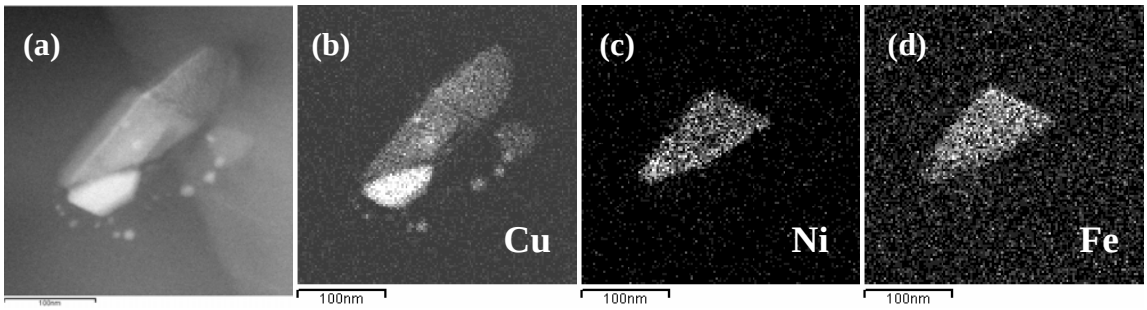

Figure 9. A large multi-metallic cluster was observed in a grain boundary. Most of the precipitates were copper-rich (b), but a platelet precipitate was found to consist of nickel (c) and iron (d) in addition to silicon.

Platelet defects

Platelet defects were observed in one of the samples, as shown in Figure 10 and 11(a). They were not studied with EDS, so their composition is unknown. Such platelet defects have been observed previously in as-grown samples [16]. However, whether they contain oxygen is not clear. The precipitates in Figure 11(b) are probably spherical amorphous SiO_2 precipitates [16].

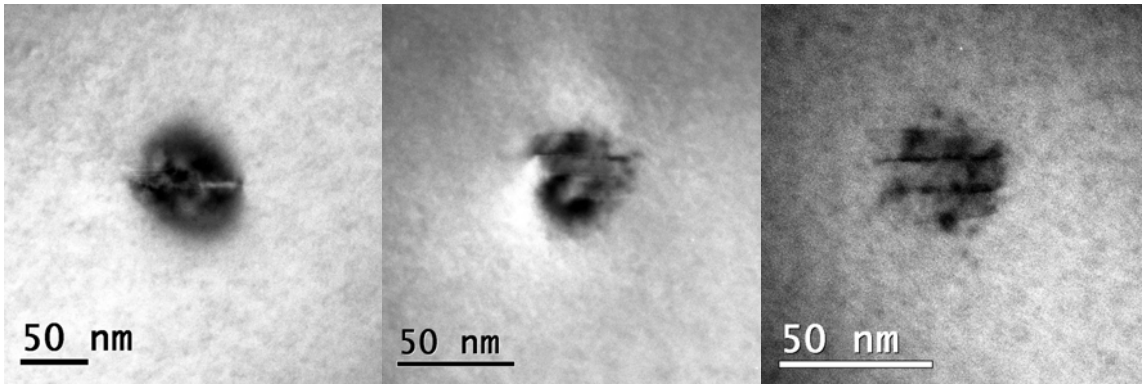

Figure 10. Platelet defects observed in the bulk silicon.

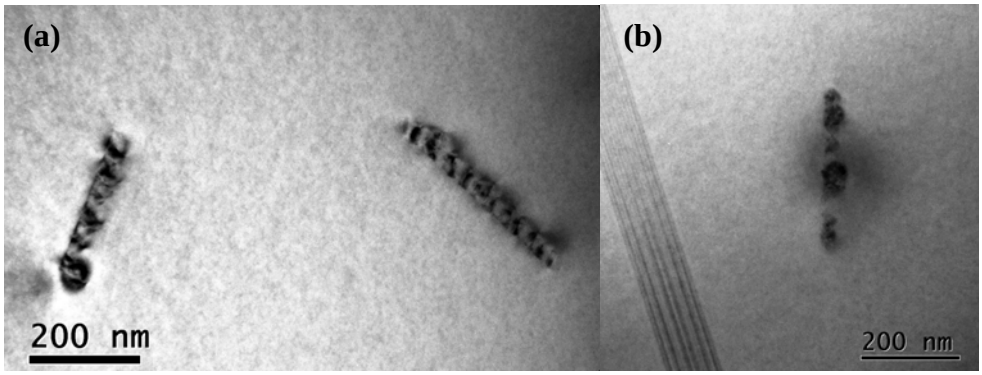

Figure 11. (a) Multi-platelet defects connected with dislocations, (b) Spherical precipitates on a dislocation.

This material was made using conventional poly-silicon feedstock, in contrast to the ingot studied in paper 1-3, where a metallurgical feedstock was used. The thermal history of the solidification and cooling is almost similar for the ingots, with a cooling rate of about 2 K/min

from high temperature. The difference in impurity precipitation is evident. In the material studied in this appendix, very few silicon oxide precipitates were observed. Only a few possibly contaminated dislocations, like the examples in Figure 10 and 11 were observed. No SiO_2 precipitates were observed in grain boundaries. This is in contrast to the material grown from metallurgical silicon where most grain boundaries and dislocations were heavily contaminated by oxides [10, paper 1-3]. This is probably due to the unusually high oxygen content in the ingot grown from metallurgical feedstock.

Apart from the oxides, mainly Ni-rich precipitates were observed in the ingot grown from metallurgical feedstock, sometimes with Cu nodule and usually containing a Fe rich core, Paper 1. Close to the bottom of the cast, the iron content in the Ni-rich precipitates was increased, Paper 2. This is probably due to the low content of Ni, compared to the high Fe content due to contamination from coating and crucible, in the bottom of the ingot. In this Ca contaminated ingot, the main part of the precipitates observed were copper silicide precipitates due to the high copper concentration that probably was incorporated during growth [2]. The copper silicides were frequently observed in some grain boundaries, probably random oriented or low angle grain boundaries [17], and where twins or stacking faults initiated from the grain boundaries. Also Fe-rich precipitates were observed in grain boundaries in a sample. They were found to be box shaped and associated with strain and dislocation formation. The Fe-rich precipitates contained small amounts of other metals, in particular Ni.

In conclusion, Fe and Ni are frequently found to coprecipitate, sometimes also with copper. The ratio between Ni and Fe in multi-metallic precipitates seems to reflect the current concentrations of the two species in the material. Ni probably lowers the nucleation barrier for Fe precipitation, due to reduced lattice mismatch, increased entropy or higher solubility of Fe in $NiSi_2$. Both silicon oxide and copper silicide precipitates are associated with a large volume expansion and form large platelet precipitates in grain boundaries when present in high concentrations.

[1] A. Borghesi, B. Pivac, A. Sastella and A. Stella, J. Appl. Phys. **77**, 4169 (1995)

[2] E. Olsen, H. Nordmark and E. Øvrelid, *Proceedings of the 20th European Photovoltaic Solar Energy Conference, Barcelona, Spain* p. 1082 (2005)

[3] M. D. Pickett and T. Buonassisi, Appl. Phys. Lett. **92**, 122103 (2008)

[4] T. Buonassisi, A.M. Lorenz, and G.J. Tarnowski, *Proc. 21st European Photovoltaic Solar Energy Conference and Exhibition*, *Dresden, Germany* p. 1505 (2006)

[5] D. A. Ramappa and W. B. Henley, J. Electrochem. Soc. **144**, 4353 (1997)

[6] K. Ryoo, R. Drosd and W. Wood, J. Appl. Phys. **63**, 4440 (1988)

[7] M. Heuer, T. Buonassisi, M. A. Marcus, A. A. Istratov, M. D. Pickett, T. Shibata and E.R. Weber, Phys. Rev. B **73**, 235204 (2006)

[8] M. Heuer, T. Buonassisi, A. A. Istratov and M. D. Pickett, J. Appl. Phys **101**, 123510 (2007)

[9] T. Buonassisi, M. Heuer, A. A. Istratov, M. D. Pickett, M. A. Marcus, B. Lai, Z Cai, S. M. Heald, E. R. Weber, Acta Materialia, **55**, 6119 (2007)

[10] H. Nordmark, M. Di Sabatino, E. J. Øvrelid, J. C. Walmsley and R. Holmestad, *Proceedings of the 22nd European Photovoltaic Solar Energy Conference, Milano, Italy* (2007)

[11] A. Ihlal and G. Nouet, Phys. Stat. Sol. A **141**, 81(1994)

[12] Seibt, V. Kveder, W. Schröter and O.Voß, Phys. Stat. Sol. (a) **202**, 911 (2005)

[13]K. Ryoo, R. Drosd and W. Wood, J. Appl. Phys. **63**, 4440 (1988)

[14] M. Heuer, T. Buonassisi, M. A. Marcus, A. A. Istratov, M. D. Pickett, T. Shibata and E.R. Weber, Phys. Rev. B **73**, 235204 (2006)

[15] M. Heuer, T. Buonassisi, A. A. Istratov and M. D. Pickett, J. Appl. Phys **101**, 123510 (2007)

[16] H. J. Möller, L. Long, S. Riedel, M. Rinio, D. Yang and M. Werner, *Proceedings of the 7th Workshop on the Role of Impurities and Defects in Silicon Device Processing, National Renewable Energy Laboratory, Golden, USA*, pp 41-50 (1997)

[17] T. Buonassisi, A. A. Istratov and M. D. Pickett, Appl. Phys. Lett. **89**, 042102 (2006)

Appendix B: Attachment to article 5

Raman and SIMS analysis of H plasma treated n and p type Czochralski silicon

Some of the samples studied in paper 4-5 were later studied by SIMS and Raman spectroscopy. The table below, using the same sample labelling as in the papers, lists all the samples studied. In addition two new p-doped samples, H plasma treated at lower temperatures, 180 °C and 120 °C for U1 and U2 respectively, are introduced. These new p-type samples were studied with SEM and TEM and compared with samples S4 and I.2/I.4 (from paper 7) to find the connection between H plasma temperature and H defect formation in the silicon sample subsurface.

Raman spectra were recorded with a multichannel spectrometer from Horiba (Jobin Yvon) model T 64000, employing a single monochromator with CCD detector at room temperature. The spectra were excited by a Milennia Pro diode-pumped ($Nd:YVO_4$ crystal) laser from Spectra-Physics (Model J 40) adjusted to give approximately 100 mW of the 532 nm line on the sample. A slit of 200 μm was used and the resolution used was ca. 2 cm^{-1}. All spectra were normalised to the maximum of the optical Si phonon line at ~ 520 cm^{-1}, and the background luminescence was subtracted from the data.

Secondary ion mass spectrometry (SIMS) was used for analysis of the hydrogen/deuterium distributions (CAMECA ims 7f instrument) in negative secondary ion mode with a 15 keV Cs^+ primary beam. The raw SIMS profiles are given as sputter time versus secondary ion intensity. The sputter time is related to depth and the conversion factor is determined by measuring the SIMS craters with a Dektak 8 surface stylus profilometer assuming a linear dependence.

Table 1. Processing parameters and H^+ plasma treatment of the samples. No means that the sample is not post annealed, denoted as 0_0 in the text.

	Sample	H^+ plasma treatment	Post annealing
U2	p-type 1 Ωcm	1h, 120 °C 110 MHz	No
U1	p-type 1 Ωcm	1h, 180 °C 110 MHz	No
S1	n-type 1.8-2.6 Ωcm	1h, 250 °C 110 MHz	No, 1h at 200-1000 °C, 100 °C step, 10 h at 200-600 °C, 100 °C step, 20 h 400 °C
S2	n-type 0.005-0.018 Ωcm	1h, 250 °C 110 MHz	No, 1h at 200-1000 °C, 100 °C step, 10 h at 200-600 °C, 100 °C step, 20 h 400 °C
S3	n-type 1.8-2.6 Ωcm	2 h, 250 °C 13.56 MHz	No, 1h at 200-1000 °C, 100 °C step, 10 h at 200-600 °C, 100 °C step, 20 h 400 °C
S4	p-type 1-10 Ωcm	0.5 h, 250 °C 110 MHz	No, 1h at 200-1000 °C, 100 °C step, 10 h at 200-600 °C, 100 °C step, 20 h 400 °C
I.2/I.4	p-type 10 Ωcm	1h, 250 °C 110 MHz	No/2h 450 °C
S5	p-type 10-20 Ωcm	1h, 250 °C 110 MHz	No, 1h at 200-1000 °C, 100 °C step, 10 h at 200-600 °C, 100 °C step, 20 h 400 °C

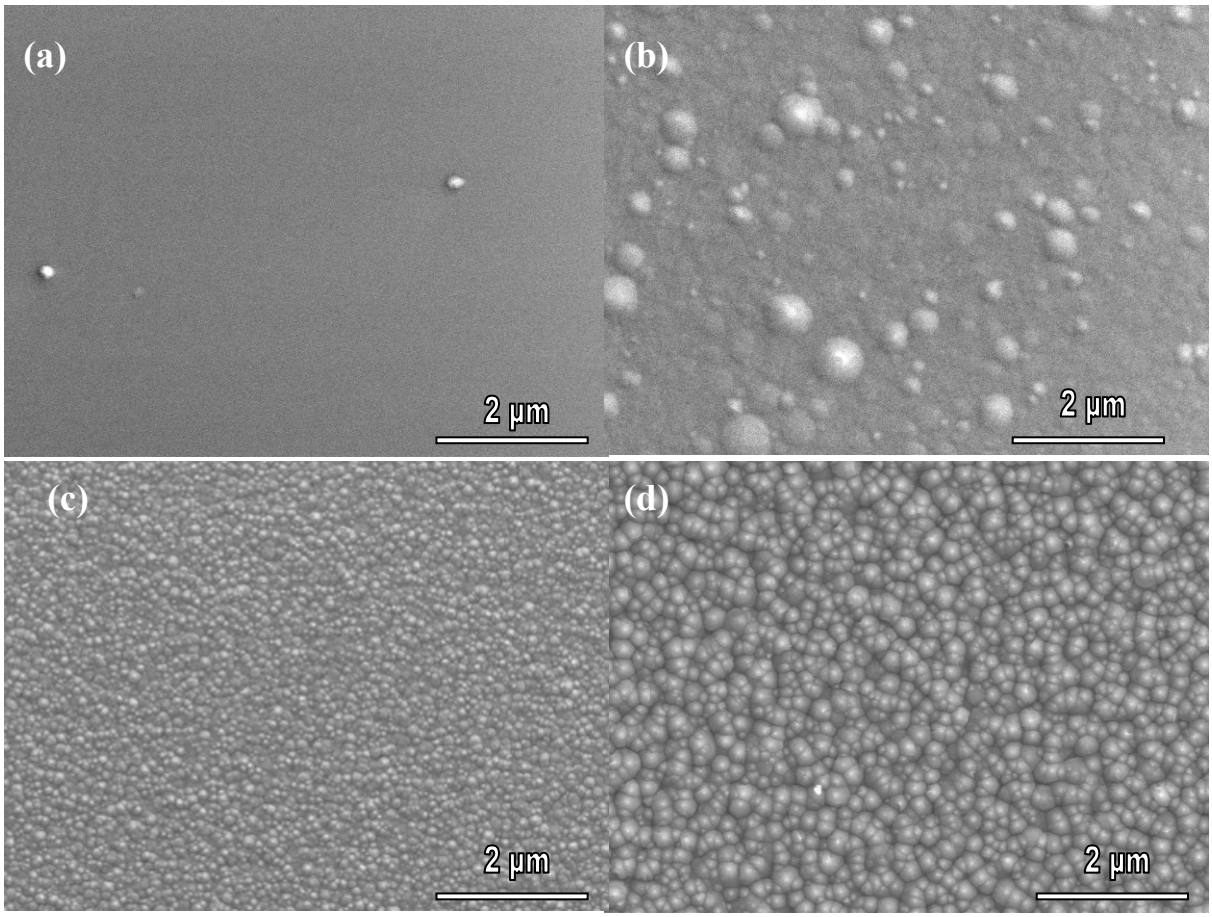

Figure 1. Surface structure as observed with SEM, (a) U2, (b) U1, (c) S4, (d) I.2.

In Figure 1, SEM images of the surface morphology of four p-doped samples with similar doping level and different H^+ plasma treatment conditions are shown. Figure 1(a) shows the non-etched surface of sample U2, H^+ plasma treated at 120 °C. After 1 hour H plasma treatment at 180 °C, a low density of cones is observed on the surface of sample U1, as shown in Figure 1(b). In Figure 1(c) and (d), samples S4 and I.2, H^+ plasma treated at 250 °C for 0.5 and 1 hours respectively are shown. The cones are found to cover the surface of both samples, but the cones are larger on the sample surface of the sample plasma treated for 1 hour.

Figure 2 (a)-(c) show TEM images of samples U1, S4 and I.2, respectively. No defects were observed in U2. In U1 a high density of small defects, ~ 20 nm, was observed, formed up to about 1.2 µm below the surface. In sample S4 and I.2 the microstructure is similar. Large platelets, 50-500 nm, are formed up to ~ 0.7 µm below surface. Lower substrate temperature during H plasma treatment gives a higher density of small platelets formed deeper into the bulk.

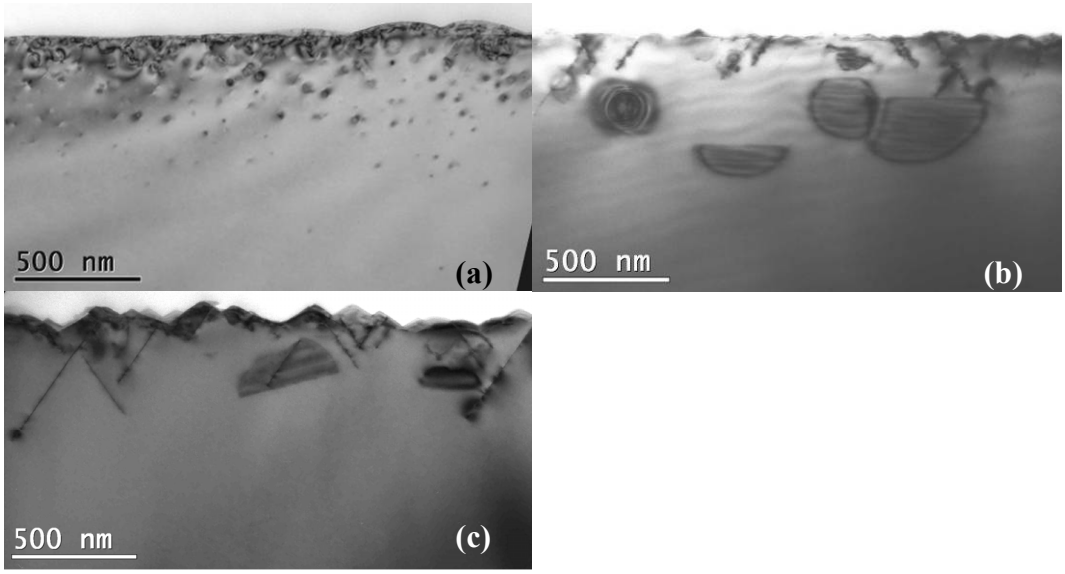

Figure 2. Microstructure as observed with TEM in samples (a) U1, (b) S4, (c) I.2.

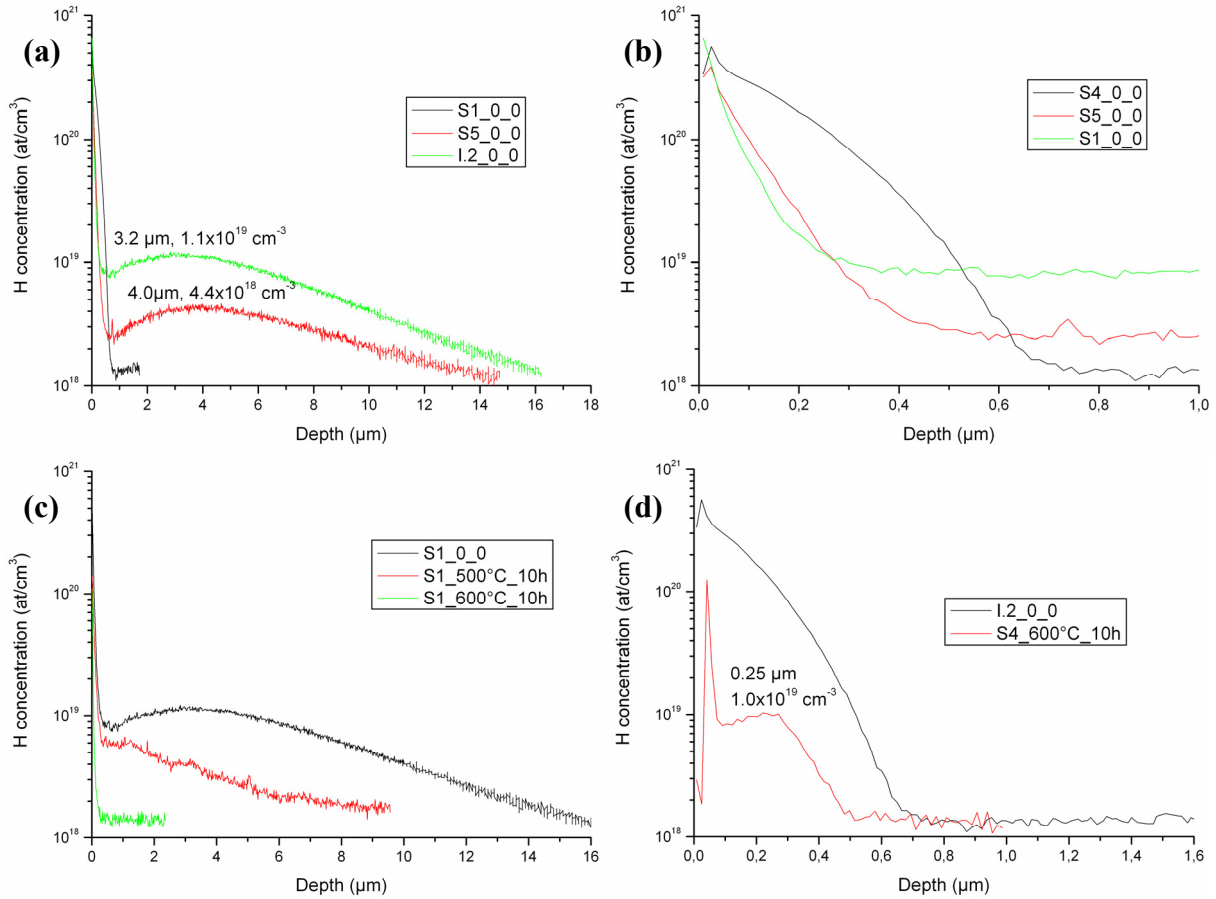

Figure 3. Hydrogen concentrations in hydrogen plasma treated samples measured by SIMS, (a) selected n and p type samples, (b) near-subsurface area, (c) S1 after post annealing (d) I.2 and S4 after post annealing.

Figure 3 shows spectra from the samples analyzed with SIMS. Sample I.2_0_0 is similar to S4_0_0 except for having twice as long hydrogenation time. The hydrogen detection limit is 10^{18} cm^{-3}. From Figure 3(a) it is observed that after hydrogenation, S1 and S5 show similar H

concentration profile with a second peak about 3-4 μm into the bulk and that hydrogen is detected up to about 12-15 μm into the bulk. In I.2_0_0, however, the hydrogen concentration drops rapidly below the detection limit already at about 0.7μm depth. Figure 3(b) shows the hydrogen profile of the samples in the near-surface area. After 1 hour hydrogenation at 250 °C, the samples contain about 1 %, or $5x10^{20}$ cm^{-3}, hydrogen in the top layer, decreasing rapidly down to 0.1 % at about 0.2-0.5 μm depending on sample doping and type. The hydrogen concentration drops faster in S1 and S5 than in S4. Hydrogen profiles after post annealing are shown for sample S1 and S4 in Figure 3(c) and (d) respectively. Sample S4 is similar to I.2, except from shorter hydrogenation duration, 0.5 h, compared to 1h. After annealing at 500 °C for 10 hours in air, hydrogen is still present in the n-type Si sample S1_0_0, but the second peak is found closer to the surface of the sample, at about 1μm below surface, and the hydrogen drops below detection limit at ~ 10 μm. After 10 hours annealing at 600 °C, almost no hydrogen is detected in S1, while in S4 a second peak at about 0.2 μm depth can be observed in Figure 3(d).

The difference in hydrogen profile for p-doped samples I.2/S4 and S5 is most likely due to the difference in doping level. Boron is well known to effectively trap hydrogen by forming B^--H^+ complexes [1, 2] which are stable up to ~ 250 °C. As a result, hydrogen diffuses deeper into the bulk in a low doped sample. Also phosphorus can trap hydrogen by forming P^+-H^- complexes, but this is less probable and the complexes are less stable. As a result, H diffuses further into the bulk in S1. An early SIMS study of deuterium [2] showed the connection between doping and diffusion. In most cases, the H concentration of n and p type samples was found to decay exponentially with depth. However, p type samples, with resistivity 0.1 and 1 Ωcm, showed trap dependent diffusivity [2]. Also the substrate temperature changed the profile [2]. Because of the very low solubility of hydrogen in silicon [3], high concentrations of in-diffused hydrogen result in hydrogen induced defect formation in the subsurface of the samples. Comparing the H concentration profiles of sample S1, I.2, S4 and S5 with the TEM observations in paper 4 and 5, there is a strong connection between the hydrogen concentration peaks and the hydrogen platelet formation. In sample S4/I.2, the platelets are formed up to ~ 0.7 μm deep into the samples, while in sample S1 and S5, a low density of large platelets is observed several μm into the sample. The density of platelets formed deep into the sample is higher in S1 than in S5, in accordance with the higher concentration of H observed in S1 than in S5 in this region.

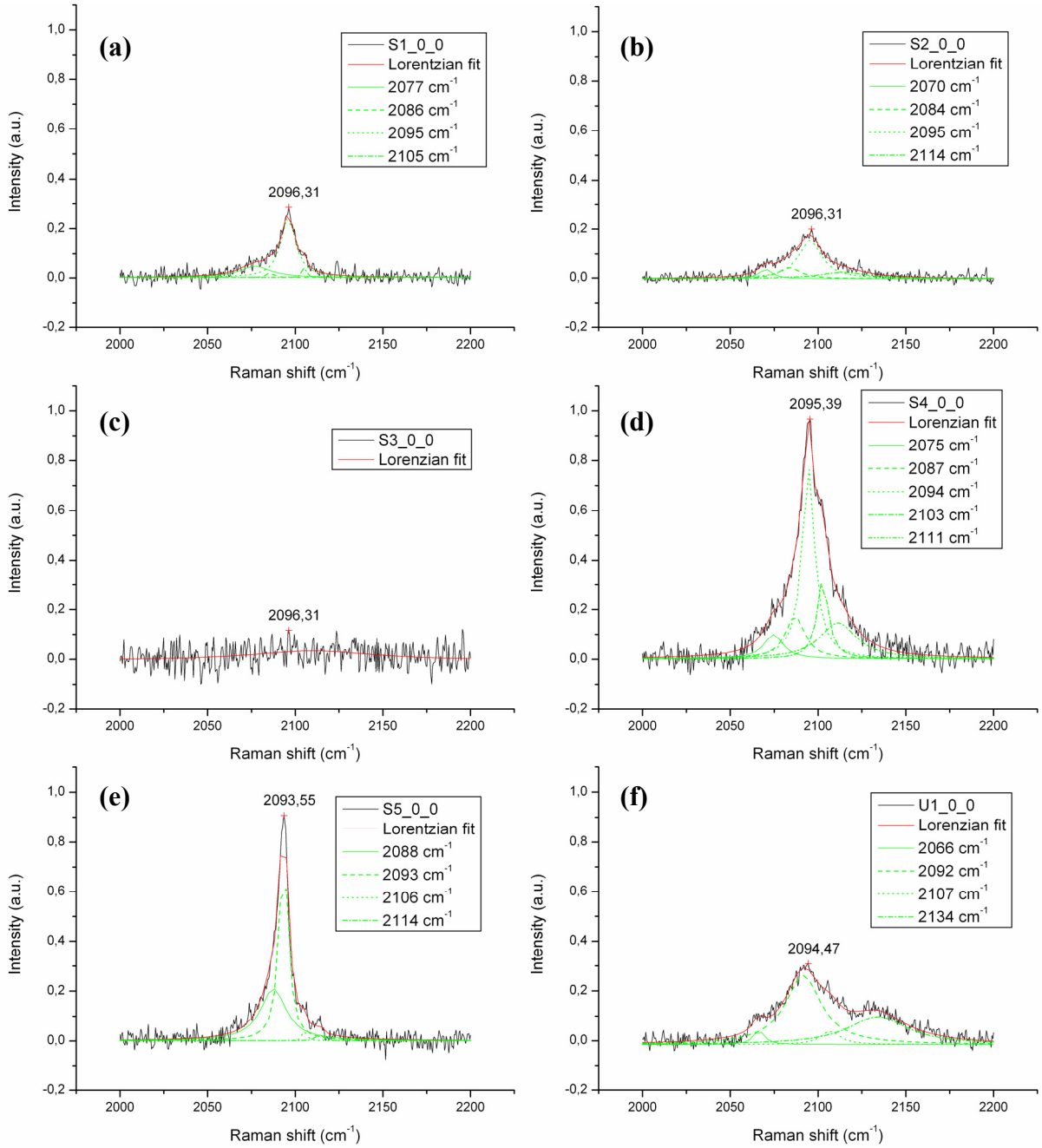

Figure 4. Raman spectra after hydrogenation for the 6 plasma treated samples, (a) S1_0_0, (b) S2_0_0, (c) S3_0_0, (d) S4_0_0, (e) S5_0_0 and (f) U1_0_0.

Figure 4 shows Raman spectra from the samples. The spectrum from U2 is not shown since no hydrogen was detected. The spectra consist of several peaks, as shown by the green lines found by Lorentzian fit (red) of the curves (black). The different lines are due to different Si-H_x complexes where x varies from 1-4 and are relatively shifted due to different internal stresses in the supersaturated subsurfaces [4]. The dominant peak in all samples after H plasma treatment, is ~ 2095 cm^{-1}. After 1 hour post annealing at 300 °C the hydrogen peak lowers slightly, but the shape is similar, indicating that the hydrogen bonds are stable at this temperature. However, after 1 h post annealing at 400 °C, only bonds in S4 are found to be stable, as shown in Figure 5. No hydrogen bonds were observed in S3. U1 (and U2) were not post annealed at this temperature. After 20 hours post annealing of S4 at 400 °C, the peak at

2095 cm^{-1} is strongly reduced and the peak at 2106 cm^{-1} dominates, Figure 6(a). After 1 hour annealing at 600 °C, SiH_x bonds are still detected in this sample as shown in Figure 6(b).

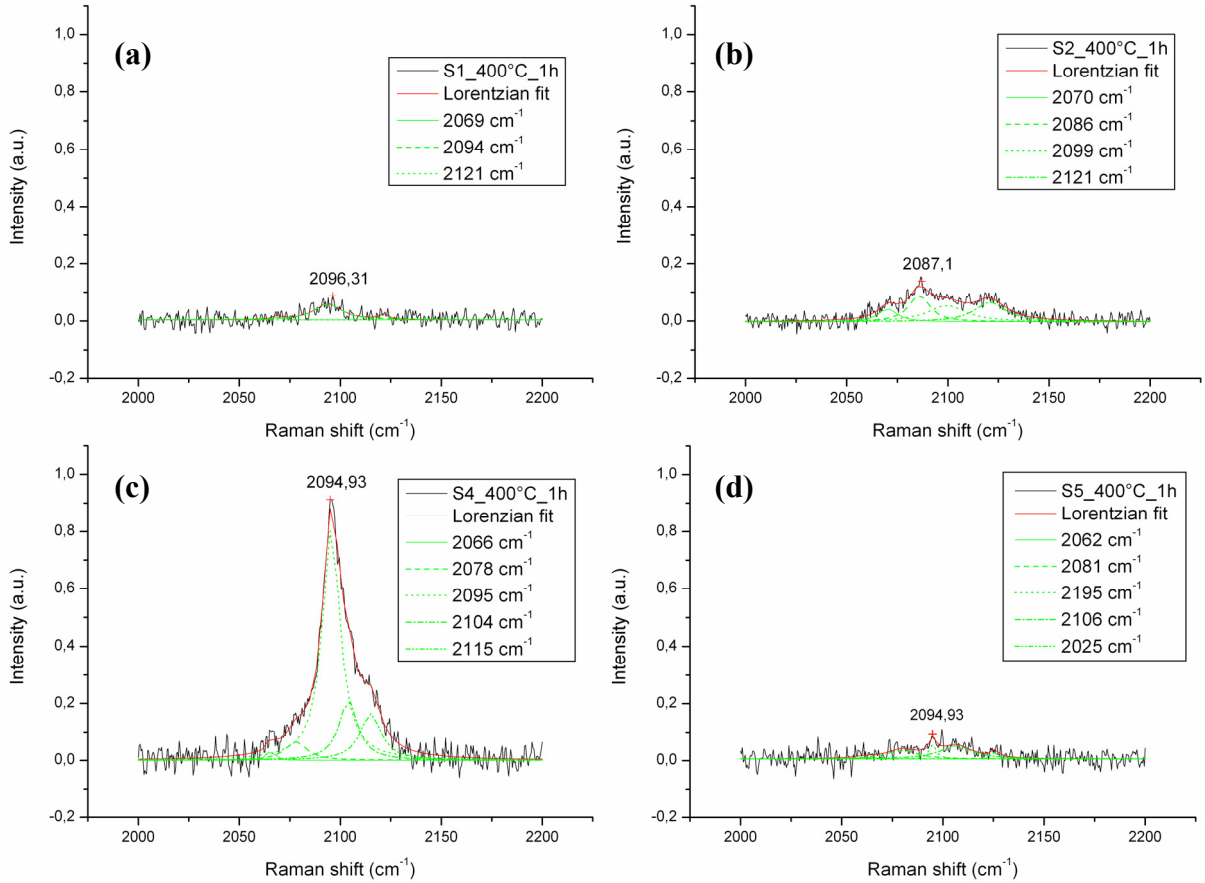

Figure 5. Hydrogen bonds studied by Raman in H plasma treated samples after 1 hour post annealing at 400 °C, (a) S1_400 °C_1h, (b) S2 _400 °C_1h, (c) S4_400 °C_1h, (a) S5_400 °C_1h

Doping type and level affect the Si-H_x bonds being formed, as has also been shown earlier [4-9]. Samples plasma treated with a frequency of 13.56 MHz have been found to contain the same amount of Si-H bonds as samples plasma treated with a frequency of 110 MHz [4]. This is not the case in this study, where hardly any Si-H bonds were observed in the low frequency treated sample S3. In this study several Si-H_x bond peaks were observed as indicated in the Raman spectra. Some of the peaks were very weak and some might be a combination of two or more overlapping peaks that were not resolved. It is hard to draw conclusions of the origin of all the peaks from these measurements. However, earlier studies of temperature evolution of the different Si-H_x bonds on bevelled samples have assigned them to hydrogen induced platelets at different stages of development [8,9]. Si-H bonds with a vibration frequency of about 2095 cm^{-1}, were assigned to the direct plasma damage layer at the top 200 nm of the substrate. Such bonds were found to be stable up to ~ 350 °C [5,9]. The peak at ~ 2105 has been assigned to Si-H_2 bonds at the platelets inner surface at a final stage, and was found to be the most stable bond above 450 °C [9]. Peaks at 2065-2075 cm^{-1} are assigned to pairs of hydrogen atoms saturating broken bonds between adjacent planes; Si-H bonds in platelets with small to medium distances between two inner surfaces of $[2Si\text{-}H]_n$ structures at an early stage [8]. Peaks at 2130 cm^{-1} and 2140 cm^{-1} are assigned to either vertical Si-H_2 steps or Si-H_3 at the inner surfaces of platelets formed at an early stage. The subpeak at 2120 cm^{-1} has

previously been assigned to Si-H species located on the inner surfaces of H_2 containing platelets formed at an intermediate stage [8]. The subpeak at 2110 cm^{-1} has been assigned to the Si-H bonds at the inner surface of the hydrogen induced platelets [5]. The observed peak at ~ 2086 cm^{-1} is very close to a peak at 2088 cm^{-1}, previously observed on a blister after annealing at 600 °C that was assigned to Si-H_x (X=1-3) bonds on internal surfaces of the platelets [6]. This peak can also be due to change of the void shape, due to the formation of rougher platelets or blisters at high temperatures [7].

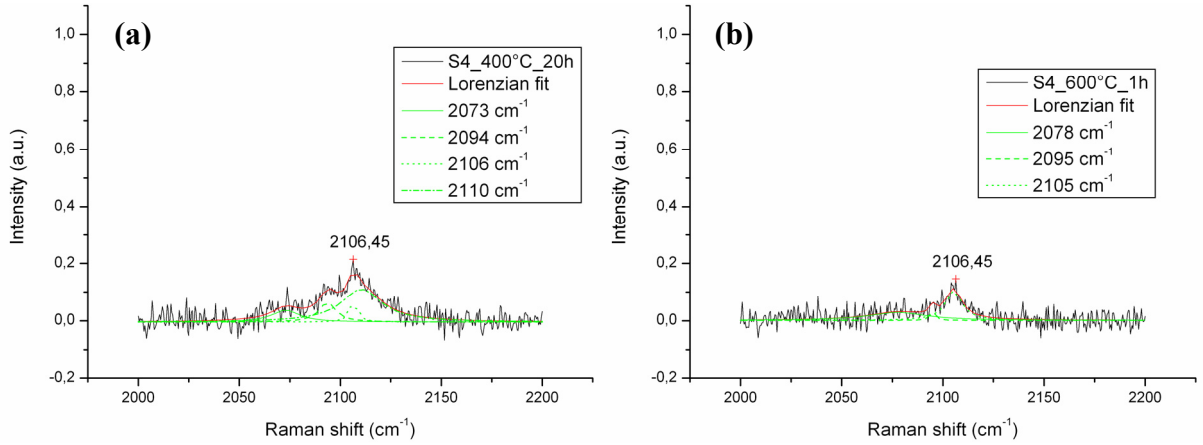

Figure 6. Hydrogen bonds detected by Raman in sample S4 after post annealing (a) 20 hours at 400 °C and (b) 1 hour at 600 °C.

The hydrogen profile observed fits well to the microstructure observed with SEM/TEM. The upper 0.2 µm of the samples consisting of surface cones and numerous defects caused by the plasma is found to be hydrogen rich, both from SIMS and Raman. After annealing at 400 °C for 1 hour, the small defects at the surface are almost annealed out in all samples, except from in S4, where no change is observed. S4 is also the only sample where the hydrogen bonds are stable after this annealing. However, after 20 hours annealing at 400 °C also in this sample the 2095 cm^{-1} peak is strongly reduced, and the peak at ~ 2106 cm^{-1} dominates. This peak, that has been found to be the most stable peak in other studies, is also the dominating peak in S4 after 1 hour annealing at 600 °C. S4, which is the only sample where the platelets in the subsurface are stable after annealing at 600 °C, still contains a large amount of hydrogen in the subsurface, while the hydrogen content is below detection limit in the similar doped n type sample S1.

[1] S.J. Pearton, J. W. Corbett and T. S. Shi, Appl. Phys. A, **43**, 153 (1987)

[2] J. W. Corbett, J. L. Lindstrøm, S. J. Pearton and A. J. Tavendale, Solar Cells, **24**,127 (1988)

[3] A. Van Wieringen and N. Warmoltz, Physica, **22**, 849 (1956).

[4] A. G. Ulyashin, R. Job, W. R. Fahrner, O. Richard, H. Bender, C. Clayes, E. Simoen and D. Grambole, J. Phys.: Condens. Matter. **14**, 13037 (2002)

[5] Y. Ma, R. Job, Y. L. Huang, W. R. Fahrner, M. F. Beufort and J. F. Barbot, J. Electrochem. Soc. **151**, G627 (2004)

[6] W. Düngen, R. Job, Y. Ma, Y. L. Huang, T. Mueller, W. R. Fahrner, L. O. Keller, J. T. Horstmann and H. Fiedler, J. Appl. Phys. **100**, 034911 (2006)

[7] W. Düngen, R. Job, T. Mueller, Y. Ma, W. R. Fahrner, L. O. Keller, J. T. Horstmann and H. Fiedler, J. Appl. Phys. **100**, 124906 (2006)

[8] Y. Ma, Y. L. Huang, W. Düngen, R. Job and W. R. Fahrner, Phys. Rev. B **72**, 085321 (2005)

[9] Y. Ma, Y. L. Huang, R. Job and W. R. Fahrner Phys. Rev. B **72**, 085321 (2005)

Appendix C: Attachment to article 7

SIMS analysis of H^+ implanted and Si^+ implanted + H plasma treated p-type Czochralski silicon

Three different samples studied in paper 7, i) I.2 H^+ plasma treated for 1 hour at 250°C, 110 MHz, 200 sccm and 50 W, ii) I.3 Si^+ implanted with a dose of 10^{15} cm^{-2} and then the same H plasma treatment as sample 1.2 and iii) II.3 H^+ implanted with a dose of 3 x 10^{16} cm^{-2} were chosen for Secondary Ion Mass Spectroscopy (SIMS) analysis. The aim was to show that it is possible to archive the same hydrogen profile by using a combination of low dose ion implantation combined with hydrogen plasma treatment, as archived by using solely a higher dose of H^+ implantation.

SIMS analysis of the hydrogen distributions (CAMECA ims 7f instrument) was performed in negative secondary ion mode with a 15 keV Cs^+ primary beam. The raw SIMS profiles are given as sputter time versus secondary ion intensity. The sputter time is related to depth and the conversion factor is determined by measuring the SIMS craters with a Dektak 8 surface stylus profilometer assuming a linear dependence. The depth resolution is 10-20 nm and the hydrogen sensitivity limit was ~ 10^{18} cm^{-2} for the hydrogen measurements.

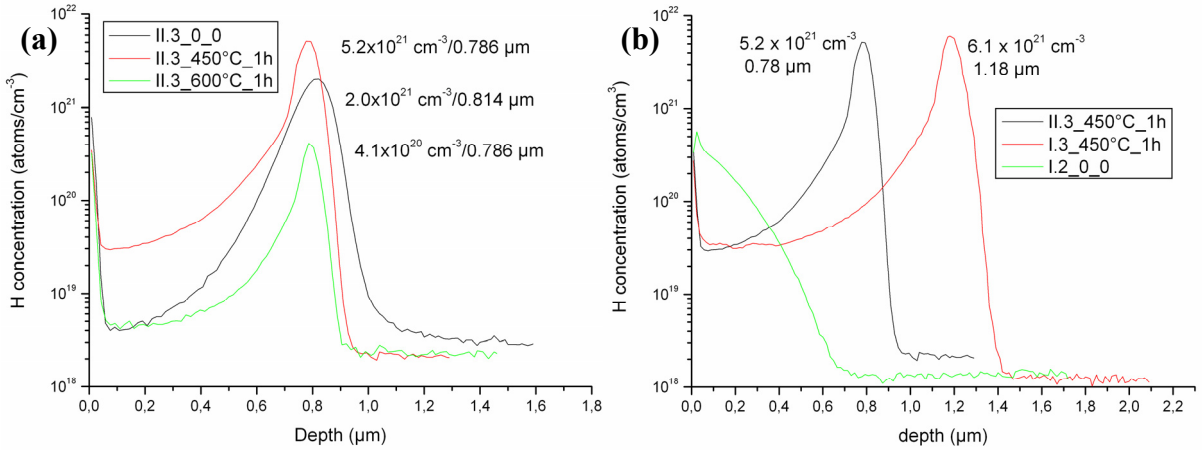

Figure 1. Hydrogen concentrations in (a) Hydrogen implanted sample for different post annealing and (b) Comparison between H plasma treated sample (green), H implanted sample (black) and H implanted + H plasma treated sample (red).

Figure 1(a) shows the hydrogen profile in the H^+ implanted sample II.3 after different post annealing temperatures. After implantation a broad H-peak at ~ 0.8 µm depth is observed. After 1 hour annealing at 450 °C the maximum H concentration has increased, the peak is sharper and slightly shifted towards shallower depth. The lattice damage peak after implantation has been found to be located slightly shallower than the H concentration peak [1]. The concentration peak shift towards shallower level suggest that the H is trapped by damage from the implantation, as also previously observed [1,2]. After 1 hour annealing at 600 °C, the shape of the peak is the same as for 450 °C or slightly sharper, but the overall hydrogen content is lowered. Just after implantation most of the hydrogen is collected in a broad peak.

Upon annealing, some of the hydrogen diffuses deeper into the sample, while some diffuses towards the sample surface [1]. The increase in hydrogen concentration in the peak after annealing proves that H atoms diffuse to and are trapped in this region during annealing at 450 °C, probably due to the growth of H induced platelets, observed by TEM in this area. At 600 °C the overall hydrogen content is lowered due to out diffusion of hydrogen, such that the H trapped by the damage at shallow depths is released. However, temperature evolution studies of hydrogen platelet formation in H plasma treated samples have shown that in 1-10 Ω cm p doped Si the platelets, both {111} and {100} were found to be stable at 600 °C, paper 4, and {100} oriented platelets, which dominate in this samples, have previously been found to be more stable than {111} platelets, up to above 600 °C [3]. A large amount of silicon is therefore still expected to be trapped in platelets at this temperature.

In Figure 1(b) the hydrogen profile of the three samples can be compared. Both hydrogen content and hydrogen profile are qualitatively similar for I.3 and II.3. The shift in depth of the peak concentration is due to the difference in voltage and implantation depth for the hydrogen and silicon ions used. The H profile of the solely H plasma treated sample I.2, is significantly different. The observed hydrogen profiles fits well to the microstructure observed with TEM in paper 7, where the hydrogen-induced platelets are located at the same depth as the maximum concentration of hydrogen. This proves that structural defects, preferentially vacancies, act as sinks for the H atoms, lowering the nucleation barrier for H induced platelet formation, in accordance with earlier results [2].

[1] T Höchbauer, PhD thesis, *On the Mechanisms of Hydrogen Implantation Induced Silicon Surface Layer Cleavage,* Philipps-Universität Marburg, (2001)

[2] A. Y. Usenko and A. G. Ulyashin, Jpn. J. Appl. Phys. **41**, 521 (2002)

[3] R. Job, M. F. Beaufort, J.-F. Barbot, A. G. Ulyashin and W. R. Fahrner, Mat. Res. Soc. Symp. Proc. **719**, 217 (2002)